Evolutionary Biomechanics of the Rostrum of *Curculio* Linnaeus, 1758

(Coleoptera: Curculionidae)

by

Michael Andrew Jansen

A Dissertation Presented in Partial Fulfillment
of the Requirements for the Degree
Doctor of Philosophy

Approved April 2019 by the
Graduate Supervisory Committee:

Nico Franz, Chair
Nikhilesh Chawla
Jon Harrison
Emilia Martins

ARIZONA STATE UNIVERSITY

May 2019

ABSTRACT

Weevils are among the most diverse and evolutionarily successful animal lineages on Earth. Their success is driven in part by a structure called the rostrum, which gives weevil heads a characteristic "snout-like" appearance. Nut weevils in the genus *Curculio* use the rostrum to drill holes into developing fruits and nuts, wherein they deposit their eggs. During oviposition this exceedingly slender structure is bent into a straightened configuration – in some species up to 90° – but does not suffer any damage during this process. The performance of the snout is explained in terms of cuticle biomechanics and rostral curvature, as presented in a series of four interconnected studies. First, a micromechanical constitutive model of the cuticle is defined to predict and reconstruct the mechanical behavior of each region in the exoskeleton. Second, the effect of increased endocuticle thickness on the stiffness and fracture strength of the rostrum is assessed using force-controlled tensile testing. In the third chapter, these studies are integrated into finite element models of the snout, demonstrating that the *Curculio* rostrum is only able to withstand repeated, extreme bending because of modifications to the composite structure of the cuticle in the rostral apex. Finally, interspecific differences in the differential geometry of the snout are characterized to elucidate the role of biomechanical constraint in the evolution of rostral morphology for both males and females. Together these studies highlight the significance of cuticle biomechanics – heretofore unconsidered by others – as a source of constraint on the evolution of the rostrum and the mechanobiology of the genus *Curculio*.

DEDICATION

To my loving parents, Mr. & Mrs. Michael and Susan Jansen, who taught me to be adventurous and steadfast in my pursuits.

To my younger brothers, Douglas and Phillip Jansen, who gave me patience, responsibility, and resilience.

To my partner, Karla Franco, who accompanied me selflessly through every journey, every hardship, and every success.

To my teachers, who showed me the great value of intellectual curiosity.

"Light is the task where many share the toil."

– Homer

ACKNOWLEDGMENTS

There are a great many people to whom I am indebted for their incredible kindness, generosity, and assistance rendered during the course of the past five years. This dissertation could not have been completed without them.

First and foremost I thank my parents and little brothers, to whom I have dedicated this work, for their constant encouragement and understanding of my intellectual pursuits. My family has been a source of unwavering support throughout my graduate studies, and I cannot thank them enough for the gift of simply being present when I needed them most. Likewise, I am forever grateful to my friends, lab-mates, and partner – the family I chose – I am privileged to have you by my side and lifting my spirits.

My advisor, Nico Franz, deserves special recognition for his role in shaping the outcome of my studies. He is a phenomenal mentor and collaborator, and I am a better scientist and person for having been under his tutelage. Many thanks to everyone at the ASU Natural History Collections, and especially the Franz Lab, for their support and guidance during my time at ASU.

Special thanks to Charlie and Lois O'Brien, who have contributed invaluable specimens and knowledge of weevil biology to my dissertation. I am also grateful to Nik Chawla and the members of the Chawla Lab, for graciously agreeing to help me with mechanical testing, and for providing me with a fantastic source of materials science expertise. Finally, I would like to thank my current and former committee members for their advice and collaboration in this work; thank you!

TABLE OF CONTENTS

Page

LIST OF TABLES ix

LIST OF FIGURES x

CHAPTER

1 INTRODUCTION 1

2 A MULTILAYER MICROMECHANICAL MODEL OF THE CUTICLE OF *CURCULIO LONGINASUS* CHITTENDEN, 1927 (COLEOPTERA: CURCULIONIDAE) 3

2.1 Introduction 5

2.1.1 Biology and Rostral Adaptations of *Curculio longinasus* Chittenden, 1927 6

2.1.2 Research Goals and Challenges 8

2.1.3 Microstructure of Insect Cuticle 10

2.1.4 Review of Prior Studies and Modeling Approach 12

2.2 Methods 13

2.2.1 Micro/Macro Method 13

2.2.2 Symbols and Notation 13

2.2.3 Homogenization Schemes and Limitations 15

Voigt Model 16

Mori-Tanaka Model 16

Non-Interaction Approximation 19

Effective Field Method 23

Isotropic Approximation of Anisotropic Media 26

Maxwell Homogenization Scheme 27

2.2.4 Chitin-Protein Nanofibrils 29

CHAPTER Page

2.2.5 Mesocuticle 31
2.2.6 Exocuticle 33
2.2.7 Endocuticle 34
2.3 Results 37
2.3.1 Chitin-Protein Nanofibrils 38
2.3.2 Mesocuticle 39
2.3.3 Exocuticle 43
2.3.4 Endocuticle 46
2.3.5 Summary of Results 50
2.4 Discussion 56
2.4.1 Major Insights 56
2.4.2 Modeling Limitations 58
3 EXOSKELETAL STRENGTH AND COMPOSITE PROFILE OF THE ACORN WEEVIL ROSTRUM 60
3.1 Introduction 61
3.2 Methods 63
3.2.1 Specimen Acquisition and Taxon Sampling 63
3.2.2 Histological Sectioning 64
3.2.3 Cold-fracture of Specimens 65
3.2.4 Tensile and Fatigue Testing 65
3.2.5 Specimen Imaging and Microscopy 68
3.2.6 Constitutive Modeling of the Cuticle 68
3.2.7 Statistical Analysis 74
3.3 Results and Discussion 77

CHAPTER Page

3.3.1 Microstructure of the *Curculio* Rostrum 77
3.3.2 Force-controlled Loading to Fracture 81
3.3.3 Load Cycling of the Pecan Weevil 84
3.3.4 Fractography of *Curculio* Test Specimens 86
3.4 Conclusions 89
4 ACORN WEEVILS UTILIZE A MODIFIED CUTICLE COMPOSITE PROFILE IN THE ROSTRUM TO REDUCE THE RISK OF CATASTROPHIC BENDING FAILURE 92
4.1 Introduction 94
4.1.1 Biology and Oviposition Behavior of *Curculio* Linnaeus, 1758 95
4.1.2 Exoskeletal Microstructure in the Rostrum 97
4.1.3 Biomechanical Implications of Cuticle Microstructure 99
4.2 Materials and Methods 100
4.2.1 Objectives and Rationale 100
4.2.2 Specimen Acquisition and Taxon Sampling 102
4.2.3 Histological Sectioning 103
4.2.4 Cold-fracture of Specimens 104
4.2.5 Microscopy and Imaging 105
4.2.6 3D-model Construction 106
4.2.7 Finite Element Analysis 110
General Approach 110
Mesh Generation 111
Material Definition and Section Assignment 112
Model Verification and Validation 115

CHAPTER Page

Loading and Boundary Conditions . . . 117
Model Output . . . 119
Limitations . . . 121
4.3 Results and Discussion . . . 122
4.3.1 Model Verification . . . 122
4.3.2 Model Validation . . . 122
4.3.3 Contribution of Apical Modifications . . . 126
4.3.4 Prescribed Displacement . . . 130
4.3.5 Bending Margin of Safety . . . 132
4.4 Conclusion . . . 135
5 ROSTRAL CURVATURE IS BIOMECHANICALLY CONSTRAINED IN FEMALE ACORN WEEVILS . . . 138
5.1 Introduction . . . 139
5.2 Methods . . . 144
5.2.1 Specimen Acquisition and Imaging . . . 144
5.2.2 Assessment of Length and Curvature . . . 145
5.2.3 Statistical Analysis . . . 148
GLMM Fitting . . . 148
Hypothesis Testing . . . 150
5.3 Results . . . 151
5.3.1 Model Fit and Variable Transformation . . . 151
5.3.2 Models of Un-adjusted Curvature . . . 154
5.3.3 Models of Length-Adjusted Curvature . . . 155
5.3.4 Sexual Dimorphism in Rostral Shape . . . 156

CHAPTER Page

5.4 Discussion 157
REFERENCES 163
APPENDIX
A COAUTHOR APPROVAL FOR CHAPTER 2 173
B SUPPLEMENTARY SCRIPT FILES FOR CHAPTER 3 175
B.1 Python Script - Tensile Test Data Processing 176
B.2 R Script - Phylogenetic Regression 184
B.3 Matlab Script - Prediction of Effective Elastic Moduli 195
C SUPPLEMENTARY SCRIPT FILES FOR CHAPTER 4 198
C.1 R Script - Predicting Margin of Safety 199
D SUPPLEMENTARY SCRIPT FILES FOR CHAPTER 5 201
D.1 Python Script - Curvature Analysis and Data Processing 202
D.2 R Script - Mixed Effects Modeling 207

LIST OF TABLES

Table Page

2.1 Summary of Elastic Constants for the Layers of Cuticle 52

2.2 Homogenization Schema Used for Cuticle Layers of *Curculio longinasus* 55

4.1 Results of Model Verification and Validation, by Species and Load 124

4.2 Results of Simulated Apical Load Using Hypothetical Cuticle Layups . . 128

4.3 Results of Simulated Prescribed Vertical Displacement of Head Capsule 131

4.4 Margin of Safety in Simulated Prescribed Displacement of Head Capsule 134

5.1 *Curculio* Species Included in Curvature Analysis 142

LIST OF FIGURES

Figure		Page
2.1	*Curculio* Rostral Anatomy and Cuticle Microstructure	7
2.2	Illustration of Idealized Cuticle Regions in *Curculio*	10
2.3	Illustration of Bouligand Structure and Pore Canal microarchitecture	11
2.4	Illustration of Transition Between Mesocuticle and Exocuticle	30
2.5	Illustration of Idealized Endocuticle Macrofiber Arrangement	34
2.6	Summary of Young's Moduli of Elasticity along Each Global Axis for Each Region of Cuticle	51
2.7	Macroscopic Young's Moduli for Exo-, Meso-, and Endocuticle	53
2.8	Point-wise Elasticity of the Macroscopic Young's Moduli for Exo-, Meso-, and Endocuticle	54
3.1	Morphology and Oviposition Behavior of Female *Curculio* Weevils	62
3.2	Gross Divisions of Cuticle in the Female *Curculio* Rostrum	78
3.3	Composite Profiles of Rostral *Curculio* Cuticle	80
3.4	Tensile Properties of the Female *Curculio* Rostrum	82
3.5	Fatigue Testing of a Female *Curculio caryae* Rostrum	85
3.6	Fractography of Female *Curculio* Rostrum	87
4.1	Gross Morphology of the *Curculio* Rostrum	96
4.2	Scanning Electron Microscopy of Rostral Cuticle	98
4.3	Serial Thin Sectioning of Female *Curculio humeralis* Rostrum	105
4.4	Confocal Microscopy of *Curculio longinasus*	107
4.5	Solid Model and Mesh Generation	109
4.6	Composite Layup and Section Assignment	114
4.7	Model Verification and Validation	123
4.8	Experimental Loading and Model Validation	125

Figure Page

4.9 Relative Contribution of Cuticle Modifications to Apical Deflection 127
4.10 Asymmetry in Layer-wise and Lengthwise Response to Load 129
4.11 Effect of Cuticle Differentiation on Rostral Response to Prescribed Motion 133
4.12 Maximum Strain, Stress, and Margin of Safety 136
5.1 Female Rostrum Diversity in North American *Curculio* Species 140
5.2 Male Rostrum Diversity in North American *Curculio* Species 141
5.3 Generalized Curve-fitting Protocol 145
5.4 Interpretation of Extracted Curvature Variables 147
5.5 Relationships Between Arc-length and Curvature in Female *Curculio* .. 152
5.6 Relationships Between Arc-length and Curvature in Male *Curculio* 153
5.7 General Effect of Length on Rostrum Shape in *Curculio* Weevils..... 158

CHAPTER 1

Introduction

Correspondence between form and function of living things is a central theme in the study of organismal biology and evolution [1]. Biomechanics provides a particularly well-suited suite of inferential methods with which to investigate evolutionary pattern and process [2]. Because of their mathematical and physical underpinnings, biomechanical systems are ideal for studying the possible causes of morphological adaptation, and to provide mechanistic interactions between these causes [3].

Nowhere is the diversity of form and function in animals more apparent than in the weevils, or snout beetles (superfamily Curculionoidea Latreille, 1802), which comprise over 60,000 described species and are collectively characterized by an elongate extension of the head called the rostrum [4]. The name-bearing genus for the weevils – *Curculio* Linnaeus, 1758 – is typified by its exaggerated and sexually dimorphic rostral morphology [5]. Female *Curculio* possess a highly elongate and strongly curved rostrum, which they use to excavate sites for oviposition (egg-laying) [6]. During the process of oviposition, females engage in a stereotypical "drilling" behavior, during which the snout is bent into a completely straight configuration (see [7] for video). In spite of the extreme degree of bending (over 90° in some species) that can take place, the rostrum suffers no apparent harm [8, 9]. Additionally, the snout can be used in this manner dozens or hundreds of times – evidently without failure or fatigue – throughout the lifespan of the adult female [10].

This dissertation is comprised of a sequence of four studies in which the performance of the rostrum is reconstructed via empirical and theoretical consideration of (1) the composition and mechanical behavior of the exoskeleton, and (2) the morphology

and loading conditions of the snout. Each chapter represents either a published manuscript [8] or manuscript in preparation, therefore each is presented as a complete and cohesive product, such that each chapter contains unique Introduction, Methods, Results, and Discussion sections. The chapters are arranged to reflect a hierarchical research sequence, beginning with a description of the micromechanical behavior of the exoskeleton [8], and expanding to encompass a reconstruction of the gross morphology and mechanical behavior of the rostrum as an integrated structure.

First, a multilayer, micromechanical mathematical model is constructed to represent the linear elastic behavior of the different parts of the exoskeleton, or cuticle, in the rostrum of *Curculio* [8]. Second, the tensile behavior of the snout is investigated, and the effect of a spatially varying gradient in the relative allocations of exocuticle and endocuticle is characterized with respect to the stiffness and fracture strength of the cuticle as a whole. Partly-based on these two studies, the third chapter presents finite element models of the rostrum and examines the adaptive role of the composite profile of the rostral cuticle for avoidance of catastrophic structural failure during bending. Finally, the curvature of the snout is assessed in 27 species, and the role of biomechanical constraint upon snout shape – or lack thereof – is considered for both males and females.

CHAPTER 2

A Multilayer Micromechanical Model of the Cuticle of *Curculio longinasus* Chittenden, 1927 (Coleoptera: Curculionidae)

(Previously published as Jansen, Singh, Chawla, and Franz 2016)

https://doi.org/10.1016/j.jsb.2016.05.007

ABSTRACT

Curculio longinasus Chittenden, 1927 (Coleoptera: Curculionidae), is a weevil species common throughout the southwestern United States that uses its rostrum – a very slender, curved, beak-like projection of the head – to excavate tunnels in plant organs (such as acorns) for egg laying (oviposition). Once the apical portion of the rostrum has been inserted into the preferred substrate for oviposition, the female begins rotating around the perimeter of the hole, elevating her head by extending the fore-legs, and rotating the head in place in a drilling motion. This action causes significant elastic deformation of the rostrum, which will bend until it becomes completely straight. To better understand the mechanical behavior of the cuticle as it undergoes deformation during the preparation of oviposition sites, we develop a comprehensive micro/macro model of the micromechanical structure and properties of the cuticle, spanning across all cuticular regions, and reliably mirroring the resultant macroscale properties of the cuticle. Our modeling approach relies on the use of multi-scale, hierarchical biomaterial representation, and employs various micromechanical schemata - e.g., Mori-Tanaka, Effective Field, and Maxwell - to calculate the homogenized properties of representative volume elements at each level in the hierarchy. We describe the configuration and behavior of this model in detail, and discuss the theoretical implications and limitations

of this approach with emphasis on future biomechanical and comparative evolutionary research. Our detailed account of this approach can thereby serve as a methodological template for exploring the biomechanical behavior of new insect structures.

2.1 Introduction

The purpose of this study is to establish a modeling approach to study how weevil (snout beetle) species respond to the mechanical stresses they face during the process of preparing sites for oviposition (egg-laying). Our project is to create a multilayer, hierarchical, micromechanical model of insect cuticle. To do so, we mathematically characterize the microstructure of the exoskeleton of beetles in general, while using certain parameters specific to an individual species, as "proof of concept" in establishing the validity of the model. The formulation of this modeling approach is a critical step towards understanding the way in which cuticular structures are optimized in form and function to accommodate mechanical loading. The methods employed herein will ultimately enable us to analyze the material response of an entire head to load, across multiple species. Thus, our study serves as a key element of a larger research sequence and is foundational to a future comparative, multi-taxon program.

The aims of this work are to (1) model the hierarchical complexity of beetle cuticle to recover the bulk elastic constants for the different regions of cuticle, (2) verify that application of the model to a common species produces robust and valid results, and (3) didactically present the results (and more critically, the methods) to be accessible to biologists with minimal knowledge of materials science. We strongly hope that "democratizing" these methods for biologists will encourage their use more widely in studying functional morphology and will enable biologists to strengthen inferences of the function and evolution of anatomical structures. Likewise, we feel that a deeper understanding of the mechanical behavior of biological materials will ultimately permit others to unlock their potential for biomimicry. Hence, we elaborate on the use of the models and homogenization schemes herein, including their assumptions, parameters,

and outputs, in an effort to make this work more accessible to other biologists.

2.1.1 Biology and Rostral Adaptations of Curculio longinasus Chittenden, 1927

The insect species examined herein, *Curculio longinasus* Chittenden, 1927 (Fig. 2.1), is an exemplary species of the genus *Curculio* Linnaeus, 1758 that is common throughout the southwestern United States and northern Mexico [5]. *Curculio* is the type (name-giving) genus of the family Curculionidae, which are a group of beetles (order Coleoptera) commonly known as weevils. Weevils are readily identified by a structure known as the rostrum (Fig. 2.1), which is a rigid extension of the cuticle (exoskeleton) of the head that bears the terminal chewing mouthparts [11]. Many weevils, including all members of genus *Curculio*, use the rostrum to excavate or otherwise prepare sites for oviposition (the process of laying eggs) in their respective host plants. This group is considered to be megadiverse, with over 62,000 species described to date [4].

The biology of *C. longinasus*, as well as its congeners in North America, is described generally in a monographic revision by Gibson [5], and has been expanded upon by others [7, 10, 12, 13]. Many species of *Curculio* are impactful pest species, the most notable of which are *C. caryae* (Horn, 1873), the pecan weevil, *C. elephas* (Gyllenhal, 1835), the chestnut weevil, and *C. nucum* Linnaeus, 1758, the hazelnut weevil [5, 10]. With respect to *C. longinasus*, Gibson [5] lists the only confirmed host plant for this species as the southern red oak *Quercus falcata* Michaux, 1801. *Curculio* females, including those of *C. longinasus*, use their rostra to excavate a hole into the kernel of an acorn or other fruiting body into which they subsequently oviposit. The developing larva feeds upon the tissue of the acorn and remains inside until pupation. During the final instar stadium, the larva will exit the acorn and burrow into the soil, where it will pupate. Eclosion generally takes place 2-3 weeks thereafter [5].



Figure 2.1: **A** Lateral habitus photograph of a female *Curculio longinasus* Chittenden, 1927 **B** Head of female *C. longinasus*; green line indicates location of cross-section **C** Scanning electron micrograph (SEM) of rostrum in cross-section; detail frames indicate size and location of subsequent magnified SEMs **D** Cross-section with chitin macrofibers ("balken") indicated **E** Cross-section with regions of cuticle indicated.

In preparation of a site for oviposition, the adult female will excavate a bore-hole into the fruit (usually an acorn) using her rostrum and mandibles. These are unusual (and phylogenetically derived) for weevils, and insects in general, in that they resemble shears and articulate along a vertical plane [5, 14, 15]. The rostrum is strongly curved (up to 90°) in most species of *Curculio*, including *C. longinasus* (Fig. 2.1), and in some species, can exceed the length of the remainder of the body [5, 7, 12, 16]. As the bore-hole is excavated, the female ingests the material removed by the action of the mandibles. Once the apical portion of the rostrum has been inserted into the acorn, the female begins rotating around the perimeter of the hole and elevates her head by straightening the fore-legs. This action causes significant elastic deformation of the rostrum, which will bend until it becomes completely straight. The rostrum is kept straight by maintaining the head capsule directly above the bore-hole, and by rotating the head from side to side about the longitudinal axis of the rostrum in a (slow) drilling motion. The female will continue to move around the perimeter of the hole, using a side-stepping gait, while simultaneously maintaining an upright stance and performing the drilling motion of the head, often until the entire rostrum is buried in the acorn, up to the anterior portion of the eyes. This action enables the strongly curved rostrum to excavate a perfectly straight, narrow hole in the acorn (fruit), into which she may deposit one or more eggs. This behavior has been described (and is easily observed) in several species of *Curculio*, and is likely manifested throughout the entire genus [7, 10, 16, 17]. This behavior has been recorded in the supplementary videos of Toju and Sota [7].

2.1.2 Research Goals and Challenges

Here we focus on the mechanical behavior of the cuticle of the *C. longinasus* rostrum as it undergoes remarkable deformation during the preparation of oviposition

sites. Upon removal from the bore hole, the rostrum instantly flexes back to its original, curved shape, without any apparent damage, and in spite of the extreme degree of bending that occurs. Indeed, a single female may excavate many such holes in her adult life period, with or without eggs, and with no evident harm [10, 12]. The way in which this is achieved is of great interest from both a functional-mechanical and an evolutionary perspective. There has been no prior attempt to characterize the behavior of the cuticle of *Curculio* weevils in this context. Absent a proper material model and/or extensive mechanical testing, it is impossible to perform *in-silico* modeling of the rostrum during deformation to assess the response of the cuticle under load. We are therefore unable to make informed statements about the biomechanical optimization and evolution of this adaptive structure as a whole [18].

Our principle aim is to create a micromechanical model of beetle cuticle, based on our specimens and the general structure of the cuticle, that will provide us with accurate estimates of the elastic parameters of the cuticle. Combined with a precise reconstruction of the physical dimensions of the head, this model will enable us to predict the response of the rostrum to simulated loads in future work.

Additionally, a better understanding of the physical response of this material to applied strains will permit us to eventually investigate whether the differential performance demands of regions of the weevil rostrum during oviposition are met by chemical/compositional changes in the cuticle, or by structural adjustments of the cuticular components themselves. In keeping with previous findings regarding the mechanical behavior of arthropod cuticle (see for example [19, 20]), we predict that the structural arrangement and relative proportions of the components of the cuticle will most greatly affect its resulting macroscale properties. With these challenges and goals in mind, we present below a brief summary of the structure of insect cuticle and review prior research that has expanded our understanding of the mechanical

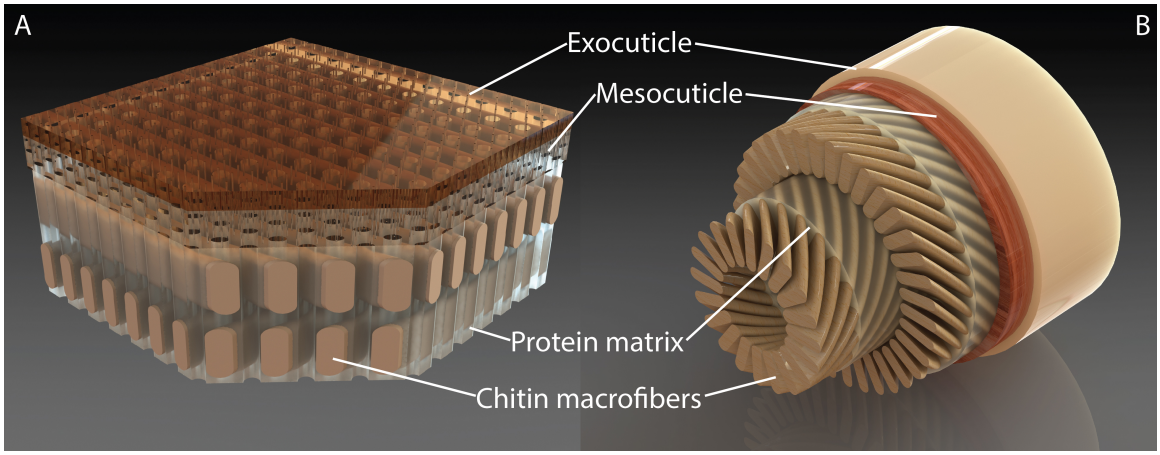


Figure 2.2: **A** Reconstruction of cuticle regions (not to scale), with pores **B** Manifestation of cuticle layering in cylindrical structures (as realized in the *C. longinasus* rostrum), without pores.

behavior of this complex material.

2.1.3 Microstructure of Insect Cuticle

The insect cuticle is comprised of three general regions (Figs. 2.1 and 2.2), including (1) endocuticle, which is the most compliant and innermost region; and (3) exocuticle, which is the outermost region, usually the hardest, and has a thin waxy covering (epicuticle) that is not of great mechanical significance in most groups. Between these regions lies (2) the mesocuticle, which is similar to exocuticle, but is less compact and exhibits a lesser degree of tanning (sclerotization) [21–23]. In general, these regions are confluent, and not necessarily sharply defined (Fig. 2.4). The cuticle of arthropods, including insects, is made up of chitin and numerous uncharacterized proteins, which effectively act as a matrix into which the chitin is embedded [19, 20, 23]. In this way, we may consider the cuticle as a fiber-reinforced composite material. Furthermore, the cuticle is laminate, and has numerous laminae of unidirectional chitin fibers embedded in a proteinaceous matrix, which are stacked at a more or less constant angle to each other in a helicoidal arrangement (Fig. 2.3). This ply arrangement is referred to as

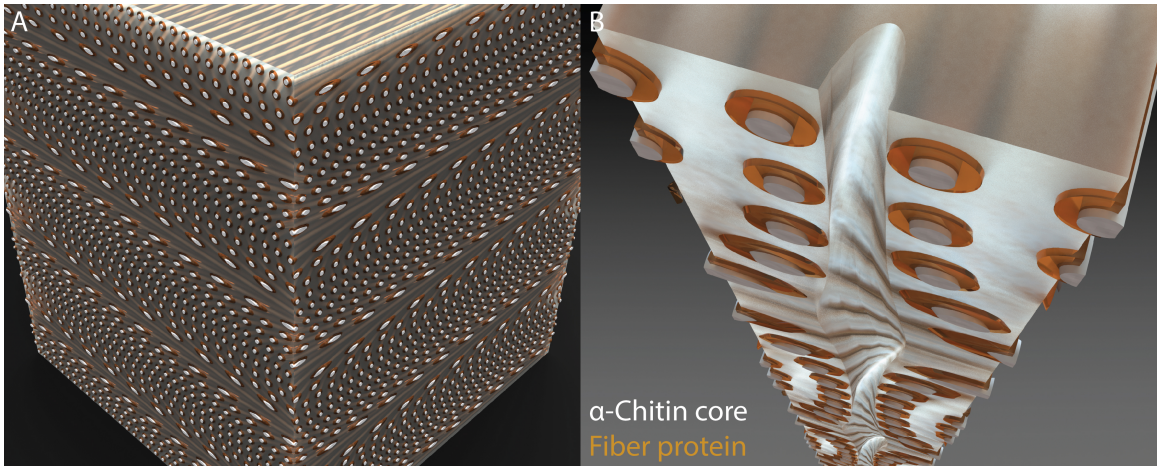


Figure 2.3: **A** Reconstruction of Bouligand structure of mesocuticle (approx. to scale), without pore canals **B** Typical "twisted-ribbon" pore canal in mesocuticle (bisected), without pore canal fiber; in reality, pores are often larger with nanofibrils wrapping around canals.

the Bouligand structure [24–26].

The cuticle is generally porous, with pore canals that have a twisted ribbon configuration and often a central pore canal fiber. These fibers likely enhance the shear stiffness of the composite by providing a form of cross-stitching [27]. Beetles in particular have a highly modified endocuticle made up of large unidirectional bundles of chitin macrofibers, called "balken" (German for beam, strut). These layers are generally pseudo-orthogonal (Figs. 2.2 and 2.5), although some other configurations have been observed [28, 29]. A thorough review of the balken structure can be found in the work of van de Kamp et al. [29, 30]. In addition to its micro-structural properties, the cuticle is also strongly influenced by its chemical properties, especially the degree of tanning and overall water content, as discussed in great detail by Klocke and Schmitz [21] and Vincent [23].

2.1.4 Review of Prior Studies and Modeling Approach

Prior mechanical simulation studies of the arthropod exoskeleton and the insect cuticle as highly structured, hierarchically organized biomaterials have greatly advanced our knowledge of the behavior of these structures. Of particular significance is the modeling approach of Nikolov et al. [19, 20] as applied to the endocuticle of *Homarus americanus* Edwards, 1873. We emulate this approach for modeling hierarchical materials using the micro/macro method (see below). Some prior analyses of the arthropod cuticle have failed to consider the layering of the exoskeleton, and have furthermore posited (for pragmatic modeling reasons) that the cuticle is homogeneously isotropic, thereby neglecting the mechanical implications of its microstructure [31–34]. However, in actuality the cuticle is a highly complex, hierarchically layered, and textured material, whose configuration and properties can vary within an individual organism and across species or higher-level taxa, and which displays a correspondingly complex response to mechanical loads [22, 35]. Our ability to apply previous material models to simulate this behavior is limited by our knowledge of the exact makeup of the cuticle, and especially knowledge of the relative water and protein content, which generally prohibits modeling of the viscoelastic response of this material [19, 20]. All mechanical simulations of the cuticle (including this work) have thus far been limited to conditions of small strain and assume linear elasticity.

We adopt the micro/macro method to achieve balance between model complexity and performance. To explain our modeling approach, we first outline the basic principles of the micro/macro method. We then develop the specific formulation, notation, and relevant assumptions of the models used to calculate the effective properties of the different regions of the cuticle observed in our specimens. Considerable space is allocated to explain our modeling approach for each region of the rostrum, focusing on

decisions related to the inclusion and specific configuration of parameters due either to mathematical contingencies, input from from relevant literature, or experimental observations. We thoroughly characterize the outputs of the micromechanical models at each hierarchical level of complexity, with the aim to reach both biologist and biomechanical engineering audiences, both of which might find our methods relevant to their respective research programs.

2.2 Methods

2.2.1 Micro/Macro Method

The micro/macro approach enables us to take into account the integrated rostrum microstructure to calculate its overall macroscopic properties [19, 20, 36, 37]. This method relies on the use of representative volume elements (RVE), which can be considered as the smallest volume of material that has the same mechanical properties as the material at the macroscale [36]. In composite materials, a single RVE shows a heterogeneous composition, having two or more constituents with different properties [38]. The effective macroscale properties of the RVE are calculated using an appropriate homogenization scheme that takes into account the relevant material properties of each component, and yields the mechanical properties of the RVE as if it were of homogeneous composition [36, 37]. By describing the homogenized properties of a RVE for each level of microstructure in the cuticle, we are able to find the bulk mechanical properties of the different types of cuticle present in the exoskeleton.

2.2.2 Symbols and Notation

In this section we summarize the definitions of terms and symbols used throughout this study. Additional information for parameters specific to each model are provided

in subsequent sections.

E_i Young's modulus of elasticity along axis i

ν_{ij} Poisson's ratio corresponding to displacement along axis j under load along axis i

G_{ij} Shear modulus along axis j in the plane normal to axis i

K Bulk modulus

θ Angle of rotation

V Volume

n Number of constituent elements within representative volume element (RVE)

φ_e Volume fraction of constituent element e (e.g. matrix or fiber)

r_f Fiber radius

s_f Lateral separation distance of fibers embedded in a matrix

C_m Fourth-order stiffness tensor of a material m

S_m Used to represent either the fourth-order compliance tensor or the Eshelby's tensor of a material m, as specified in the respective context.

A_m Strain concentration tensor of a material m

I Identity matrix

R Rotation matrix

T^{α}_{ijkl} Elements of standard tensor basis

H_i Fourth-order compliance contribution tensor for an inhomogeneity i

P_m Fourth-order Hill's tensor of a material m (typically used for ***fibers*** embedded in a matrix)

Q_m Fourth-order Hill's tensor of a material m (typically used for ***voids*** embedded in a matrix)

: Indicates the tensor product contracted over two indices

M^{-1} Indicates the inverse of a matrix M

M^T Indicates the transpose of a matrix M

2.2.3 Homogenization Schemes and Limitations

In this section, we specify the models and homogenization schemes utilized to calculate the effective properties of the weevil rostrum cuticle. We list each in order of its simplicity and appearance in the study. For each, we give a summary of the parameters of the model, conditions under which the model may be considered valid, and the mathematical formulation of the model. In general, the six models presented herein can be classified as belonging to one of three higher "families" of models: (1) numerical/volumetric averaging of RVEs, specifically the Voigt model and isotropic approximation of anisotropic media; (2) homogenization of a single inclusion (or multiple non-interacting inclusions) in a matrix, specifically the Mori-Tanaka model and non-interaction approximation; and (3) homogenization of multiple interacting inclusions in a matrix, specifically the effective field method [1] and Maxwell scheme. The application of each method is discussed in Section 2.3.

[1]Note that this collapses to a specific subset of possible solutions that coincides with the Mori-Tanaka model, when the "correlation hole" is concentric and of the same shape as the inclusions.

Voigt Model

Assumptions: The Voigt model assumes that an imposed macro strain will result in a uniform strain field within a RVE [39]. Under conditions of linear elasticity, this model is generally taken as the upper bound for the calculation of a homogenized stiffness tensor for a material, while the Reuss model, which assumes uniform stress, is taken as the lower bound [36, 39]. The Reuss model is not considered herein, as it consistently underestimates cuticle elastic constants and is thus of limited utility. The Voigt model relies upon the assumption of linear elasticity (i.e. linear relationship between stress resulting from strain imposed on a material) so that the macro strain is equal to the average strain within the RVE [36]. We calculate the effective tensor, C_{eff}, of an RVE by taking the volumetric average of the stiffness tensors of the individual constituents of the RVE.

Parameters: The following are parameters specific to this model.

C_{eff} Effective stiffness tensor of the RVE

V_i Volume of the i^{th} element of the RVE

V_{RVE} Volume of the RVE

C_i Stiffness tensor of the i^{th} element of the RVE

Formulation: Below we present the formulation of this model:

$$C_{\mathit{eff}} = \sum_{i=1}^{n} \frac{V_i}{V_{RVE}} C_i \,. \tag{2.1}$$

Mori-Tanaka Model

Assumptions: The Mori-Tanaka model was developed to calculate the effective properties of two phase composites containing dilute, aligned, ellipsoidal inclusions, under conditions of linear elasticity, where the inclusions have the

same properties as the matrix and are isotropic [37, 40]. This model generally treats each inclusion as if it were isolated in an infinite matrix so that the inclusions do not interact with each other, and thus produces optimal results when the volume fraction of inclusions is less than 20-30% [19, 36]. See also [41] for problems associated with this method. When the inclusions have different properties than the matrix material, they are referred to as inhomogeneities, and may be simulated by an equivalent inclusion with the properties of the matrix with a uniform eigenstrain, using the equivalent inclusion method [37, 42].

By incorporating the equivalent inclusion method, a reformulation of the Mori-Tanaka model was created to accommodate the calculation of the effective properties of transversely orthotropic or anisotropic inclusions (such as cracks or fibers) embedded in an isotropic matrix, depending solely on the properties of the matrix material and the shape of the inhomogeneities [42]. We therefore assume that the material is a linear elastic, two-phase composite with perfect bonding between an isotropic matrix material and the inclusions, which are identical, dilute, aligned, and ellipsoidal in shape.

Parameters: The following are parameters specific to this model.

C_{eff} Effective stiffness tensor of the RVE

φ_M Volume fraction of the isotropic matrix

φ_F Volume fraction of the fibrous inhomogeneities

ν_M Poisson's ratio of the isotropic matrix

C_M Stiffness tensor of the isotropic matrix

C_F Stiffness tensor of the fibrous inhomogeneities

A_F Strain concentration factor for the fibrous inhomogeneities

S_F Eshelby's tensor for a cylindrical inclusion

Formulation: Below we present the formulation of this model.

$$C_{\mathit{eff}} = C_M + \varphi_F \left[(C_F - C_M) : A_F \right] \left[\varphi_M I + \varphi_F A_F \right]^{-1} , \tag{2.2}$$

Where:

$$A_F = \left[I + S_F : (C_M)^{-1} : (C_F - C_M) \right]^{-1} . \tag{2.3}$$

For an infinite isotropic elastic matrix, with a single embedded circular cylinder, whose longitudinal axis is aligned with axis 1, the non-zero components of the Eshelby's tensor, S_F, are as follows:

$$\begin{gathered}
S_{2211} = S_{3311} = \frac{\nu_M}{2\left(1-\nu_M\right)} , \\
S_{2222} = S_{3333} = \frac{1}{2\left(1-\nu_M\right)} \left[\frac{3}{4} + \frac{\left(1-2\nu_M\right)}{2} \right] , \\
S_{2233} = S_{3322} = \frac{1}{2\left(1-\nu_M\right)} \left[\frac{1}{4} - \frac{\left(1-2\nu_M\right)}{2} \right] , \\
S_{2323} = \frac{1}{2\left(1-\nu_M\right)} \left[\frac{1}{4} + \frac{\left(1-2\nu_M\right)}{2} \right] , \\
S_{1212} = S_{1313} = \frac{1}{4} , \\
\text{*note that:} S_{1111} = S_{1122} = S_{1133} = 0 ,
\end{gathered} \tag{2.4}$$

Where:

$$S_F = \begin{bmatrix}
S_{1111} & S_{1122} & S_{1133} & 0 & 0 & 0 \\
S_{2211} & S_{2222} & S_{2233} & 0 & 0 & 0 \\
S_{3311} & S_{3322} & S_{3333} & 0 & 0 & 0 \\
0 & 0 & 0 & 2S_{2323} & 0 & 0 \\
0 & 0 & 0 & 0 & 2S_{1313} & 0 \\
0 & 0 & 0 & 0 & 0 & 2S_{1212}
\end{bmatrix} . \tag{2.5}$$

Non-Interaction Approximation

Assumptions: For our purposes, the non-interaction approximation is similar to the Mori-Tanaka model in its assumptions; namely, that we are finding the effective properties of a linear elastic two-phase composite containing a matrix phase and identical inclusions that are ellipsoidal in shape and do not interact with each other [43–46]. As in the Mori-Tanaka model, this method simulates the effect of adding a single inclusion to the matrix material, thus assuming no interaction between inclusions. The effective properties of the composite are assumed to be equal to the sum of the stiffness (or compliance) of the matrix and the effect of the inclusions either as a stiffness or compliance contribution tensor, respectively [43, 46]. Because we use this method in a matrix that is transversely isotropic, with inclusions (specifically pores) whose longitudinal axes are aligned with the axis of transverse isotropy, we use the formulation of Sevostianov et al. [46], which utilizes explicit inversions made simpler by representation of fourth-order tensors in "tensorial basis", as indicated below. See [43, 46] for more information.

Parameters: The following are parameters specific to this model.

S_{eff} Effective compliance tensor of the RVE

S_M Compliance tensor of the matrix

V_i Volume of the i^{th} inhomogeneity

V_{RVE} Volume of the RVE

φ_I Volume fraction of the inclusions

H_i Compliance contribution tensor of the i^{th} inhomogeneity

H_{NI} Compliance contribution tensor of all inhomogeneities for the non-interaction model

h_α Components of compliance contribution tensor H_i in standard tensor basis

C_M Stiffness tensor of the matrix

C_α Components of C_M expressed in standard tensor basis

T^α_{ijkl} Tensors for expression in standard tensor basis

Formulation: Below we present the formulation of this model.

In general, the non-interaction approximation for a two-phase composite is given by:

$$S_{\mathit{eff}} = S_M + H_{NI}\,, \tag{2.6}$$

Where H_{NI} is given by the sum of the compliance contribution tensors for n inhomogeneities in the RVE, such that:

$$H_{NI} = \sum_{i=1}^{n} H_i\,. \tag{2.7}$$

The i^{th} inhomogeneity has a compliance contribution tensor H_i, expressed in tensorial basis as:

$$H_i = \frac{V_i}{V_{RVE}} \sum_{\alpha=1}^{6} h_\alpha T^\alpha_{ijkl}\,. \tag{2.8}$$

By substitution of Eq. (2.8) into Eq. (2.7):

$$H_{NI} = \sum_{i=1}^{n} \left(\frac{V_i}{V_{RVE}} \sum_{\alpha=1}^{6} h_\alpha T^\alpha_{ijkl} \right)\,. \tag{2.9}$$

However, assuming all inhomogeneities are identical, this can be expressed as:

$$H_{NI} = \frac{nV_i}{V_{RVE}} \sum_{\alpha=1}^{6} h_\alpha T^\alpha_{ijkl} \,. \tag{2.10}$$

Therefore, because $\frac{nV_i}{V_{RVE}} = \varphi_I$:

$$H_{NI} = \varphi_I \sum_{\alpha=1}^{6} h_\alpha T^\alpha_{ijkl} \,. \tag{2.11}$$

If we assume the general form of a 6×6 matrix, then a symmetrical tensor M, expressed as a 6×6 matrix, has the following components [36]:

$$M = \begin{bmatrix} M_{1111} & M_{1122} & M_{1133} & M_{1123} & M_{1113} & M_{1112} \\ M_{2211} & M_{2222} & M_{2233} & M_{2223} & M_{2213} & M_{2212} \\ M_{3311} & M_{3322} & M_{3333} & M_{3323} & M_{3313} & M_{3312} \\ M_{2311} & M_{2322} & M_{2333} & M_{2323} & M_{2313} & M_{2312} \\ M_{1311} & M_{1322} & M_{1333} & M_{1323} & M_{1313} & M_{1312} \\ M_{1211} & M_{1222} & M_{1233} & M_{1223} & M_{1213} & M_{1212} \end{bmatrix} . \tag{2.12}$$

Any symmetrical fourth-order tensor expressed with components expressed in 6×6 matrix form can also be represented in a "standard tensor basis" as:

$$M = \sum_{\alpha=1}^{6} M_\alpha T^\alpha_{ijkl} \,, \tag{2.13}$$

Where M_α are of the same form as C_α, given in Eqs. (2.16), and the non-zero components of tensors T^α_{ijkl} are as follows:

$$
\begin{gathered}
T^1_{1111} = T^1_{2222} = T^1_{1122} = T^1_{2211} = 1\,, \\
T^2_{1212} = T^2_{2121} = T^2_{1221} = T^2_{2112} = T^2_{1111} = T^2_{2222} = \frac{1}{2}\,, \\
T^2_{1122} = T^2_{2211} = -\frac{1}{2}\,, \\
T^3_{1133} = T^3_{2233} = 1\,, \\
T^4_{3311} = T^4_{3322} = 1\,, \\
T^5_{1313} = T^5_{2323} = T^5_{1331} = T^5_{2332} = T^5_{3113} = T^5_{3223} = T^5_{3131} = T^5_{3232} = \frac{1}{4}\,, \\
T^6_{3333} = 1\,.
\end{gathered}
\tag{2.14}
$$

The coefficients $h_\alpha$are:

$$
\begin{gathered}
h_1 = \frac{2C_3C_4 - C_6\left(2C_1 + C_2\right)}{4C_2\left(C_3C_4 - C_1C_6\right)}\,, \\
h_2 = \left(\frac{1}{C_1} + \frac{2}{C_2}\right)\,, \\
h_3 = h_4 = \frac{C_3}{2\left(C_3C_4 - C_1C_6\right)}\,, \\
h_5 = \frac{8}{C_5}\,, \\
h_6 = \frac{C_1}{C_3C_4 - C_1C_6}\,.
\end{gathered}
\tag{2.15}
$$

Where C_α are given in terms of the 6×6 matrix components of the stiffness tensor C_M such that:

$$
\begin{aligned}
C_1 &= \frac{C_{1111} + C_{1122}}{2}\,, \\
C_2 &= 2C_{1212}\,, \\
C_3 &= C_{1133}\,, \\
C_4 &= C_{3311}\,, \\
C_5 &= 4C_{1313}\,, \\
C_6 &= C_{3333}\,.
\end{aligned}
\tag{2.16}
$$

Effective Field Method

Assumptions: With the effective field method, all preceding assumptions for the non-interaction approximation are applicable, except the inhomogeneities are expected to interact with each other (the interaction is assumed to be geometrical, see [47]). This method simulates the interaction between inclusions by placing them into an local strain field. Additionally, it is assumed, for simplicity, that the strain field of each inclusion is identical to that of any other inclusion, and that this field does not depend on the geometry or elastic properties of the inclusions, but rather, is determined by the elastic properties of the matrix and orientation of the inclusions [46]. By additionally assuming that there is symmetry to the distribution of inhomogeneities, and that the "correlation hole" (the region within which it is unlikely that the centers of other inclusions will be found) is of the same shape and concentric with the inhomogeneity, it is possible to provide an explicit solution for this method that coincides with the Mori-Tanaka Model [46]. This is the case if the inclusions under consideration are aligned, identical, and arranged such that the distance between any two neighboring fibers is identical [41]. We use the formulation of [46], which utilizes explicit inversions made simpler by representation of fourth-order tensors in

"tensorial basis", in the form indicated by Eq. (2.13). It is assumed that axis 3 is the axis of transverse isotropy, aligned with the axes of rotation of the inclusions.

Parameters: The following are parameters specific to this model.

C_{eff} Effective stiffness tensor of the RVE

C_M Stiffness tensor of the matrix

C_α Components of C_M expressed in standard tensor basis

C_D Inverse of S_D

C_D^α Components of C_D expressed in standard tensor basis

S_I Compliance tensor of an inclusion

S_M Compliance tensor of the matrix

S_D Difference of the compliance tensors of the inclusions and matrix, respectively

φ_I Volume fraction of the inclusions

φ_M Volume fraction of the matrix

P Hill's tensor

p_α Components of P expressed in standard tensor basis

Δ_1 Coefficient of tensor inversion defined in Eq. (2.19)

Δ^* Coefficient of tensor inversion defined in Eq. (2.20)

T_{ijkl}^α Tensors for expression in standard tensor basis

Formulation: Below we present the formulation of this model.

$$C_{eff} = \sum_{\alpha=1}^{6} C_{eff}^\alpha T_{ijkl}^\alpha \,, \tag{2.17}$$

Where $C^{\alpha}_{\mathit{eff}}$ are the components of C_{eff} given by:

$$\begin{aligned}
C^{1}_{\mathit{eff}} &= C_1 + \frac{\varphi_I}{2\Delta^*}\left[\frac{2C^1_D}{\Delta_1} + \varphi_M P_6\right], \\
C^{2}_{\mathit{eff}} &= C_2 + \varphi_I\left[\frac{1}{C^2_D} + \varphi_M P_2\right]^{-1}, \\
C^{3}_{\mathit{eff}} &= C^{4}_{\mathit{eff}} = C_3 + \frac{\varphi_I}{\Delta^*}\left[\frac{C^3_D}{\Delta_1} - \varphi_M P_3\right], \\
C^{5}_{\mathit{eff}} &= C_5 + 4\varphi_I\left[\frac{4}{C^5_D} + \varphi_M P_5\right]^{-1}, \\
C^{6}_{\mathit{eff}} &= C_6 + \frac{\varphi_I}{2\Delta^*}\left[\frac{2C^6_D}{\Delta_1} + \varphi_M P_1\right],
\end{aligned} \tag{2.18}$$

Where [2] :

$$\Delta_1 = 2\left[C^1_D C^6_D - C^3_D C^4_D\right], \tag{2.19}$$

$$\Delta^* = 2\left[\frac{C^6_D}{2\Delta_1} + \varphi_M P_1\right]\left[\frac{2C^1_D}{\Delta_1} + \varphi_M P_6\right] - 2\left[\frac{C^3_D}{\Delta_1} + \varphi_M P_3\right]^2, \tag{2.20}$$

Given:

$$C_D = C_I - C_M\,. \tag{2.21}$$

Additionally, C^{α}_D and C_α are components of the stiffness tensors C_D and C_M, respectively, that may be derived from Eqs. (2.16). Furthermore, p_α are the components of Hill's tensor, and are given by:

$$\begin{aligned}
p_1 &= \frac{1}{2\left(2C_1 + C_2\right)}, \\
p_2 &= \frac{1}{2\left(2C_1 + C_2\right)} + \frac{1}{C_2}, \\
p_3 &= p_4 = p_6 = 0, \\
p_5 &= \frac{2}{C_5}\,.
\end{aligned} \tag{2.22}$$

[2] Note that in [46], this is erroneously produced as: $\Delta_1 = C^1_D C^6_D - \left(C^3_D\right)^2$; see [48], Eq. A.4, for the correct formulation of Δ for tensor inversion in tensorial basis.

Isotropic Approximation of Anisotropic Media

Assumptions: For slightly anisotropic media, it is possible to create an isotropic approximation of the material from its elastic constants [49, 50]. For this particular formulation, we assume that the material in question is transversely isotropic.

Formulation: Below we present the formulation of this model. From Hook's Law, we may derive the elastic constants of orthotropic media from their stiffness and compliance tensors as follows:

$$S_m = [C_m]^{-1} = \begin{bmatrix} \frac{1}{E_1} & -\frac{\nu_{21}}{E_2} & -\frac{\nu_{31}}{E_3} & 0 & 0 & 0 \\ -\frac{\nu_{12}}{E_1} & \frac{1}{E_2} & -\frac{\nu_{32}}{E_3} & 0 & 0 & 0 \\ -\frac{\nu_{13}}{E_1} & -\frac{\nu_{23}}{E_2} & \frac{1}{E_3} & 0 & 0 & 0 \\ 0 & 0 & 0 & \frac{1}{G_{23}} & 0 & 0 \\ 0 & 0 & 0 & 0 & \frac{1}{G_{31}} & 0 \\ 0 & 0 & 0 & 0 & 0 & \frac{1}{G_{12}} \end{bmatrix} . \tag{2.23}$$

For a transversely isotropic material, the isotropic approximations of the shear and bulk moduli may be calculated, respectively, as:

$$\begin{aligned} G^{-1} &= 4\left[(1+\nu_{12})\,E_1^{-1} + (1+\nu_{23})\,E_2^{-1} + (1+\nu_{31})\,E_3^{-1}\right] , \\ &\quad +3\left(G_{12}^{-1} + G_{23}^{-1} + G_{31}^{-1}\right) , \\ K^{-1} &= (1-2\nu_{12})\,E_1^{-1} + (1-2\nu_{23})\,E_2^{-1} + (1-2\nu_{31})\,E_3^{-1} . \end{aligned} \tag{2.24}$$

From these, we may also find the isotropic approximations of Poisson's ratio and Young's modulus:

$$\begin{aligned} \nu &= \frac{3K-2G}{2\,(3K+G)} , \\ E &= \frac{9KG}{3K+G} . \end{aligned} \tag{2.25}$$

The stiffness tensor of the isotropic approximation may then be calculated, by Hook's Law, such that:

$$C = \frac{E}{(1+\nu)(1-2\nu)} \times \begin{bmatrix} (1-\nu) & \nu & \nu & 0 & 0 & 0 \\ \nu & (1-\nu) & \nu & 0 & 0 & 0 \\ \nu & \nu & (1-\nu) & 0 & 0 & 0 \\ 0 & 0 & 0 & \frac{(1-2\nu)}{2} & 0 & 0 \\ 0 & 0 & 0 & 0 & \frac{(1-2\nu)}{2} & 0 \\ 0 & 0 & 0 & 0 & 0 & \frac{(1-2\nu)}{2} \end{bmatrix}. \tag{2.26}$$

Maxwell Homogenization Scheme

Assumptions: For the Maxwell homogenization scheme, we observe the same assumptions *shared* between the previous models. The approach of Maxwell was to remove a domain Ω from a composite material and insert it into the matrix, where its effect will invariably be described by either the sum of the compliance (or stiffness) contribution tensors of the inclusions, or by the compliance (or stiffness) contribution tensor of the entire domain, which is assumed to have unknown properties. By equating these quantities, it is possible, given the aforementioned assumptions of our system, to explicitly calculate the effective properties of Ω as our RVE, while accounting for the interactions between inhomogeneities [47, 48, 51, 52]. We follow the formulation of Sevostianov et al. [47], which has been successfully used to calculate the effective properties of cortical bone, another biomaterial with a complex microstructure [52].

Parameters: The following are parameters specific to this model.

S_{eff} Effective compliance tensor of the RVE

S_M Compliance tensor of the matrix

S_F Compliance tensor of a fiber

φ_F Volume fraction of the fibers

G_M Shear modulus of elasticity of the matrix

ν_M Poisson's ratio of the matrix

H_F Compliance contribution tensor of all fibers in the RVE

Q Hill's tensor

q_α Components of Q expressed in standard tensor basis

κ Coefficient defined in Eq. (2.30)

f_0 Coefficient defined in Eq. (2.31)

f_1 Coefficient defined in Eq. (2.32)

γ Aspect ratio of an inhomogeneity

$g(\gamma)$ Shape function for an inhomogeneity with aspect ratio γ

Formulation: Below we present the formulation of this model.

$$S_{\mathit{eff}} = S_M + \left\{ [H_F]^{-1} - Q \right\}^{-1} , \tag{2.27}$$

Where:

$$H_F = \varphi_F \left[(S_F - S_M)^{-1} + Q \right]^{-1} . \tag{2.28}$$

The Hill's tensor for the fibers, Q, has the components q_α, in standard tensor basis:

$$
\begin{aligned}
q_1 &= G_M[4\kappa - 1 - 2\,(3\kappa - 1)\,f_0 - 2f_1]\,, \\
q_2 &= 2G_M[1 - (2 - \kappa)\,f_0 - f_1]\,, \\
q_3 = q_4 &= G_M[(2\kappa - 1)\,f_0 + 2f_1]\,, \\
q_5 &= 4G_M\,[f_0 + 4f_1]\ , \\
q_6 &= 8G_M\,[\kappa f_0 - f_1]\ ,
\end{aligned}
\tag{2.29}
$$

Given:

$$
\kappa = \frac{1}{2\,(1 - \nu_M)}\,, \tag{2.30}
$$

$$
f_0 = \frac{\gamma^2\,[1 - g\,(\gamma)]}{2\,(\gamma^2 - 1)}; \text{ for cylinders, } f_0 = \frac{1}{2}\,, \tag{2.31}
$$

$$
f_1 = \frac{\kappa\gamma^2}{4\,(\gamma^2 - 1)^2}\,\left[\left(2\gamma^2 + 1\right) g\,(\gamma) - 3\right] \text{ for cylinders, } f_1 = 0\,. \tag{2.32}
$$

Additionally, the shape function $g\,(\gamma)$ is expressed in terms of the aspect ratio, γ, of the inhomogeneities. We assume that the inhomogeneities are fibers, and therefore are cylindrical and can be considered as prolate spheroids with an infinite aspect ratio ($\gamma \to \infty$). The general form of the shape function for prolate spheroids is:

$$
g\,(\gamma) = \frac{1}{2\gamma\sqrt{\gamma^2 - 1}} \ln \frac{\gamma + \sqrt{\gamma^2 - 1}}{\gamma - \sqrt{\gamma^2 - 1}}\,. \tag{2.33}
$$

2.2.4 Chitin-Protein Nanofibrils

The effective properties of a single chitin-protein nanofibril were determined using (1) a Mori-Tanaka model (Section 2.2.3) and (2) the ab-initio calculations of

Nikolov et al. [19, 20] for the effective properties of α-chitin and fiber proteins. We assume, based on previous research on beetles and other arthropods, that the α-chitin crystals are wrapped in cylindrical proteins in a hexagonal arrangement and are of uniform diameter [24, 26, 53]. In some arthropod species, the resulting chitin-protein nanofibrils are tightly packed in a uniform, quasi-hexagonal arrangement to form a single chitin-protein microfiber, while in others, such as *C. longinasus*, the chitin-protein nanofibrils are embedded into a protein matrix (Figs. 2.3 and 2.4) to form layers in the Bouligand structure [24, 35, 54–56]. For fibers embedded in a matrix with a hexagonal arrangement [20]:

$$\varphi_F = \frac{2\pi r_f^2}{\sqrt{3}\,(2r_f + s)^2}\,. \tag{2.34}$$

Because the microfibers are comprised solely of parallel nanofibrils, and given the assumptions of the Mori-Tanaka model, we may consider the effective properties of a homogenized microfiber and a homogenized nanofibril to be equivalent, physically differing only in radius. We therefore use data from Neville [26] for chitin-rich structures in beetles to calculate the volume fractions of chitin and protein from which we can derive, via the Mori-Tanaka model, the effective properties of a single chitin-protein nanofibril. We note that the values for the effective properties of the protein matrix come from relevant literature, as discussed below,

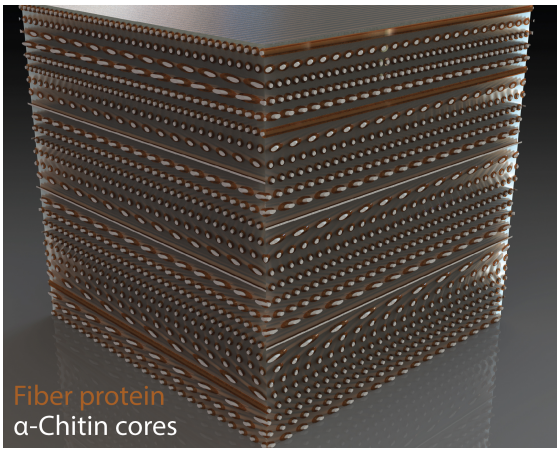


Figure 2.4: Interface of Bouligand structure between mesocuticle (bottom layers) and exocuticle (upper layers), showing gradual decrease in number of laminae per 180° alternation (decreasing pitch) and a gradual increase in the number of chitin-protein nanofibrils per lamina (increasing volume fraction).

and are different for the exocuticle, to reflect the increased cross-linking between the nanofibrils and the protein matrix that results from the process of tanning (sclerotization); also see Sections 2.3.1 and 2.3.3.

2.2.5 Mesocuticle

The effective properties of the helicoidal ply (Bouligand) structure of the mesocuticle can be ascertained in a three-step procedure that generally follows the method of [19, 20]:

1. We first calculate the effective properties of a single, imperforate lamina by using the Mori-Tanaka method. We assume that a single ply (the RVE) in the Bouligand structure can be effectively modeled as a layer consisting of aligned, identical, evenly spaced, cylindrical inclusions (fibers) embedded in a matrix. As input, we take the effective stiffness tensor of a single chitin-protein nanofibril, the effective stiffness tensor of the protein matrix into which the nanofibrils are embedded, and the volume fraction of the nanofibrils, as calculated from Eq. (2.34). The exact separation distance between the nanofibrils is unknown, but it is possible to estimate this value based on the number of layers in the Bouligand structure, the size of the chitin-protein nanofibrils, and the pitch of the ply in our samples. We outline this method in greater numerical detail below (see Section 2.3.2).

2. Next, we simulate the helicoidal stacking of these layers to generate a transversely isotropic approximation of the Bouligand structure with a Voigt estimate (Section 2.2.3). At the macroscale, the Bouligand structure can be considered a transversely isotropic composite, so long as the number of plies is large (and can thus be considered infinitesimally thin) and the pitch of the ply (number

of layers per 180° rotation of the ply) is correspondingly small. Given the very large number of layers in the cuticle and relatively small pitch, the Bouligand structure can be considered transversely isotropic at small strains. We simulate this by considering n layers (per 180° alternation) stacked at θ degrees relative to each other along the normal axis, then taking a Voigt estimation (see Eq. (2.1)) over each layer where the properties of the i^{th} layer are given by [38]:

$$C_i = R : C : R^T \,, \tag{2.35}$$

Where C is the stiffness tensor for a single lamina, and R is given in terms of θ [38]:

$$R = \begin{bmatrix} \cos^2\theta & \sin^2\theta & 0 & 0 & 0 & \sin 2\theta \\ \sin^2\theta & \cos^2\theta & 0 & 0 & 0 & -\sin 2\theta \\ 0 & 0 & 1 & 0 & 0 & 0 \\ 0 & 0 & 0 & \cos\theta & -\sin\theta & 0 \\ 0 & 0 & 0 & \sin\theta & \cos\theta & 0 \\ -\sin\theta\cos\theta & \sin\theta\cos\theta & 0 & 0 & 0 & \cos^2\theta - \sin^2\theta \end{bmatrix} . \tag{2.36}$$

The Voigt estimate is therefore given, from Eqs. (2.1), (2.35), and (2.36):

$$C = \frac{1}{n}\sum_{i=1}^{n} C_i \,. \tag{2.37}$$

3. Finally, we model the effect of adding pore canals to the structure. To calculate the effective properties of the helicoidal ply including pore canals, we utilize a non-interaction approximation (Section 2.2.3) from [46] rather than the three-point approximation scheme of [57]. We assume that the pores are cylindrical, rather than helico-ellipsoidal (Fig. 2.3), and have the same cross sectional area throughout. While sufficient for [19, 20], the three-point approximation scheme is not optimal for our purposes. Our scheme requires estimation of a complete effective stiffness tensor; yet the three point approximation only generates the in-plane elastic constants, not addressing the remaining constants. Sevostianov et al. [46] found an explicit solution for calculating the effective

properties of a material consisting of aligned spheroidal inclusions in a transversely isotropic matrix, when the axis of rotation of the inhomogeneities is aligned with the axis of transverse isotropy. For this reason we use their method and a non-interaction approximation to estimate the properties of the Bouligand structure with pores, based on the low volume fraction of pores in the cuticle of our samples, as explained below (see Section 2.3.2).

2.2.6 Exocuticle

The process for calculating the effective stiffness tensor of exocuticle is the same as that of mesocuticle, where we consider the material in three hierarchical levels: a single (imperforate) lamina, a laminate composite of stacked plies, and finally the Bouligand structure with pores. In our model, there are three main structural differences between the mesocuticle and exocuticle (see Section 2.3.3):

1. The packing of the laminae of the Bouligand structure is estimated to be approximately three times closer than mesocuticle, based on the pitch of the ply in exocuticle of our samples and data from other arthropods [25, 27, 54]. The reduced spacing also greatly increases the fiber fraction of the exocuticle so that the Mori-Tanaka method is no longer effective. To accommodate a high volume fraction of fibers and account for interactions between them, we utilize the effective field method (Section 2.2.3) for calculating the macroscale properties of the resulting individual ply [46].

2. We estimate the effective Young's modulus of the fiber proteins to be significantly higher than in the endocuticle and mesocuticle, due to increases in cross-linking between the individual chitin-protein nanofibrils present in the exocuticle, as well as decreased water content. We use value presented by Vincent [22], who

provides measurements for the protein matrix of anatomical structures that exhibit large degrees of fiber cross-linking.

3. The effective Young's modulus of the protein matrix in which the nanofibrils are embedded is also estimated to be higher than in the mesocuticle, in keeping with the findings of Ker [58], for highly sclerotized cuticle.

2.2.7 Endocuticle

Beetle endocuticle differs significantly in microstructural arrangement when compared to other layers of cuticle; namely, the endocuticle is characterized by the presence of unidirectional chitin macrofibers or balken [29]. In these structures, the individual chitin cores surrounded by protein (the chitin-protein nanofibrils) are embedded in a protein matrix to form chitin-protein microfibers (Fig. 2.5). The latter, in turn, are tightly conjoined to form the macrofibers [28, 29, 56]. The endocuticle generally exhibits the smallest degree of fiber cross-linking in the cuticle as a whole, and is the least sclerotized portion of this tissue [22, 23]. We therefore adjust the properties of the protein matrices accordingly in our formulation of a micromechanical model for the endocuticle, as described in Section 2.3.4.

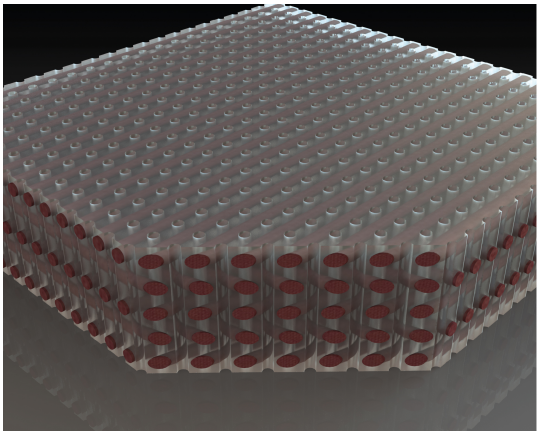


Figure 2.5: Typical "Balken-type" endocuticle, represented as orthogonally-stacked layers of chitin macrofibers embedded in a porous protein matrix; the pores exhibit a square arrangement between the macrofibers (not illustrated to scale).

Among the Coleoptera, there are two main types of structural arrangements of the

macrofibers that can occur [29]. The first type is considered the "classical" balken-type cuticle, where the macrofibers are arranged unidirectionally and are connected by a thin layer of protein matrix with interspersed pores. The second type is referred to as "reticulate" balken-type cuticle, which is characterized by cross-linking fibers between the balken that connect the macrofibers and also reinforce the pores. The latter type creates a linear mesh, where the gaps are filled by protein matrix and have central pores [28]. In between these there are cuticles that exhibit only a small amount of cross-linking between macrofibers, and are very similar to the classical type; this was observed in *Anthonomus grandis* by [59]. To simulate the micromechanical properties of a layer comprised of multiple balken, protein matrix, and pores, it is necessary to replicate the arrangement and volume fractions of these components within a RVE. We describe our general approach for endocuticle in four steps:

1. We first compute the effective properties of a single chitin macrofiber (our RVE at this step), given the properties of a homogenized chitin-protein nanofibril, the diameter and separation of the nanofibrils within the microfibers, and the properties of the protein matrix in which the nanofibrils are embedded. The lateral separation of the nanofibrils is known from recent work in weevils by van de Kamp [30] (see Section 2.3.4), thus leaving the effective properties of the matrix as the only unknown. We therefore take these properties from Nikolov et al. [20]. Although their data relate to the lobster endocuticle, we presume that their estimations are similar enough to be applicable the weevil endocuticle. This reasoning is supported both by the results outlined below and by findings for other insects [22, 23, 58]. Based on the volume fraction of microfibers observed in our samples, we utilize the effective field method to calculate the effective properties for a single, unidirectional macrofiber.

2. We assume, based on the observations of weevil balken ([59, 60]), that the even spacing of the macrofibers in our samples is due to a reduced amount of cross-linking between macrofibers, such that they can be considered effectively separated along most of their length by protein matrix. We may thus model a single balken layer by assuming that the overall architecture is that of a unidirectional, fiber-reinforced composite with a transversely isotropic fiber fraction and an isotropic matrix embedded with cylindrical pores. This enables us to calculate the volume fractions of the layers of protein matrix, pores, and macrofibers, respectively, from the cross sectional areas of the respective elements of the structure and based on our samples. Furthermore, we assume a square arrangement of the pores due to the linear mesh arrangement of the balken layers, wherein:

$$\varphi_F = \frac{2\pi r_f^2}{(2r_f + s)^2}\,. \tag{2.38}$$

   Because the volume fraction of pores in our sample is quite low (see Section 2.3.4), we utilize a non-interaction approximation to homogenize the pore-embedded matrix.

3. Our strategy then follows the approach of Vilchevskaya et al. [52] for two-phase composites. We do not attempt to simultaneously calculate the combined effect of pores and fibers, which are assumed to be cylindrical, aligned, identical (within each respective phase, pore or fiber), and orthogonal to each other in the matrix, since it is possible that the combined effect of a stiff phase and a compliant phase can lead to numerical singularity at certain volume fractions [47]. Rather, we first calculate the effective properties of the pore-embedded matrix, and then create an isotropic approximation of the resulting transversely isotropic,

homogenized material. Because the resulting degree of transverse isotropy is correspondingly low, an isotropic approximation (Section 2.2.3) can be used with reasonable accuracy to calculate the Hill's tensor for the macrofibers [3] , as explained below.

4. Given an isotropic approximation for the protein matrix embedded with cylindrical pores, we can now simulate the effect of adding macrofibers to the (porous) matrix via a Maxwell homogenization scheme Section 2.2.3). The isotropic approximation is used to calculate the Hill's tensor for the macrofibers, Q, used in Eq. (2.28), and whose components are given in Eqs. (2.29). We assume that the interaction between pores and the fiber fraction is essentially negligible, though we utilize the compliance tensor of the transversely isotropic, pore-embedded matrix, rather than the isotropic approximation, to calculate the effective compliance tensor of the balken layer in Eq. (2.27).

2.3 Results

In this section, we examine the explicit numerical solutions of the models as outlined in the preceding section. We begin at the lowest hierarchical level for each region of cuticle, building up to the complete structure sequentially, at each level in the structural hierarchy. We also report, where appropriate, values obtained from relevant literature for certain parameters that we were not able to measure experimentally. With this foundation, we are able to present the macroscale properties of each layer of the cuticle, as well as examine the robustness of the resultant elastic constants with respect to literature-extracted model parameters.

[3] This crucial step enables us to approximate the effective properties of this two-phase composite, while simultaneously sidestepping two particular complications: potential numerical singularity during tensor inversion [47], and the problem of explicitly calculating the effective properties of fibers embedded in a transversely isotropic matrix, where the fibers are aligned *orthogonal* to the axis of transverse isotropy [49, 52].

2.3.1 *Chitin-Protein Nanofibrils*

Nikolov et al. [19, 20] specify the stiffness tensor for crystalline α-chitin, with the longitudinal axis of the fiber aligned with axis 1, in 6×6 matrix notation configured as:

$$C_{CH} = \begin{bmatrix} 119 & 0.10 & 1.1 & 0 & 0 & 0 \\ 0.10 & 28 & 2.0 & 0 & 0 & 0 \\ 1.1 & 2.0 & 24 & 0 & 0 & 0 \\ 0 & 0 & 0 & 5.0 & 0 & 0 \\ 0 & 0 & 0 & 0 & 8.0 & 0 \\ 0 & 0 & 0 & 0 & 0 & 2.0 \end{bmatrix}. \tag{2.39}$$

Assuming that the fiber protein matrix is isotropic and that Young's modulus and Poisson's ratio are $E_{FP} = 0.004$ GPa and $\nu_{FP} = 0.49$, respectively [19, 20], and given the general form of a stiffness tensor for isotropic media from Eq. (2.26), the stiffness tensor of the fiber proteins is specified as:

$$C_{FP} = \begin{bmatrix} 0.068 & 0.066 & 0.066 & 0 & 0 & 0 \\ 0.066 & 0.068 & 0.066 & 0 & 0 & 0 \\ 0.066 & 0.066 & 0.068 & 0 & 0 & 0 \\ 0 & 0 & 0 & 0.0013 & 0 & 0 \\ 0 & 0 & 0 & 0 & 0.0013 & 0 \\ 0 & 0 & 0 & 0 & 0 & 0.0013 \end{bmatrix}. \tag{2.40}$$

In Coleoptera belonging to two different families (Scarabaeidae and Tenebrionidae), the α-chitin crystallites in chitin-rich structures show a quasi-hexagonal arrangement [26]. The diameter of individual α-chitin crystallites have been measured, on average, as $2r_f = 2.71$, 2.86 nm, with the center to center distances as 5.9, 5.3 nm respectively, and translating into lateral separation distances of $s = 3.19$, 2.44 nm, respectively [26]. Nikolov et al. [19] reported that these values can vary without noticeable influence on the resultant macro-scale properties of the cuticle. Hence we apply averages of these measures such that $2r_f = 2.785$ nm and $s = 2.815$ nm, and consequently (given Eq. [2.34]), $\varphi_{CH} = 0.22$ and $\varphi_{FP} = 0.78$. Because the volume fraction is less than 30%, we use the Mori-Tanaka model described in Section 2.2.3.

The Eshelby's tensor for the α-chitin crystallites is dependent only on Poisson's ratio of the matrix ($\nu_{FP} = 0.49$), and can be found by Eqs. (2.4) and (2.5):

$$S_{CH} = \begin{bmatrix} 0 & 0 & 0 & 0 & 0 & 0 \\ 0.45 & 0.75 & 0.24 & 0 & 0 & 0 \\ 0.45 & 0.24 & 0.75 & 0 & 0 & 0 \\ 0 & 0 & 0 & 0.51 & 0 & 0 \\ 0 & 0 & 0 & 0 & 0.50 & 0 \\ 0 & 0 & 0 & 0 & 0 & 0.50 \end{bmatrix}. \tag{2.41}$$

We can thus calculate the strain concentration factor from Eq. (2.3):

$$A_{CH} = \begin{bmatrix} 1.0 & 0 & 0 & 0 & 0 & 0 \\ 0.0019 & 0.0024 & 0.0022 & 0 & 0 & 0 \\ -0.043 & 0.0026 & 0.0028 & 0 & 0 & 0 \\ 0 & 0 & 0 & 0.00053 & 0 & 0 \\ 0 & 0 & 0 & 0 & 0.00034 & 0 \\ 0 & 0 & 0 & 0 & 0 & 0.0013 \end{bmatrix}. \tag{2.42}$$

Given Eq. (2.2), the stiffness tensor of a chitin protein nanofibril is specified as:

$$C_{NF} = \begin{bmatrix} 27 & 0.067 & 0.067 & 0 & 0 & 0 \\ 0.067 & 0.089 & 0.085 & 0 & 0 & 0 \\ 0.067 & 0.085 & 0.089 & 0 & 0 & 0 \\ 0 & 0 & 0 & 0.0021 & 0 & 0 \\ 0 & 0 & 0 & 0 & 0.0021 & 0 \\ 0 & 0 & 0 & 0 & 0 & 0.0021 \end{bmatrix}. \tag{2.43}$$

2.3.2 Mesocuticle

Here we present the numerical results of the four-step procedure outlined in Section 2.2.5.

1. To calculate the effective properties of a single layer of the Bouligand structure as a fiber-reinforced matrix, we need to account for the stiffness tensor of the chitin-protein nanofibrils and protein matrix, as well as their respective volume fractions. The stiffness tensor of the chitin-protein nanofibrils is given by Eq. (2.43). The volume fractions may be calculated from Eq. (2.34), assuming a quasi-hexagonal arrangement of the fibers. The exact separation between the nanofibrils is unknown, but it is possible to estimate their separation based on the number of layers in the Bouligand structure, the size of the chitin-protein nanofibrils, and the pitch of the ply. In our samples, there are (on average) approximately ten 180° alternations per 1 µm. We therefore estimate approximately 100 nm per 180° alternation. The nanofibrils have an estimated diameter of 5.6 nm each, based on Section 2.3.1. If we assume a separation distance of 1.5 times the radius of a nanofibril ($s = 4.2$ nm), the resulting structure has

roughly 10 layers per 180° alternation. This number agrees with experimentally measured stacking in the mesocuticle of beetles [27]. Moreover, these parameters give the model macroscale properties that show very good correspondence with fresh mesocuticle [21].

The above specifications yield $\varphi_{NF} = 0.30$ as an upper bound for the volumetric fraction of nanofibrils in the apparent mesocuticle and therefore $\varphi_{PM} = 0.70$. The volume fraction of chitin is therefore nearly 6.5%, which agrees with experimentally measured values of chitin inclusion [22, 23]. Given this result, the Mori-Tanaka model may be used to find the effective stiffness tensor of a single ply within the Bouligand structure of the apparent mesocuticle, without pore canals. This volume fraction is generally considered to be at the upper limit (30%) for this method; in this instance, however, we find that estimation of the effective tensor for mesocuticle using the Maxwell scheme yields nearly identical results.

Young's moduli, E_{PM}, for matrix proteins have been reported by Ker [58] to vary from 0.12 GPa in tendons to 1.7 GPa in the highly sclerotized tissue (tibia). Poisson's ratio, ν_{PM}, of these proteins is unknown for insects, but was found by [19] to be 0.45 for lobsters. To calculate the stiffness tensor of the protein matrix, we assume $E_{PM} = 1.2\,\text{GPa}$ and $\nu_{PM} = 0.45$ because of the degree of tanning and sclerotization in the mesocuticle. We therefore specify:

$$C_{PM} = \begin{bmatrix} 4.6 & 3.7 & 3.7 & 0 & 0 & 0 \\ 3.7 & 4.6 & 3.7 & 0 & 0 & 0 \\ 3.7 & 3.7 & 4.6 & 0 & 0 & 0 \\ 0 & 0 & 0 & 0.41 & 0 & 0 \\ 0 & 0 & 0 & 0 & 0.41 & 0 \\ 0 & 0 & 0 & 0 & 0 & 0.41 \end{bmatrix}. \tag{2.44}$$

Accordingly, Eshelby's tensor for a chitin-protein nanofibril is:

$$S_{NF}=\begin{bmatrix} 0 & 0 & 0 & 0 & 0 & 0 \\ 0.41 & 0.73 & 0.18 & 0 & 0 & 0 \\ 0.41 & 0.18 & 0.73 & 0 & 0 & 0 \\ 0 & 0 & 0 & 0.55 & 0 & 0 \\ 0 & 0 & 0 & 0 & 0.50 & 0 \\ 0 & 0 & 0 & 0 & 0 & 0.50 \end{bmatrix}. \tag{2.45}$$

The strain concentration factor for the nanofiobrils is modeled as:

$$A_{NF} = \begin{bmatrix} 1.0 & 0 & 0 & 0 & 0 & 0 \\ 3.7 & 5.6 & 3.5 & 0 & 0 & 0 \\ 3.7 & 3.5 & 5.6 & 0 & 0 & 0 \\ 0 & 0 & 0 & 2.2 & 0 & 0 \\ 0 & 0 & 0 & 0 & 2.0 & 0 \\ 0 & 0 & 0 & 0 & 0 & 2.0 \end{bmatrix}. \tag{2.46}$$

Lastly, the stiffness tensor of a single lamina of the Bouligand structure is:

$$C_L = \begin{bmatrix} 9.5 & 0.82 & 0.82 & 0 & 0 & 0 \\ 0.82 & 1.1 & 0.71 & 0 & 0 & 0 \\ 0.82 & 0.71 & 1.1 & 0 & 0 & 0 \\ 0 & 0 & 0 & 0.22 & 0 & 0 \\ 0 & 0 & 0 & 0 & 0.23 & 0 \\ 0 & 0 & 0 & 0 & 0 & 0.23 \end{bmatrix}. \tag{2.47}$$

2. A Voigt estimate (Section 2.2.3) can be applied to find the effective upper bound of the stiffness tensor of the entire Bouligand structure according to Eqs. (2.35)-(2.37). The rotation matrix is necessary to find the effective properties of all three plies in the same coordinate system, as they are rotated relative to each other. Axis 3 is used as the transverse normal to the laminae, while axes 1 and 2 are the in-plane laminar axes. The simplest laminate composite conforming to the generalized Bouligand structure is a stack of three laminae each rotated 60° to each other along the normal axis. We therefore assume that $i = 1$ represents the instance of the lamina whose properties are already represented in the appropriate coordinate system, where $\theta = 0°$, and given in Eq. (2.47). Thus, given that $\theta = 60°$, 120°, when $i = 2$, 3, respectively:

$$C_1 = C_L\,,$$

$$C_2 = \begin{bmatrix} 1.7 & 2.3 & 0.80 & 0 & 0 & 0.93 \\ 2.3 & 5.9 & 0.80 & 0 & 0 & 2.7 \\ 0.80 & 0.80 & 1.1 & 0 & 0 & 0.050 \\ 0 & 0 & 0 & 0.22 & 0.0042 & 0 \\ 0 & 0 & 0 & 0.0042 & 0.22 & 0 \\ 0.93 & 2.7 & 0.050 & 0 & 0 & 1.7 \end{bmatrix}, \tag{2.48}$$

$$C_3 = \begin{bmatrix} 1.7 & 2.3 & 0.80 & 0 & 0 & -0.93 \\ 2.3 & 5.9 & 0.80 & 0 & 0 & -2.7 \\ 0.80 & 0.80 & 1.1 & 0 & 0 & -0.050 \\ 0 & 0 & 0 & 0.22 & -0.0042 & 0 \\ 0 & 0 & 0 & -0.0042 & 0.22 & 0 \\ -0.93 & -2.7 & -0.050 & 0 & 0 & 1.7 \end{bmatrix}.$$

Therefore, for the Bouligand structure without pores [4] :

$$C_{PW} = \begin{bmatrix} 4.3 & 1.8 & 0.77 & 0 & 0 & 0 \\ 1.8 & 4.3 & 0.77 & 0 & 0 & 0 \\ 0.77 & 0.77 & 1.1 & 0 & 0 & 0 \\ 0 & 0 & 0 & 0.22 & 0 & 0 \\ 0 & 0 & 0 & 0 & 0.22 & 0 \\ 0 & 0 & 0 & 0 & 0 & 1.2 \end{bmatrix}. \tag{2.49}$$

3. Sevostianov et. al. [46] calculated the effective properties of a transversely isotropic matrix embedded with spheroidal inhomogeneities whose rotational axes are aligned with the axis of symmetry in the matrix. If the Bouligand structure can be effectively represented as a transversely isotropic matrix, and the pore canals as cylinders, rather than helices, then we can calculate the additional compliance added to the material by an arbitrary number of pores. In general, this is as two-step procedure: first, the additional compliance imbued by a single pore must be ascertained, then the influence of multiple pores can be calculated, based on the shape and number of pores.

   Unlike the cuticle of other arthropods, such as lobsters, beetle cuticle does not have an extensively developed pore canal system, and often appears in SEM or TEM to have a solid surface area, φ_S, in excess of $\varphi_S = 0.96$ [27, 28, 57, 61]. In keeping with their findings, we assume a pore fraction of $\varphi_{PC} = 0.04$ as an upper bound, although the exact area fraction of the pores is not known for any

[4] This result is accurate to at least twelve decimal places regardless of the number of laminae used.

member of the genus *Curculio*, and is quite possibly much lower. Because the pore canal fraction is very low, we can assume that the interaction between pore canals is essentially negligible. We therefore use a non-interaction approximation, described in Section 2.2.3, to simulate the effect of introducting pore canals into the Bouligand structure [44, 46, 62].

We begin by calculating the compliance tensor of the stacked laminae, S_{PW}, from the stiffness tensor presented in Eq. (2.49):

$$S_{PW} = [C_{PW}]^{-1} = \begin{bmatrix} 0.30 & -0.10 & -0.13 & 0 & 0 & 0 \\ -0.10 & 0.30 & -0.13 & 0 & 0 & 0 \\ -0.13 & -0.13 & 1.1 & 0 & 0 & 0 \\ 0 & 0 & 0 & 4.5 & 0 & 0 \\ 0 & 0 & 0 & 0 & 4.5 & 0 \\ 0 & 0 & 0 & 0 & 0 & 0.81 \end{bmatrix}. \tag{2.50}$$

From Eq. (2.11)-(2.16), we derive:

$$H_{NI} = \begin{bmatrix} 0.027 & -0.019 & -0.0053 & 0 & 0 & 0 \\ -0.019 & 0.027 & -0.0053 & 0 & 0 & 0 \\ -0.0053 & -0.0053 & 0.042 & 0 & 0 & 0 \\ 0 & 0 & 0 & 0.090 & 0 & 0 \\ 0 & 0 & 0 & 0 & 0.090 & 0 \\ 0 & 0 & 0 & 0 & 0 & 0.023 \end{bmatrix}. \tag{2.51}$$

Therefore, given Eq. (2.6), the compliance tensor for mesocuticle is:

$$S_M = \begin{bmatrix} 0.32 & -0.12 & -0.14 & 0 & 0 & 0 \\ -0.12 & 0.32 & -0.14 & 0 & 0 & 0 \\ -0.14 & -0.14 & 1.1 & 0 & 0 & 0 \\ 0 & 0 & 0 & 4.6 & 0 & 0 \\ 0 & 0 & 0 & 0 & 4.6 & 0 \\ 0 & 0 & 0 & 0 & 0 & 0.83 \end{bmatrix}, \tag{2.52}$$

And, the stiffness tensor for mesocuticle is specified as:

$$C_M = \begin{bmatrix} 4.1 & 1.8 & 0.74 & 0 & 0 & 0 \\ 1.8 & 4.1 & 0.74 & 0 & 0 & 0 \\ 0.74 & 0.74 & 1.1 & 0 & 0 & 0 \\ 0 & 0 & 0 & 0.22 & 0 & 0 \\ 0 & 0 & 0 & 0 & 0.22 & 0 \\ 0 & 0 & 0 & 0 & 0 & 1.2 \end{bmatrix}. \tag{2.53}$$

2.3.3 Exocuticle

In our model, we identify three primary differences between mesocuticle and exocuticle (see also Section 2.2.6):

1. The packing of the laminae is estimated to be approximately 2-3 times closer than mesocuticle based on the pitch of the ply in exocuticle of our samples, and data from other arthropods [21, 25, 27, 54]. We posit that the diameter of the nanofibrils remains the same, but that the pitch of the ply and separation distance between nanofibrils are reduced. Assuming a lateral separation equal to one-quarter of the radius ($s = 0.7\,\text{nm}$) and half as many laminae per 180° alternation, the resulting structure has three times as many alternations as mesocuticle. The reduced spacing also greatly increases the fiber fraction of the exocuticle, such that $\varphi_{NF} = 0.72$ (total volume of chitin rises to 16.1%). This volume fraction violates the assumption of dilute inclusions used by the Mori-Tanaka model, and we therefore use the effective field method presented in [46] to derive the effective properties of a single lamina of the exocuticle.

2. We estimate the effective Young's modulus of the fiber proteins as $E_{FP} = 0.12\,\text{GPa}$, on the basis of Vincent [22], who provides measurements for the protein matrix of anatomical structures that exhibit large degrees of fiber cross-linking. Changing this parameter of the Mori-Tanaka model presented in Section 2.3.1 yields:

$$C_{NF} = \begin{bmatrix} 28 & 1.9 & 1.9 & 0 & 0 & 0 \\ 1.9 & 2.6 & 2.4 & 0 & 0 & 0 \\ 1.9 & 2.4 & 2.6 & 0 & 0 & 0 \\ 0 & 0 & 0 & 0.063 & 0 & 0 \\ 0 & 0 & 0 & 0 & 0.063 & 0 \\ 0 & 0 & 0 & 0 & 0 & 0.062 \end{bmatrix}. \tag{2.54}$$

3. The effective Young's modulus of the protein matrix in which the microfibers are embedded is estimated as $E_{PM} = 1.7\,\text{GPa}$, in keeping with the findings of Ker [58], for highly sclerotized cuticle.

To use the effective field method, it is necessary to first transform the tensors used as input so that the axis of rotation of an inclusion and the axis of transverse isotropy of the matrix are aligned with the global axis 3. The stiffness tensor presented above has

the longitudinal axis of the fiber aligned with global axis 1. The transformed matrix representation can be specified as:

$$C_{NF} = \begin{bmatrix} 2.6 & 2.4 & 1.9 & 0 & 0 & 0 \\ 2.4 & 2.6 & 1.9 & 0 & 0 & 0 \\ 1.9 & 1.9 & 28 & 0 & 0 & 0 \\ 0 & 0 & 0 & 0.062 & 0 & 0 \\ 0 & 0 & 0 & 0 & 0.063 & 0 \\ 0 & 0 & 0 & 0 & 0 & 0.063 \end{bmatrix}. \tag{2.55}$$

The protein matrix is isotropic and does not need to be rotated; however, given the higher Young's modulus of the matrix, we determine:

$$C_{PM} = \begin{bmatrix} 6.4 & 5.3 & 5.3 & 0 & 0 & 0 \\ 5.3 & 6.4 & 5.3 & 0 & 0 & 0 \\ 5.3 & 5.3 & 6.4 & 0 & 0 & 0 \\ 0 & 0 & 0 & 0.59 & 0 & 0 \\ 0 & 0 & 0 & 0 & 0.59 & 0 \\ 0 & 0 & 0 & 0 & 0 & 0.59 \end{bmatrix}, \tag{2.56}$$

And, from Eq. (2.21):

$$C_D = \begin{bmatrix} -3.9 & -2.8 & -3.4 & 0 & 0 & 0 \\ -2.8 & -3.9 & -3.4 & 0 & 0 & 0 \\ -3.4 & -3.4 & 22 & 0 & 0 & 0 \\ 0 & 0 & 0 & -0.52 & 0 & 0 \\ 0 & 0 & 0 & 0 & -0.52 & 0 \\ 0 & 0 & 0 & 0 & 0 & -0.52 \end{bmatrix}. \tag{2.57}$$

Therefore, for a single lamina we can specify (following rotation back to the original coordinate system) [5] :

$$C_L = \begin{bmatrix} 22 & 2.5 & 2.5 & 0 & 0 & 0 \\ 2.5 & 3.2 & 2.9 & 0 & 0 & 0 \\ 2.5 & 2.9 & 3.2 & 0 & 0 & 0 \\ 0 & 0 & 0 & 0.15 & 0 & 0 \\ 0 & 0 & 0 & 0 & 0.16 & 0 \\ 0 & 0 & 0 & 0 & 0 & 0.16 \end{bmatrix}. \tag{2.58}$$

For the Bouligand structure (using a Voigt estimate):

$$C_{PW} = \begin{bmatrix} 10 & 4.8 & 2.7 & 0 & 0 & 0 \\ 4.8 & 10 & 2.7 & 0 & 0 & 0 \\ 2.7 & 2.7 & 3.2 & 0 & 0 & 0 \\ 0 & 0 & 0 & 0.15 & 0 & 0 \\ 0 & 0 & 0 & 0 & 0.15 & 0 \\ 0 & 0 & 0 & 0 & 0 & 2.6 \end{bmatrix}. \tag{2.59}$$

Assuming the same porosity as the mesocuticle, the effective tensor for the exocuticle is:

[5] It is worth noting that the formulation of the effective field method presented herein is for *transversely isotropic* fibers, rather than fully orthotropic ones. We treat the nanofibrils as transversely isotropic; however, reformulating to allow for orthotropic fibers does change the resultant stiffness tensor very slightly. Because these numerical differences are beyond the ninth decimal place for the values used herein, and essentially disappear with the Voigt estimate, we feel that this is not a critical factor in the calculation of the effective properties of the exocuticle.

$$C_X = \begin{bmatrix} 9.5 & 4.7 & 2.6 & 0 & 0 & 0 \\ 4.7 & 9.5 & 2.6 & 0 & 0 & 0 \\ 2.6 & 2.6 & 3.1 & 0 & 0 & 0 \\ 0 & 0 & 0 & 0.15 & 0 & 0 \\ 0 & 0 & 0 & 0 & 0.15 & 0 \\ 0 & 0 & 0 & 0 & 0 & 2.5 \end{bmatrix} . \tag{2.60}$$

2.3.4 Endocuticle

Here we present the results of the general approach outlined for the derivation of the effective properties of endocuticle, as outlined in Section 2.2.7:

1. Beetle endocuticle is characterized by the presence of unidirectional chitin macrofibers [29]. In these structures, the individual chitin cores surrounded by protein (the chitin-protein nanofibrils) form chitin-protein microfibers that can vary in size from 20-90 nm in diameter [56]. These microfibers are tightly conjoined to form the macrofibers. Hepburn and Ball [28] found the approximate size of microfibers in *Pachynoda sinuata* (Fabricius 1775) to be approximately 30 nm. This is close to the diameter and separation of fibers that can be seen in *Anthonomus grandis* Boheman 1843 [59]. In our samples, we observed that these fibers are of a similar size on average. Because these microfibers appear to be tightly bound, and are not visibly separated in transmission electron micrographs [see [30]], we treat the macrofibers as if they are solely comprised of aligned nanofibrils embedded in a matrix.

   We can readily calculate the effective tensor for a single macrofiber in a manner similar to calculating the effective properties of a single ply in the exocuticle or mesocuticle, without canals. If we assume that the nanofibrils are separated by a distance equal to their own radius [as seen in [30]] in a quasi-hexagonal arrangement, we find, given Eq. (2.34), $\varphi_F = 0.40$. We also assume $E_{FP} = 0.004\,\text{GPa}$, to reflect the reduced cross-linking in the endocuticle, and that $E_{PM} = 1.0\,\text{GPa}$, in keeping with the value used for endocuticle by Nikolov et al. [20]. With these

values, we find the stiffness tensor for a the protein matrix as:

$$C_{PM} = \begin{bmatrix} 3.8 & 3.1 & 3.1 & 0 & 0 & 0 \\ 3.1 & 3.8 & 3.1 & 0 & 0 & 0 \\ 3.1 & 3.1 & 3.8 & 0 & 0 & 0 \\ 0 & 0 & 0 & 0.34 & 0 & 0 \\ 0 & 0 & 0 & 0 & 0.34 & 0 \\ 0 & 0 & 0 & 0 & 0 & 0.34 \end{bmatrix}, \tag{2.61}$$

And the effective stiffness tensor for a single chitin macrofiber:

$$C_{MF} = \begin{bmatrix} 12 & 0.50 & 0.50 & 0 & 0 & 0 \\ 0.50 & 0.71 & 0.43 & 0 & 0 & 0 \\ 0.50 & 0.43 & 0.71 & 0 & 0 & 0 \\ 0 & 0 & 0 & 0.14 & 0 & 0 \\ 0 & 0 & 0 & 0 & 0.15 & 0 \\ 0 & 0 & 0 & 0 & 0 & 0.15 \end{bmatrix}. \tag{2.62}$$

2. In order to calculate the properties of a single balken layer, we posit that the layer is comprised of macrofibers, with effective stiffness C_{MF}, aligned in an isotropic protein matrix with stiffness identical to C_{PM}. In addition we assume that the layer is porous, and that the pores are embedded in the protein matrix between the macrofibers. From our samples, we find that the area fraction (and, equivalently, the volume fraction) of protein matrix layers varies, by layer, from roughly 14-18%. We therefore take the average and set $\varphi_L = 0.16$ and $\varphi_{MF} = 0.84$. Additionally, the ratio of the diameter of a pore and its separation distance to the closest pore is equal to the area fraction of the protein layers in cross-section. We assume a square arrangement of the pores due to the linear mesh arrangement of the balken layers; thus, given Eq. (2.38), we find $\varphi_p \approx 0.015$.

We now consider an isotropic protein matrix with effective properties equal to C_{PM}. We assume a global coordinate system where axis 1 is the long axis of the macrofibers, axis 2 is the in-plane axis that, along with axis 1, defines the plane of a single layer of balken, and axis 3 is the cuticle normal. We then introduce into this matrix a system of identical, cylindrical pores with the same arrangement of our samples, whose long axis is aligned with global axis 3. Because the pores in our samples are effectively embedded in the protein matrix

between the macrofibers and occupy a very small volume, we can estimate the properties of the homogenized matrix, before introducing the macrofibers, using a non-interaction approximation (Section 2.2.3).

From the non-interaction approximation outlined in Section 2.2.3, we derive the following:

$$H_{NI} = \begin{bmatrix} 0.031 & -0.017 & -0.0067 & 0 & 0 & 0 \\ -0.017 & 0.031 & -0.0067 & 0 & 0 & 0 \\ -0.0067 & -0.0067 & 0.015 & 0 & 0 & 0 \\ 0 & 0 & 0 & 0.022 & 0 & 0 \\ 0 & 0 & 0 & 0 & 0.022 & 0 \\ 0 & 0 & 0 & 0 & 0 & 0.028 \end{bmatrix}. \tag{2.63}$$

Thus, given C_{PM} and Eq. (2.6), the effective compliance tensor for a layer of protein separating the macrofibers is obtained as:

$$S_L = \begin{bmatrix} 1.0 & -0.47 & -0.46 & 0 & 0 & 0 \\ -0.47 & 1.0 & -0.46 & 0 & 0 & 0 \\ -0.46 & -0.46 & 1.0 & 0 & 0 & 0 \\ 0 & 0 & 0 & 2.9 & 0 & 0 \\ 0 & 0 & 0 & 0 & 2.9 & 0 \\ 0 & 0 & 0 & 0 & 0 & 2.9 \end{bmatrix}, \tag{2.64}$$

And, therefore:

$$C_L = \begin{bmatrix} 3.6 & 2.9 & 3.0 & 0 & 0 & 0 \\ 2.9 & 3.6 & 3.0 & 0 & 0 & 0 \\ 3.0 & 3.0 & 3.6 & 0 & 0 & 0 \\ 0 & 0 & 0 & 0.34 & 0 & 0 \\ 0 & 0 & 0 & 0 & 0.34 & 0 \\ 0 & 0 & 0 & 0 & 0 & 0.34 \end{bmatrix}. \tag{2.65}$$

3. Because the pores occupy a small volume, the anisotropic generated by their inclusion will be relatively small. We are therefore able to generate an isotropic approximation of the matrix to calculate the stiffness contribution tensor N_{MF} and Hill's tensor Q_{MF} for a macrofiber. Considering a transversely isotropic layer of porous protein matrix, with stiffness tensor C_L, the isotropic approximation of the shear modulus G and bulk modulus K , as well as Young's modulus E and Poisson's ratio ν are given by Eqs. (2.24) and (2.25), respectively:

$$
\begin{aligned}
G &= 0.34\,\mathrm{GPa}\,, \\
K &= 3.2\,\mathrm{GPa}\,, \\
E &= 0.98\,\mathrm{GPa}\,, \\
\nu &= 0.45\,.
\end{aligned}
\tag{2.66}
$$

From these elastic constants, and through application of Eq. (2.23), we can calculate the isotropic approximations of the effective stiffness and compliance tensors of the protein matrix:

$$
S_{IL} = \begin{bmatrix}
1.0 & -0.46 & -0.46 & 0 & 0 & 0 \\
-0.46 & 1.0 & -0.46 & 0 & 0 & 0 \\
-0.46 & -0.46 & 1.0 & 0 & 0 & 0 \\
0 & 0 & 0 & 2.9 & 0 & 0 \\
0 & 0 & 0 & 0 & 2.9 & 0 \\
0 & 0 & 0 & 0 & 0 & 2.9
\end{bmatrix} . \tag{2.67}
$$

4. Using the isotropic approximation of the porous matrix, we now calculate the effective properties of a single balken layer by simulating the effect of embedding macrofibers into the matrix, using the Maxwell homogenization scheme described in Section 2.2.3. Given the elastic constants in Eq. (2.66) and the components of Hill's tensor, Q, presented in Eqs. (2.29), we obtain [6] :

$$
Q_{MF} = \begin{bmatrix}
1.2 & 0.28 & 0.28 & 0 & 0 & 0 \\
0.28 & 0.46 & 0.15 & 0 & 0 & 0 \\
0.28 & 0.15 & 0.46 & 0 & 0 & 0 \\
0 & 0 & 0 & 0.15 & 0 & 0 \\
0 & 0 & 0 & 0 & 0.17 & 0 \\
0 & 0 & 0 & 0 & 0 & 0.17
\end{bmatrix} . \tag{2.68}
$$

Thus, given Eq. (2.28), the compliance contribution tensor for the macrofibers is:

$$
H_{MF} = \begin{bmatrix}
-9.0 & 4.0 & 4.0 & 0 & 0 & 0 \\
4.0 & -1.1 & -2.1 & 0 & 0 & 0 \\
4.0 & -2.1 & -1.1 & 0 & 0 & 0 \\
0 & 0 & 0 & 2.1 & 0 & 0 \\
0 & 0 & 0 & 0 & 1.9 & 0 \\
0 & 0 & 0 & 0 & 0 & 1.9
\end{bmatrix} . \tag{2.69}
$$

[6] The formulation of Q presented in Eqs. 2.29 assumes that the longitudinal axis of the inhomogeneities is aligned with global axis 3. We therefore rotate the resultant tensor to align the macrofibers with global axis 1, and assign the transverse normal to global axis 3.

Using Eq. (2.27), the compliance stiffness tensors for a single balken layer are, respectively:

$$S_B = \begin{bmatrix} 0.12 & -0.057 & -0.047 & 0 & 0 & 0 \\ -0.057 & 1.9 & -1.2 & 0 & 0 & 0 \\ -0.047 & -1.2 & 1.9 & 0 & 0 & 0 \\ 0 & 0 & 0 & 6.1 & 0 & 0 \\ 0 & 0 & 0 & 0 & 5.8 & 0 \\ 0 & 0 & 0 & 0 & 0 & 5.8 \end{bmatrix}, \tag{2.70}$$

$$C_B = \begin{bmatrix} 9.0 & 0.63 & 0.60 & 0 & 0 & 0 \\ 0.63 & 0.86 & 0.53 & 0 & 0 & 0 \\ 0.60 & 0.53 & 0.86 & 0 & 0 & 0 \\ 0 & 0 & 0 & 0.16 & 0 & 0 \\ 0 & 0 & 0 & 0 & 0.17 & 0 \\ 0 & 0 & 0 & 0 & 0 & 0.17 \end{bmatrix}. \tag{2.71}$$

2.3.5 Summary of Results

In Eq. (2.72) [see following page] we present the effective stiffness tensors (in 6×6 matrix notation) for the exocuticle, mesocuticle, and a single balken layer of the endocuticle, as C_X, C_M, and C_B, respectively. Additionally, we list the elastic constants that can be calculated from the inverse of these tensors in Tab. 2.1 and Fig. 2.6, and summarize the models from which these tensors were derived in Tab. 2.2. Accordingly, the in-plane (axes 1 and 2) Young's moduli of exocuticle and mesocuticle are 6.39 GPa and 3.08 GPa, respectively, while the transverse (axis 3) moduli for these regions are 2.14 GPa and 0.91 GPa, respectively. Interestingly, Young's modulus of endocuticle along the major axis of the macrofibers is much stiffer than either of the other regions, at 8.47 GPa; however, Young's moduli for endocuticle along axes 2 and 3 are substantially lower, at 0.52 GPa. Due to this anisotropy, cuticular stiffness will depend upon the stacking angle of the balken layers [38].

We note that the values for several constants were extracted from relevant literature, as we were unable to accurately measure these quantities in the species considered herein. These values do not necessarily represent the actual values present in *C. longinasus*, and we consider these estimates as useful and necessary for the construction of this model, while considering the possible error introduced by their

inclusion. We therefore investigate the potential error introduced by the following variables: (1) Young's modulus of fiber proteins, E_{FP}; (2) Poisson's ratio of fiber proteins, ν_{FP}; (3) Young's modulus of matrix proteins, E_{PM}; (4) Poisson's ratio of matrix proteins, ν_{PM}; (5) volume fraction of chitin-protein nanofibrils, φ_{NF}, and; (6) volume fraction of pore canals, φ_{PC}. We do not examine the volume fraction of α-chitin in a nanofibril, which was investigated by Nikolov et al.[20], and found to have minimal effects on the resultant macroscopic elastic moduli with relatively large variation.

In Fig. 2.7, we graphically represent estimates of the macroscopic Young's moduli of each cuticular layer as these parameters change individually, with all others kept constant. The in-plane macroscopic Young's moduli exhibit little or no change with respect to the elastic constants of the fiber and matrix proteins, given the range of values used in the model. We observe that the structural arrangement of the chitin-protein nanofibrils has a strong influence on the resulting macroscopic properties of the cuticle, and influences which factors will contribute most to the overall stiffness of each region. For instance, the Bouligand structure greatly reduces the anisotropy of the cuticle compared to the parallel bundles of chitin in the endocuticle; increasing the volume fraction of nanofibrils in the mesocuticle to levels seen in the exocuticle results in an increase of the in-plane

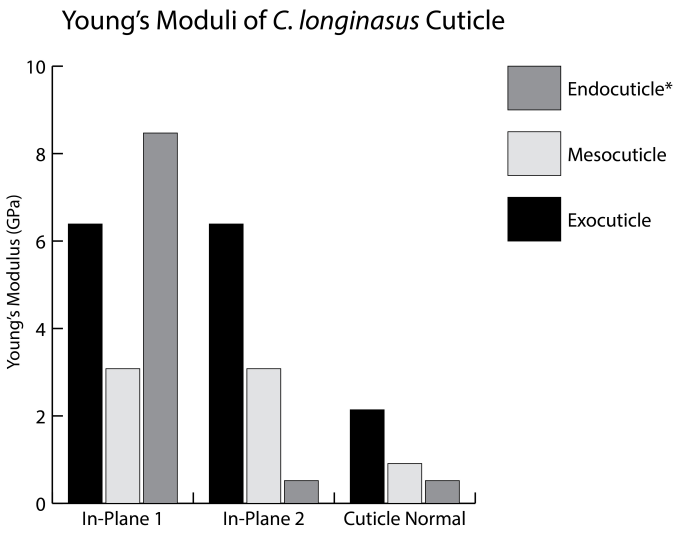


Figure 2.6: Summary of Young's moduli of elasticity along each global axis for each region of cuticle.

Table 2.1: Summary of elastic constants for the layers of cuticle. Young's and bulk moduli are given in GPa.

Constant	**Exocuticle**	**Mesocuticle**	**Endocuticle***
E_1	6.4	3.1	8.5
E_2	6.4	3.1	0.52
E_3	2.1	0.91	0.52
G_{12}	2.5	1.2	0.17
G_{31}	0.15	0.22	0.17
G_{23}	0.15	0.22	0.16
ν_{12}	0.36	0.37	0.49
ν_{21}	0.36	0.37	0.03
ν_{23}	0.54	0.42	0.63
ν_{32}	0.18	0.13	0.63
ν_{31}	0.18	0.13	0.06
ν_{13}	0.54	0.42	0.42

*Single layer of chitin macrofibers

Young's modulus of about 3 GPa, while doing the same for the endocuticle results in an increase of almost 5 GPa (along axis 1). Due to the parallel arrangement of chitin fibers in the endocuticle, smaller variations in the volume fraction of nanofibrils or pores elicit a larger change in the longitudinal Young's modulus compared to either mesocuticle or exocuticle.

The Bouligand structure is also responsible for the sensitivity of the normal Young's moduli to the properties of the fiber proteins. In Fig. 2.8 we present the point-wise elasticity of the model with respect to each of these variables. We observed that the macroscale Young's moduli are most sensitive to the volume fraction of nanofibrils

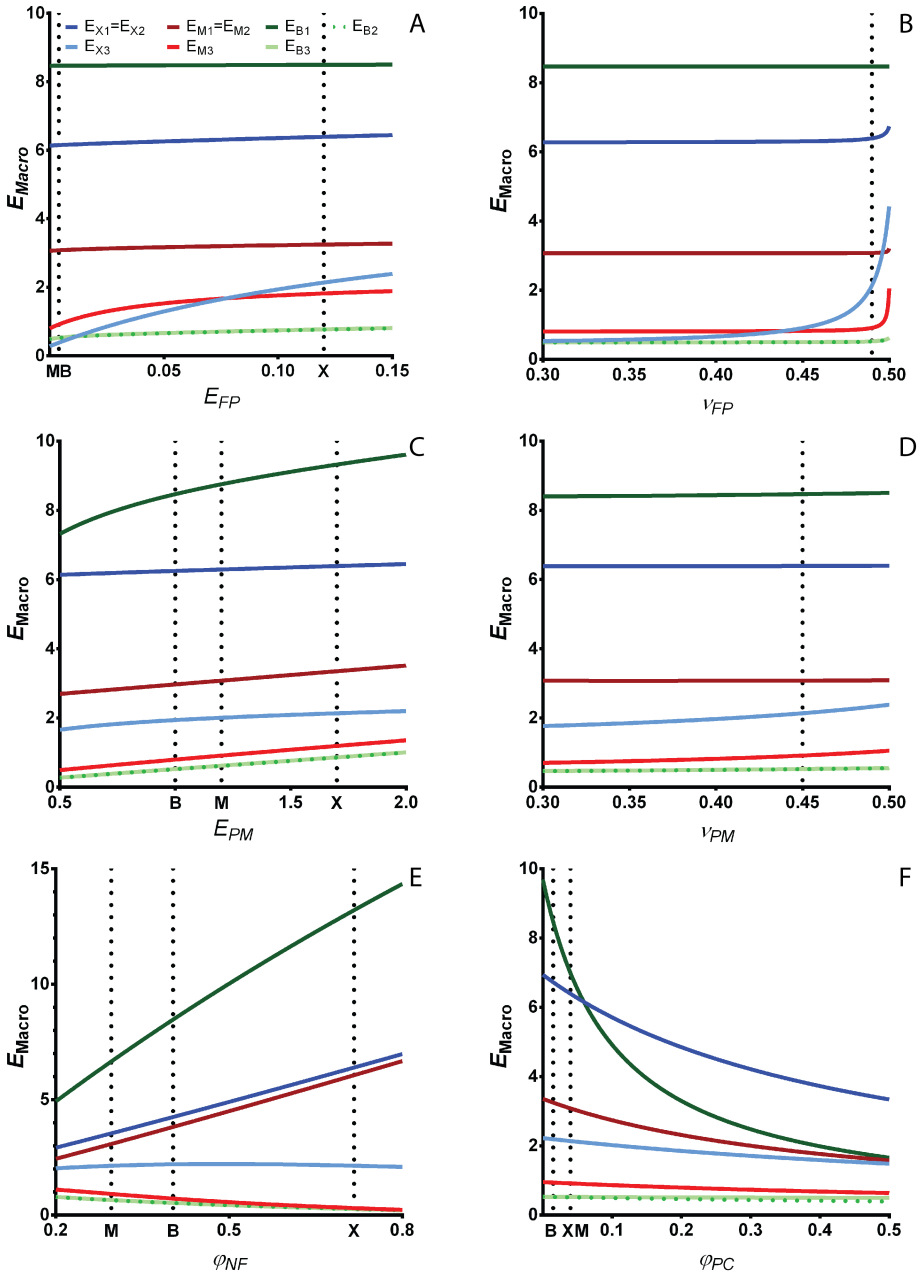


Figure 2.7: Macroscopic Young's moduli for exo-, meso-, and endocuticle (as indicated by subscripts X, M, B, respectively), along transverse axes 1 and 2, and normal axis 3, given variation in: **A** fiber protein modulus, **B** fiber protein Poisson's ratio, **C** protein matrix modulus, **D** protein matrix Poisson's ratio, **E** volume fraction of nanofibrils, **F** volume fraction of pore canals.

*Vertical lines are placed at values used in the model, for each cuticle region, as indicated; a single, unlabeled line indicates that the same value was used for all regions.

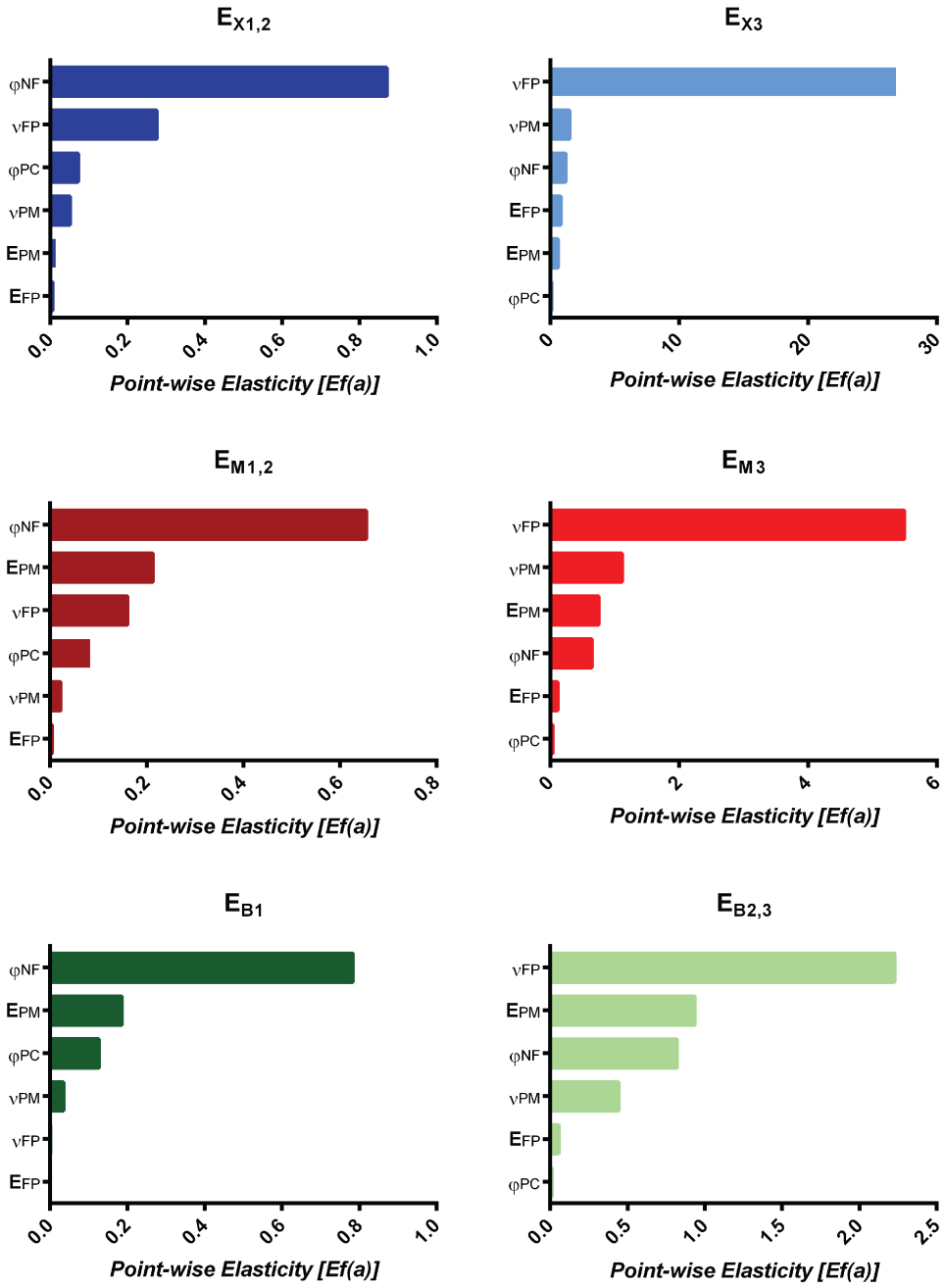


Figure 2.8: Point-wise elasticity of the macroscopic Young's moduli for exo-, meso-, and endocuticle (as indicated by subscripts X, M, B, respectively), along transverse axes 1 and 2, and normal axis 3, with respect to literature extracted parameters. Elasticity is highest with respect to Poisson's ratio of the fiber proteins (for normal moduli) and the volume fraction of nanofibrils (for transverse moduli).

Table 2.2: Homogenization Schema Used for Cuticle Layers of *Curculio longinasus*

RVE	**Exocuticle**	**Mesocuticle**	**Endocuticle***
Chitin Nanofibril	Mori-Tanaka	Mori-Tanaka	Mori-Tanaka
Single Lamina	Effective Field	Mori-Tanaka	—
Laminae *sans* Pores	Voigt Estimate	Voigt Estimate	—
Laminae with Pores	Non-Interaction	Non-Interaction	—
Chitin Macrofiber	—	—	Effective Field
Porous Protein Matrix	—	—	Non-Interaction
Balken Layer	—	—	Maxwell Scheme

*Single layer of chitin macrofibers

$$
\begin{aligned}
C_X &= \begin{bmatrix} 9.5 & 4.7 & 2.6 & 0 & 0 & 0 \\ 4.7 & 9.5 & 2.6 & 0 & 0 & 0 \\ 2.6 & 2.6 & 3.1 & 0 & 0 & 0 \\ 0 & 0 & 0 & 0.15 & 0 & 0 \\ 0 & 0 & 0 & 0 & 0.15 & 0 \\ 0 & 0 & 0 & 0 & 0 & 2.5 \end{bmatrix}, \\
C_M &= \begin{bmatrix} 4.1 & 1.80 & 0.74 & 0 & 0 & 0 \\ 1.8 & 4.1 & 0.74 & 0 & 0 & 0 \\ 0.74 & 0.74 & 1.1 & 0 & 0 & 0 \\ 0 & 0 & 0 & 0.22 & 0 & 0 \\ 0 & 0 & 0 & 0 & 0.22 & 0 \\ 0 & 0 & 0 & 0 & 0 & 1.2 \end{bmatrix}, \\
C_B &= \begin{bmatrix} 9.0 & 0.63 & 0.60 & 0 & 0 & 0 \\ 0.63 & 0.86 & 0.53 & 0 & 0 & 0 \\ 0.60 & 0.53 & 0.86 & 0 & 0 & 0 \\ 0 & 0 & 0 & 0.16 & 0 & 0 \\ 0 & 0 & 0 & 0 & 0.17 & 0 \\ 0 & 0 & 0 & 0 & 0 & 0.17 \end{bmatrix}.
\end{aligned}
\tag{2.72}
$$

(transverse) and Poisson's ratio of the fiber proteins (normal). Due to the significantly denser arrangement of the chitin-protein nanofibrils, the normal Young's modulus of the exocuticle is highly sensitive to changes in Poisson's ratio of the fiber proteins, with an elasticity of 26.8, as compared to mesocuticle (5.5) and endocuticle (2.2). However, given the comparatively low elasticities of the normal Young's moduli for the other variables (the highest value is for exocuticle at 1.5 for ν_{PM}), and the transverse Young's moduli to all parameters (the highest value is for exocuticle at 0.87), we infer that the model is generally quite robust over a wide range of input conditions. This

observation corroborates the findings of Nikolov et al. [19], who came to a similar conclusion.

2.4 Discussion

2.4.1 Major Insights

Our analysis indicates that the substantial differences between the regions of cuticle along the *C. longinasus* rostrum appear to be largely due to structural modifications, rather than chemical/compositional changes. In particular, the structural arrangement and volume fraction of the chitin nanofibrils appear to have the greatest influence on the macroscale properties of the corresponding cuticular region. We observed that significant variation in certain properties, such as the elastic modulus of the protein matrix, have comparatively little effect on the macroscale moduli. These results are largely consistent with previous studies that demonstrate the importance of microstructure in determining the macroscopic properties of biomaterials [19, 20, 23, 27]. Furthermore, as noted in Section 2.3.5, the endocuticle is much stiffer along axis 1 (corresponding to the longitudinal axis of the macrofibers) than either the exocuticle or mesocuticle. By contrast, in other arthropods, where the innermost region of the cuticle also conforms to the Bouligand structure, the endocuticle is often the most compliant region [19–21]. While the stiffness of beetle endocuticle is balanced by the comparatively low Young's modulus along the other axes, the stiffness of any cuticular structure in beetles is most likely dependent upon the stacking angle of the balken layers, due to the high degree of anisotropy of this material.

Additionally, we notice an inverse correlation between the in-plane and normal Young's moduli of the exocuticle and mesocuticle, with respect to fiber fraction. This is a result of the high degree of anisotropy of the chitin-protein nanofibrils, the effect of

which is even more pronounced in the endocuticle. Within the chitin macrofibers, the properties of the protein matrix largely determine the macroscale moduli normal to the longitudinal axis (axis 1), especially at lower volume fractions of nanofibrils. As the volume fraction of nanofibrils increases, we observe a strong decrease in these moduli, as the chitin nanofibrils are significantly more compliant than the protein matrix along axes 2 and 3, while simultaneously an increase in stiffness is seen along axis 1. In the exocuticle and mesocuticle, this effect is somewhat mitigated by the arrangement of nanofibrils in the Bouligand structure, which results in a degree of averaging of the moduli in the 1 and 2 axes. In general, the mesocuticle and endocuticle are of similar composition; however, the Bouligand structure creates a greater degree of isotropy in the mesocuticle due to the lower volume fraction of chitin.

How then do our outcomes explain the differences in elasticity between exocuticle and mesocuticle? We observe that differences between the elastic constants of exocuticle and mesocuticle are primarily correlated with the volume fraction of nanofibrils and the elastic properties of the fiber proteins. For the in-plane moduli, the volume fraction of nanofibrils is the primary contributing factor of the increased stiffness of the exocuticle, which is not strongly affected by variation of other parameters. In contrast, we note that the properties of the fiber proteins have a strong influence on the elastic constants of the exocuticle in the normal direction, due to the high volume fraction of the nanofibrils. The values of Young's modulus and Poisson's ratio of the fiber proteins must therefore be carefully considered, due to their influence on the properties of the exocuticle in the normal direction.

If we presume that these values are the same for both exo- and mesocuticle, then the resulting exocuticle would be significantly weaker in the normal direction than the mesocuticle. Based on the data reviewed in the work of Klocke and Schmitz [21], this is unlikely for insects. We instead consider the reduced water content and increased

cross-linking between nanofibrils and matrix (due to sclerotization), as well as the work of Vincent et al. [22, 23] and Ker [58], in estimating Young's modulus and Poisson's ratio of the fiber proteins. This enables us to utilize more appropriate and realistic values that account for these factors, and provide results that closely match what is observed in insects [7] (i.e., the exocuticle is stiffer than the mesocuticle in the normal direction [21]). Further investigation is needed to more accurately determine these parameters for members of the genus *Curculio*.

2.4.2 Modeling Limitations

Our model suffers from two critical limitations. The first is the pragmatic constraint of approximating certain values based on the literature. Generally, these values can vary by nearly an order of magnitude without creating a correspondingly large variation in the model output. We are also able to mitigate the potential for significant error by comparing the results of the model to the known elastic properties of insect cuticle. The second limitation concerns the scope of the model, which is restricted to conditions of small strains and linear-elastic mechanical behavior. The viscoelastic and viscoplastic behavior of the cuticle during significant deformation has been explored in lobster cuticle, but has not been accurately described by any micromechanical model, mainly because of the numerous and difficult-to-measure factors that require assessment in order to accurately formulate such a model. For example, we would require a full characterization of the makeup of the protein matrix, degree of interconnection between chitin fibers, and presence of interply fibers [19, 30, 63]. In spite of these limitations, our model yields useful insights7 into the interplay of structural and compositional

[7] It is interesting to consider that increasing the fiber fraction of the exocuticle results in transverse (in-plane) stiffening at the expense of stiffness in the normal direction. We speculate that sclerotization might occur more strongly in the exocuticle to counter this effect, and thereby increase stiffness in the normal direction.

factors in relation to the macroscale properties of each region of cuticle. Specifically, we provide a predictive framework within which we may systematically compare the optimization of the female *C. longinasus* cuticle in response to the mechanical stresses to that of different species in this genus, as well as in other phylogenetically related groups. Refining our approach to accommodate experimentally validated data for multiple species can produce novel insights into the evolutionary and developmental trade-offs of this system.

Future research should focus in particular on the degree of optimization that has occurred in related *Curculio* species in response to mechanical stress, and consider the evolutionary trajectory of this genus as a whole. The elastic constants generated by our approach can now be applied to full-scale three-dimensional models of the head of *C. longinasus*. In conjunction with data about the orientation angles of the endocuticular macrofibers in this species, these constants will permit us to perform finite element analysis to simulate mechanical loads encountered by females during oviposition. By examining the responses of different species and the localization of stress and strain on their heads during deformation, and aligning these variations phylogenetically, we hope to better mechanistically understand the process of structural adaptation and optimization that has occurred during the evolution of this group of weevils [7, 13, 16].

ACKNOWLEDGMENTS

This research was funded in part by the National Science Foundation (DEB-1155984) and the United States Department of Agriculture – Agricultural Research Service (Agreement 58-1275-1-335).

CHAPTER 3

Exoskeletal Strength and Composite Profile of the Acorn Weevil Rostrum

ABSTRACT

The acorn weevil (*Curculio* Linnaeus, 1758) rostrum (snout) exhibits remarkable flexibility and toughness derived from the microarchitecture of its exoskeleton. Here we characterize modifications to the composite profile of the rostral cuticle that simultaneously enhance the flexibility and toughness of the distal portion of the snout. Using Classical Laminate Plate Theory, we estimate the effect of these modifications on the elastic behavior of the exoskeleton. We show that the tensile behavior of the rostrum across six *Curculio* species with high morphological variation correlates with changes in the relative layer thicknesses and orientation angles of layers in the exoskeleton. Accordingly, increased endocuticle thickness is strongly correlated with increased tensile strength. Rostrum stiffness is shown to be inversely correlated with work of fracture; thus allowing a highly curved rostrum to completely straighten without structural damage. Finally, we identify exocuticle rich invaginations of the occipital sutures both as a likely site of crack initiation in tensile failure, and as a source of morphological constraint on the evolution of the rostrum in *Curculio* weevils.

3.1 Introduction

The exoskeleton of Coleoptera (beetles) is a hierarchically structured, fibrous composite – characterized by variously arranged α-chitin (N-acetylglucosamine) nanofibrils that are embedded in a heterogeneous protein matrix [8, 23, 28]. Although α-chitin is brittle and strongly anisotropic, beetle cuticle is simultaneously rigid and tough due to its unique laminate microstructure (reviewed in [26, 29, 30]), characterized in detail below. Impact-prone areas and exaggerated structures in arthropods generally exhibit cuticle organization that resists deformation and fracture [34, 64–67]. However, acorn weevils in the genus *Curculio* Linnaeus, 1758 [1] (Curculionidae in the sense of [60]) instead exhibit unusual distal flexibility in an elongate extension of the head called the rostrum (snout) [5, 7–9]. The rostrum is a hollow, strongly curved (over 90° in some species), cylindrical, exoskeletal extension of the otherwise nearly-spherical head, which bears at its apex the terminal chewing mouthparts [5, 11, 14, 15, 69]. This structure is used by the female to feed on fruit (plant) tissue and to excavate sites for egg-laying (oviposition, see Fig. 3.1). The rostrum can be repeatedly bent, without evident damage, and despite being composed of the same material as other rigid body parts [5, 7–9]. By maintaining constant pressure on the snout and rotating around the bore-hole, females are able to flex the rostrum into a straightened configuration and produce a linear channel into the fruit. A single adult female may prepare hundreds of such sites [7, 10, 17].

Despite its documented performance in many *Curculio* species [5, 7, 10, 17], it remains unknown how the rostrum of female acorn weevils can withstand the repeated,

[1] Pursuant to the International Code of Zoological Nomenclature, the first mention of any specific epithet will include the full genus and species names as a binomen (two-part name) followed by the author and date of publication of the name. This is not an in-line reference; it is a part of the name itself and refers to a particular act establishing the validity and fixing the identity of the corresponding name by that author [68].

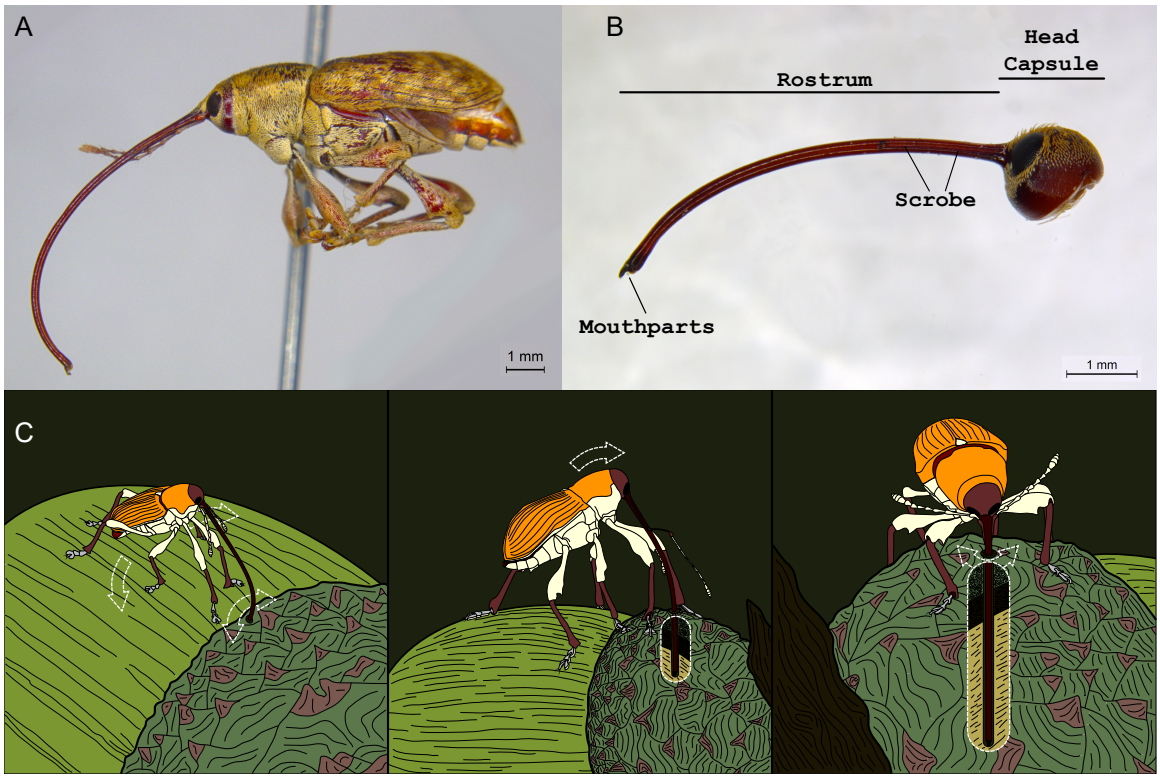


Figure 3.1: Morphology and oviposition behavior of female *Curculio* weevils. **A** Lateral habitus image of female *Curculio sayi* (Gyllenhal, 1836) featuring the elongate, strongly curved rostrum. **B** Lateral view of head of female specimen of *Curculio longinasus* Chittenden, 1927, with major anatomical features indicated. **C** Illustration of oviposition behavior, proceeding from left to right: female makes incision in host fruit, flexes head directly over bore-hole using front legs, then maintains tension on snout while rotating to excavate linear channel into fruit. During this process, female rostrum is bent until completely straight.

often extreme bending incurred during the process of egg-chamber excavation. In this study, we therefore characterize the composite profile of the rostral cuticle to account for the observed flexibility of the snout. We show that the relative layer thicknesses and fiber orientation angles of the exocuticle and endocuticle of the rostrum are strongly differentiated from the head capsule and other body parts. The effect of these differences on the elasticity of the cuticle is estimated using Classical Laminate Plate Theory (CLPT). Recent studies have shown that the yield strength of the beetle exoskeleton is lower in tension than compression [70]. To assess the validity of

these findings, we compare the ultimate tensile strength of the rostrum across species and snout morphotypes. We also report displacement-controlled load cycling results for the snout of one *Curculio* species with strongly curved morphology. Our results indicate that an increase in the volume fraction of endocuticle in the rostrum conveys higher tensile strength at the rostral apex across all tested species; and further, that a strongly curved rostrum can be flexed repeatedly without harm to the structure.

We additionally describe the fracture mechanics of the snout, while considering how modification of the cuticle may prevent crack formation during oviposition. Accordingly, the flexibility and tensile strength of the rostrum appear to be derived *exclusively* from modification of the composite architecture of the exoskeleton. This is the first time that a modified composite profile has been reported as a means of enhancing structural elasticity in the insect exoskeleton (though see [71]).

3.2 Methods

3.2.1 Specimen Acquisition and Taxon Sampling

Specimens for use in tensile and fatigue testing came from the Hasbrouck Insect Collection at Arizona State University [ASUHIC]. This set of specimens was supplemented with material housed in the following collections, using the codens of Arnett et al. [72]:

CMNC Canadian Museum of Nature Collection, Ottawa, Ontario, Canada

USNM National Museum of Natural History, Washington, D.C., USA

Cold fracture, semi-thin sectioning, and tensile testing were conducted on randomly chosen female specimens belonging to six *Curculio* species obtainable through field work in the southwestern United States and northwestern Mexico. Taxon sampling

was targeted to represent a mixture of disparate radiations and sister taxa with a variety of rostral morphotypesin accordance with the phylogenetic hypotheses of Hughes et al. [12, 73] and Bonal et al. [74]. The six species of *Curculio* used herein are (in alphabetical sequence): *Curculio caryae* (Horn, 1873), *Curculio humeralis* (Casey, 1897), *Curculio proboscideus* Fabricius, 1775, *Curculio sulcatulus* (Casey, 1897), *Curculio uniformis* (LeConte, 1857), and *Curculio victoriensis* (Chittenden, 1904). Specimens were identified to taxonomic (species) concepts using [5] and other resources.

3.2.2 Histological Sectioning

To illustrate the relative proportions of the cuticle regions in cross-section, serial semi-thin sectioning was conducted on exemplary female specimens of *Curculio humeralis* and *Curculio longinasus* Chittenden, 1927. Live specimens of both species were collected into 95% ethanol for preservation. A female specimen was selected; and the rostrum was separated from the head capsule with a fine-edged razor blade. The apical $1/4^{\text{th}}$ of the rostrum was also removed and then discarded. The remaining portion of the rostrum and the head capsule were then embedded in EMbed812, as follows.

The cuticle was first immersed in acetone for 24 hours, and then transferred to a 2:1 mixture of acetone to epoxy resin. Samples remained at 21°C for 12 hours on a shaker table to prevent hardening. They were then transferred into a 1:1 mixture of acetone to resin, followed by a 1:2 mixture (each for 12 hours and at 21°C on a shaker table), before finally being placed into a silicone mold with pure resin. The mold was placed into an oven heated to 38°C, and the resin was allowed to cure for 24 hours. The resulting blocks were machined to prepare the apical surface of each sample for microtomy.

A Leica Ultracut R Microtome and diamond knife were used to expose a cross-section (transverse plane) of the apical and basal portions of the rostrum and to remove excess material. Semi-thin sections (0.5 µm thick) were kept and stained with toluidine-blue-borax for light microscopy and imaging.

3.2.3 Cold-fracture of Specimens

Two pinned female specimens of each *Curculio* species were selected at random and retained for cold-fracturing of the rostrum. The heads of the specimens were removed and cleaned using a 95% ethanol solution and a thin paintbrush. Any muscles protruding from the occipital foramen were removed with a fine-edged razor blade. The antennae were removed directly using forceps to pull the scape (basal section of antenna) from the antennal insertion. Cleaned specimens were stored at −80°C for 24 hours, then fractured using forceps over a chilled aluminum block. To fracture each specimen, the head capsule and rostrum were each gripped firmly in a pair of forceps. The forceps were then sharply rotated to fracture the base of the snout via dorsal flexion. The rostrum was fractured a second time, after separation from the head capsule, using the same procedure. The segmented specimens were then placed into individual glass vials to protect the fracture surfaces from contamination prior to microscopy.

3.2.4 Tensile and Fatigue Testing

Force-controlled Loading to Failure. Five female specimens of each *Curculio* species were randomly allocated for use in tensile testing. The head of each specimen was removed, cleaned, and prepared as described above in the cold-fracture protocol. To avoid destroying the delicate, brittle specimens when gripping the ends of each head, a method was devised to create solid handles that could be clamped tightly into

grips without risk of damage to the cuticle.

For each head, four $1\,\mathrm{cm}^2$ strips of gaffer tape were cut; these were used as gripping and mounting points for the specimen. A strip of tape would be laid flat, with a large drop of cyanoacrylate glue placed upon the upturned surface. The curved portion of the snout was then placed into the drop, such that the straight portion of the rostrum was aligned perpendicular to the edge of the strip. Hardening of the cyanoacrylate effectively embedded the curved portion of the snout in a solid mass, isolating a straight section of the snout – from the base to a point distad of the apex of the scrobe – for testing. A second strip of tape was fixed over this mass with an additional layer of cyanoacrylate to provide a dorsal gripping surface for the mass. A small mark was made to indicate the extent of the head inside the mass. This embedding procedure was repeated for the head capsule, resulting in a finished specimen with anterior and posterior handles for testing.

Prior to testing, each specimen was placed in de-ionized water for 24 hours to allow full saturation of the cuticle, simulating the condition of live tissue [21]. Once removed for testing, the specimen was gripped using the cyanoacrylate handles at the marked locations immediately beyond the anterior margin of the rostrum and the posterior margin of the head capsule The exposed section of the snout was coated in petroleum jelly using a cotton swab to prevent loss of moisture and stiffening of the specimen during the test. Specimens were loaded in a Tryton 250 Microforce Testing System equipped with a 5N load cell and mechanical clamp grip. All specimens were subjected to force-controlled uniaxial tension at a rate of $1.0\,\mathrm{gf}\cdot\mathrm{s}^{-1}$ until failure, with a sampling interval of $0.1\,\mathrm{s}$. Engineering stresses ($\sigma_0 = F/A_0$) and strains ($\epsilon_0 = \Delta l/l_0$) were reported only for specimens that did not fracture due to strain accumulation at the interface between the rostrum and the cyanoacrylate handles.

Displacement-controlled Cyclic Loading. To confirm that repeated, complete extension of a strongly curved rostrum would not result in fracture of the cuticle, a representative female specimen of *Curculio caryae* was allocated for fatigue testing. The head capsule of the specimen was fixed to a push-pin using cyanoacrylate glue. This served as a pedestal and gripping location for the posterior portion of the specimen. The apex of the rostrum was fixed to a strip of ripstop nylon fabric equal in length to the head, using cyanoacrylate glue. As with tensile testing, the specimen was placed in de-ionized water for 24 hours, then coated in petroleum jelly using a cotton swab immediately prior to load cycling.

The end of the fabric was gripped and used to elongate the rostrum in tension by pulling on the fabric, thus isolating the effect of tension on the fatigue life of the rostral cuticle. In this way, the rostrum would return to its original configuration in a spring-like manner, as in living specimens, rather than being forced to return to the initial position. The rostrum was aligned such that complete elongation of the curved section would take place in tension, with minimal off-axis deflection of the un-curved section. The specimen was subjected to displacement-controlled loading sufficient to fully extend the rostrum and generate a load stress of 1 N, or approximately 20% of the tensile strength of the species average. Load cycling took place at a rate of 0.33Hz, and was continued for 14 days – i.e., 400,000 cycles – until the tensile stress in the sample approached an asymptotic minimum.

Once the test was concluded, the specimen was placed in a 50% ethanol solution for 24 hours to clean the petroleum jelly from the rostrum. The specimen was examined for surface fractures and micro-tears, then subjected to tensile testing via the same protocol as the other specimens to assess whether the cuticle had begun to fatigue.

3.2.5 Specimen Imaging and Microscopy

The fracture surfaces of cold-fractured specimens were examined using scanning electron microscopy to characterize the composite profile and microstructure of the rostrum. Fracture behavior of tensile testing specimens was assessed using both light microscopy and SEM to image the fracture surfaces of the specimens in transverse view. Electron microscopy was conducted using a JEOL JSM6300 scanning electron microscope. Light microscopy was conducted using a Leica M205 C stereomicroscope and attached computer running the software Leica Application Suite (LAS); as well as a Visionary Digital Passport II system using a Canon EOS Mark 5D II camera outfitted with interchangeable macro lenses. Specimen length, layer thicknesses, macrofiber orientation angles, and cross-sectional areas were measured in the LAS and in Adobe Illustrator, using pixel-wise measurements multiplied by a scaling factor for the image.

3.2.6 Constitutive Modeling of the Cuticle

General Approach. The effective uni-axial membrane and transverse flexural elastic moduli of idealized cuticle organizations, representing both the rostral apex and head capsule, were estimated using Classical Laminate Plate Theory (CLPT). For general information on this approach see [38, 75]. The composite profiles of both types of cuticle were idealized using the layer thicknesses and stacking sequences observed in *Curculio longinasus*. This particular species was chosen because we derived the effective elastic constants of the individual components of the cuticle in previous work [8, 9]. In addition, *Curculio longinasus* exhibits a profile that is typical and representative for the genus *Curculio*, based on examination of the six species used for tensile testing.

For *Curculio longinasus* the total thickness of the cuticle in the head and ros-

trum is roughly 50 µm, as in most specimens of the other examined species. In the head capsule, the exocuticle occupies between 30-50% of the through-thickness of the laminate, with the remaining thickness nearly evenly divided between 12 layers of endocuticle. We use the maximum (50% of through-thickness, or 25 µm) for the model, since the cuticle appears to deviate from this value only in regions with sulci (grooves), pores, and other scattered features of the surface sculpture. The macrofiber laminae of the endocuticle were assigned a stacking sequence of $0°, 90°, 30°, -60°, 60°, -30°, 90°, 0°, -60°, 30°, -30°, 60°$; thereby representing pairs of orthogonal plies stacked at a constant rotation angle of 30°, in approximation of the living tissue.

In the rostral apex, the exocuticle is reduced to a thin shell approximately 5 µm in thickness, or 10% of the total cuticle thickness. The endocuticle displays a more complex pattern of layer thicknesses in the rostral apex than in the head capsule. Each of the eight outermost layers are of nearly equal thickness to the exocuticle (5 µm), whereas the four innermost layers have a combined thickness equal to that of the exocuticle or to a single layer of outer endocuticle ($h_{outer} = 5$ µm, $h_{inner} = 1.25$ µm). The stacking sequence with respect to the longitudinal axis of the rostrum forms an antisymmetric angle-ply laminate of ±45°.

To assess the individual contributions of layer thickness and stacking angle sequence to cuticle flexibility in the rostral apex, two hypothetical cuticle lay-ups were modeled – each with only one of the modifications present in the cuticle of the rostral apex. The first of these models has the layer thicknesses of the rostral apex, but fiber orientations of the head capsule; whereas the second has the fiber orientations of the rostral apex, but the layer thicknesses of the head capsule.

Because these laminates are not symmetric, each has a bending-extension coupling matrix $[B]$ populated with non-zero terms; thus complicating the calculation of

effective in-plane elastic moduli. To circumvent this difficulty and enable meaningful comparisons between each laminate, all of the lay-ups are reflected about their inner surface. This effectively doubles their thickness while producing a balanced, symmetric laminate with no coupling between bending and extension (i.e., $[B] = 0_{3,3}$). Estimation of in-plane elastic constants from the extension($[A]$) and bending ($[D]$) matrices is described in detail below. The program Matlab R2018b was used to numerically evaluate the final values of the effective elastic constants [76].

Classical Laminate Plate Theory. We begin by calculating the 2D reduced stiffness matrix for each part of the cuticle. For orthotropic materials with the principal axes parallel to the ply edges, the reduced stiffness matrix is defined as follows:

$$[Q] = \begin{bmatrix} Q_{11} & Q_{12} & 0 \\ Q_{21} & Q_{22} & 0 \\ 0 & 0 & Q_{66} \end{bmatrix}, \tag{3.1}$$

where:

$$\begin{aligned} Q_{11} &= \frac{E_1}{1-\nu_{12}\nu_{21}}, \\ Q_{12} &= \frac{E_1\nu_{21}}{1-\nu_{12}\nu_{21}} = Q_{21}, \\ Q_{21} &= \frac{E_2\nu_{12}}{1-\nu_{12}\nu_{21}} = Q_{12}, \\ Q_{22} &= \frac{E_2}{1-\nu_{12}\nu_{21}}, \\ Q_{66} &= G_{12}. \end{aligned} \tag{3.2}$$

For each layer k, the reduced stiffness matrix is transformed to account for the layer orientation angle θ within the laminate coordinate system, yielding a reduced transformed stiffness matrix according to:

$$[\bar{Q}] = [T]^{-1}[Q][T]^{-T}\,, \tag{3.3}$$

where the transformation matrix $[T]$ is defined as:

$$[T] = \begin{bmatrix} \cos^2\theta & \sin^2\theta & 2\cos\theta\sin\theta \\ \sin^2\theta & \cos^2\theta & -2\cos\theta\sin\theta \\ -\cos\theta\sin\theta & \cos\theta\sin\theta & \cos^2\theta - \sin^2\theta \end{bmatrix}. \tag{3.4}$$

Using the lay-ups specified for each type of cuticle described above, we calculate the extensional stiffness matrix $[A]$, bending stiffness matrix $[D]$, and bending-extension coupling matrix $[B]$ for each laminate consisting of n layers at a distance z from the laminate mid-plane. The elements of these matrices can be identified according to:

$$\begin{aligned} A_{ij} &= \sum_{k=1}^{n} (\bar{Q}_{ij})_k (z_k - z_{k-1})\,, \\ B_{ij} &= \frac{1}{2}\sum_{k=1}^{n} (\bar{Q}_{ij})_k (z_k^2 - z_{k-1}^2)\,, \\ D_{ij} &= \frac{1}{3}\sum_{k=1}^{n} (\bar{Q}_{ij})_k (z_k^3 - z_{k-1}^3)\,. \end{aligned} \tag{3.5}$$

These stiffness matrices respectively relate vectors of resultant forces $\{N\}$ and bending moments $\{M\}$ to mid-surface strains and curvatures $\{\epsilon^{\circ}\}$ and $\{\kappa\}$ in the laminate, according to the following relationship:

$$\begin{Bmatrix} \{N\} \\ \{M\} \end{Bmatrix} = \begin{bmatrix} [A] & [B] \\ [B] & [D] \end{bmatrix} \begin{Bmatrix} \{\epsilon^{\circ}\} \\ \{\kappa\} \end{Bmatrix}. \tag{3.6}$$

For symmetric laminates, $[B] = 0_{3,3}$, and therefore:

$$\begin{aligned} \{N\} &= [A]\{\epsilon^{\circ}\}\,, \\ \{M\} &= [D]\{\kappa\}\,, \end{aligned} \tag{3.7}$$

or, in expanded form:

$$\begin{Bmatrix} N_{xx} \\ N_{yy} \\ N_{xy} \end{Bmatrix} = \begin{bmatrix} A_{11} & A_{12} & A_{16} \\ A_{21} & A_{22} & A_{26} \\ A_{61} & A_{62} & A_{66} \end{bmatrix} \begin{Bmatrix} \mathring{\epsilon}_{xx} \\ \mathring{\epsilon}_{yy} \\ \mathring{\gamma}_{xy} \end{Bmatrix}, \\ \begin{Bmatrix} M_{xx} \\ M_{yy} \\ M_{xy} \end{Bmatrix} = \begin{bmatrix} D_{11} & D_{12} & D_{16} \\ D_{21} & D_{22} & D_{26} \\ D_{61} & D_{62} & D_{66} \end{bmatrix} \begin{Bmatrix} \kappa_{xx} \\ \kappa_{yy} \\ \kappa_{xy} \end{Bmatrix}. \tag{3.8}$$

If we make the simplifying assumptions [38, 75] that **(1)** the laminate experiences pure axial loading and transverse bending (i.e., $N_{yy} = N_{xy} = 0$ and $M_{yy} = M_{xy} = 0$, respectively), and **(2)** the laminate is a beam of sufficiently high aspect ratio to minimize the Poisson effect and anisotropic shear coupling (i.e., below we effectively let $A^*_{12} = A^*_{16} = 0$ and $D^*_{12} = D^*_{16} = 0$), then we can calculate the in-plane effective flexural and axial Young's moduli of the laminate along the x-axis.

For axial Young's modulus of the laminate, we first define the average membrane stresses in the laminate as:

$$\{\bar{\sigma}^m\} = \frac{\{N\}}{z_1 - z_n}. \tag{3.9}$$

By substitution in Eq. 3.7, we obtain:

$$\begin{Bmatrix} \bar{\sigma}^m_{xx} \\ \bar{\sigma}^m_{yy} \\ \bar{\tau}^m_{xy} \end{Bmatrix} = \frac{1}{(z_1 - z_n)} \begin{bmatrix} A_{11} & A_{12} & A_{16} \\ A_{21} & A_{22} & A_{26} \\ A_{61} & A_{62} & A_{66} \end{bmatrix} \begin{Bmatrix} \epsilon^m_{xx} \\ \epsilon^m_{yy} \\ \gamma^m_{xy} \end{Bmatrix}, \tag{3.10}$$

and, by inverting this equation (let $A^* = A^{-1}$) and substituting $A^*_{12} = A^*_{16} = 0$ based on the assumptions above, we infer:

$$\epsilon_{xx}^{m} = (z_1 - z_n) A_{11}^{*} \bar{\sigma}_{xx}^{m} \,. \tag{3.11}$$

We therefore define Young's modulus for effective axial elasticity as:

$$E_{xx}^{m} = \frac{\bar{\sigma}_{xx}^{m}}{\epsilon_{xx}^{m}} = \frac{1}{(z_1 - z_k) A_{11}^{*}} \,. \tag{3.12}$$

To find the transverse flexural Young's modulus of the laminate, we first specify the moment-curvature relation of an Euler-Bernoulli beam:

$$M = EI\kappa \,. \tag{3.13}$$

Along the x-axis, the second moment of area for a rectangular cross-section is:

$$I_{yy} = \frac{b(z_1 - z_n)^3}{12} \,. \tag{3.14}$$

Given the assumption that $M_{yy} = M_{xy} = 0$, the moment along the x-axis is related to the moment of the beam by:

$$M = M_{xx} b \,. \tag{3.15}$$

Thus, given the assumption that $D_{12}^{*} = D_{16}^{*} = 0$, Young's modulus for the effective transverse flexural elasticity of the laminate can be found by making Eq. 3.13 specific to transverse flexure of the x-axis and rearranging the terms:

$$E_{xx}^{f} = \frac{12 M_{xx}}{(z_1 - z_n)^3 \kappa_{xx}} \,. \tag{3.16}$$

From inversion of Eq. 3.7 (let $D^{*} = D^{-1}$), this reduces to:

$$E_{xx}^{f} = \frac{12}{(z_1 - z_n)^3 D_{11}^{*}} \,. \tag{3.17}$$

3.2.7 Statistical Analysis

Model Selection and Fitting. In order to explore the relationships between the composite structure and mechanical properties of the cuticle, we fit phylogenetic linear mixed-effects models (PGLMM) to the tensile testing data using maximum likelihood estimation [77–80]. Raw data was processed using a custom script in Python version 3.5.2 [81]. Model exploration and fitting was conducted in `R version 3.5.1 (2018-07-02) -- ‘‘Feather Spray’’`, using the `‘nlme’` and `‘ape’` packages [82–84]. Response variables and covariates were natural-log transformed, as needed, to ensure that the normalized model residuals were normally distributed [`R:shapiro.test`] and homoscedastic [`R:levene.test`], using numerical and graphical analysis. In order to control for phylogenetic non-independence in the data, we included the species of each specimen as a random effect in all models. We also allowed for correlation in the error term of the models, as specified by a variance-covariance matrix generated from a Brownian motion model of trait evolution [`R:‘ape’:corBrownian`] along a phylogeny [84, 85].

The preferred phylogeny for select North American *Curculio* species is that of Bonal et al. [74]. This phylogeny was generated using Maximum-Likelihood methods; it is untrametric yet has uniform internal branch lengths. The preferred tree was pruned to include only those species used in tensile testing, with a polytomy at each species' root node to represent the individual specimens examined for that species. Because the branch lengths of the tree were not specified, all branch lengths were set equal to 1. Underestimation of branch lengths causes overestimation of phylogenetic signal [85–87]. We were unable to detect statistically significant phylogenetic signal for any of our models. For this reason we consider our study's principal findings to be unaffected by branch length underestimation. However, because of the relatively poor

taxonomic resolution afforded by a sample of five species, we are unable to conclude whether significant phylogenetic signal exists in the traits examined herein.

Other models of trait evolution were considered during model exploration; including Ornstein-Uhlenbeck [`R:'ape':corMartins`] and variable rate (AC/DC) models [`R:'ape':corBlomberg`] [84, 85]. These models were chosen to compare among competing hypotheses of trait evolution, namely stabilizing selection and variable-rate evolution, respectively. We additionally tested a Brownian motion model of trait evolution, corresponding to variation constrained by clade membership (i.e., sister taxa are more similar to each other than to an out-group). However, neither of the former produced a significantly better fit to the data than the Brownian motion model for any comparison, as measured by likelihood score and residual variance; viz. R^2_σ, and $R^2_{\beta*}$ [`R:'r2glmm':r2beta`]. R^2_σ is the proportion of generalized variance explained by fixed effects. This measure is generally used for comparison of covariance structures [88–90]. $R^2_{\beta*}$ measures the multivariate association between the outcome and the fixed effects within a given correlation structure, and is generally used to compare fixed effects [88–90]. Using the `R` package `'phytools'` [85, 91], we also estimated the phylogenetic signal in the residual variance of each model; taking into account two measures of spatial autocorrelation (Abouheif's $\bar{C}$ and Moran's I), and two measures of phylogenetic signal (Pagel's λ and Blomberg's κ).

In all models, we tested whether the inclusion of phylogenetic correlation in the model error produced significantly better model fit, using a likelihood-ratio test [`R:'lmtest':lrtest`] and R^2_σ-difference test [`R:'r2glmm':r2beta(method='sgv')`] between the fully-specified model and a model lacking the phylogenetic effect [90, 92]. Models that incorporated covariance due to Brownian motion consistently produced higher likelihood scores and fit to the data. However, no model exhibited statistically significant phylogenetic signal in any of the variables. Our findings imply that *residual*

variance in the examined traits does not exhibit significant rate-variation or stabilizing selection in the amount or direction of residual variance between groups; rather, variation within and between clades is distributed randomly by clade, with limited phylogenetic dependence. Once models were fitted to the data, T- and F-statistics were calculated to determine whether each cofactor was significantly different from zero.

Hypothesis Testing. Our objectives for hypothesis testing using the PGLMMs were threefold: **(1)** to assess whether the altered ratio of exocuticle to endocuticle in the rostral apex has an effect on the tensile strength of the rostrum; **(2)** to test whether a trade-off exists between specimen stiffness and resistance to fracture; and **(3)** to examine whether rostrum length and flexibility are correlated.

To test the relationship between relative layer thicknesses and tensile strength, we fitted a fully-specified model with the cross-sectional area of exocuticle and endocuticle at the site of fracture as fixed effects, including an interaction term, and with the maximum tensile force sustained prior to fracture as a response variable. This model was then compared to models with only cross-sectional area of either endocuticle or exocuticle, but not both, as the sole fixed effect in the model. We then tested whether one or both regions were significantly correlated to the maximum force sustained in tension, using likelihood-ratio tests and $R^2_{\beta^*}$-difference tests between each of the three models. Only the cross-sectional area of endocuticle produced a significant fixed effect. We therefore elected to make the model more parsimonious by removing cross-sectional area of exocuticle as a fixed effect. The final model generated for our first aim featured the ratio of exocuticle to endocuticle in cross-section as a fixed effect, with ultimate tensile strength as the response variable.

For our second aim we examined the relationship between specimen stiffness and

resistance to fracture. Specimen stiffness was characterized using a low strain elastic modulus – averaged across the first 33% of the stress-strain curve – and the secant modulus at failure. Resistance to fracture was quantified in terms of ultimate strain and work of fracture, measured as area under the stress-strain curve. Four models were fitted, two of which had ultimate strain as the response variable, and two with work of fracture as response variable. Each model then used one of the different measures of specimen stiffness as a fixed effect.

Finally, for the third aim we explored whether a size-effect might exist in the *Curculio* rostrum; and specifically if longer and typically more curved rostra were more flexible than shorter, straighter rostra. We generated two models; the low strain and secant elastic moduli individually served as response variables, with specimen length as the fixed effect in both.

3.3 Results and Discussion

3.3.1 Microstructure of the Curculio Rostrum

In arthropods – including beetles - the exocuticle is comprised of numerous unidirectional laminae of chitin nanofibrils. Each layer is the thickness of a single fiber (2-4 nm) embedded in a proteinaceous matrix [19, 20]. These layers are stacked at a more or less constant angle to each other, forming a quasi-isotropic laminate known as the Bouligand structure [24–26]. This layout effectively mitigates the strong anisotropy of α-chitin, thus yielding a versatile building material for the exoskeleton [19, 20, 22, 23]. Beetle endocuticle, however, is unique among arthropods and is comprised of large – 1-5 µm diameter in *Curculio* – unidirectional bundles of chitin, called macrofibers. Chitin macrofibers are orthotropic (axial: $E_1 = 8.5$ GPa; transverse: $E_2 = E_3 = 0.52$ GPa [8]), and arranged in unidirectional plies, as

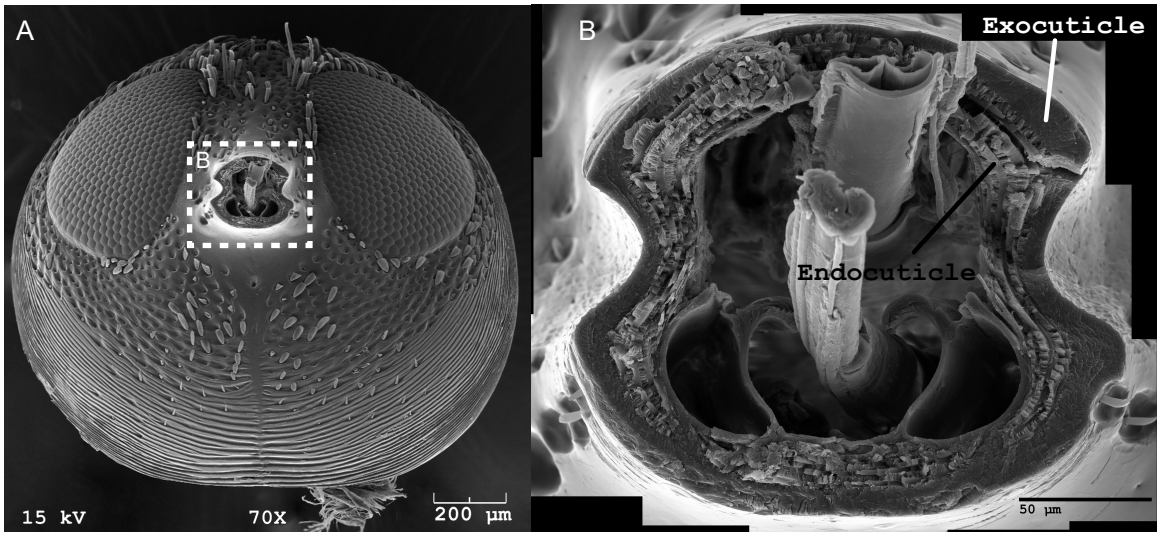


Figure 3.2: Gross divisions of cuticle in the female *Curculio* rostrum. **A** Scanning electron micrograph of head capsule, in frontal view, of female *Curculio sulcatulus* (Casey, 1897), with rostrum removed. **B** Magnified view of junction between rostrum and head capsule, showing division of cuticle into two general regions: exocuticle and endocuticle.

depicted in Figs. 3.2, 3.3 [29, 30]. Typically, adjacent macrofiber laminae are paired and pseudo-orthogonal – i.e., angled nearly 90° to each other (see Fig. 3.3; [27]) – with a constant stacking angle *between* pairs, although other configurations have been observed [28–30, 59]. This geometric sequence of the macrofiber laminae yields an approximately transversely isotropic composite, similar to the Bouligand structure [20, 30]. Notably, the resulting laminate is less rigid than the exocuticle, but exhibits greater toughness because the pseudo-orthogonal plies effectively inhibit crack formation and propagation between successive layers [28–30].

Serial thin sectioning and scanning electron microscopy of fractured *Curculio* specimens reveals that endocuticle in the head capsule fits this general profile, with an angle of nearly 30° between successive pairs of pseudo-orthogonal plies. Additionally, in the head capsule, the thickness of the exocuticle and endocuticle in cross-section is nearly equal – typically between 20-30 µm. However, the cuticle composite lay-up of the rostral apex is strongly differentiated from the head capsule, as shown in Fig. 3.3.

Distally the exocuticle is reduced to a thin shell (ca. 5 µm), with the endocuticle thickened to offset this reduction and maintain a constant cuticle thickness (ca. 50 µm total) throughout its length. Moreover, the endocuticular macrofibers exhibit no rotation between successive pseudo-orthogonal plies; and are oriented at approximately $\pm 45^\circ$ to the longitudinal axis of the snout (i.e., an antisymmetric [$\pm 45^\circ$] angle-ply laminate). We previously identified these modifications to the composite structure of the cuticle within a single species, *Curculio longinasus* Chittenden, 1927 [8, 9]. However, this composite profile is herein reported in the rostrum of six additional, phylogenetically disjoint, species, suggesting that this is an evolutionarily conserved trait throughout the genus *Curculio*. In all examined species, the portion of the snout between the head capsule and apex of the scrobe exhibits a gradual transition in composite profile along an anterior-posterior gradient.

Here we estimate the effect of differential cuticle organization on uni-axial membrane and on transverse-flexural Young's moduli of the cuticle in the rostral apex and head capsule using CLPT [38, 75]. The effective elastic constants of the cuticle regions of *Curculio longinasus* – estimated previously [8] – are used to construct constitutive equations for the entire cuticle of that species. The cuticle of the head capsule is estimated to have membrane and flexural moduli of $E_m = 4.77$ GPa and $E_f = 6.04$ GPa, respectively. In the rostral apex these values are reduced by approximately 72% and 60%, respectively ($E_m = 1.36$ GPa; $E_f = 2.44$ GPa). Two hypothetical cuticle lay-ups are also modeled to individually assess the contributions of either modified layer thickness or stacking angle sequence to the cuticle's flexibility. The effective moduli of a configuration with the angle stacking sequence of an otherwise typical cuticle (i.e., in the head capsule) that shows layer thicknesses of the rostral apex are calculated as $E_m = 3.73$ GPa, $E_f = 4.31$ GPa; representing 22% and 29% decreases from unmodified cuticle, respectively. Similarly, a hypothetical cuticle with

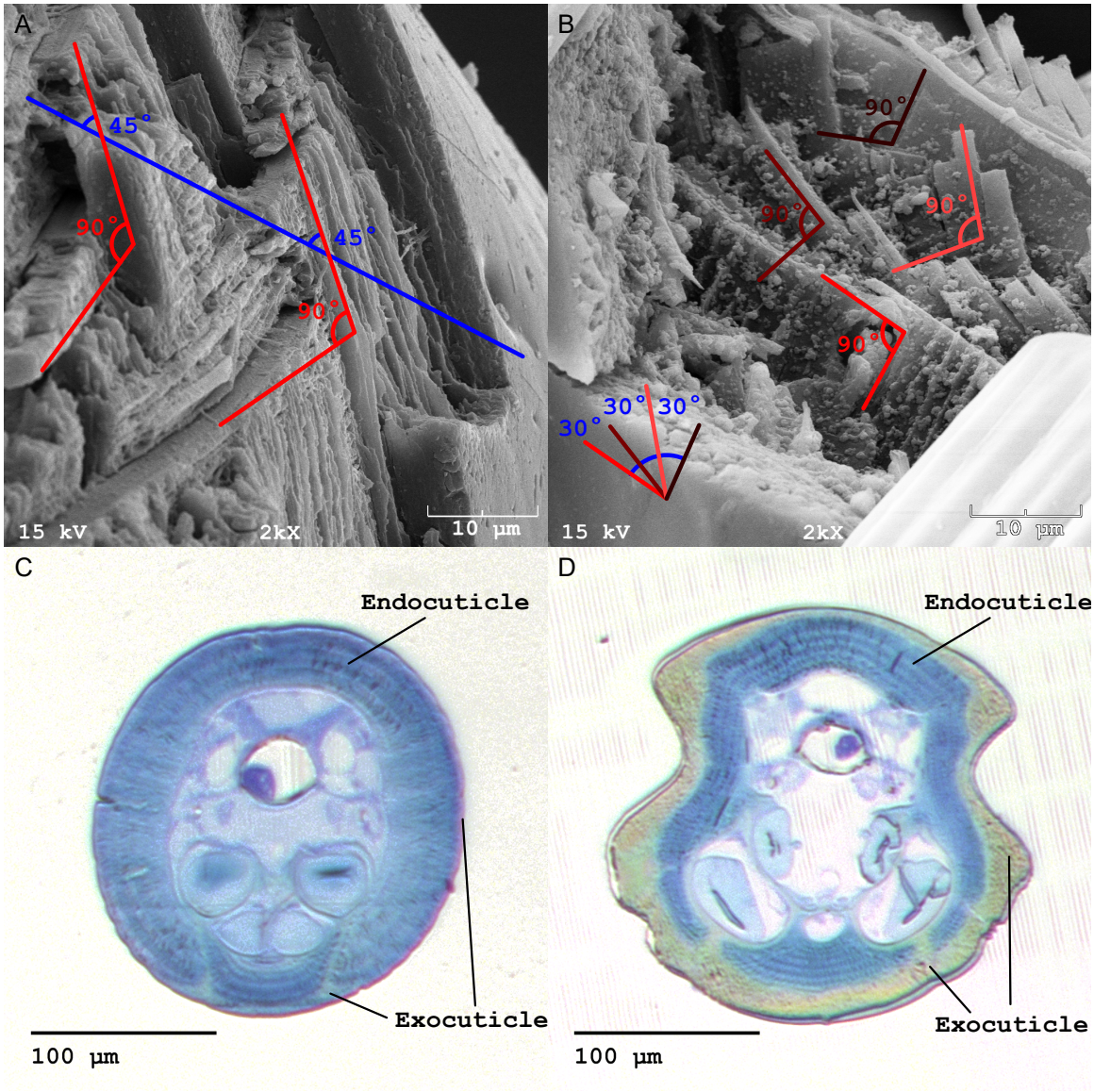


Figure 3.3: Composite profiles of rostral *Curculio* cuticle. **A** Scanning electron micrograph of fractured specimen of *Curculio humeralis* (Casey, 1897), showing that cuticle of rostral apex is organized as ±45° angle-ply laminate. **B** Scanning electron micrograph of fractured specimen of *Curculio caryae* (Horn, 1873), showing that cuticle of rostral base and head capsule has approximately 30° stacking angle between each pair of pseudo-orthogonal plies. **C**–**D** Semi-thin sections of cuticle from specimen of *Curculio humeralis*, stained with toluidine-blue-borax; demonstrating: (**C**) that exocuticle of rostral apex is reduced to thin shell close to 5 µm thick, with endocuticle thickened to maintain a constant laminate thickness; and, (**D**) that exocuticle of head capsule and base of snout occupies nearly half of through-thickness of cuticle.

the layer thicknesses of ordinary cuticle yet possessing the angle stacking sequence of the rostral apex (i.e., $\pm 45^{\circ}$ angle-ply in the endocuticle) has effective elastic moduli of $E_m = 3.77$ GPa, $E_f = 5.76$ GPa; representing 21% and 4.7% decreases from unmodified cuticle, respectively. Each of the cuticle modifications noted in the rostral apex individually decrease the elastic moduli of the cuticle. However, they appear to have a synergistic combined effect on cuticle elasticity, rather than a simple additive effect. This result suggests that both modifications are necessary in order for the snout to function properly in the living individual – where the combined effect allows the rostrum to bend until completely straight without fracture.

3.3.2 Force-controlled Loading to Fracture

To better characterize the failure behavior of the female rostrum, we performed tensile testing on the snouts of six *Curculio* species that representing a mixture of closely and distantly related taxa [6, 12, 73, 74]. Each specimen was first immersed in di-H_2O for 24 hours to simulate the living tissue (see [21]), then subjected to force-controlled, uniaxial loading to fracture at a constant stress rate of $1.0\,\mathrm{gf}\cdot\mathrm{s}^{-1}$. In general, the specimens exhibited a non-linear viscoelastic response curve characterized by a sharp increase in stress at higher strains, terminating in brittle fracture [93]. We suggest that strain hardening occurs as the longitudinal axis of the macrofibers becomes more closely aligned to the cylindrical axis of the rostrum, thereby resisting tension more directly with increasing strain [94].

We also examined the correspondence between composite structure and mechanical behavior of the snout in an evolutionary, comparative context. Phylogenetic linear mixed effects models (PGLM, Fig. 3.4) were used to account for phylogenetic non-independence in residual variance, with species membership included as a random effect [95, 96]. The resulting models show that the maximum force sustained at the

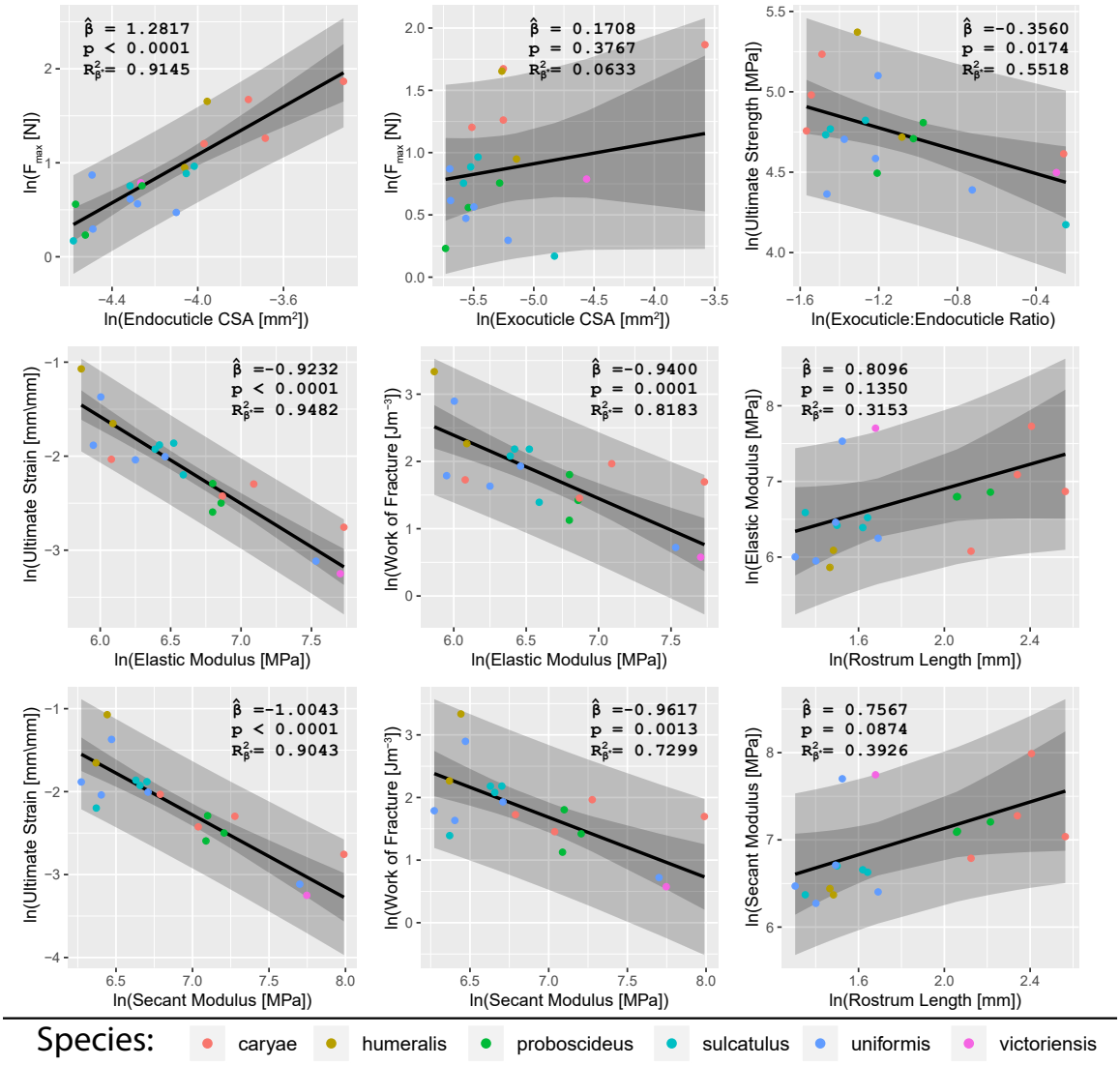


Figure 3.4: Tensile properties of the female *Curculio* rostrum. Each plot shows relationship between two variables as predicted by phylogenetic linear mixed-effect model; with species as random effect and variance-covariance matrix generated from Brownian motion over preferred phylogeny of [74]. Gray regions represent the prediction interval and bootstrapped 95% confidence interval of model. The estimated fixed effect $\hat{\beta}$ is given, along with p-value of t-test assessing whether $\hat{\beta}$ is significantly different from zero. Generalized marginal $R^2_{\beta^*}$ for assessing fixed effects is also reported. In general, increased endocuticle thickness is associated with greater tensile strength, and stiffness is inversely correlated with toughness.

site of failure is strongly correlated with the cross-sectional area of the endocuticle ($\hat{\beta} = 1.28,\ p < 0.0001$), and not the exocuticle ($\hat{\beta} = 0.17,\ p = 0.38$), at that site. There is thus a negative correlation between ultimate tensile strength of the specimen and the cross-sectional exocuticle-to-endocuticle area ratio at the fracture site ($\hat{\beta} = -0.36,\ p = 0.017$). Although CLPT predicts a positive association between the proportion of exocuticle and stiffness of a generalized cuticle, we found no evidence of correspondence between the cross-sectional properties of the fracture site and the overall performance of the rostrum. This result is not too surprising however; because the cross-sectional areas of the cuticle regions vary across the length of the head along an anterior-posterior gradient, it is not possible to correlate measurements from the fracture surface to properties of the entire rostrum.

Instead, we found that the uniaxial elastic modulus (low strain: E_{low}) and secant modulus at failure (E_{sec}) were inversely correlated with ultimate strain and work of fracture (see Fig. 3.4). This implies that stiffer specimens – and by extension, stiffer cuticle profiles – are generally more brittle. We also observed a moderate, but not statistically significant, stiffening size-effect with respect to rostral length. This runs contrary to our expectation that a longer, more strongly curved rostrum would require increased flexibility to avoid fracture during oviposition [6, 12]. It is possible that longer rostra also have a longer transition gradient from basal to apical profile; thereby reinforcing the junction between the rostrum and head capsule against buckling. Young's modulus of the rostrum would be comparatively higher in such species, due to the higher volume fraction of exocuticle. We therefore posit that the gross elastic performance of the cuticle is consistent across the weevil genus *Curculio*. A *single* mechanism – i.e., the modified composite profile – likely confers increased flexibility and tensile strength to the rostral apex across all *Curculio* species. In addition, the endocuticle demonstrably contributes more to rostral tensile strength than the

exocuticle; likely because of its organization into large bundles of aligned, anisotropic fibers, and amounting a trade-off between rigidity and toughness. Consequently, the altered composite profile of the cuticle in the rostral apex makes the rostrum simultaneously more flexible and fracture-resistant.

3.3.3 Load Cycling of the Pecan Weevil

To confirm that repeated, prescribed straightening of the rostrum does not result in damage to the cuticle, we performed displacement-controlled fatigue testing on a typical female specimen of the pecan weevil *Curculio caryae* (Horn, 1873) – a species that exhibits extreme ($80 - 90°$, Fig. 3.5) rostral curvature [5, 10]. The specimen was aligned so that uniaxial tension would induce elongation of the distal portion of the rostrum with minimal off-axis deflection of the uncurved section. The strain per cycle was fixed at an amplitude sufficient to completely elongate the rostrum and generate a tensile load of 1.0 N in the straightened configuration (ca. 20% ultimate strength), at a frequency of 0.33 Hz. The test was terminated after a period of two weeks – i.e., ca. 400,000 cycles – when the stress amplitude appeared to reach an asymptotic minimum. The rostrum behaved viscoelastically, indicated by histeresis in the stress-strain relationship during each cycle. Strain amplitude decreased logarithmically with cycle number, and the specimen appeared to have been deformed plastically and permanently during the test. However, after cleaning the specimen in a 24-hour wash with ethanol and water, the rostrum had returned to its original shape (Fig. 3.5).

While we cannot fully determine the cause for rostrum stress relaxation *after* testing, we speculate that it arose from the general mechanism associated with cuticle viscoelasticity. The endocuticle is made of aligned α-chitin nanofibrils whose crystalline structure is enforced by hydrogen bonds between individual chitin chains and through the protein matrix along their length. Macroscopic viscoelastic behavior results from

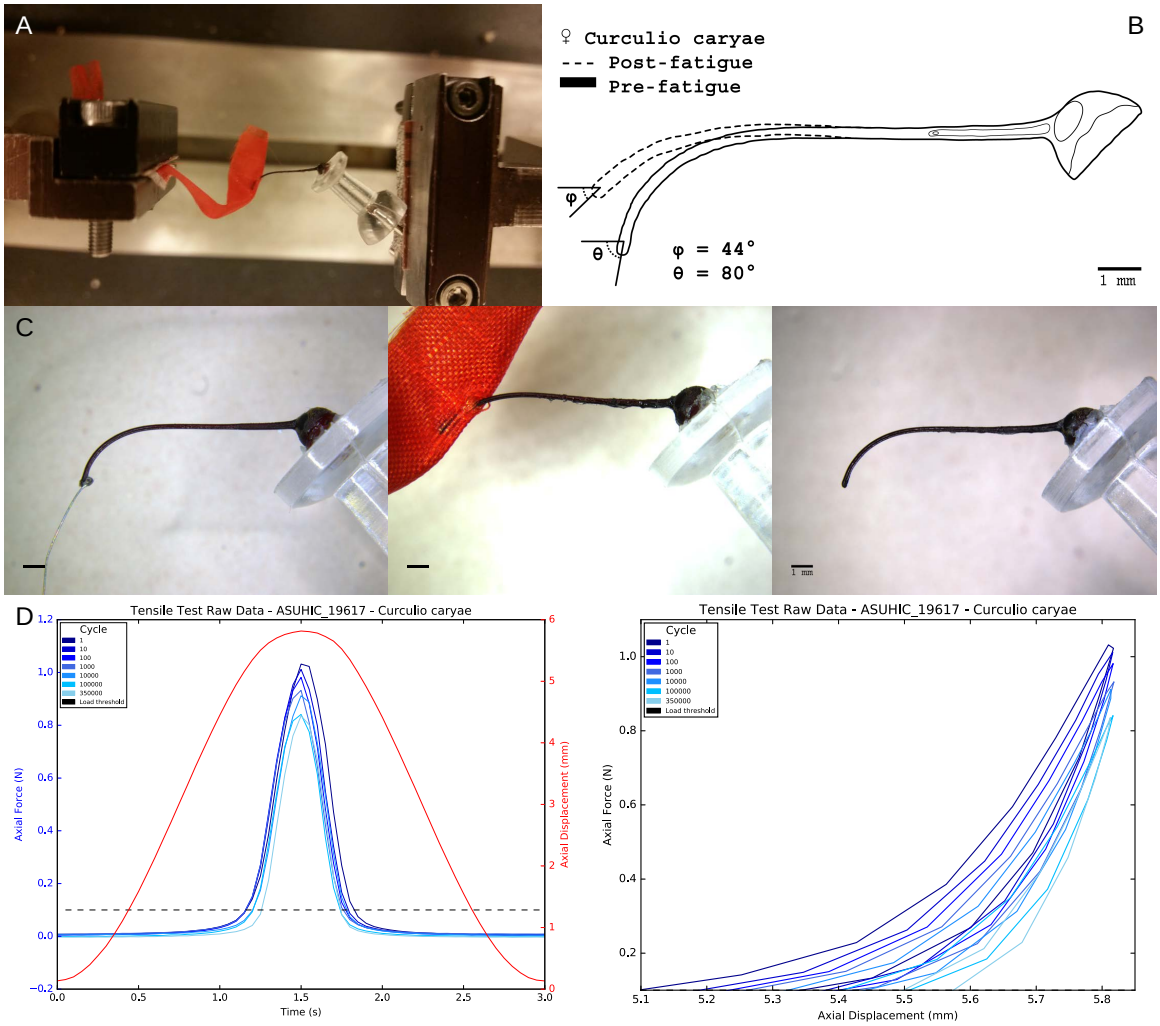


Figure 3.5: Fatigue testing of a female *Curculio caryae* rostrum. **A** Set-up of fatigue testing, with female's head capsule fixed to pedestal and rostrum attached to strip of rip-stop nylon fabric using cyanoacrylate adhesive. Specimen was loaded in tension, as opposed to compression, therefore isolating effect of tension on fatigue behavior of rostrum. **B** Overlay of pre- and post-fatigue states of head, showing clear (short-term) effect from repeated prescribed strain. **C** Three-photograph sequence of pre- and post-fatigue states of the rostrum; with left and central panels showing conditions immediately prior to and after testing, respectively, whereas right panel shows head having returned to its original shape after 24 hours off soaking in a water/ethanol mixture. Hence immediate post-fatigue shape is not permanent. **D** Raw force data (left) and displacement data (right) plots for fatigue test. Displacement data plot shows clear viscoelastic behavior, indicated by histeresis in stress-strain response of specimen, and exhibits logarithmic decrease stress amplitude over time.

slippage between these chains in response to shearing between the chitin molecules [23, 97, 98]. Repeated strain may have caused such slippage in the endocuticle of the rostral apex during the fatigue test Without sufficient time for the material to *completely* relax after deformation, the rostrum would slowly accumulate strain and deform viscoelastically [94]. After immersion in ethanol and water, however, the cuticle would be sufficiently plasticized to allow the rostrum to return to its original configuration, thus dissipating the accumulated strain.

The specimen did not show any evidence of fractures, micro-tears, or shear cusps anywhere in the surface of the exocuticle. Moreover, the tensile strength of the tested specimen's rostrum was consistent with that of other species members ($F_{max} = 5.02$ N). Surprisingly, the specimen remained undamaged by the testing. We therefore conclude that under normal life conditions, repeated bending of the rostrum does not exceed the yield strength of the cuticle.

3.3.4 Fractography of Curculio Test Specimens

In light of the complex failure modes evident in the fractured specimens, it was not always possible to identify void nucleation and crack initiation sites. We observed several patterns characteristic of both the micro-scale behavior of the cuticle and the meso-scale behavior of the rostrum during uniaxial tensile failure (Fig. 3.6). These patterns are described below.

In transverse view, the exocuticle consistently presented a nearly continuous fracture surface. This is characteristic of comparatively brittle failure – presumably due to the relatively homogeneous arrangement of α-chitin laminae in the Bouligand structure [19, 20]. The exocuticle typically appeared to fracture at lower strains than the endocuticle, with shear-cusp formation evident both at the fracture surface and across exocuticle adjacent to the plane of fracture [99]. Conversely, the endocuticle

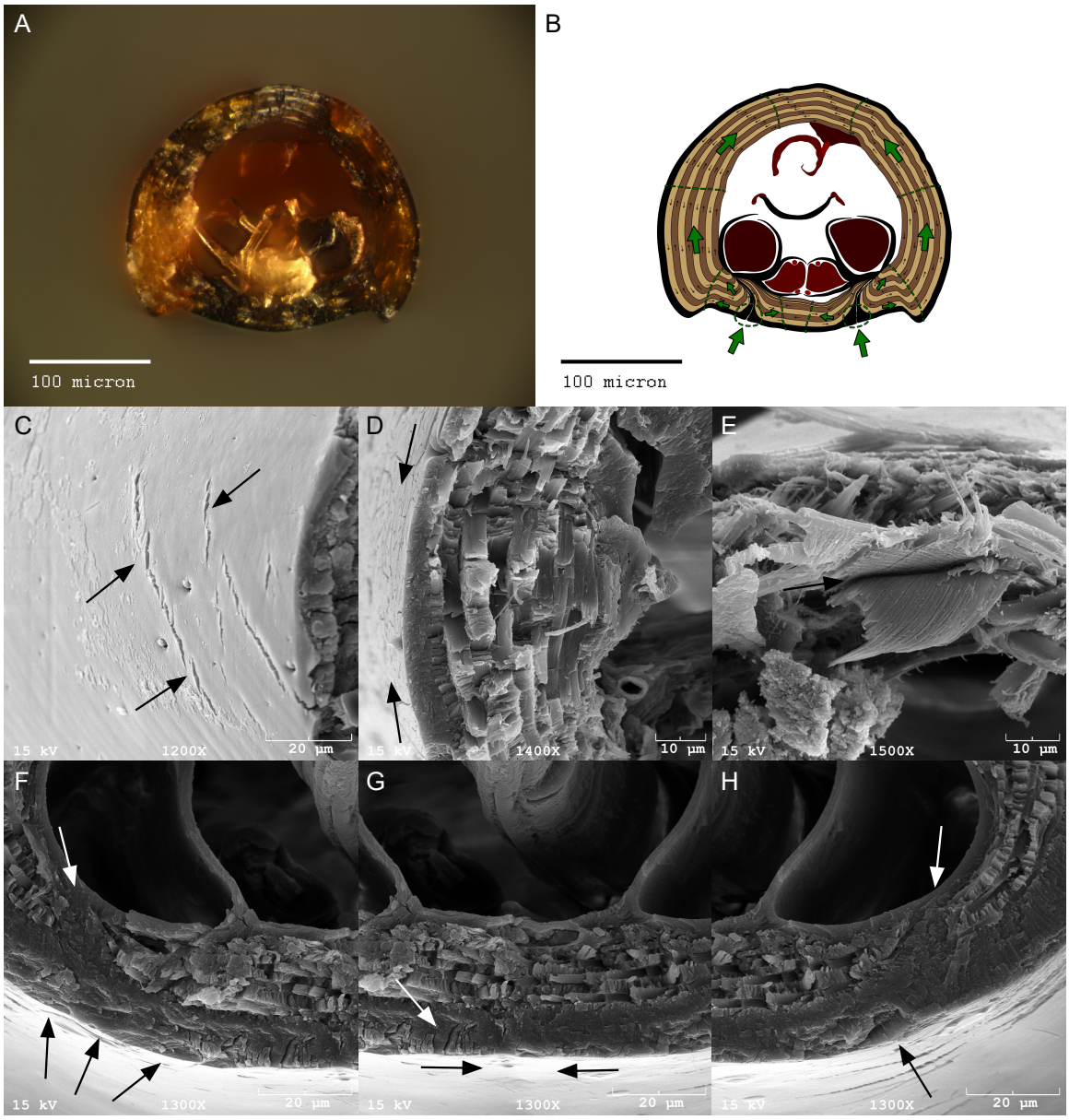


Figure 3.6: Fractography of female *Curculio* rostrum. **A** Light micrograph showing the fracture surface of tensile tested *Curculio caryae* rostrum, displaying typical failure mode; illustrated in **B**: Small, black arrows indicate the winding direction of macrofiber lamina; green arrows and dotted lines indicate the direction of crack. Scanning electron micrographs highlight: **C** shear cusp formation; **D** tensile failure and off-axis macrofiber fiber-pulling; **E** interlaminar delamination; **F**-**H** crack formation near invaginated exocuticle; and **G** ventral crack-front coalescence and shear cusp formation.

exhibited severe delamination, off-axis ply-splitting, and fiber-pulling away from the fracture surface. This is indicative of the relatively high toughness of the unidirectional α-chitin organization within the macrofibers [29, 30]. Because the exocuticle of weevils is anchored to the endocuticle by cross-linking fibers (see [30, 70]), exocuticular shear-cusp formation in uniaxial tension suggests extension-shear coupling within individual endocuticle laminae; and further implies that ply-splitting occurred via mode II fracture between macrofibers at high strain [38, 75]. We hypothesize that intra-laminar extension-shear coupling also yielded off-axis, in-plane resultant forces as a function of lamina orientation angle. Mode III shearing then occurred between laminae with opposing in-plane resultant forces, causing the observed inter-ply delamination. Tensile failure of the macrofiber laminae would ultimately occur via mixed-mode I/II – i.e., transverse tension/intra-laminar shear – fracture, due to an increase in applied stress caused by ply-splitting in adjacent laminae [99].

At the meso-scale, most specimens fractured along a single plane across and between the occipital sulci, which are cuticular invaginations that traverse the entire length of the rostrum [60, 69]. These sulci increase the volume fraction of exocuticle in the ventral part of the snout. They contain large interfaces ideal for void nucleation (Fig. 3.6). The exocuticle of the occipital sulci usually displayed shear cusps oriented outward from the center of the invagination, and continuing dorsolaterally and ventromedially. Ventrally, the cusps converged toward a prominent scarp where the crack fronts joined. This scarp was often obscured by delaminated endocuticular macrofibers in specimens with large cross-sectional areas of endocuticle,

The first layer of endocuticle usually fractured along the same plane as the exocuticle. Ventrally, the endocuticle laminae typically converged toward a scarp-like region characterized by severe delamination and numerous de-bonded macrofibers. Moreover, macrofibers aligned with the direction of crack propagation exhibited extensive

ply-splitting with intermittent transverse shearing. In contrast, macrofibers oriented against the direction of crack propagation primarily displayed fracture by transverse shear along the plane of ply-splitting in adjacent laminae. Because the laminae form a cylinder, contralateral fibers in the same lamina display opposing fracture modes. The ventrolateral surfaces often exhibited extensive inter-ply delamination and fiber de-bonding in scarp-like prominences. This is likely due to a combination of tensile failure and shearing along the dorsally-radiating crack front. Dorsally, the coalescent crack fronts often caused significant de-bonding and ply-splitting, followed by broom-like tensile failure. In some specimens, the contralateral crack fronts were out of plane and coalesced via transverse shear through a large dorsal section of cuticle.

Based on these failure patterns, we hypothesize that the exocuticle-rich occipital sulci are the most likely site for the initiation of void nucleation and catastrophic failure of the integrated rostral cuticle in cross section, as illustrated in Fig. 3.6. Structural failure would take place as cracks propagate through the endocuticle from these sutures, and ultimately penetrating the entire thickness of the laminate [60]. Although other, more complex failure modes have been observed, we posit that in live specimens this is the most likely mechanism of tensile failure because typical bending behavior generates tension *only* along the ventral surface of the rostrum.

3.4 Conclusions

The rostrum of *Curculio* is characterized by a discontinuous composite profile. The cuticle is strongly differentiated in terms of relative layer thicknesses and orientation angles along an anterior-posterior gradient. These modifications are sufficient to achieve a marked reduction in the effective membrane and flexural moduli of the cuticle – 72% and 60%, respectively – in constitutive models based on CLPT, thereby accounting for the observed flexibility of the rostral apex in live specimens. However,

the reductions can only be realized with *both* modifications to the cuticle, which have a non-additive effect on cuticle elasticity. *Curculio* females require both modifications to function properly during oviposition.

Likewise, tensile and fatigue testing reveal a trade-off between stiffness and fracture resistance – measured by ultimate strain and toughness – mediated by the relative proportion of endocuticle in the laminate. The altered composite profile of the cuticle in the rostral apex makes the rostrum simultaneously more flexible and fracture resistant, permitting the structure to be flexed without exceeding the elastic limits of the cuticle.

This is to our knowledge the first time in arthropods that the composite profile of the cuticle has been related to a gradient in elasticity and tensile performance across a cuticular structure. Because these associations are independent of species membership, we posit that the behavior of the cuticle is consistent across the genus. Rostral flexibility is achieved exclusively in all *Curculio* species through a modified cuticle lay-up. This inference raises the intriguing possibility that a single ancestral shift in cuticle organization at the rostral apex – yielding higher flexibility and tensile strength – enabled the evolutionary "exploration" of a large morphospace region, promoting the the high species-level diversity of this lineage.

Based on fractographic analysis of the test specimens, we infer that the exocuticle exhibits brittle fracture at a comparatively low strain, due to shearing between the endocuticle macrofibers to which it is anchored. These macrofibers fail at higher strain, mediated by mixed-mode shearing and tensile fracture within and between laminae. This outcome is consistent with behavior shown in previous studies, as well as theoretical consideration of cuticle microstructure in CLPT. The latter predicts extension shear-coupling ($A_{16}, A_{26} \neq 0$) for individual off-axis macrofiber laminae [38, 75].

Our results imply that fracture initiation occurs in the comparatively brittle exocuticle. The reduction in exocuticle thickness in the rostral apex might serve to mitigate crack formation in rostral bending. Based on this pattern of fracture behavior, we identified the exocuticle-rich occipital suture as a common point of void nucleation and crack initiation. From an evolutionary perspective, these findings reveal an unexpected morphological source of constraint on rostral flexibility, raising the intriguing possibility that this system evolved primarily via negative selection of fracture, rather than positive selection of flexibility. In particular, the cuticle is invaginated in precisely the portion of the snout that experiences the greatest degree of tension during antero-dorsal flexion. The doubly-thick exocuticle in the invagination thus creates an unavoidable, brittle weak-point in an otherwise endocuticle-dominated rostral apex. This constraint – in conjunction with the minimization of exocuticle thickness in the rostral apex and the increased toughness derived from a thickened endocuticle – lead us to consider that avoidance of catastrophic structural failure has been a driving selective pressure in the evolution of the female *Curculio* rostrum.

ACKNOWLEDGMENTS

I am grateful to Robert Anderson (CMNC), Lourdes Chamorro (USNM), and Charlie O'Brien (CWOB) for their assistance and provision of *Curculio* specimens used in this study. I thank Salvatore Anzaldo, Andrew Johnston, Brian Reilly, Sangmi Lee, and other Arizona State University Hasbrouck Insect Collection (ASUHIC) members for their assistance in procuring, treating, and maintaining specimen loans upon entry into the ASUHIC. I would also like to thank David Lowry (ASU CLAS Bioimaging Center) for his training and assistance with resin embedding, scanning electron microscopy, and microtomography; and Salvatore Anzaldo for his assistance with histological staining.

CHAPTER 4

Acorn Weevils Utilize a Modified Cuticle Composite Profile in the Rostrum to Reduce the Risk of Catastrophic Bending Failure

ABSTRACT

With over 300 species worldwide, the genus *Curculio* Linnaeus, 1758 is a widespread, morphologically diverse lineage of weevils that mainly parasitize nuts. Females use the rostrum, an elongate cuticular extension of the head, to excavate oviposition sites. This process causes extreme bending and deformation of the rostrum, without apparent harm to the structure. The cuticle of the rostral apex exhibits substantial modifications to its composite structure that enhance the elasticity and resiliency of this structure. Here we develop finite element models of the head and rostrum for three *Curculio* species representing disparate North American clades and rostral morphotypes. The models were subjected to varying apical loads and to prescribed dislocation of the head capsule, with and without representing the cuticular modifications of the rostral apex. We found that the altered layer thicknesses and macrofiber orientation angles of the rostral apex fully explain the observed elasticity of the rostrum. These modifications have a synergistic effect that greatly enhances the flexibility of the rostral apex. Consequently, the cuticle composite profile of the rostral apex substantially mitigates the risk of fracture in dorso-apical flexion. Removing the cuticular modifications, in turn, causes a negative margin of safety for rostral bending, implying strong risk of catastrophic structural failure. The occipital sulci were identified as an important source of biomechanical constraint upon the elasticity of the rostrum, and exhibit the greatest risk of failure within this structure. The apical cuticle profile greatly reduced

the maximum stresses and strain energy accumulated in the rostrum, thereby resulting in a positive margin of safety and reducing the risk of fracture. Our findings imply that the primary selective pressure influencing the evolution of the rostral cuticle was most likely negative selection of structural failure caused by bending.

4.1 Introduction

Finite element analysis (FEA) of biological structures has become a widely available and powerful tool for reconstructing and investigating organismal mechanobiology and evolution [18, 100, 101]. Biomechanical models are well suited for testing hypotheses about functional morphology that cannot be experimentally verified, especially when the model is based on a fossil of an extinct taxon, or when the conditions imposed upon the model can only exist *in-silico* [100]. Such models are particularly apt for constraining evolutionary hypotheses regarding the fit between form and function by ruling out conditions that are either not observed or not possible in the living organism [3].

In this study, we use finite element models representing three species of acorn weevils (snout beetles) in the genus *Curculio* Linnaeus, 1758 to investigate the bending mechanics of an exaggerated structure of the head, called the rostrum (snout). We demonstrate that differentiation in the microstructure of the rostrum – specifically the composite profile of the exoskeleton – is required for the structure to bend without breaking, as is seen in adult female specimens. We also consider which parts of the structure experience the greatest stresses and strains in tension and compression across species, and explore their contribution to the dominant tensile failure mode observed in this structure. Finally, we use the models to identify the most-likely driving selective pressure acting upon the evolution of the rostrum, while obviating others.

The decision to use FEA in our analytical approach was motivated by: 1) the level of control and flexibility afforded by this method with respect to composite profile specification; and 2) the insight that several of the loading conditions and composite layups we tested would be difficult or impossible to recreate in a laboratory setting. In keeping with the recommendations of Erdemir et al. [101] and Dumont et al. [18]

for reporting FEA workflows, we provide extensive detail on the methods used to generate, verify, and validate the models. We also discuss the load and boundary conditions specified for the models and the mechanical domain of the simulations. In the following sections, we first introduce the biological phenomenon investigated herein; then briefly describe aspects of cuticle mechanobiology relevant to this study.

4.1.1 Biology and Oviposition Behavior of Curculio Linnaeus, 1758

Curculio is a widespread and highly diverse genus of weevils (Coleoptera: Curculionidae), with over 300 species found across every continent except South America and Antarctica [73, 102]. Both sexes are characterized by an elongate, tubular extension of the cuticle (exoskeleton) of the head called the rostrum, or snout (Fig. 4.1) [5, 103, 104]. The rostrum is a rigid structure and bears at its apex the terminal chewing mouthparts [11, 14, 15]. Prior work has established that the length and curvature of this structure are correlated strongly with body size and nut volume of the host plant [6, 12]. However, no study to date has assessed the degree of optimization of rostral morphology with respect to ecomorphological selective pressures in the context of biomechanical constraint [3]. The mechanobiology of this structure is of singular importance to the females, as the rostrum is highly exaggerated compared to males and is used to excavate a site for oviposition (egg-laying) in various types of nuts [5–7, 12, 16].

To prepare a site for oviposition, the adult female will excavate a deep bore-hole into a fruit, usually an acorn, using her rostrum and mandibles. This action relies upon a unique "drilling" behavior that causes significant elastic deformation of the rostrum, which is bent into a completely straight configuration [17]. This behavior only superficially resembles true drilling – the plant material is cut by the mandibles, then ingested by the female [5, 10]. The mouthparts of this genus are phylogenetically derived and also taxonomically diagnostic for this lineage; they are uniquely actuated

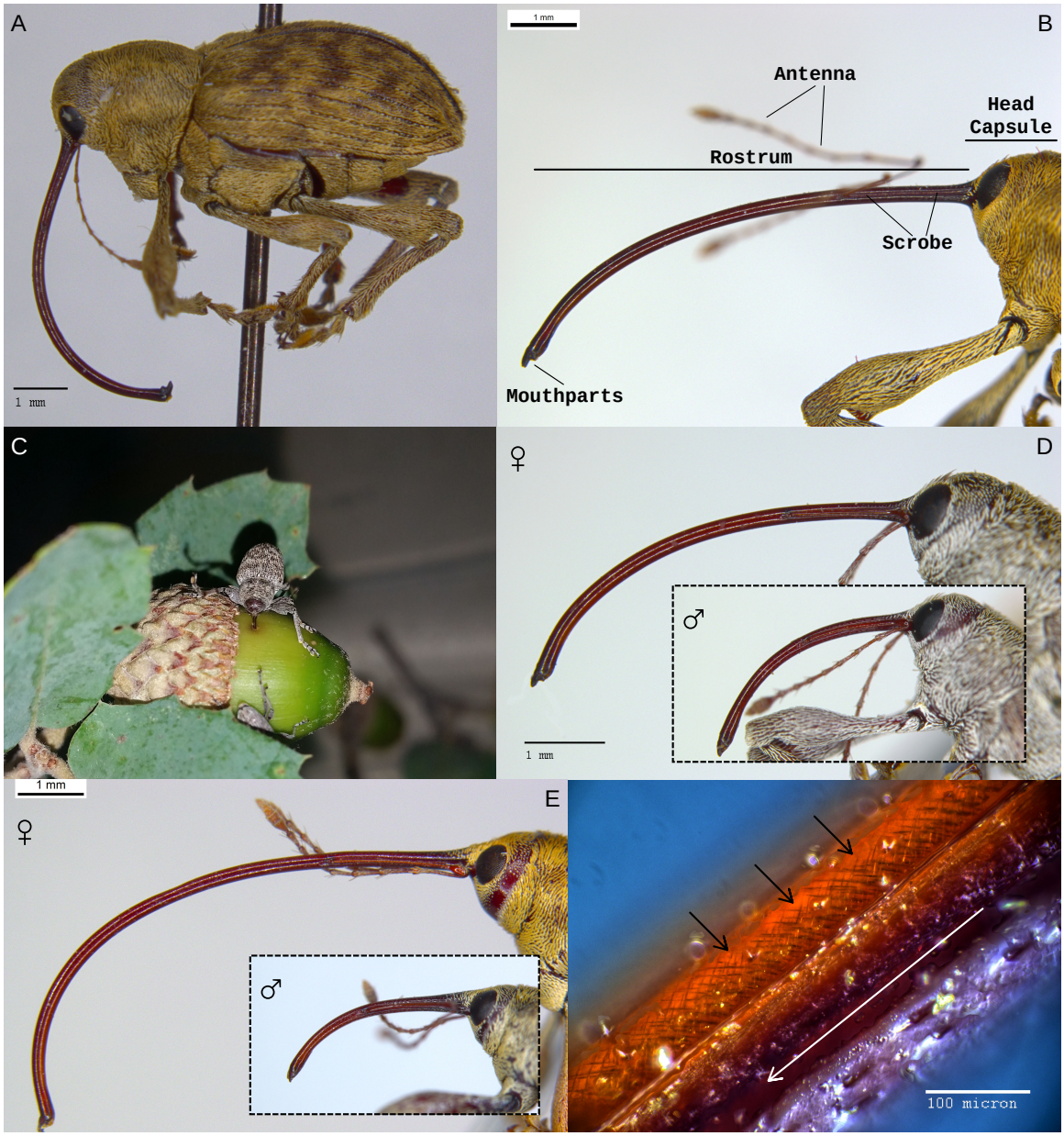


Figure 4.1: Gross morphology of the *Curculio* rostrum. **A** Female specimen of *Curculio pardalis* (Chittenden, 1908) exhibiting strongly curved rostral morphology. **B** Labeled diagram of anatomical landmarks of the rostrum in female *C. pardalis*. **C** Female *Curculio wenzeli* Chittenden, 1927 excavating site for oviposition and engaging in stereotyped "drilling" behavior. **D** Example of moderate sexual dimorphism in the rostrum of male and female *C. wenzeli*. **E** Example of extreme sexual dimorphism in the rostrum of male and female *Curculio sayi* (Gyllenhal, 1836). **F** Light micrograph of rostral cuticle in *Curculio longinasus* Chittenden, 1927, showing characteristic 45° angle-ply lamination of endocuticle.

along a nearly vertical plane similar to shears [11, 14, 15]. The rotating motion of the head and body around the bore-hole serves to change the plane of cutting and keep tension on the rostrum. Throughout the entire excavation process, which can last 2-3 hours, the female uses her fore-legs to elevate and align the head capsule along the drilling axis above the bore-hole, thus flexing the rostrum into a straight configuration (see Toju and Sota [7] for video). Upon removal from the bore hole, the rostrum returns to its original, curved shape. It is typically undamaged in spite of the extreme degree of bending that occurs. Remarkably, a single female may produce dozens or even hundred of such sites during the adult reproductive phase of development [10, 12].

4.1.2 Exoskeletal Microstructure in the Rostrum

Based on the observed behavior of adult female *Curculio*, it is evident that the rostrum can be repeatedly bent without damage, despite being composed of the same material as other rigid body parts [5, 7–9]. The cuticle of the rostral apex exhibits two key modifications to its composite profile that can explain this performance, as characterized previously in a constitutive model and briefly summarized here [8, 9].

The exoskeleton of beetles – including *Curculio* – is divided into two distinct regions of biomechanical significance [8, 28–30]. The outermost region is called the exocuticle and is comprised of numerous unidirectional laminae of chitin nanofibrils – each 2-4 nm thick – embedded in protein, resulting in a quasi-isotropic laminate known as the Bouligand structure [19, 20, 24, 25, 105]. The innermost region is called endocuticle and is comprised of large – 1-5 μm diameter in *Curculio* – unidirectional bundles of chitin, called macrofibers, which are orthotropic and arranged in unidirectional plies (Fig. 4.2) [29, 30]. Adjacent macrofiber laminae are paired and pseudo-orthogonal – i.e., angled nearly 90° to each other [27]) – with a constant stacking angle *between* pairs (30° in *Curculio*) [28–30, 59]. This stacking sequence of the macrofiber laminae yields

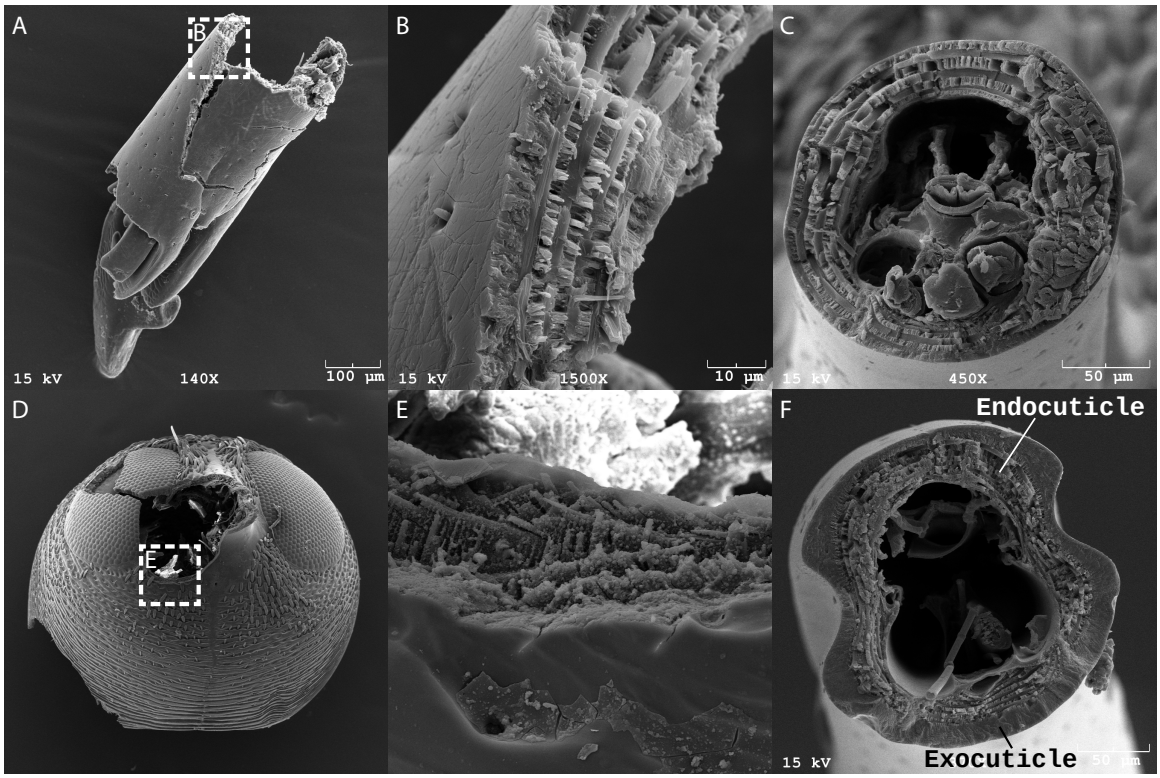


Figure 4.2: Scanning electron microscopy of rostral cuticle. **A** Rostrum from specimen of *Curculio humeralis* (Casey, 1897) fractured near mandibular insertion. B Inset showing detailed view of apical cuticle profile characterized by 45° angle-ply lamination of the endocuticle. **C** Cross section of fractured specimen of *Curculio sulcatulus* (Casey, 1897), showing typical thickening of endocuticle with concomitant thinning of exocuticle near rostral apex. **D** Specimen of *Curculio caryae* (Horn, 1873) fractured across base of rostrum and head capsule. **E** Insert showing detailed view of cuticle organization in head capsule and rostral base, characterized by regular stacking of pseudo-orthogonal plies, as described in-text. **F** Rostrum of *Curculio victoriensis* (Chittenden, 1904), showing typical allocation of cuticle regions near rostral base.

an approximately transversely isotropic composite [20, 30]. Notably, the endocuticle is less rigid as a whole than the exocuticle, but exhibits greater toughness because the pseudo-orthogonal plies effectively inhibit crack propagation within and between layers [28–30].

In *Curculio*, the cuticle composite profile of the rostral apex is strongly differentiated from the head capsule and the rest of the body (see Fig. 4.2). Distally the exocuticle is reduced to a thin shell (ca. 5 µm), with the endocuticle thickened to offset this

reduction and maintain a constant cuticle thickness (ca. 50 µm total) [8, 9]. The endocuticular macrofibers are oriented at approximately ±45° to the longitudinal axis of the snout (i.e., an antisymmetric [±45°] angle-ply laminate) [8, 9]. These modifications to the composite structure of the cuticle have now been observed in the rostra of seven phylogenetically-disjoint species, suggesting conservation of this trait throughout the genus *Curculio*. In all examined species, the portion of the snout between the head capsule and apex of the scrobe exhibits a more or less gradual transition in composite profile along an anterior-posterior gradient; this gradient is variously approximated in our finite element models, as described in **Material Definition and Section Assignment**.

4.1.3 Biomechanical Implications of Cuticle Microstructure

We previously estimated the effect of differential cuticle organization on uni-axial membrane and transverse-flexural Young's moduli of the rostral apex using Classical Laminate Plate Theory (CLPT) [38, 75]. While each modification decreased the uniaxial membrane stiffness of the cuticle by approximately 20%, they appear to have a synergistic effect on cuticle elasticity – membrane stiffness decreased by 70% with both modifications – rather than a simple additive effect. This suggests that snout functionality is dependent on the presence of both modifications in the living animal, where the combined effect allows the rostrum to flex without fracture. Below we describe how the finite element models similarly predict a multiplicative combinatory effect of the cuticle modifications on snout elasticity, in corroboration of the CLPT estimates, and discuss a possible explanation for this outcome.

Arthropod cuticle generally has a higher ultimate strength in compression than in tension, including the rostral cuticle of weevils [23, 70]. Because the endocuticle is tougher than the exocuticle, we hypothesized that the dominant failure mode

of the rostrum during bending is tensile failure initiated in the exocuticle. Our models corroborate this hypothesis, by demonstrating that artificially increasing the proportion of exocuticle in the rostral apex results in a negative margin of safety in tension, and a greatly reduced margin of safety in compression. On the other hand, the lifelike composite profile – i.e., increased endocuticle proportion – has a positive margin of safety in tension and compression for all models. Based partly on these results, we postulate that avoidance of catastrophic structural failure was most likely the driving selective pressure acting upon the evolution of the rostral cuticle.

Under conditions of dorso-apical deflection seen in live specimens, the venter of the snout experiences tension while the dorsum undergoes compression. The underside of the rostrum is characterized by a pair of longitudinal invaginations of the cuticle called the occipital sulci, which serve as internal supports for the mandibular and maxillary tendons [69, 106]. Because the cuticle is invaginated, the thickness of the exocuticle in these sutures is much greater than in the surrounding cuticle. These sulci are particularly susceptible to failure, and they exhibited the highest tensile stresses and strain energy densities – and thus the lowest margins of safety – in the rostra of all of the models. Our models show that the occipital sulci constitute an unavoidable, brittle weak-point in the region of the rostrum that is most vulnerable to failure, and therefore act as a biomechanical constraint on rostral bending.

4.2 Materials and Methods

4.2.1 Objectives and Rationale

Our primary objective for finite element modeling of the rostrum was to test the hypothesis that the same two modifications of the composite structure of the rostral cuticle are used across species to 1) enhance cuticular elasticity, as predicted by

Classical Laminate Plate Theory, and 2) mitigate the risk of catastrophic structural failure of the rostrum. Secondarily, we assessed the relative contributions of each cuticle modification to the flexibility of the snout during dorso-apical flexion, and investigated whether any broad-scale, interspecific patterns were apparent in the relative distribution of stresses and strains along the rostrum.

Two types of load conditions were specified in the models, as outlined in **Finite Element Analysis**. The first set of loads were experimentally verifiable apical loads, corresponding to the addition of weights to the rostral apex. These were used to validate the models and confirm that their behavior is lifelike. The second set of loads correspond to more realistic use of the rostrum by adult females during the oviposition process, and rely on a prescribed dorsal displacement of the head capsule with the snout apex fixed as if inserted into a bore-hole. These load conditions were repeated with and without the cuticular modifications observed in the rostral apex, in order to assess the relationship between the relative performance of the snout and composite profile of the cuticle.

In contrast to other studies employing FEA in arthropods (see [31–34, 107–110]), we took a "bottom-up" approach to creating solid model geometry, generating material and composite definitions, and meshing and sectioning each model. Our rationale for this approach, outlined below, is that we are interested in how cuticle composite microstructure, rather than cross-sectional geometry or gross morphology, affects snout elasticity. The mechanical behavior of the snout was reconstructed using simplified geometry not only to gain greater control over regional composite definitions and material assignments, but with the intent of revealing the general principles governing the relationship between cuticle microstructure and rostral flexibility. We therefore strove to incorporate a greater degree of material realism in our models; by segmenting each model into regions with distinct composite layups, defining spatially varying layer

thicknesses and macrofiber orientation angles in each region, and, most significantly, specifying fully orthotropic behavior for the exocuticle and endocuticle. Such full specification of cuticle composite layup and orthotropic behavior has never before been attempted in any model of an insect structure.

We document in detail: how our models were created using CAD software; our criteria for specimen and taxon selection; and the protocols used for light, scanning electron, and confocal laser scanning microscopy. We also transparently explain the steps in our finite element analysis procedure so that others may repeat or adapt our approach for other study systems.

4.2.2 Specimen Acquisition and Taxon Sampling

The three species of *Curculio* used herein are *Curculio caryae* (Horn, 1873), *Curculio longinasus* Chittenden, 1927, and *Curculio sulcatulus* (Casey, 1897). Specimens used for destructive sampling to generate material definitions and 3D models of rostral composite structure – viz. serial sectioning, cold fracture, tensile testing, and confocal microscopy – came from the Hasbrouck Insect Collection at Arizona State University [ASUHIC] and targeted field work in the state of Arizona. This set of specimens was supplemented with material housed in the following collections, using the codens of Arnett et al. [72]:

CMNC Canadian Museum of Nature Collection, Ottawa, Ontario, Canada

USNM National Museum of Natural History, Washington, D.C., USA

Finite element analysis was conducted using 3D models of randomly chosen female specimens belonging to three species native to the southwestern Unites States and northwestern Mexico. Taxon sampling was targeted to include a mixture of rostral morphotypes at different length scales [12]. Specifically, *C. caryae* represents one of the

most extreme rostrum lengths of extant North American *Curculio* species, with a snout longer than the maximum length of the body. The female rostrum of *C. sulcatulus* is comparatively short, and roughly 75% as long as the body. *Curculio longinasus* has a rostrum length that is near the midpoint between the other two species on an absolute scale, and is slightly shorter than the maximum length of the body.

Curculio caryae and *C. sulcatulus* are recovered as non-sister species placed in disparate phylogenetic radiations, according to the phylogenetic hypotheses of Hughes et al. [73] and Bonal et al. [74]. *Curculio longinasus* has not been included in any phylogenetic study to date, but was grouped morphologically near *Curculio occidentis* (Casey, 1897), on the basis of the male genitalia by Gibson [5, 111], and with *Curculio pardus* Chittenden, 1927 by Chittenden [112], on the basis of femoral and rostral morphology, in the respective revisions of the North American representatives of the genus. *Curculio occidentis* and *C. pardus* belong to a western radiation of *Curculio* that is phylogenetically distinct from both *C. caryae* and *C. sulcatulus* [74]. Due to these species' morphological and phylogenetic dissimilarity, we posit that similarities in the mechanical behavior of the rostrum between the three models are most likely indicative of deep homologous phenomena in rostral mechanobiology across *Curculio*, rather than being restricted to a unique clade or representing convergently evolved morphotypes within the genus.

4.2.3 Histological Sectioning

To measure the relative proportions of the cuticular regions across the length of the rostrum in cross-section, serial semi-thin sectioning was conducted on exemplary female specimens of *Curculio humeralis* (Casey, 1897) and *C. longinasus* Chittenden 1927. Live specimens of both species were collected into 95% ethanol for preservation. A female specimen was selected and the rostrum was separated from the head capsule

with a fine-edged razor blade. The apical $1/4^{\text{th}}$ of the rostrum was also removed and then discarded. The remaining portion of the rostrum and the head capsule were then embedded in EMbed812, as follows.

The cuticle was first immersed in acetone for 24 hours, and then transferred to a 2:1 mixture of acetone to epoxy resin. Samples remained at 21°C for 12 hours on a shaker table to prevent hardening. These were then transferred into a 1:1 mixture of acetone to resin, following by a 1:2 mixture (each for 12 hours and at 21°C on a shaker table), before finally being placed into a silicone mold with pure resin. The mold was placed into an oven heated to 38°C, and the resin was allowed to cure for 24 hours. The resulting blocks were machined to prepare the apical surface of each sample for microtomy.

A Leica Ultracut R Microtome and diamond knife were used to expose a cross-section (transverse plane) of the apical and basal portions of the rostrum and to remove excess material. Semi-thin sections (0.5 µm thick) were kept, and separated into three groups: the first group were left unstained, the other two groups were stained with either toluidine-blue-borax or methylene-blue for light microscopy and imaging (Fig. 4.3).

4.2.4 Cold-fracture of Specimens

Two pinned female specimens of *C. caryae* and *C. sulcatulus* were selected at random and retained for cold-fracturing of the rostrum. The heads of the specimens were removed and cleaned using a 95% ethanol solution and a thin paintbrush. Any muscles protruding from the occipital foramen were removed with a fine-edged razor blade. The antennae were removed directly using forceps to pull the scape (basal section of antenna) from the antennal insertion. Cleaned specimens were stored at −80°C for 24 hours, then fractured using forceps over a chilled aluminum block. To

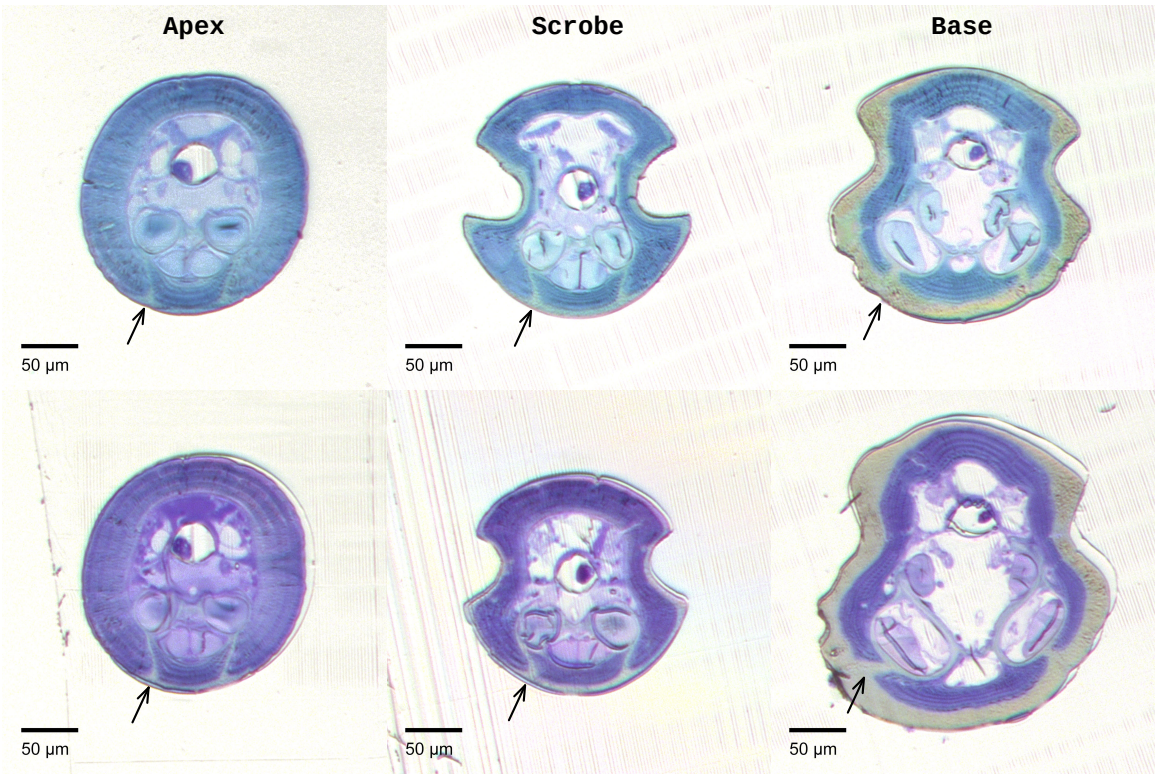


Figure 4.3: Serial thin sectioning of female *Curculio humeralis* (Casey, 1897) rostrum. Serial semi-thin sections (0.5 µm) from locations across rostrum, including rostral apex, base of snout, and region of scrobes. Sections in upper panels stained with methylene-blue, lower panels stained with toluidine-blue-borax. White arrows indicate invaginated cuticle of occipital sulcus.

fracture each specimen, the head capsule and rostrum were each gripped firmly in a pair of forceps; the forceps were then sharply rotated to fracture the base of the snout via dorsal flexion. The rostrum was fractured a second time, after separation from the head capsule, using the same procedure. The segmented specimens were then placed into individual glass vials to protect the fracture surfaces from contamination prior to microscopy.

4.2.5 Microscopy and Imaging

The fracture surfaces of cold-fractured specimens were examined using scanning electron microscopy to characterize the composite profile and microstructure of the

rostrum. Fracture surfaces of tensile testing specimens of female *C. caryae* and *C. sulcatulus* (**??**) were assessed using both light microscopy and SEM to image the fracture surfaces of the specimens in transverse view. Electron microscopy was conducted using a JEOL JSM6300 scanning electron microscope. Light microscopy was conducted using a Leica M205 C stereomicroscope and attached computer running the software Leica Application Suite (LAS), as well as a Visionary Digital Passport II system using a Canon EOS Mark 5D II camera outfitted with interchangeable microptic lenses. Specimen length, layer thicknesses, macrofiber orientation angles, and cross-sectional areas were assessed in the Leica Application Suite and in Adobe Creative Suite using pixel-wise measurements multiplied by a scaling factor for the image.

Confocal microscopy of female *C. longinasus* was conducted on a Leica TCS SP5 AOBS Spectral Confocal System equipped with a 405 nm laser excitation line. Insect cuticle is auto-florescent when illuminated by ultraviolet light, but must first be cleared to permit excitation of the tissue [113, 114]. Specimens were prepared by first removing the head, which was then bisected using a fine-edged razor blade and cleared in 5% hydrogen peroxide solution for 24 hours. The bisected, cleared specimen was placed onto a glass slide and excited using a 405 nm laser line, with emission detection tuned to 420-480 nm. Montage images were stitched together within the LAS software prior to export (see Fig. 4.4).

4.2.6 3D-model Construction

Solid models of the rostrum of exemplary female specimens belonging to each of the three species were manually generated using SolidWorks 2018 (SP0.1, Dassault Systèmes SolidWorks Corp., Vélizy-Villacoublay, France). Images of identical magnification and extent, featuring the lateral and dorsal habitus of the head, were

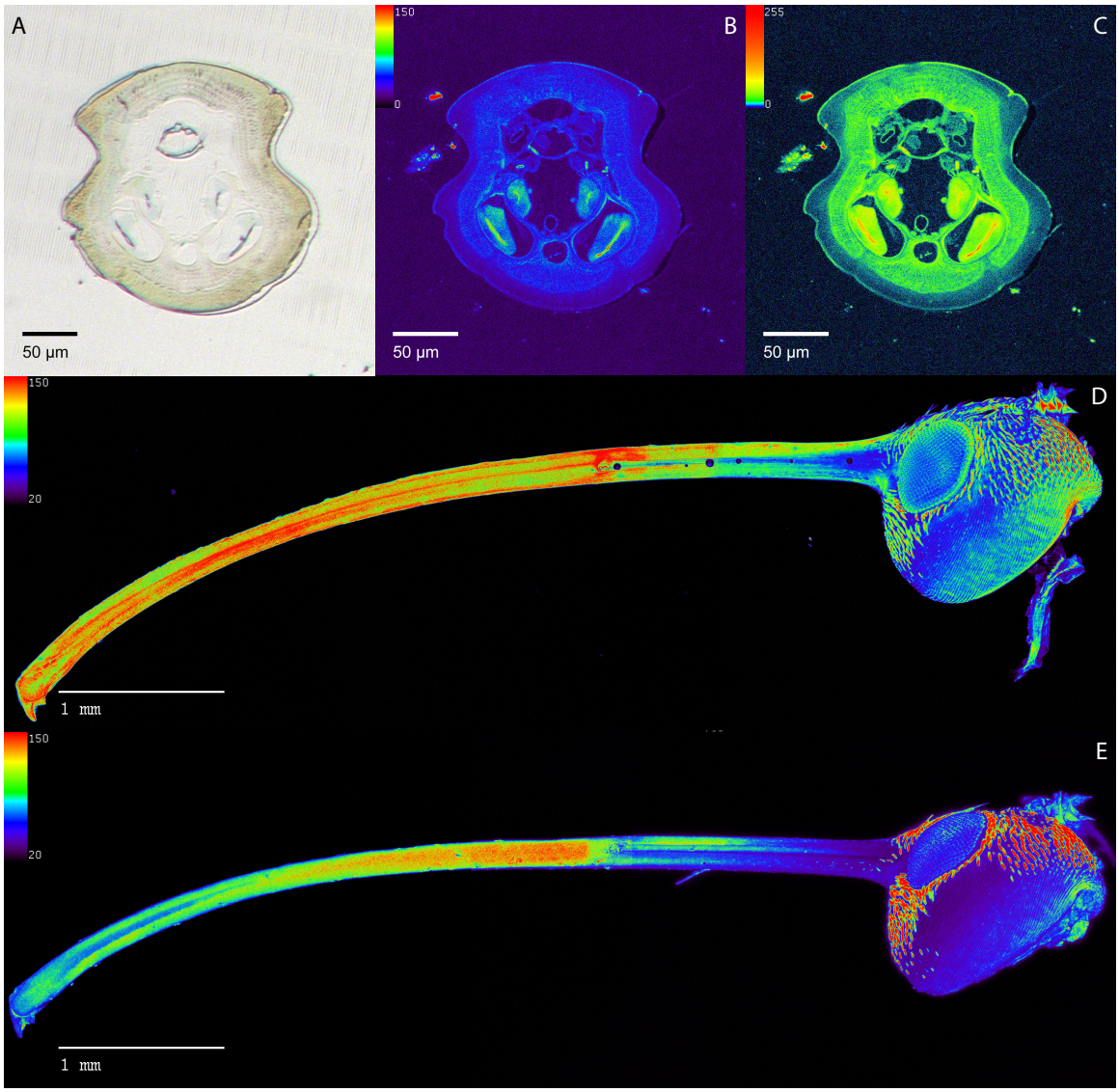


Figure 4.4: Confocal microscopy of *Curculio longinasus*. 405 nm UV laser line was used for excitation in all specimens, with emission detected from 420-480 nm. **A** Unstained semi-thin section used for confocal laser scanning microscopy. **B** Linear-filtering and **C** log-filtering show that endocuticle is more luminous than exocuticle when excited by UV light, possibly due to florescence of protein matrix between chitin macrofibers. Endocuticle-rich tissues fluoresce more strongly than exocuticle-rich cuticle; leading to gradients observed in D: longitudinally-bisected specimen fully immersed in de-ionized water; and E: dry specimen.

imported and placed along orthogonal planes of view with the endpoints of the head and rostrum aligned. Tangent splines were aligned in lateral view with the entire dorsal and ventral margins of the rostrum, up to the head capsule, and to the mid-line of the apical portion of the rostrum up to the apex of the scrobe. A 3D-plane was fit to the rostral apex orthogonal to the end-tangent of the mid-line spline, and a scaled image of the rostral cross-section was placed onto the plane. This image was traced over to generate a solid sectional area, which was then used for an extruded sweep over the mid-line spline path using the dorsal and ventral margin splines as curvature guides. *Curculio longinasus* and *C. sulcatulus* are approximately circular in cross-section up to the head-rostrum junction, with approximately circular cutouts along the lateral mid-line for the scrobe. *Curculio caryae* is roughly "D"-shaped, apically with ventrolateral flanges beyond the scrobe, and thereafter exhibiting a ventrally-flattened, dorsally-arched junction with the head near the base of the scrobe. This is the first time that a species-specific rostral cross-section has been reported in *Curculio*, and may constitute a novel diagnostic character for this species.

To capture the geometry of the scrobe and junction with the head capsule, representative cross-sections of this region were used to trace splines in transverse view. Measurements of the lateral extent in dorsal view were used to trace lateral mid-lines and transverse construction lines, as needed, to scale and connect the cross-sections. The head capsule was represented in lateral view with a circle of appropriate diameter, centered at the midpoint of the capsule, and with a circular cross-section in transverse view. The posterior margin was represented by an angled circular cross-section offset from the midpoint by a construction line. All cross-sectional areas, construction geometry, and head capsule were aligned to the dorsal and ventral spline margins traced over the image in lateral view, which were taken to represent the sagittal plane of the head. The basal face of the solid body representing the rostral apex

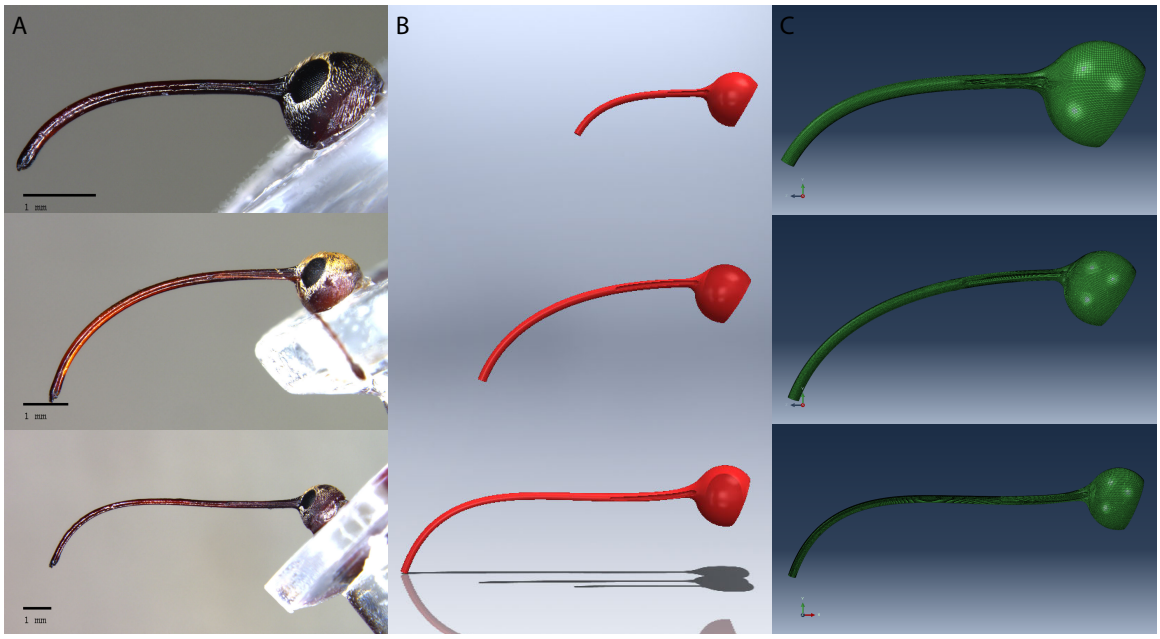


Figure 4.5: Solid model and mesh generation. **A** Heads of three female specimens belonging, from top to bottom, to *C. sulcatulus*, *C. longinasus*, and *C. caryae*. **B** Solid models (to scale) of each specimen, as seen in modeling software. **C** Finest meshes generated for each solid model; global element size of 0.02.

was used as a starting point for a lofted extrusion through each cross-section up to the posterior margin of the head, using the dorsal and ventral margins and lateral splines as curvature guides. Finally, the scrobe was created as a swept cut along a predefined path corresponding to a trace of the mid-line of the scrobe in lateral view, projected onto the lateral surface of the solid body. The result of this procedure is a smooth, feature-based (and thus fully customizable), parametric representation of the specimen (see Fig. 4.5). The models were scaled to the actual size of the specimen and exported as parasolid binary files for finite element analysis.

4.2.7 Finite Element Analysis

General Approach

Finite element analysis was conducted in Abaqus/CAE (release 6.13, Dassault Systèmes, Providence, RI, USA) using the solid models generated for each species to simulate the *in-vivo* behavior of the rostrum. Our general approach was to use negative-offset thin-shell elements, where the outer surface of each solid models is the reference surface. These elements were given material definitions based on their location on the head to approximate the distribution of cuticle layer thicknesses and fiber orientation angles observed in fractured and thin-sectioned specimens, using four or six discrete arrangements depending on the species. We verified our models using the approach of Roache [115–117] to confirm mesh convergence in a test load under linear-elastic static conditions (implicit solver), using three levels of h-refinement. The results of this simulation were validated against experimental loading of the actual specimens used to generate the solid models.

Following verification and validation of the models under experimentally testable conditions, we modified the material definitions to assess the relative contributions of layer thickness and macrofiber orientation angle on rostral flexibility, as measured by dorso-apical deflection of the snout under a given load. This was accomplished by making either or both of these properties uniform across the length of the snout, in all regions, to match the head capsule and base of the rostrum. We further applied more realistic loading conditions with respect to the drilling behavior of live female *Curculio*, by using prescribed dislocation of the head capsule over a fixed location representative of a bore-hole. In addition to displacement, we report stresses and strains across regions of the snout for each species, comparing trends in differential behavior across species and composite architectures along the length of the snout,

including both lifelike and hypothetical "basal" layups.

Below we describe our analytical procedure, generally adhering to the recommendations of Erdemir et al. [101] and others [18, 100] to make our protocol as transparent and reproducible.

Mesh Generation

Each parasolid binary solid model was imported into Abaqus/CAE, via the import-part dialogue; our unit system was taken to be SI(mm) units. The apical and basal faces were removed to create a cylindrical surface model, which was bisected about the sagittal plane. The right side of each bisected model was retained for meshing, the left half was deleted. The surfaces were initially partitioned using the auto-partition tool, with further partitioning on regions with more complex geometry where sweep and structured meshing failed. Each part was seeded using an initial global element size at a coarse granularity of 0.08, with curve control enabled at a size of 0.05 across the entire model. Meshing rules were assigned first by structured quad-only meshing with minimization of the mesh transition, then by applying quad-only sweep meshing to the model, excluding those areas where the geometry was too complex, such that all partitions used either sweep or structured meshing with only quadrilateral elements. Quad-meshing was used to allow more precise control over the material orientation angles within each element, and to simplify manual selection of cuticle regions across the length of the head on the finer-scale meshes. This procedure was repeated for two levels of h-refinement, where the model was re-seeded at global sizes of 0.04 and 0.02 (see Fig. 4.5), with curvature control set to 0.025 and 0.0125, respectively, for an effective h-refinement ratio of 2.0 at each level of re-meshing.

The element type definition for all model partitions was conventional thin-shell elements with reduced-integration (S4R), with default settings for this element type.

We explored the use of full-integration and thick-shell elements (S8R) at the finest mesh settings, but were unable to recover any substantial differences in the results of simulation outputs. Once the mesh was complete for the right-hand side of the head, the mesh was converted to an orphan mesh, and the mesh instance in the assembly was mirrored across the sagittal plane to yield a fully-symmetric mesh. The nodes along the sagittal plane were merged to create a new part and new instance of the full mesh geometry for the model.

Material Definition and Section Assignment

Three materials were defined in a custom library, using the elastic constants reported from a constitutive model of the cuticle of *C. longinasus* [8], converted to MPa for SI (mm) unit consistency:

1. Exocuticle, which is the outermost region of the cuticle and displays in-plane transverse isotropy (i.e., along the 1 and 2 axes), and is characterized by the Bouligand structure [25].

2. Endocuticle, which is an inner, orthotropic ($E_1 \gg E_2$) multilayer region comprised of large bundles of aligned chitin called macrofibers that are arranged in unidirectional laminae [29, 30].

3. Invaginated exocuticle, which is found along the underside of the head and rostrum in the occipital sulci. These sulci are cuticulat invaginations that form ridges to support the maxillary and mandibular tendons [11, 69, 106]. This material was generated by duplicating the exocuticle definition and interchanging the 2 and 3 axes.

The density of all materials and sections was set to $\rho = 1.20 \times 10^{-12}$ tonne/mm, based on the work of Vincent et al. [23]. Idealized composite sections were defined

for each species, based on the cuticle microstructure observed in semi-thin sections, fracture surfaces of cold-fractured and tensile-testing specimens, and gradients observed in confocal and light microscopy. For each refined mesh within a species, care was taken to assign the same composite sections to the same portions of the snout across element sizes. The material orientations were assigned relative to the element axes and the longitudinal axis of the rostrum.

Curculio longinasus and *C. sulcatulus* each were assigned four distinct composite layups (Fig. 4.6), corresponding to apical-type cuticle, basal-type cuticle, occipital sulci (invaginated cuticle), and a "dorsal" cuticle, which has the same macrofiber angles as the basal layup, but thinner exocuticle. This dorsal-type cuticle is observed in the region of the scrobe, where the exocuticle is proportionately thinner along the mid-line of the dorsum (Figs. 4.2-4.4). *Curculio caryae* was assigned six layups, including those found in the other two species, but with the addition of two "transitional" layups between the scrobe and rostral apex to reflect the gentler anterior-posterior gradient between the cuticle arrangements of these regions. These layups have the same macrofiber orientation angles as the apical cuticle, but progressively thicker exocuticle towards the scrobe. In assigning all cross-sectional composite properties, we made the simplifying assumption that the total cuticle thickness was invariant across the head, reflecting the nearly-constant thickness observed in living specimens. Additionally, because we did not destructively sample the specimens used to make the models, but rather kept them intact as vouchers, we used total thickness values corresponding to approximate averages of each species.

In addition to the "realistic" layups and section assignments, we also created models with hypothetical layups to individually assess the contributions of modified layer thickness and stacking angle sequence to cuticle flexibility, each with only one of the modifications present in the cuticle of the rostral apex. The first of these models

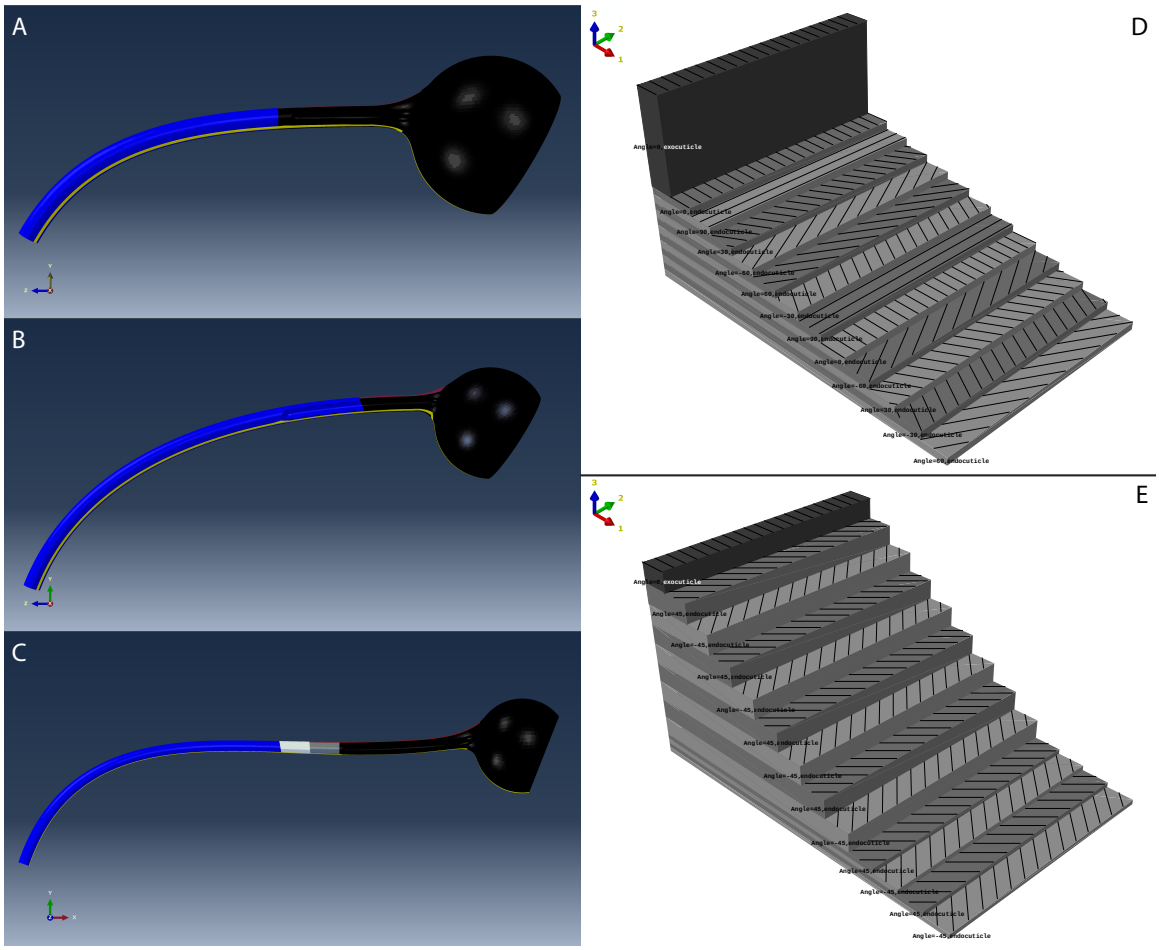


Figure 4.6: Composite layup and section assignment. Panels on left detail composite layup distribution in finest meshes for **A** *C. sulcatulus*, **B** *C. longinsaus*, and **C** *C. caryae*. Color-scheme: black – basal-type cuticle layup, red – dorsally thinned basal-type cuticle, yellow – invaginated exocuticle representative of the occipital sulci, blue – apical-type cuticle, gray/white – transitional layups with intermediate layer thicknesses between basal and apical layups in *C. caryae*. **D** Ply-stack plot of "basal-type" cuticle found in head capsule and base of rostrum. **E** Ply-stack plot of "apical-type" cuticle found in rostral apex.

has the layer thicknesses of the rostral apex, but fiber orientations of the head capsule, while the second has the fiber orientations of the rostral apex, but the layer thicknesses of the head capsule; the final condition was to have both modifications absent entirely. Using these composite layups, we were able to test whether the cuticle modifications noted in the rostral apex have a synergistic combined effect on cuticle elasticity or a simple additive effect. For the models subjected to apical load, all three hypothetical conditions were tested, but for the models subjected to prescribed displacement, we instead only compare the realistic section assignments with the fully unmodified layup.

Model Verification and Validation

To verify mesh convergence in the fine-scale mesh ($h = 0.02$), we adopt the strategy outlined by Roache [115–117], which we summarize below for reference. Here a grid convergence index (GCI) is estimated between each successive pair of meshes, based on a quantity of interest, f, (in this case apical deflection under load, see below); simulation output is then compared to an extrapolated solution for a mesh-spacing of zero.

Specifically, for quantities f_1 and f_2 that are estimated using grids of spacing h_1 and h_2, respectively, where h_1 is the finer mesh and the grid refinement ratio is defined as $r = h_2/h_1$, the Richardson extrapolation of the asymptotic continuum value $f_{h=0}$ at the p^{th} order of convergence can be found by:

$$f_{h=0} \cong f_1 + \frac{f_1 - f_2}{r^p - 1}\,. \tag{4.1}$$

With a third estimated solution f_3 at grid spacing h_3, and a constant mesh-refinement ratio (for us $r = 2$), the order of convergence can be calculated as:

$$p = \ln\left(\frac{f_3 - f_2}{f_2 - f_1}\right) / \ln(r)\,. \tag{4.2}$$

The grid convergence index (GCI_{12}) of a parameter estimated from two grids, f_1 and f_2, indicates the relative distance (not absolute) of the estimate from the finer grid (i.e., f_1) to the asymptotic solution, and can be evaluated via:

$$\mathrm{GCI}_{12} = \frac{F_s|\epsilon|}{r^p - 1}\,, \tag{4.3}$$

where the the relative error is given by $\epsilon = (f_2 - f_1)/f_1$ (the absolute error is simply $\epsilon = f_2 - f_1$). The term F_s refers to a "factor of safety" in error estimation, for which it is recommended that $F_s = 1.25$ for comparison of three or more grids approaching the asymptotic solution. For the mesh-convergence study, we report $f_{h=0} \pm \mathrm{GCI}_{abs}$, where $\mathrm{GCI}_{abs} = \mathrm{GCI}_{12} \times f_1$, and is the absolute estimated error at the finest mesh scale. For three grids approaching the asymptotic continuum value of a parameter of interest, $\mathrm{GCI}_{23} = \mathrm{GCI}_{12} \times r^p$. Convergence can be evaluated as a ratio of these terms, constancy (denoted C), where asymptotically:

$$C \cong \frac{\mathrm{GCI}_{23}}{\mathrm{GCI}_{12} \times r^p} \cong 1\,. \tag{4.4}$$

Thus, at a value of $C \approx 1$, the mesh can be considered to have converged upon the asymptotic continuum value of f.

Using this method, the convergence of the three mesh sizes was tested for each species under three different loads in which force was applied vertically to the apex of the rostrum. These models were experimentally validated by application of weights to the specimens after which the solid models were designed. The posterior margin of the

head capsule of each specimen was fixed to a push-pin using cyanoacrylate adhesive, then submerged in de-ionized water for four hours to simulate the *in-vivo* moisture content of the cuticle (cuticle can become saturated as quickly as ten minutes post-immersion [21]). The specimens remained submerged and were oriented upside-down, with the base of the snout protruding horizontally. Aluminum (100 mg and 500 mg) and stainless steel (1000 mg) scale-calibration weights were suspended from the rostral apex by tying 40 AWG (0.0799 mm) nichrome wire to each weight and looping the free end of the wire around the mandibles with fine-tipped forceps. Images of the submerged specimen were acquired immediately before and after the application of each weight to mitigate the effects of long-term viscoelasticity in the cuticle [9]. The displacement of the rostral apex was measured and compared with the predicted displacement of the model (see Model Validation).

Loading and Boundary Conditions

For verification and validation, three loads were imposed that corresponded to application of submerged weights to the rostral apex. This load was modeled as a concentrated force equal to the force of the solid mass due to gravity ($m_s g$) minus the buoyant force cause by the displaced fluid acting on the mass ($-m_f g$). In static equilibrium, the effective force from the weight acting on the snout is related to these two forces by:

$$F_{\mathit{eff}} = (m_s - m_f)g\,. \tag{4.5}$$

Because the volume of displaced liquid is equal to the volume of the weight, the masses and densities of the solid weight and liquid are related as:

$$\frac{m_s}{\rho_s} = \frac{m_f}{\rho_f}\,, \tag{4.6}$$

and, therefore:

$$F_{\mathit{eff}} = \left(m_s - \frac{m_s}{\rho_s}\rho_f\right) g\,. \tag{4.7}$$

Using Eq. 4.7, we can deduce the force created by an apically-suspended, immersed weight using the mass of the weight, density of the weight (steel: $7.7\,\mathrm{g/cm^3}$, aluminum: $2.7\,\mathrm{g/cm^3}$), and density of de-ionized water ($1.0\,\mathrm{g/cm^3}$). This relation also allows us to estimate the effective gravitational acceleration acting on the cuticle, given its density ($1.2\,\mathrm{g/cm^3}$) and the effect of buoyancy on an arbitrary mass of cuticle (replace F_{eff} with $m_s a$ and solve for a). This value was added as a field oriented in the same direction as the concentrated mass (i.e., vertically/dorsally). Finally, a displacement boundary condition was applied to the posterior margin of the head, such that no motion or rotation could occur along the selected nodes. These conditions were applied in single step, ramped linearly over the interval and solved directly using the implicit solver. To assess the effect of each cuticle modification on the flexibility of the rostrum, the fine-mesh ($h = 0.02$) models assigned hypothetical cuticle layups were subjected to the same loading and boundary conditions as the 1000 mg validation model.

To evaluate the effect of the cuticle modifications on the behavior of the rostrum under more realistic conditions, we applied a prescribed dislocation of the head capsule over a fixed location representative of a bore-hole for both a fully-specified model and a model completely lacking modifications to the cuticle. The prescribed motion was applied as a vertical dislocation of a node near the posterior margin of the head capsule, with no constraints on displacement or rotation along other axes. The exact

magnitude of the dislocation was sufficient to achieve near-complete extension of the snout; the magnitude of the dislocation varied based on the length of the snout in that species at full extension. The apex of the snout was assigned a zero-magnitude dislocation/rotation boundary condition to simulate the effect of inserting the rostrum into a tight bore-hole; gravity was not added to this model. The dislocation and boundary conditions were ramped linearly in a single step, which was solved using the iterative implicit solver with non-linear geometry (option nlgeom turned on).

Model Output

The magnitude of apical displacement of the rostrum under load was the primary output of the verification and validation models, as wells as for the models used for comparison of the hypothetical cuticle composite sections. For the more realistic load conditions characterized by vertical dislocation of the head capsule, the primary output variables were maximum principle in-plane stress and strain in tension and compression, strain energy density, and von Mises stress. Stresses and strains for all layers and section integration points were requested as field output, with maxima (tension) and minima (compression) reported. Sectional forces and forces at nodes and section integration points were also requested as field output. Where possible, all variables were requested for individual plies, and reported from the exocuticle, first layer of endocuticle, and invaginated cuticle representative of the occipital sulci. The plies exhibiting maximum output values were also identified.

For the more realistic loading condition, we report the factor of safety (FS) and margin of safety (MS) for the snout at the location of maximum stress in tensile and compression. Based on tensile testing data, a phylogenetic linear mixed-effect model was previously fit to measurements of the natural-log transformed cross-sectional area of the endocuticle (fixed-effect), with the natural-log transformed maximum

uniaxial tensile force as the response variable. This model was used to predict the maximum sustainable force F_u in cross-section prior to fracture, and therefore the (nominal) ultimate tensile strength of the cuticle [1] . The compressive strength of the rostrum in *Cyrtotrachelus longimanus* (Fabricius, 1775) was reported to be three times higher than its tensile strength [70]; we used this to estimate an upper bound on the compressive strength of the cuticle based on tensile strength.

To approximate the area of endocuticle for each composite layup across the entire snout cross-section, rather than that of a single element, we assume a circular cross section, and estimate that the occipital sulci occupy a combined 30° section of the circle, thus:

$$\mathrm{A}_{endo} = \frac{11\pi}{12}\left[\left(\frac{\mathrm{OD}}{2} - h_1\right)^2 - \left(\frac{\mathrm{OD}}{2} - \sum_{i=1}^{13} h_i\right)^2\right] . \tag{4.8}$$

Because *C. longinasus* was not included in tensile testing due to lack of representation in the preferred phylogeny, we assumed that the random effect for species membership is zero, with no error from phylogeny (essentially reducing the model to a simple slope-intercept form).

To evaluate the factor of safety for the cuticle as a whole, we estimated the ultimate strength of the cuticle using the total cross-sectional area of the snout: $\sigma_u = F_u/A$. The factor of safety was calculated as:

$$\mathrm{FS} = \frac{\sigma_u}{\sigma} , \tag{4.9}$$

Where σ is the average membrane stress through an entire element. The margin of safety was then evaluated from the factor of safety:

[1] The fracture strength of exocuticle is uncharacterized in *Curculio*.

$$\mathrm{MS} = \mathrm{FS} - 1\,. \tag{4.10}$$

When $FS > 1$ and $MS > 0$, the strain in the model has not exceeded the known fracture strength of the cuticle and can theoretically bear additional load; conversely, $FS \leq 1$ and $MS \leq 0$ indicate that the applied load has exceeded the minimum fracture strength of the cuticle, implying a risk of structural failure.

Limitations

We note that there are three principal limitations to the finite element models. First and foremost, these models are purely linear-elastic static in formulation, and cannot provide information on fracture behavior or fatigue. Nonetheless we indicate that, under lifelike conditions, rostral bending appears to be elastic, or very nearly so, given that the maximum strain in any of these species was 3.35%. Second, the models are of different sizes for each species, making cross-species comparison of applied forces and model outputs difficult due to scaling between model size and outputs. In particular, structural strength scales with increasing force per unit area, while strain energy scales with model volume and length [18]. To circumvent this difficulty, we rely on the application of all hypothesized cuticle layups to each model and report similarities in the differential responses of the models (for instance, reporting whether or not a change in layer stacking sequence has the same type of effect across species). Third, the models do not include internal structures, which prevents any inference with respect to the functionality of the rostrum as a feeding and cutting mechanism during the excavation of sites for oviposition. Presently these considerations are outside the scope of this work, but the formulation of our models nonetheless precludes the use of our models for investigation of feeding mechanobiology.

4.3 Results and Discussion

4.3.1 Model Verification

Mesh convergence was achieved at a global element size of 0.02 in the models of all species for the three validated loading conditions. The estimated apical displacement, U, and continuum value, U_0, of each model are reported in Table 4.3.1 (see also Fig. 4.7). For all models, $0.99 < C < 1.00$ – indicating that the estimated values of U for the models are within 1.0% of the asymptotic value U_0. We consider this as an indicator of mesh convergence at the finest level of grid spacing (Table 4.3.1). Notably, the order of convergence was found to be within $p = 4 \pm 0.5$ for most models. The lowest order of convergence was observed in the model of *C. sulcatulus* at the 100 mg loading condition, with a value of $p = 1.50$, whereas the highest order of convergence of any model was the 500 mg loading condition for this same species, at an order of $p = 4.52$. We found that the estimates of U were typically quite close in value. The greatest degree of variation – i.e., for the model with the lowest order of convergence – between the coarsest and finest meshes was a decrease of 3.38% from the coarse mesh. We thus infer that mesh independence is achieved at a global element size of 0.02 for each species, making the fine meshes suitable for further simulations under different load conditions and with hypothetical material definitions.

4.3.2 Model Validation

The finite element models exhibit strong correspondence with validation experiments. Predicted apical displacement was generally within 10% of experimentally measured values (Table 4.3.1). Importantly, the general shape of the deformed rostra in the models also displayed remarkably lifelike behavior when compared to observed snout deformation in the experiments (Fig. 4.8). Deflection generally appeared to scale

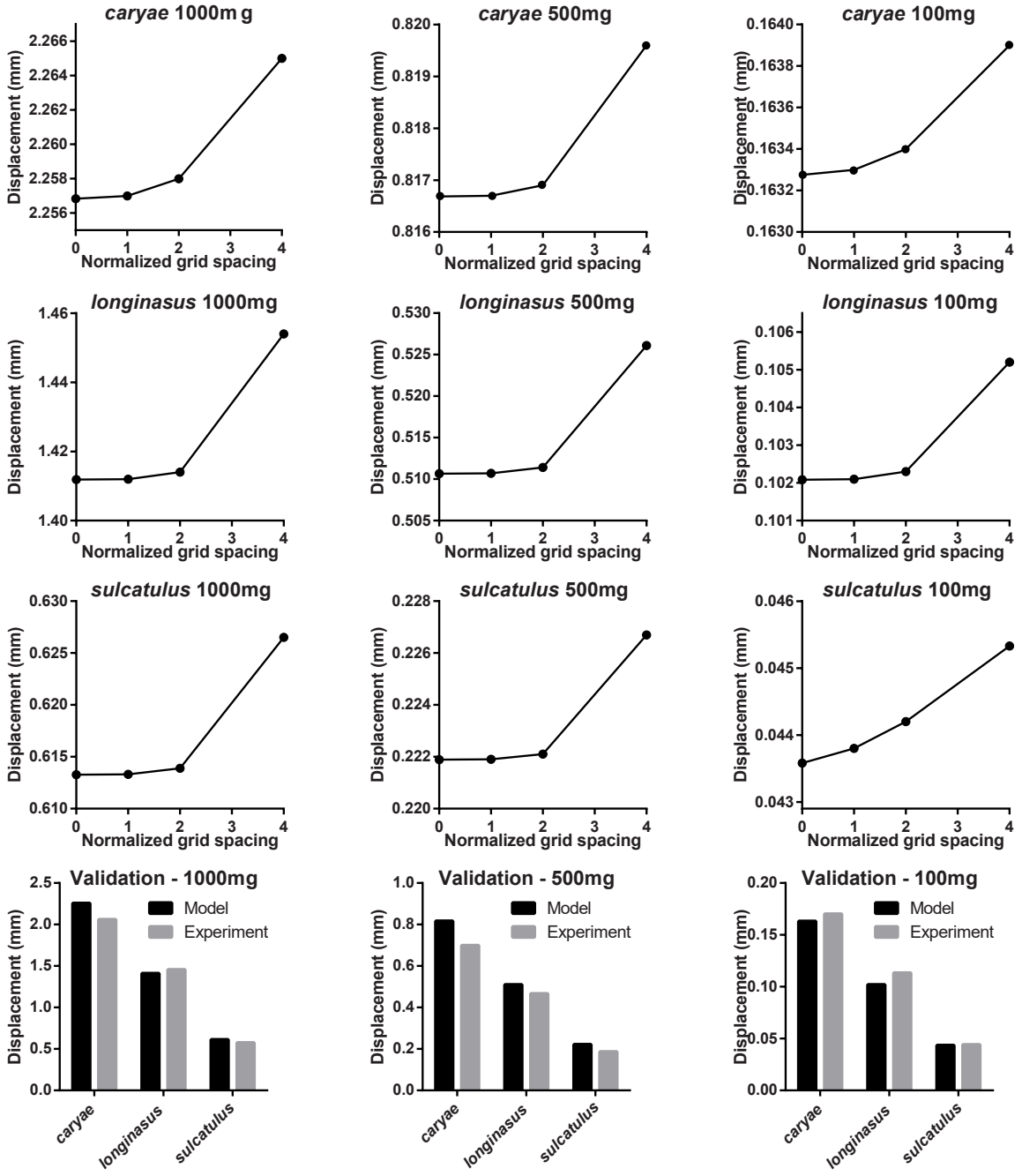


Figure 4.7: Model verification and validation. Each species and load condition represented across three successively refined meshes. Asymptotic value for quantity of interest – apical displacement – displayed as y-intercept. All models converged with respect to apical displacement of snout under varying load. Bottom three panels show asymptotic predicted displacement – in most models within 10% of experimentally obtained values.

Table 4.1: Results of model verification and validation, by species and load.

Species	M (mg)	U_0 (mm)	$\mathrm{GCI}_{\mathrm{abs}}$ (mm)	p	C	U_x (mm)	ϵ_x (%)
C. caryae	1000	2.257	$\pm 1.903 \times 10^{-4}$	2.81	0.9996	2.062	9.44
	500	0.817	$\pm 1.712 \times 10^{-5}$	3.75	0.9998	0.699	16.8
	100	0.163	$\pm 3.257 \times 10^{-5}$	2.32	0.9994	0.170	-4.06
C. longinasus	1000	1.412	$\pm 1.359 \times 10^{-4}$	4.32	0.9986	1.458	-3.16
	500	0.511	$\pm 4.004 \times 10^{-5}$	4.39	0.9986	0.467	9.25
	100	0.102	$\pm 2.057 \times 10^{-5}$	3.86	0.9980	0.113	-9.96
C. sulcatulus	1000	0.613	$\pm 3.524 \times 10^{-5}$	4.39	0.9990	0.576	6.40
	500	0.222	$\pm 9.575 \times 10^{-6}$	4.52	0.9991	0.187	18.7
	100	0.0436	$\pm 2.769 \times 10^{-4}$	1.50	0.9910	0.0443	-1.56

From left to right: [M] mass of applied load, [U_0] predicted apical displacement (asymptotic), [$\mathrm{GCI}_{\mathrm{abs}}$] grid convergence index (absolute), [p] order of convergence, [C] constancy, [U_x] experimentally-measured apical displacement, and [ϵ_x] prediction error; see text for variable definitions.

with rostrum length, with models for *C. caryae* exhibiting the greatest dorso-apical deflection under load, and those of *C. sulcatulus* the least. Even though *C. longinsaus* was used to calibrate the constitutive model from which the elastic constants of the exocuticle and endocuticle were derived, all species showed a similar pattern in the margin of error in response to increased load. The lowest margin of error is found in comparison to the smallest load, whereas the highest error is found in comparison to the intermediate load.

The smallest observed margin of error was -1.56% for *C. sulcatulus* with the 100 mg calibration weight. The greatest margin of error between the models and experiments was at a 500 mg load, where the models for *C. caryae* and *C. sulcatulus* over-estimated apical deflection by 16.8% and 18.7%, respectively, but otherwise remained within a 10% margin of error for the 1000 mg and 100 mg loads. We observed that simulated

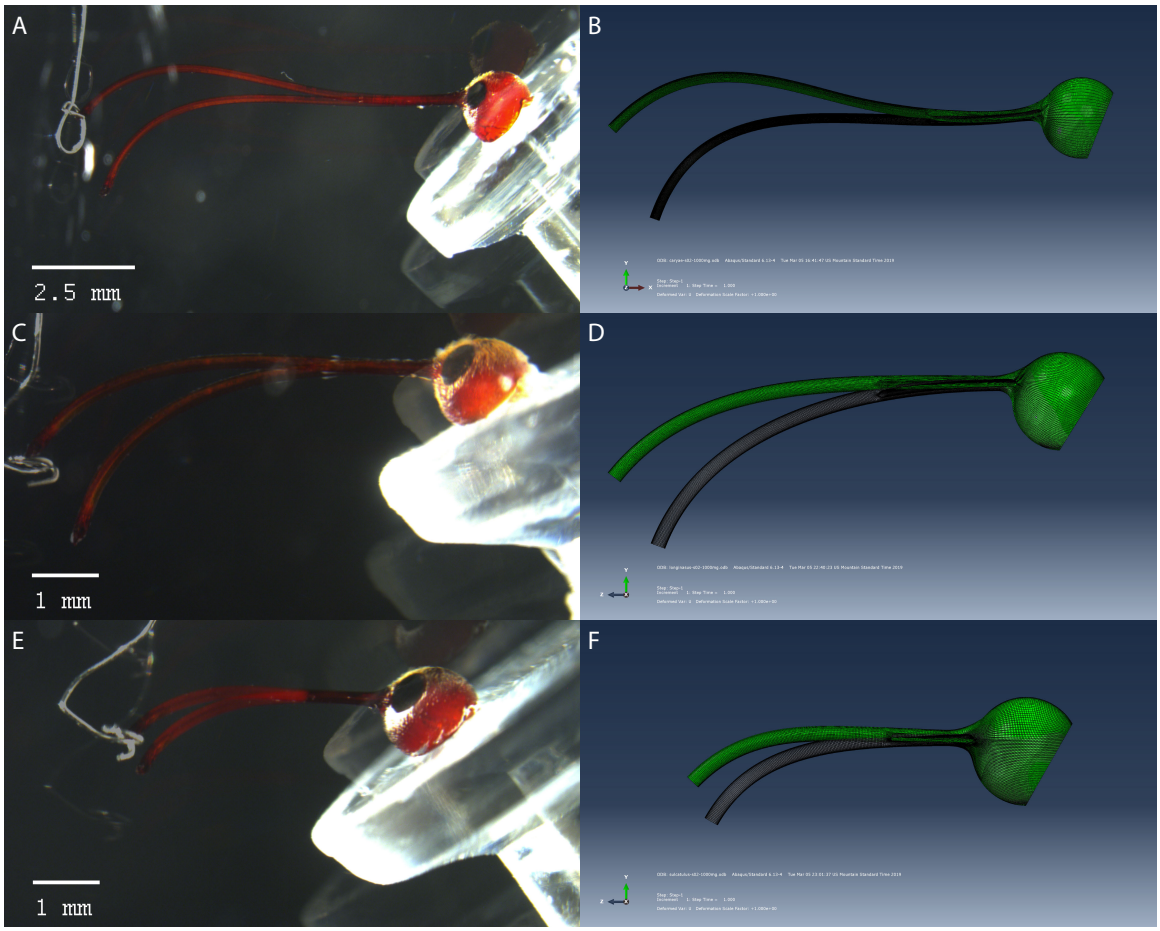


Figure 4.8: Experimental loading and model validation. Panels **A** - **C** and **B** - **F** correspond to specimens and models, respectively, subjected to 1000 mg apical load in *C. caryae*, *C. longinsasus*, and *C. sulcatulus*, from top to bottom. Finite element models exhibit lifelike responses to apical load.

dorso-apical displacement increased approximately linearly with greater loads, whereas the experimentally measured deflections did not. The non-linear relationship between the measured displacements for each load condition leads us to hypothesize that an uncharacterized, mild strain-hardening effect in the specimens may have caused a slight reduction in deflection at moderate loads. This would lead to overestimation in the models, which assume a linear response to increasing load. We nonetheless find that the margin of error between the experiments and models is acceptable, and conclude that the models are sufficiently validated to proceed with additional, more

exploratory simulations.

4.3.3 Contribution of Apical Modifications

We previously estimated that the apical-type cuticle had 72% and 60% lower membrane and flexural moduli, respectively, than the basal-type cuticle (head capsule) as estimated by CLPT. According to these estimates, each modification to the rostral cuticle individually can reduce the uniaxial membrane stiffness of the resulting composite by approximately 20%. Our finite element models corroborate these findings, as the combined effect of the modifications appears to surpass the magnitude of their individual contributions to apical deflection, in excess of what would be expected from a simple additive effect (Fig. 4.9). This suggests that the rostrum bending functionality is indeed dependent on the presence of both modifications in the living animal, where the combined effect allows the rostrum to flex without fracture.

We expand upon the theme of fracture strength in the next sections. Here we first discuss the relative contribution of each modification to the elasticity of the rostral apex. In Table 4.3.3, we present the apical displacement of models of each species subjected to a 1000 mg load using both realistic and hypothetical cuticle composite layups; secondary outputs corresponding to maximum stress and strain in each model are also reported.

In agreement with our first-principles estimates of the elastic behavior of the cuticle, we observed that the predicted magnitude of apical displacement was between 44-78% greater with apically modified cuticle than with unmodified basal-type cuticle. Although each modification (either layer thicknesses or orientation angles) individually contributed to the flexibility of the rostrum, the individual contribution of the layer thicknesses was consistently nearly double that of the layer orientation angles, in contrast to the predictions of CLPT. The anisotropy of the endocuticle appears to

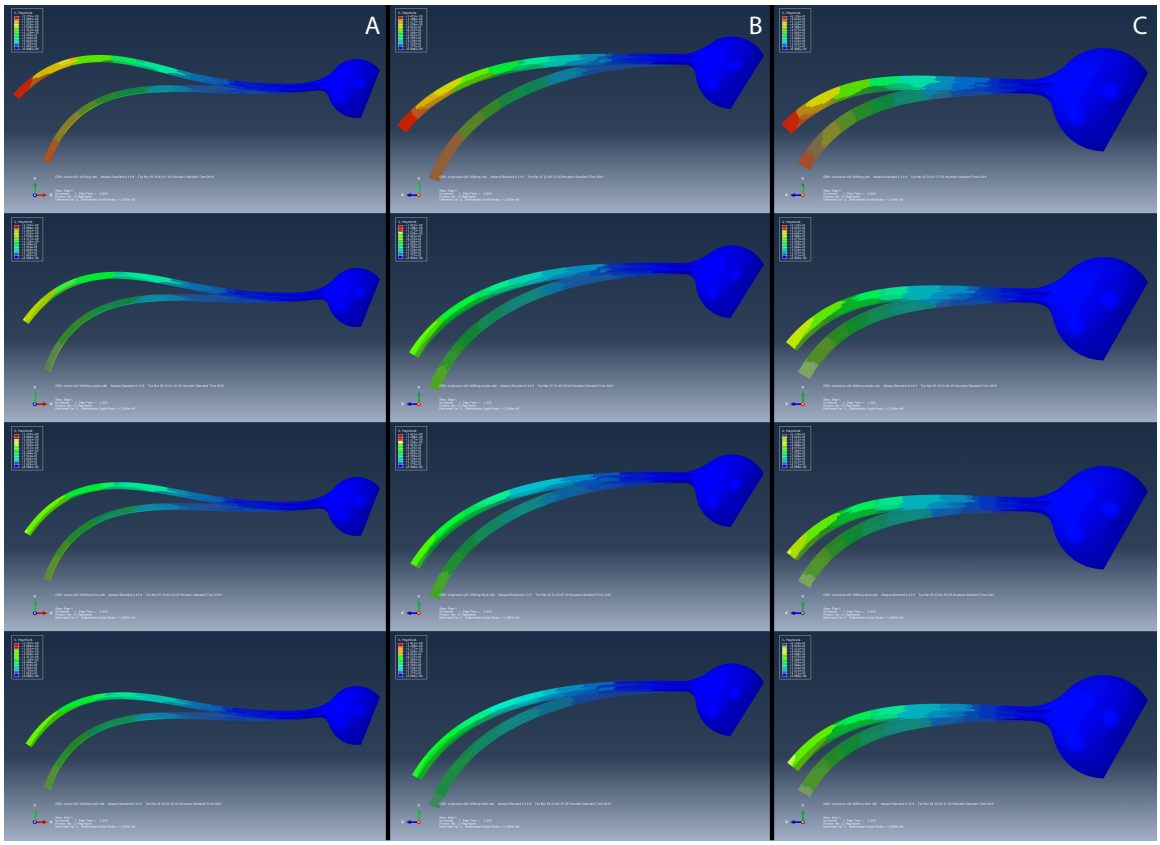


Figure 4.9: Relative contribution of cuticle modifications to apical deflection. Model correspond to 1000 mg apical loading condition, with color-scale normalized to response of lifelike cuticle models for each species. Each column contains, from top to bottom: lifelike cuticle profile, apically modified layer thicknesses only, apically modified stacking angles only, and no apical modifications. From left to right: **A** *C. caryae*, **B** *C. longinsasus*, and **C** *C. sulcatulus*. Apical modification of layer thicknesses has greater impact on apical displacement under load than orientation angles. Gains in displacement for each modification individually do not display additive combined effect, but synergistic or multiplicative effect.

have a greater effect on apical displacement than predicted by CLPT. We suggest two reasons for this effect. First, the CLPT-based model was made to be symmetric to counter bending-extension and shear coupling so that purely axial elastic moduli could be estimated. The cuticle of the rostrum, in contrast, is neither symmetric nor balanced, so these couplings would be pronounced in the real structure during apical deflection, even in the less-rigid 45° angle-ply configuration. The strongly asymmetric response to load of the endocuticle laminae is demonstrated clearly in

Table 4.2: Results of simulated apical load using hypothetical composite layups.

Species	Cuticle type	U (mm)	$\Delta U_{\%}$	ϵ_t (%)	ϵ_c (%)	σ_t (MPa)	σ_c (MPa)	Mises (MPa)
C. caryae	Realistic	2.257	53.33	1.380	-1.443	52.92	-83.05	99.11
	Apical heights	1.666	13.18	1.150	-0.7000	34.63	-46.35	44.41
	Apical angles	1.560	5.978	1.135	-0.5815	33.91	-38.39	39.51
	Both basal	1.472	——	1.135	-0.5814	32.31	-38.38	38.87
C. longinasus	Realistic	1.412	77.86	1.346	-1.250	54.53	-69.59	87.83
	Apical heights	0.9179	15.62	1.344	-0.7617	50.53	-52.36	48.13
	Apical angles	0.8613	8.490	1.307	-0.6765	48.81	-46.02	43.00
	Both basal	0.7939	——	1.306	-0.6682	48.79	-46.02	42.99
C. sulcatulus	Realistic	0.6133	44.07	1.686	-1.482	61.79	-81.62	106.7
	Apical heights	0.4670	9.702	1.686	-0.9132	46.16	-63.16	57.74
	Apical angles	0.4455	4.651	1.660	-0.8502	44.21	-58.44	53.73
	Both basal	0.4257	——	1.660	-0.8501	44.21	-58.44	53.72

All variables correspond to model maxima. From left to right: [U] predicted dorso-apical displacement, [$\Delta U_{\%}$] percent increase in displacement compared to basal-type cuticle, [ϵ_t] nominal tensile strain, [ϵ_c] nominal compressive strain, [σ_t] maximum principal tensile stress, [σ_c] maximum principal compressive stress, and von Mises stress; see text for more information on cuticle definitions and variable definitions.

Fig. 4.10. For this reason, the anisotropy of the endocuticle laminae would more strongly influence the elastic behavior of the laminate than predicted using the CLPT model, and regardless of fiber orientation.

Second, the CLPT model only considers two types of cuticle, apical and basal. The finite element models instead have up to six different regions, four of which have the apical-type layer angles. The layer thicknesses transition from basal to apical along the length of the snout with intermediate layer thickness profiles. Changing only the layer angles affects all of these regions to the same degree if the layer thicknesses are equal throughout, leading to relatively uniform stiffness across the length of the rostrum. Adjusting layer thicknesses disproportionately affects the apical regions, leading to greater deformation, strain, and stress with increasing magnitude towards the apex (Fig. 4.10). The relative contributions of each modification to the cuticle could thus not have been accurately estimated from theory alone – i.e., without further consideration

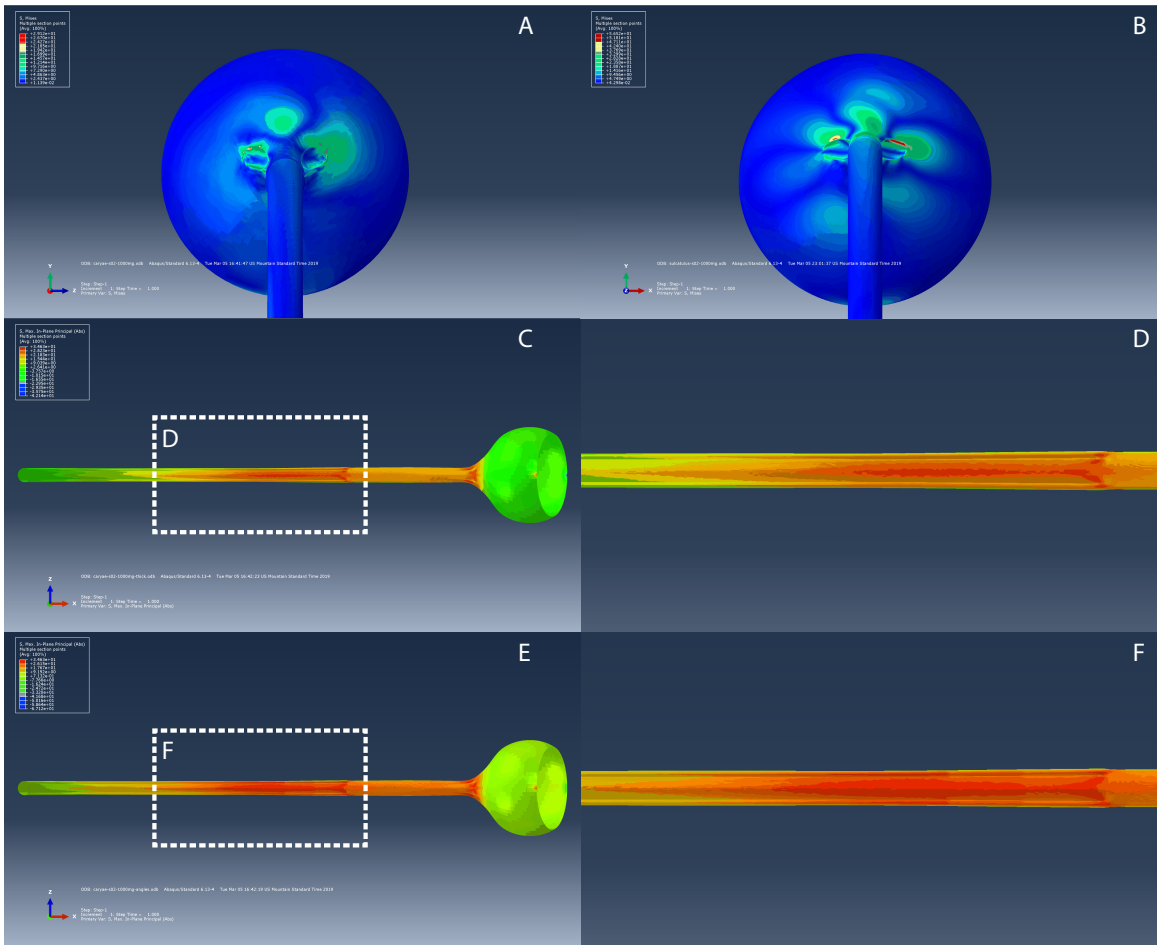


Figure 4.10: Asymmetry in layer-wise and lengthwise response to load. **A** Innermost (ply 13) endocuticle lamina in *C. caryae;* and **B** *C. sulcatulus;* exhibiting asymmetric Mises stress distribution caused by off-axis ply orientation angle, with respect to longitudinal axis. **C** – **F** detail maximum in-plane principle stress in response to 1000 mg apical load for *C. caryae*, with color-scale normalized to response of model shown in panel **E**. **C** and **D** apical modification to layer orientation angles. **E** and **F** apical modification to layer thicknesses. Models **C** – **F** show that modification of the layer thicknesses disproportionately affects rostral apex, leading to increased deflection and maximum stress, with increased apical stress concentrations.

of rostral anatomy – given the complex geometry and cuticle differentiation patterns in this structure.

Under apical load, the realistic cuticle distribution experienced maximum tensile and compressive strains between approximately 1.3-1.7% and 1.2-1.5%, respectively. These values are below the known elastic limits of living arthropod cuticles, which are

generally capable of achieving comparatively large displacements without failure [23, 28, 63, 118]. Interestingly, adding apical-type layer orientation angles to the basal-type layup resulted in little or no change to the maximum strains and stresses in the models, unlike the addition of modified layer thicknesses. Rather, as indicated previously, the increased displacement of the rostral apex in this condition appears to be a consequence of evenly distributed increases in strain along the length of the rostrum. This observation highlights why the two modifications have a synergistic effect, rather than (just) a linearly additive effect. The modification of layer thicknesses – i.e., thickening of the endocuticle – along an anterior-posterior gradient exaggerates and intensifies the reduction of stiffness caused by alteration of the lamina orientation angles. As the relative proportion of endocuticle increases, the behavior of the laminate becomes closer to that of pure endocuticle. Thus, a reduction in endocuticle stiffness is multiplied as the exocuticle thins from base to apex across the length of the snout, precisely because a greater proportion of the apical cuticle is affected by the change in macrofiber orientation angle than at the rostral base.

4.3.4 Prescribed Displacement

To more accurately simulate the oviposition behavior of live female *Curculio*, the apex of the rostrum was assigned zero-displacement and zero-rotation boundary conditions, while the postero-dorsal margin of the head capsule was subjected to a prescribed vertical displacement sufficient to induce near-complete straightening. Nodal rotation was not constrained, resulting in a lifelike rotation of the head around a fixed point, as though inserting the rostrum into a bore-hole. In Table 4.3.4 we present the maximum nominal strains and uniaxial membrane stresses (element average) experienced by each model using both lifelike (modified) and hypothetical (unmodified) composite profiles in the rostral apex; maximum element-wise total

strain energy density is also reported. The rostral flexion that accompanied the prescribed dislocation of the head was characterized by tensile and compressive strains between approximately 1.9-3.4% and 2.5-3.3%, respectively, in models using realistic composite profiles. These values are within the known elastic limits of beetle cuticle (e.g., see [28]), in agreement our hypothesis that rostral bending is elastic.

Table 4.3: Results of simulated prescribed vertical displacement of head capsule.

Species	Cuticle type	ϵ_t (%)	ϵ_c (%)	$\bar{\sigma}_t$ (MPa)	$\bar{\sigma}_c$ (MPa)	W (mJ/mm^3)
C. caryae	Realistic	3.351	-2.585	64.53	-42.58	0.7688
	All basal	3.776	-2.409	91.51	-90.00	0.9553
C. longinasus	Realistic	1.937	-2.680	77.15	-33.42	0.4785
	All basal	2.316	-2.246	101.9	-90.93	0.9384
C. sulcatulus	Realistic	2.371	-3.300	101.2	-44.62	0.8115
	All basal	2.732	-2.860	129.3	-115.5	1.633

All variables correspond to model maxima. From left to right: [ϵ_t] nominal tensile strain, [ϵ_c] nominal compressive strain, [σ_t] uniaxial membrane stress (tensile, element average), [σ_c] uniaxial membrane stress (compressive, element average), [W] strain energy density (element total); see text for more information on cuticle definitions and variable definitions.

Removal of apical cuticle modifications resulted in tensile strain increases and compressive strain decreases, indicating that the apical composite profiles reduce tensile strain at the expense of increased compressive strain. As we explain below, this trade-off is particularly advantageous because the cuticle is stronger in compression than it is in tension [23, 70]. Contrary to our expectations, removing the modifications to the rostral apex did *not* result in increased strains that are obviously beyond the elastic limits of the cuticle. In fact, the general similarity in the displaced configuration of the models suggests that a modified apical cuticle is not required to produce targeted apical extension. Instead, the boundary conditions – i.e., prescribed displacement of the head capsule about a fixed apical point – and geometry of the head are sufficient

to produce this effect. However, in all species the maximum stresses and strain energy densities greatly increased in magnitude, both in tension and compression, when the apical composite profile was not specified (Fig. 4.11). In addition, the tensile stress distributed along the venter of the rostrum became more concentrated towards the apex. This suggests that the simultaneous increase in magnitude of maximum tensile stress and concentration of stress towards the rostral apex would greatly increase the risk of fracture. We further examine this apparent relationship below.

In addition to increased apical stress magnitude and concentration, we observed that the greatest accumulation of strain energy was found in the exocuticle-rich occipital sulci (Fig. 4.11). Because the exocuticle is more brittle than endocuticle, increased strain energy densities in exocuticle-rich structures would increase the likelihood of fracture. We therefore reiterate our hypothesis, based upon prior fractographic analysis of tensile testing specimens, that the occipital sutures are the most likely source of void nucleation and crack formation in the rostrum during failure, and that catastrophic structural failure is initiated under tension in these sutures. The occipital sulci constitute an unavoidable, brittle weak point in the rostrum, and have likely constrained the evolution of rostral flexibility by limiting the maximum achievable strain in the rostrum.

4.3.5 Bending Margin of Safety

To assess whether modified apical cuticle mitigates the risk of bending fracture, we estimated the tensile strength of the cuticle and margin of safety in bending, based on previously acquired tensile testing data. We observed that with the apically modified layup, the observed maximum stresses in the model never exceed the predicted ultimate strengths of the cuticle (Table 4.3.5). The estimated margin of safety in tension for the rostrum is fairly low, allowing for only an additional 20% stress in *C. sulcatulus*.

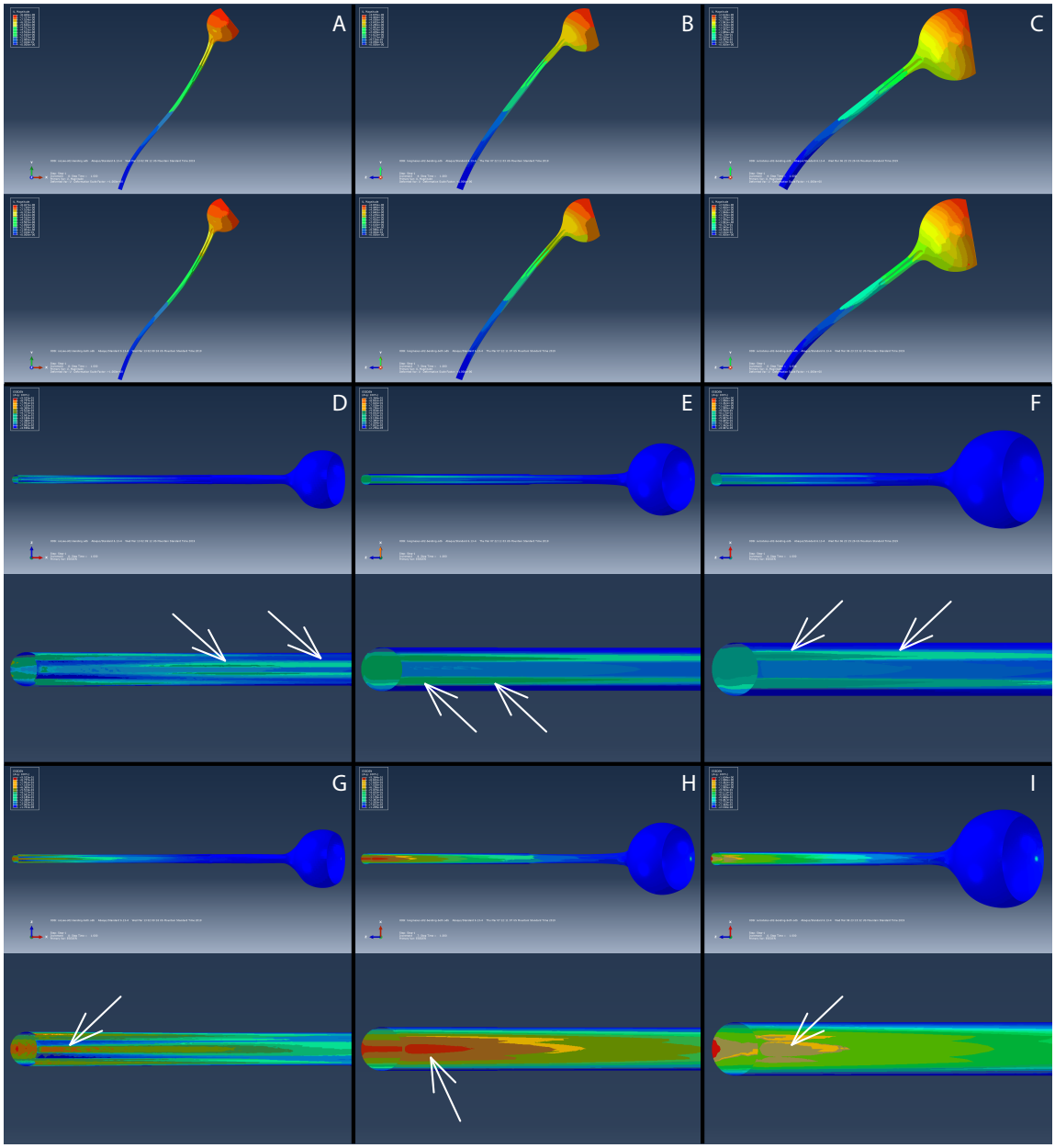


Figure 4.11: Effect of cuticle differentiation on rostral response to prescribed motion. The columns represent, from left to right, *C. caryae*, *C. longinsasus*, and *C. sulcatulus*. **A** – **C** show comparisons between models with lifelike cuticle profiles (top), and models lacking apical cuticle profile (bottom). Panels **D** – **F** strain energy density along ventral surface in models with realistic cuticle composite profiles. Panels **G** – **I** strain energy densities for models without apically modified cuticle. Color-coded scales for panels **D** – **I** normalized to response of unmodified cuticle models for each species. Arrows indicate location of occipital sulci (**D** – **F**) and greatest strain energy densities (**G** – **I**). Apical cuticle profile reduces strain energy density in ventral cuticle of lifelike models, greatest strain energy densities are found instead in occipital sulci.

We note however, that the values against which we compare the simulated stresses are averages for the entire cross-section of the rostrum in uniaxial tension, and the exact margin of safety likely differs somewhat [2] from the values reported here. Nonetheless, this finding aligns well with studies of other elongate cuticle structures in insects, such as grasshopper legs and beetle horns [34, 66, 67] (but see [23]), which appear to be stressed almost to their ultimate strength in regular use. In these models, the margin of safety ranged from 0.19-1.49 in tension, whereas the margin of safety in compression was significantly higher, ranging from 7.1-12.7. According to these models, the rostrum is far more likely to fail in tension than in compression. This result gives additional support to our hypothesis that the dominant failure mode of the rostrum is in tension, particularly in the exocuticle-rich occipital sulci.

Table 4.4: Margin of safety in simulated prescribed displacement of head capsule.

Species	Layup	σ_{ut} (MPa)	σ_{uc} (MPa)	$\bar{\sigma}_t$ (MPa)	$\bar{\sigma}_c$ (MPa)	FS_t	FS_c	MS_t	MS_c
	Apical	160.4	-481.1	64.53	-42.58	2.485	11.30	1.485	10.30
C. caryae	Basal	61.75	-185.3	91.51	-90.00	0.6748	2.058	-0.3252	1.058
	Apical	153.0	-459.1	77.15	-33.42	1.984	13.74	0.9838	12.74
C. longinasus	Basal	60.77	-182.3	101.9	-90.93	0.5964	2.005	-0.4036	1.005
	Apical	120.6	-361.7	101.2	-44.62	1.191	8.106	0.1913	7.106
C. sulcatulus	Basal	49.90	-149.7	129.3	-115.5	0.3859	1.296	-0.6141	0.2961

All variables correspond to model maxima. From left to right: [σ_{ut}] predicted ultimate tensile strain, [σ_{uc}] predicted ultimate compressive strain, [$\bar{\sigma}_t$] uniaxial membrane stress (tensile, element average), [$\bar{\sigma}_c$] uniaxial membrane stress (compressive, element average), [FS_t] tensile factor of safety, [FS_c] compressive factor of safety, [MS_t] tensile margin of safety, [MS_c] compressive margin of safety; see text for more information on cuticle definitions and variable definitions.

However, the data in Table 4.3.5 also show that removing the apical modifications to the cuticle composite profile reduces the predicted ultimate tensile and compressive

[2] Assuming iso-strain throughout the cuticle cross-section in uniaxial tension, any elastic strain would result in stresses higher than average in the exocuticle and lower than average in the endocuticle, simply because the exocuticle is stiffer. However, the exocuticle appears to fracture at a lower strain than the endocuticle, and the plastic behavior of both regions remains uncharacterized. For this reason it is not possible to estimate the ultimate strength of either endocuticle or exocuticle individually from our tensile testing data, necessitating comparison with the cross-sectional average. We do not believe this difficulty changes our conclusions based on the available data and congruence with other studies.

strengths of the rostrum. Critically, this reduction is accompanied by a sharp increase in the maximum estimated stresses in the models. We observed decreases in the ultimate tensile and compressive strengths of over 50%, with increases in the maximum observed tensile and compressive stresses up to 40% and over 100% (Fig. 4.12), respectively. Because of these shifts, the margin of safety in tension becomes negative for all models without apically modified cuticle; and the margin of safety in compression drops by approximately 90% (Fig. 4.12).

Without the apical composite profile, observed tensile stresses exceed the ultimate stress of the cuticle, implying that without the cuticle modifications seen in *Curculio*, any attempt to bend the snout would incur a strong risk of tensile structural failure. Considering that the maximum tensile and compressive strains do not greatly decrease with the addition of cuticle modifications, and that selective extension of the rostral apex appears to be a product of the displacement and geometry of the head, the flexibility of the rostral apex appears to function primarily as a means of mitigating strain energy accumulation and fracture. Our results point towards negative selection of fracture, rather than positive selection of flexibility *per se,* as the primary driving force behind the evolution of the modified apical profile of the rostral cuticle.

4.4 Conclusion

Finite element analysis of the *Curculio* rostrum has corroborated our hypothesis that the altered layer thicknesses and macrofiber orientation angles of the snout apex are sufficient to explain the observed elasticity and resilience of the rostrum during oviposition. Moreover, our models demonstrate that these modifications have a *synergistic* effect – rather than just an additive, linear one – on apical deflection and concomitant stresses and strains under an imposed apical load. This synergistic effect allows the modifications of the rostral cuticle to substantially mitigate the risk of

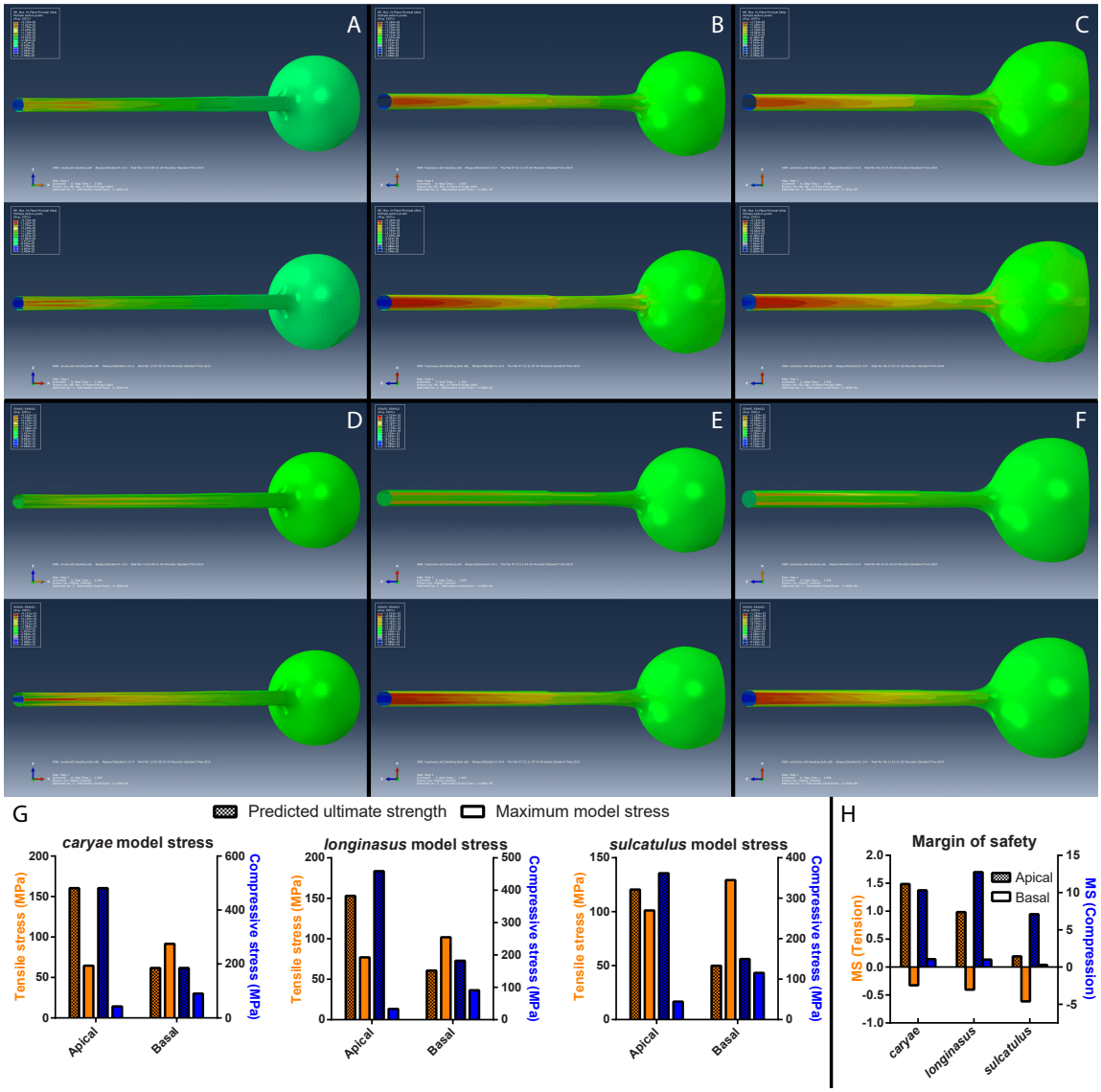


Figure 4.12: Maximum strain, stress, and margin of safety. Columns represent, from left to right, *C. caryae*, *C. longinsasus*, and *C. sulcatulus*. **A** – **C** compare maximum in-plane nominal strains between models with lifelike cuticle profiles (top), and models lacking apical cuticle profile (bottom). **D** – **F** compare maximum membrane stress (averaged though element) between models with lifelike cuticle profiles (top), and models lacking the apical cuticle profile (bottom). **G** Plots of predicted ultimate strengths and maximum model stresses in both tension and compression, for use in estimating rostral margin of safety (MS, shown in panel **H**). Color-coded scales in panels **A** – **F** are normalized to response of unmodified (bottom) cuticle models for each species. Apical cuticle profile reduces strain and stress across ventral cuticle of lifelike models, leaving unmodified occipital sulci with highest stresses. Unmodified models consistently exceeded predicted fracture strength of the rostrum, while lifelike models did not.

tensile fracture in dorso-apical flexion. Absent the apical cuticle composite profile, the estimated margin of safety in tension becomes negative, implying a risk of catastrophic structural failure as a result of rostral bending.

The greatest concentrations of stress and strain energy, as well as the lowest margin of safety, were found in the occipital sulci towards the apex of the snout. We conclude that these sulci constitute an important source of biomechanical constraint upon the evolution of rostral elasticity by creating an upper bound on maximum bending strain. Simulation of prescribed displacement of the head show that the load conditions and geometry of the head are sufficient to produce targeted extension of the rostrum, with similar tensile and compressive strains regardless of cuticle composite profile. The apical cuticle profile greatly reduces the maximum stresses and strain energy accumulated in the rostrum, thereby resulting in a higher margin of safety and reducing the risk of fracture. Our findings imply that the primary selective pressure influencing the evolution of the rostral cuticle in *Curculio* weevils was most likely the avoidance – or negative selection – of structural failure caused by bending of the rostrum.

ACKNOWLEDGMENTS

I am are grateful to Robert Anderson (CMNC), Lourdes Chamorro (USNM), and Charlie O'Brien (CWOB) for their assistance and provision of *Curculio* specimens used in this study. I also thank Salvatore Anzaldo, Andrew Johnston, Brian Reily, Sangmi Lee, and other Arizona State University Hasbrouck Insect Collection (ASUHIC) members for their assistance in procuring, treating, and maintaining specimen loans upon entry into the ASUHIC. I would also like to thank David Lowry (ASU CLAS Bioimaging Center) for his assistance with resin embedding, microscopy, and microtomography; and Salvatore Anzaldo for his assistance with histological staining.

CHAPTER 5

Rostral Curvature is Biomechanically Constrained in Female Acorn Weevils

ABSTRACT

The genus *Curculio* Linnaeus, 1758 is a morphologically diverse and evolutionarily successful lineage of weevils. Females use the rostrum, an elongation of the head, to excavate oviposition sites in a variety of host plant fruiting bodies. Diversity of form in this structure is considered a canonical example of adaptive radiation; however, the establishment of reliable metrics relevant to characterizing of rostral shape variation within *Curculio* has been lacking. We measured snout curvature using three measures from differential geometry: point curvature, total curvature, and bending strain energy. Using these measures and degree-8 polynomial representation of the rostral mid-line, we examined the relationship between the length and shape of the snout in both sexes across all 27 currently recognized species native to the United States. We explored whether snout curvature is evolutionarily constrained by the mechanobiology of female oviposition behavior, or simply a developmental by-product of selection for longer rostra. Maximum curvature and curve energy correlate with rostral arc-length, with increasingly concentrated apical curvature in longer rostra, exhibiting stronger signal in females than males. Total curvature was correlated with arc-length of the rostrum in males, but not females. We conclude that the sexual dimorphism in the relationship between snout length and curvature is indicative of biomechanical evolutionary constraint on the female rostrum.

5.1 Introduction

Weevils are among the most diverse and evolutionarily successful animal lineages on Earth [4]. Their success is driven in part by a structure called the rostrum, which gives weevil heads a characteristic "snout-like" appearance [4]. Acorn weevils in the genus *Curculio* Linnaeus, 1758 use the rostrum to excavate oviposition sites in developing fruits and nuts [5]. With over 300 species worldwide, the genus *Curculio* is exemplary as a widespread, morphologically diverse lineage of weevils [73, 102, 103]. Adult female *Curculio* individuals possess a highly elongate and curved rostrum that exhibits a striking degree of diversity (Figs. 5.1–5.2) and apparent evolutionary lability [5, 6, 12, 74]. During oviposition the snout is bent into a straightened configuration – in some species deformed over 90° in relation to the original shape – as part of a unique drilling behavior, but does not suffer any damage during this process [7–9]. By inserting eggs into a deep bore hole, the offspring are safeguarded from parasitism and predation. The hatched larva remains within the fruit, next to its food source and inside of the outer defensive tissues of the plant, until ready for pupation [4].

In light of these effective life history or developmental attributes, the exaggerated morphology of the rostrum in the genus *Curculio* is considered by some to be a canonical example of adaptive radiation [7, 13, 16]. Others have argued that allometry between body size and rostrum length can obscure the relationship between ecological pressures and phenotypic differentiation in this structure [6, 12, 73]. Comparisons of rostrum/body size allometry within and between species have produced conflicting accounts of whether rostral morphology is a response to selective pressure or merely a developmental byproduct of selection for larger body size [6, 7, 12]. The conflicting accounts or uncertainty implied by these studies highlighted two methodological

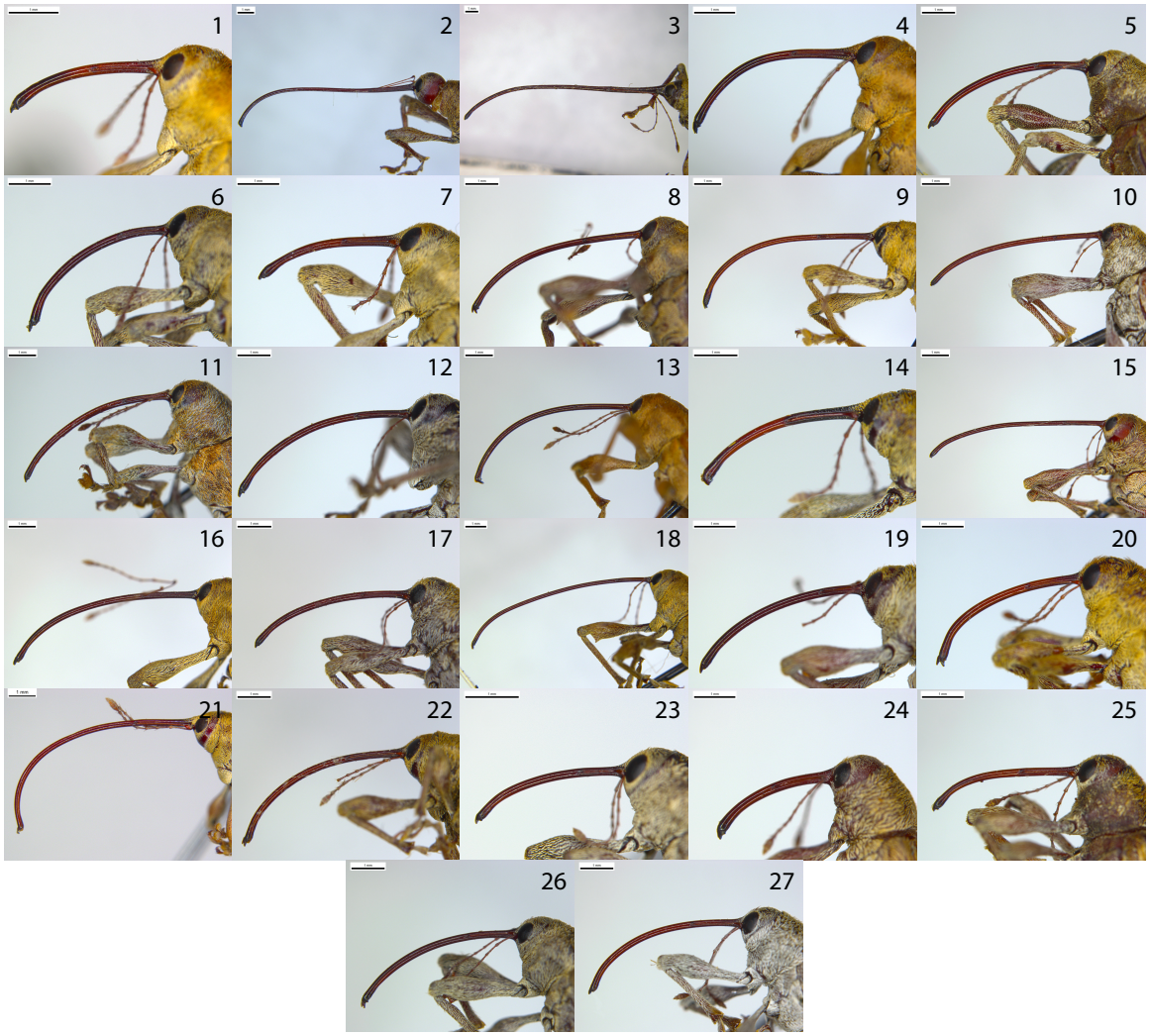


Figure 5.1: Female rostrum diversity in North American *Curculio* species. Montage of lateral habitus images of female specimens belonging to 27 *Curculio* species endemic to the United States. Magnification of each image is variable; scale bar in upper left of each image indicates a length of 1 mm. Images are arranged alphabetically by species name as recognized in [119], and indicated in upper right corner of each image. See Tab. 5.1 for corresponding species names.

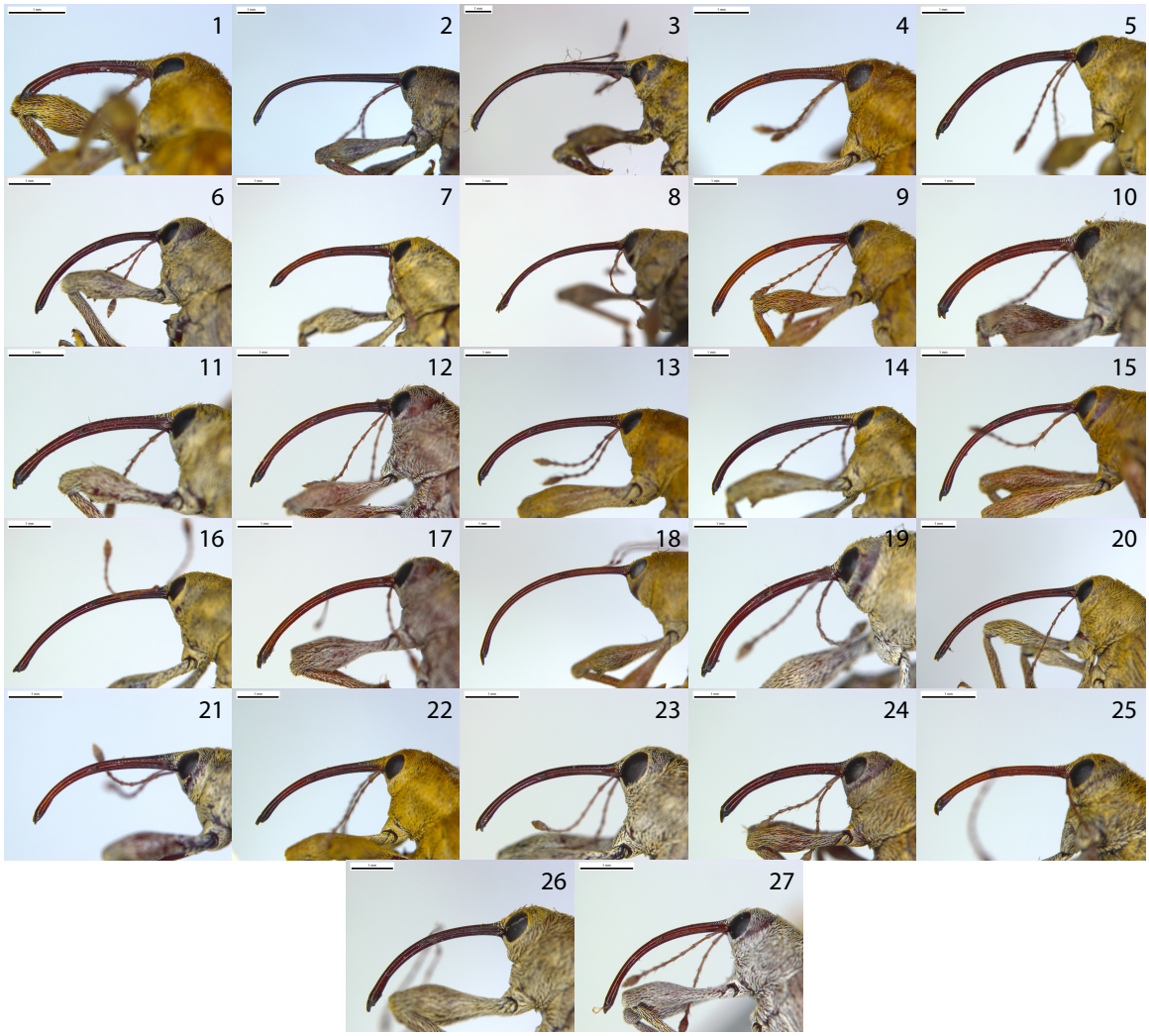


Figure 5.2: Male rostrum diversity in North American *Curculio* species. Montage of lateral habitus images of male specimens belonging to 27 *Curculio* species endemic to the United States. Magnification of each image is variable; scale bar in upper left of each image indicates a length of 1 mm. Images arranged alphabetically by species name, indicated in upper right corner of each image. See Tab. 5.1 for corresponding species names.

Table 5.1: *Curculio* species included in curvature analysis.

Panel №	Taxon name	(authorship)	♀	♂
1	*Curculio aurivestis*	Chittenden, 1927	3	1
2	*Curculio caryae*	(Horn, 1873)	2	2
3	*Curculio caryatrypes*	(Boheman, 1843)	1	1
4	*Curculio confusor*	(Hamilton, 1893)	2	2
5	*Curculio fulvus*	Chittenden, 1927	2	2
6	*Curculio humeralis*	(Casey, 1897)	2	2
7	*Curculio iowensis*	(Casey, 1910)	2	2
8	*Curculio longidens*	Chittenden, 1927	2	2
9	*Curculio longinasus*	Chittenden, 1927	2	2
10	*Curculio macrodon*	Chittenden, 1927	2	2
11	*Curculio monticola*	(Casey, 1897)	2	2
12	*Curculio nanulus*	(Casey, 1897)	2	2
13	*Curculio nasicus*	(Say, 1831)	2	2
14	*Curculio obtusus*	(Blanchard, 1884)	1	2
15	*Curculio orthorhynchus*	(Chittenden, 1908)	2	2
16	*Curculio pardalis*	(Chittenden, 1908)	2	2
17	Curculio pardus	Chittenden, 1927	1	1
18	*Curculio proboscideus*	Fabricius, 1775	2	2
19	*Curculio quercusgriseae*	(Chittenden, 1908)	2	2
20	*Curculio rubipililineus*	Gibson, 1969	1	3
21	*Curculio sayi*	(Gyllenhal, 1836)	3	2
22	*Curculio strictus*	(Casey, 1897)	2	2
23	*Curculio sulcatulus*	(Casey, 1897)	4	4
24	*Curculio timidus*	(Casey, 1910)	2	2
25	*Curculio uniformis*	(LeConte, 1857)	2	2
26	*Curculio victoriensis*	(Chittenden, 1904)	2	2
27	*Curculio wenzeli*	Chittenden, 1927	2	2

The 27 species included in this study are listed with author name and year of publication. All species correspond to valid names included in the O'Brien and Wibmer catalogue of the North American weevil fauna [119]. Species names are arranged alphabetically and indicate the corresponding panel numbers of Figs. 5.1-5.2. The number of female and male specimens sampled for this study is also given for each species.

difficulties in studying the putative adaptive response of rostral morphology. First, length is the only well-studied parameter of rostral morphology [6, 12]. Second, rostrum length cannot be satisfactorily decoupled from the influence of body size – without extensive study of population structure within each species [7, 13, 16]. To gain a more complete understanding of the evolution of the rostrum, rostral morphology must be represented with additional parameters that can be decoupled from rostral length while retaining information about shape [34, 120, 121].

Presently, the only shape parameter examined in *Curculio* is the average radius of curvature of the rostral apex. Variation in this trait has been interpreted to be a by-product of selection for large body size [12]. Here we challenge this prior finding, by defining and examining three separate measures of *Curculio* rostral curvature while correcting for body-size based on the *shape* of the curve defining the mid-line of the rostrum. To enable exact quantification of curvature variables, plane curve representations – i.e., degree-8 polynomial curves – were generated for the snouts of males and females of all 27 currently recognized *Curculio* species occurring in the United States. In particular, we evaluated: **(1)** *maximum* curvature, defined as the inverse of radius of curvature, and measured as the rate of change in tangent angle with respect to arc-length; **(2)** *total* curvature, defined as the angle traversed by a tangent line moving along the curve; and **(3)** curve *energy,* which is the functional of bending strain energy of an Euler-Bernoulli beam [122–125]. We also record the location of the point of maximum curvature and explore how the shape of the rostrum changes at increasing length scales.

Critically, we contextualize our results within the scope of rostral functionality as a source of constraint upon rostral shape [3]. The oviposition behavior of female *Curculio* weevils has never been considered as a primary selective driver of rostral morphology. Our results point to the presence of a biomechanical constraint upon

the female rostrum: the mandibles must be able to contact the host plant such that it is possible to initiate vertical drilling in the preparation of an oviposition site. As the length of the rostrum increases disproportionately – relative to the size of the body and the front legs which are used to pivot the head over the bore-hole – this becomes impossible *unless* the rostrum is *also* strongly curved. After correcting for body size, length-correlated changes in shape of the rostrum are aligned with this physical limitation. Therefore, rostrum shape in *Curculio* is evolutionarily constrained by the mechanobiology of the oviposition process.

5.2 Methods

5.2.1 Specimen Acquisition and Imaging

Specimens for use in tensile and fatigue testing came from the Hasbrouck Insect Collection at Arizona State University [ASUHIC]. This set of specimens was supplemented with material housed in the following collections, using the codens of Arnett et al. [72]:

CMNC Canadian Museum of Nature Collection, Ottawa, Ontario, Canada

USNM National Museum of Natural History, Washington, D.C., USA

Taxon sampling included all 27 *Curculio* species currently recognized to occur in the United States [5, 119]; see Tab.5.1 for a complete list of valid species names, with author and year information. Where available, two each of males and females were randomly selected from series of each species. A total of 110 specimens (55 ♀, 55 ♂) were selected and measured. Exceptions to this protocol – commensurate with limited specimen availability – were: *Curculio aurivestis* Chittenden, 1927 (3 ♀, 1 ♂); *Curculio caryatrypes* (Boheman, 1843) (1 ♀, 1 ♂); *Curculio obtusus* (Blanchard, 1884)

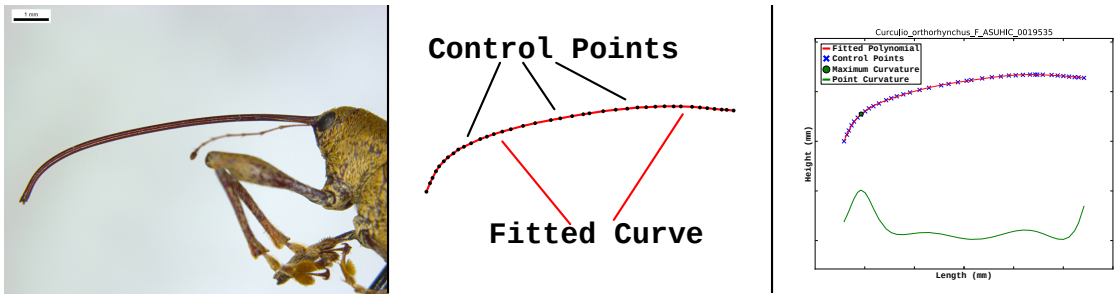


Figure 5.3: Generalized curve-fitting protocol. Left – Lateral habitus image of female *Curculio orthorhynchus* (Chittenden, 1908) rostrum; middle – control points from SVG file with fitted degree-8 polynomial; right – plot of fitted curve and overlaid control points, with point curvature (Y-axis) along length of curve (X-axis) and point of maximum curvature overlaid on curve.

(1 ♀, 2 ♂); *Curculio pardus* Chittenden, 1927 (1 ♀, 1 ♂); *Curculio rubipililineus* Gibson, 1969 (1 ♀, 3 ♂); *Curculio sayi* (Gyllenhal, 1836) (3 ♀, 2 ♂); and *Curculio sulcatulus* (Casey, 1897) (4 ♀, 4 ♂).

Light microscopy was conducted using a Leica M205 C stereomicroscope and attached computer running the software Leica Application Suite (LAS). Specimens were imaged in lateral view, with the base of the snout oriented horizontally. All extracted variables and fitted curves were based on pixel-wise measurements multiplied by a scaling factor for the image.

5.2.2 Assessment of Length and Curvature

Each image was imported into InkScape (www.inkscape.org), and annotated by hand with a series of control points in order to define a scalable vector graphic overlaying the mid-line of the rostrum up to the head capsule. Control point density along the length of the rostrum was determined on a specimen-by-specimen basis, using a sufficient number of points ($n \approx 15 - 20$) to describe the geometry of the curve. The SVG files were then batch-manipulated using a custom script in Python, version 3.5.2 [81]. Each file was scaled according to the pixel size defined in the XML meta-data files and the image scaling factor used in InkScape, thereby converting the SVG file to

actual size. A degree-8 polynomial curve ($f(x) = Ax^8 + Bx^7 + ... + Gx^2 + Hx + I$) was then fit to the points extracted from the SVG file, using the curve-fit function in SciPy [126]. The coefficients A–I of the polynomial function were initially stored as a list, then passed to poly-1d in NumPy [127] to generate a function object. The function was translated such that the apex of the rostrum was always on the left-hand side and located at the point (0.5,2). This point was chosen to avoid singularities during log-transformation of point-curvatures and coordinates at values of 0. Curves were visually inspected for fit and general shape by plotting both the polynomial function and maximum curvature graphs in the same plot (e.g., Fig. 5.3). All curves were judged to be of sufficient accuracy to proceed with variable extraction.

The extracted variables were drawn from relevant publications on smooth-curve interpolation and differential geometry; with a focus on metrics that are applicable to plane curves [122–125, 128, 129]. We identified curvature (κ, not signed, also known as point-curvature), total curvature (K), and bending energy (E), as the most directly applicable and easily interpreted measures of curvature. We define each here for reference and reproducibility, and further illustrate the definitions in Fig. 5.4. All variables were evaluated using function objects generated from the polynomial function, and corresponding to the quantity of interest, using the `'optimize'` and `'integrate'` packages in SciPy [126].

Arc-length (s) of a function along an interval $[a, b]$ is defined as:

$$s = \int_a^b \sqrt{1 + (f'(x))^2}\, ds\,. \tag{5.1}$$

Curvature is defined as the rate of change in the direction of the tangent vector of curve (θ), with respect to arc-length (s). It is therefore equal to the inverse of the radius of curvature of an osculating circle at that point ($r(s)$) [124, 128]. Point-curvature was evaluated across the fitted curves by solving for the derivative of each

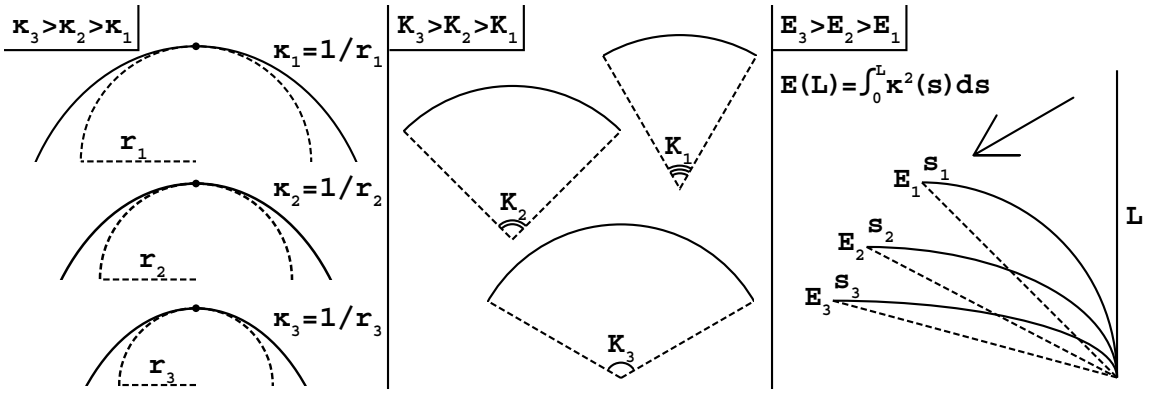


Figure 5.4: Interpretation of extracted curvature variables. Illustrations of curvature, total curvature, and curve energy, respectively, proceeding from left to right. `r` - radius of curvature, κ - curvature, `K` - total curvature, `L` - segment of arbitrary length, `s` - arc-length of segment L, `E` - curve energy.

polynomial function ($f(x)$) and adapting the above definition of curvature to the local Cartesian plane of the graph (using primes for derivatives):

$$\kappa = \frac{d\theta}{ds} = \frac{1}{r(s)} = \frac{|f''(x)|}{\left(\sqrt{1 + (f'(x))^2}\right)^3}\,. \tag{5.2}$$

Total curvature (K) is defined as the integral of curvature with respect to arc-length of a curve segment along an arbitrary interval $[a, b]$ [122, 129]. This is equivalent to the angle inscribed by a mapping of the curve to a unit circle (i.e., based on tangent (θ) or normal angles ϕ). Consequently, total curvature is independent of the length of a curve, and determined solely by its shape. Therefore, for a given curve segment with tangent angle extrema at its endpoints – i.e., with constant turning direction along its length, as in most *Curculio* rostra – the total curvature can be calculated simply as the difference between the normal angles at the endpoints. The normal angle, in turn, is evaluated as the arctangent of the derivative at the endpoints. For continuously increasing functions in the first quadrant of the Cartesian plane, this leads to the relation:

$$K = \int_a^b \kappa(s)\, ds = \phi_b - \phi_a \; = \arctan(f'(b)) - \arctan(f'(a))\,. \tag{5.3}$$

Via Euler-Bournoulli beam theory, the two-dimensional bending strain-energy (U) of a curve of length L is defined (see [124, 128]) for a homogeneous beam with Young's modulus of elasticity E as:

$$U = \frac{\mathrm{E}I}{2} \int_o^L \kappa(s)^2\, ds\,. \tag{5.4}$$

However, for a body in equilibrium, where $\delta U = 0$, bending energy is directly proportional to the functional, which is commonly defined as the 'curve energy', E:

$$E = \int_0^L \kappa(s)^2\, ds\,. \tag{5.5}$$

However, substituting Eq. 5.2, this becomes (see [123, 124, 128]):

$$E = \int_0^L \frac{(f''(x))^2}{\left(\sqrt{1 + (f'(x))^2}\right)^5}\, ds\,. \tag{5.6}$$

For all of these quantities, we calculated an initial, un-scaled ("absolute-scale") value, including the X and Y coordinates of the point of maximum curvature. The polynomial curves were then scaled to an arbitrary arc-length of 10 mm, and normalized values of these quantities were re-estimated, except for total curvature (K) which is size-independent.

5.2.3 Statistical Analysis

GLMM Fitting

In order to explore the relationships between the composite structure and mechanical properties of the cuticle, we fit generalized linear mixed-effects models (GLMM)

to the data using maximum likelihood estimation [77]. Raw data was processed using a custom script in Python, version 3.5.2 [81]. Model exploration and fitting was conducted in `R version 3.5.1 (2018-07-02) -- ''Feather Spray''`, using the `'nlme'` package [82, 83]. Response variables and covariates were natural-log transformed, as needed, to ensure that the normalized (conditioned) model residuals were normally distributed as indicated using numerical [`R:shapiro.test`] and graphical analysis [`R:qqplot`].

Although we included the species or taxonomic identity of each measured specimen as a random effect in all models, we did not account for the effect of phylogenetic relationships on the data for two reasons. First, a comprehensive phylogeny for the nearctic members of *Curculio* does not yet exist, making accurate assessment of phylogenetic signal difficult and possibly unreliable, even in a subset of species represented in a partial phylogeny. Second, according to Hughes and Vogler [12], the length and curvature of the *Curculio* rostrum are not strongly or significantly correlated with phylogenetic relationship or lineage membership. These parameters instead vary primarily as a function of the ecomorphological, selective pressures acting upon this structure [3, 12]. Because it was not deemed necessary to control for phylogenetic non-independence in the data, we did not allow phylogenetic correlation in the error term of the models (i.e., the variance-covariance matrix in the `'nlme'` package). However, males and females *were* modeled separately, due to strong sexual dimorphism in rostral morphology [5, 6, 12, 74].

Comparisons of model fit between transformed and un-transformed variables were based on likelihood score and residual variance; viz. $R^2_{\beta*}$ [`R:'r2glmm':r2beta`] (see Supplementary Data). $R^2_{\beta*}$ measures the multivariate association between the outcome and the fixed effects within a given correlation structure, and is generally used to compare fixed effects [88–90]. Once models were fitted to the data, T- and F-statistics

were calculated to determine whether each cofactor was significantly different from zero. Because seven independent comparisons were made for each sex (see below), we adjusted our criterion for statistical significance using a simple Bonferroni correction ($\alpha = 0.05/7 \approx 0.00714$).

Hypothesis Testing

Our objectives for hypothesis testing and rostral-shape characterization using the GLMMs were threefold: **(1)** to test whether the arc-length and curvature of the snout are correlated; **(2)** to asses the correspondence between rostral length and curvature *after* correcting for size differences; and **(3)** to examine whether the location of maximum curvature is stable across species.

To first test the relationship between absolute rostral arc-length and curvature, we fitted models that individually compare arc-length against the maximum curvature, total curvature, and bending energy of each specimen. We then examined the relationship between arc-length and curvature, using length-adjusted variables for curvature. Models were fitted with arc-length as the fixed effect, while adjusted maximum point-curvature and bending energy were used as response variables. Total curvature was not used because it is invariant with respect to scaling (see variable definition above), and is therefore not dependent on size. Finally, for the third aim we explored whether or not the point of maximum point-curvature has a stable location in the *Curculio* rostrum, in relative (size-adjusted) coordinates along increasing arc-length. We generated two models using the X and Y coordinates of the point of maximum curvature as response variables, with specimen length as the fixed effect in both.

5.3 Results

Our results (Figs. 5.5–5.6) show very clearly that the maximum curvature and curve energy of the rostrum are strongly influenced by arc-length. We observed that, in females, increasing rostrum length is associated with stronger, more abrupt, and apically concentrated curvature. In male *Curculio* individuals, total curvature increased with arc-length due to the generally rounder shape of the male rostrum. However, the total curvature of the female rostrum did not scale with increasing length, suggesting that there are aspects of the shape of the snout that are constrained either by ecomorphological selective pressures or by the mechanobiology of oviposition.

Below, first we summarize the statistical output of the herein generated models. We then discuss each individual comparison in the context of these general observations, and explore the possible implications of our findings with respect to the evolutionary trajectory of the morphology of the *Curculio* rostrum.

5.3.1 Model Fit and Variable Transformation

Degree-8 polynomial curves of best-fit were successfully overlaid on the control points for each specimen image. Visual inspection of the plotted curves did not reveal any unexpected deviation from the projected mid-line. All curves appeared smooth and continuously differentiable, with no discontinuities or disjoint behavior. Two female specimens of *Curculio sayi* had to be rotated slightly in order to fit a non-parametric curve to the control points. However, this did not impact the measurements of length or curvature, which are invariant with rotation of the curve. Even though their X and Y coordinates for the point of maximum curvature were skewed, this affected neither the outcome of the comparisons nor our conclusions. Scaling of the curves with respect to arc-length was successful to within a maximum rounding error of 0.0005%.

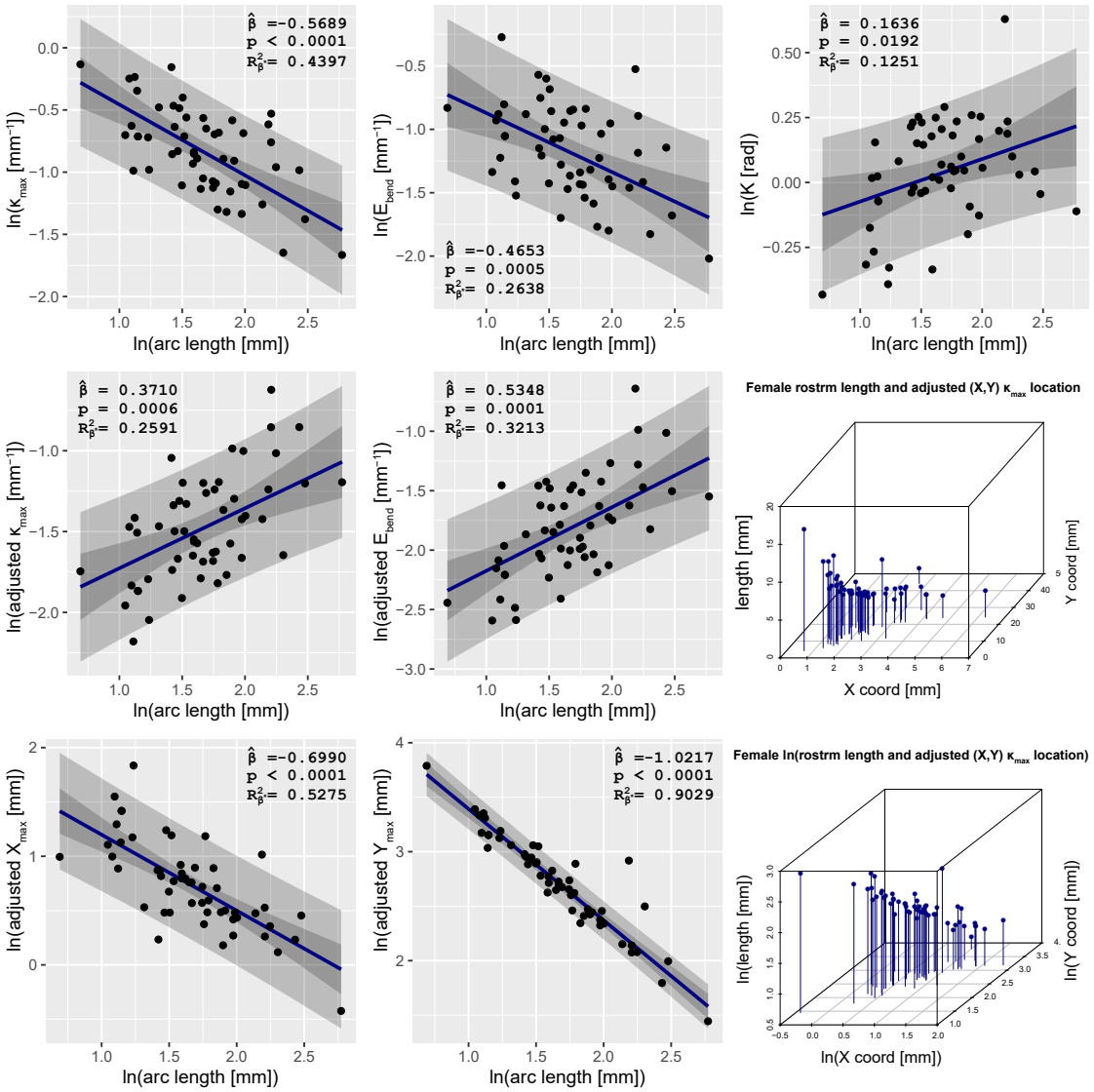


Figure 5.5: Relationships between arc-length and curvature in female *Curculio*. Each plot shows the relationship between the curvature response variable and arc-length predicted by the linear mixed-effect model, with species membership as random effect. Adjusted variables indicate values calculated after fixing arc-length. Gray regions represent the model's prediction intervals and bootstrapped 95% confidence intervals. The estimated fixed effect $\hat{\beta}$ is given, with p-value of t-test assessing whether $\hat{\beta}$ is significantly different from zero ($\alpha = 0.00714$). The generalized marginal $R^2_{\beta^*}$ for assessing fixed effects is added. 3D plots show relationships between raw X, Y coordinates of the point of maximum curvature and rostrum length. Overall, arc-length is significantly correlated with maximum curvature and curve energy; whereas the point of maximum curvature is located more towards the apex in longer rostra. In females, arc-length of the rostrum is *not* correlated with total curvature.

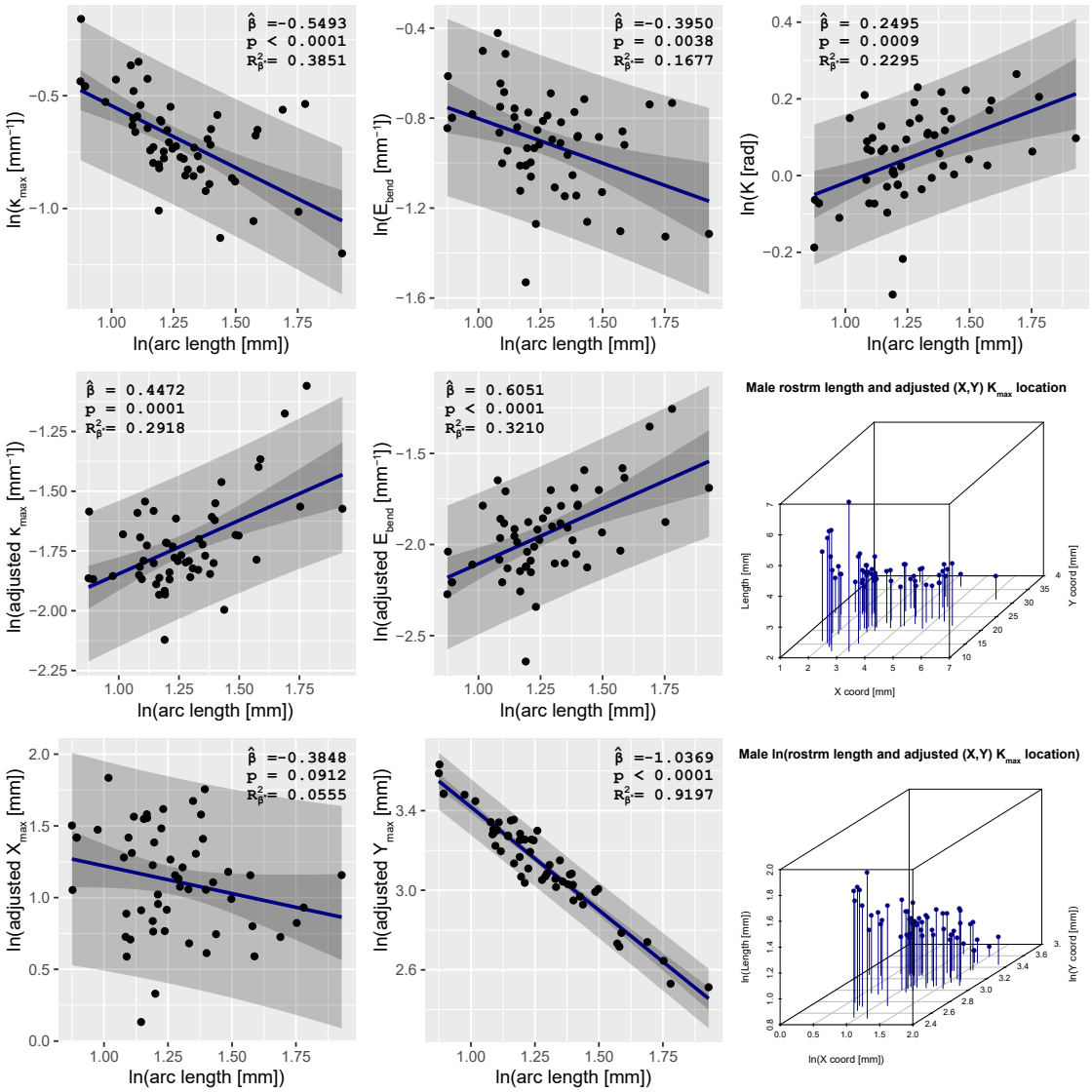


Figure 5.6: Relationships between arc-length and curvature in male *Curculio*. See legend of Fig. 5.5 for a general explanation of analysis, visualization, and model/test reporting conventions. Overall, arc-length is significantly correlated with maximum curvature and curve energy; whereas the point of maximum curvature is located more towards the apex along the Y-axis in longer rostra. In males, arc-length of the rostrum *is* correlated with total curvature.

Log-transformation of all variables resulted in normality as indicated by a Shapiro-Wilk test, with the exception of the Y coordinate model for the females and the total curvature model for the males. The former had two outliers – viz. the rotated specimens of *Curculio sayi* – that unduly influenced the results of the test. Removal of these data-points resulted in normality as indicated by a Shapiro-Wilk test, and by visual inspection of the quantile-quantile plot of the conditioned residuals. Nonetheless, including these data does not affect the general outcome of the model. We therefore considered that the departure from normality caused by these two points did not warrant their removal from the GLMM. The greater variance in the X coordinate masked this effect, and the respective data points did not affect the normality of the conditioned residuals for that model.

The conditioned residuals of the male total curvature model were *not* normally distributed as indicated by a Shapiro-Wilk test. Transformation of the response variable (total curvature) alone, and not the fixed effect (length), *did* result in normality of the residuals. The difference appears to have been caused by a pair of outliers.

We note that transforming both variables – and not just the response variable – did not change the outcome of the model. A significant relationship between arc-length and total curvature was obtained either way. We decided to report the outcome of the model based on the log-log transformed variables, for the following reasons: **(1)** to allow comparisons with the female specimens rostra; and **(2)** to account for, or manage, the higher log-likelihood score (19.85 vs. 18.00, $\chi^2 = 3.71, p < 0.0001$) and otherwise approximately normal distribution of the residuals (while ignoring outliers).

5.3.2 Models of Un-adjusted Curvature

A statistically significant negative correlation between rostrum arc-length and maximum curvature was recovered in the GLMMs of both females ($\hat{\beta} = -0.57, p <$

0.0001) and males ($\hat{\beta} = -0.55, p < 0.0001$). Similarly, a significant negative correlation between rostrum length and bending energy of the curves was noted for both sexes (females: $\hat{\beta} = -0.47, p = 0.0005$; males: $\hat{\beta} = -0.40, p = 0.0038$). These results are fully aligned with finite element models of three *Curculio* species with differentially sized and shaped rostra, wherein the greatest strain energy densities were observed in the shortest models, even though they exhibited a comparatively much straighter morphology (see Chapter 4).

The most likely explanation for this somewhat paradoxical result can be derived from Eqs. 5.1 and 5.6. In the functional definition of curve energy, the denominator can be reduced to $s^{2.5}$, while the numerator approximates (and is proportional to) κ^2. If the length and curvature of the snout are both scaled-up linearly by an arbitrary amount, and considering that the denominator has a greater exponent than the numerator, then the resultant quantity will decrease. Moreover, if a rostrum were augmented in size without changing its shape – i.e., by multiplying all coordinates by a scalar – then the denominator would increase. However, the numerator would decrease, causing a sharp decline in bending energy with increased arc length. Because κ is the inverse of the radius of curvature, a larger curve is actually less curved than a smaller curve of identical shape (e.g., Fig. 5.4). Correspondingly, the slope of the models is equal to the difference in the exponents of the numerator and denominator of Eqs. 5.2 and 5.6, for maximum curvature and curve energy, respectively.

5.3.3 Models of Length-Adjusted Curvature

In contrast to the un-scaled curvature measurements, we obtained statistically significant positive correlations between **(1)** maximum curvature and arc-length (females: $\hat{\beta} = 0.37, p = 0.0006$; males: $\hat{\beta} = 0.45, p = 0.0001$) and **(2)** curve energy and arc-length (females: $\hat{\beta} = 0.53, p = 0.0001$; males: $\hat{\beta} = 0.61, p < 0.0001$) for both sexes.

We therefore infer that the shape of the rostrum is in effect more strongly, and less evenly, curved in longer specimens. The apparent reversal of this trend after scaling rostral length highlights the significance of the inverse scaling relationship between these quantities for a given shape: increasing the size of a fixed shape decreases its curvature.

This simple, yet counter-intuitive, relationship between arc-length, curvature, and curve energy has confounded previous analyses. The mathematical linkage between these quantities obscures – or worse, reverses – trends in rostrum shape, unless a size correction is first applied to the data. As we have shown, applying such a correction results in the exact *opposite* outcome, and completely reverses the inferences drawn from the GLMMs. We must therefore reiterate the importance of correcting for length when comparing curved structures. In the case of the *Curculio* rostrum, prior analyses [12] recovered morphotypes that either **(1)** exhibited relatively even curvature across the rostrum, or **(2)** had an elongate basal region, with "a small curvature at the tip". These morphotypes patterns are generally in agreement with ours, as discussed below. Yet without considering the aforementioned effect of size on curvature, the authors [12] concluded that longer rostra are *straighter in shape* than shorter rostra. Our data directly contradict this finding, once the rostra are scaled to the same arc-length.

5.3.4 Sexual Dimorphism in Rostral Shape

Although the rostrum in both sexes is more strongly curved in shape with increased length, the manifestation of this extra curvature is sexually dimorphic. We found that the Y coordinate of the point of maximum curvature (Y_{max}) was negatively correlated with arc-length in both sexes (females: $\hat{\beta} = -1.02, p < 0.0001$; males: $\hat{\beta} = -1.04, p = 0.0001$). This indicates that the point of maximum curvature is located

further towards the rostral apex along the vertical axis in longer-snouted specimens. However, the X coordinate of the point of maximum curvature (X_{max}) was significantly negatively correlated with arc-length *only* in females (females: $\hat{\beta} = -0.70, p < 0.0001$; males: $\hat{\beta} = -0.38, p = 0.0912$).

The physical interpretation of this difference is clear once we consider the relationship between total curvature and rostrum length in males and females. In females, there is no significant association between total curvature and rostrum length (females: $\hat{\beta} = 0.16, p = 0.0192$). But there *is* such a correlation in the male rostra (males: $\hat{\beta} = 0.25, p = 0.0009$). Consequently, with increased snout size, the point of maximum curvature ($P_\kappa = (X_{max}, Y_{max})$) exhibits a different trajectory through morphospace for males than for females, with the female rostral curvature exhibiting a clearer signal in both the vertical and horizontal components. We conclude that for *Curculio* males, there is a physical tendency towards more circumferential increases in length with comparatively even curvature throughout. In contrast, in females of *Curculio* there is a tendency towards elongation of the base of the rostrum, with and exaggerated curvature towards the apex (see Fig. 5.7). This finding agrees well with the work of Hughes and Vogler [12], who similarly concluded that elongation of the rostral base occurred with increasing rostrum length in female *Curculio* species and/or specimens.

5.4 Discussion

Sexual dimorphism in the shape of the *Curculio* rostrum – specifically the arc-length – appears to be strongly influenced by functional constraints shaping the evolutionary history of this structure. We caution that these differences may be the result of a cluster of factors, such as sexual selection for longer, more curved rostra by the males. Nonetheless, biomechanical constraint as a primary driver of rostrum shape evolution remains our preferred hypothesis due to the critical significance of snout functionality

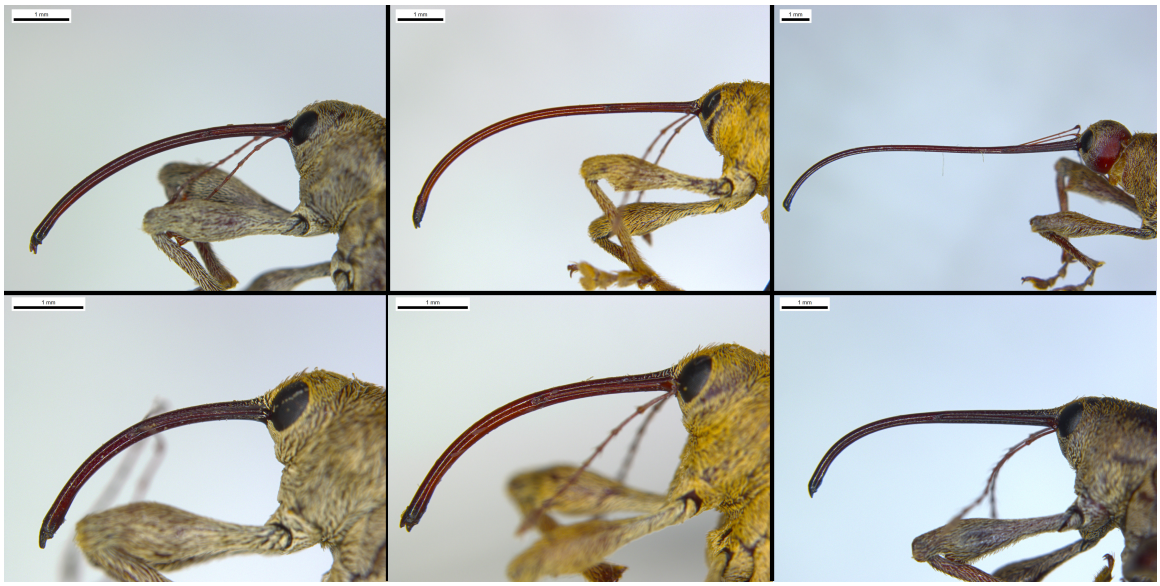


Figure 5.7: General effect of length on rostrum shape in *Curculio* weevils. Upper panel – females, lower panel – males; left – *Curculio victoriensis* (Chittenden, 1904), middle – *Curculio longinasus* Chittenden, 1927, right – *Curculio caryae* (Horn, 1873). The progression from left to right corresponds to increasing rostral arc-length. The curvature generally increases after correcting for size, and becomes more apically concentrated.

in the reproductive success of the females and apparent correspondence between host plant and rostral morphologies [7, 12, 13, 16]. In particular, the agreement between rostrum length and host plant defenses (such as pericarp thickness, spine length, and cap thickness), *independent of body size*, indicates that biomechanical constraints and need for deep placement of eggs are likely dominant over other factors [7, 13, 16]. Accordingly, because acorn weevil males do not need to engage in fruit tissue drilling and oviposition, the shape and size of the male rostrum are not subject to the same selective pressures as that of females. Female *Curculio* individuals, in turn, appear to have been selected to maximize the depth of drilling, i.e. rostrum length, thereby either bypassing plant defenses such as spines or pericarp layers, and/or to reducing the risk of parasitoid infestation of their eggs [4, 7, 10, 12, 13, 16]. Female rostrum length is known to scale allometrically with body size, leg length, and volume of the host plant nut or fruit [6, 7, 12, 13, 16, 74].

We hypothesize that disproportionate increases in female rostrum length and in relation to body size, are accompanied by changes in shape *not* as a simple by-product of selection for larger body size but because of selective constraint from two *biomechanical* factors. First, female *Curculio* individuals must be able to successfully initiate and complete an oviposition hole penetrating through the curved surface of a host plant fruit or nut while standing upon that convex surface. Second, the rostrum must be able to bend into a straightened configuration, while minimizing the risk of catastrophic structural failure. We envision two opposing scenarios – at different length scales – to illustrate how these constraints might impact the functional morphology of an abstracted rostrum model.

The first constraint, viz. accessing the surface of the host plant, is likely less forceful for smaller bodied, short-snouted *Curculio* females, which have relatively long forelegs in proportion to the length of the snout. Under this scenario, very little apical curvature is required to initiate vertical drilling into the fruit. The female is able to simply elevate the head using the forelegs, rotate the rostrum below the body, and begin excavation in a nearly vertical "angle of attack" configuration. A relatively small amount of rostral curvature would likely be required to overcome the difference in angle between the body, rostrum, and surface of the fruit, as determined by the relative lengths of the legs, snout, and curvature of the surface. The second constraint might then determine the distribution of this curvature across the structure, as follows. A relatively shallow, even curve would provide maximum mechanical advantage while minimizing the bending energy – and risk of fracture – of the excavation process. This is especially important in smaller *Curculio* species, where decreasing size at a constant shape yields increased bending energy, as discussed above.

In larger-bodied, long-snouted *Curculio* species, however, the constraint imposed by the need to initiate vertical drilling into the fruit would necessitate strong apical

curvature, proportionate to rostral arc-length. This trend is supported by our data. In particular, the female must be able to elevate and rotate the head in such a way that the alignment of rostral apex with the surface is suitable to initiate strictly vertical excavation of the bore-hole. A straight rostrum that is longer than the forelegs could not possibly be inserted vertically into a fruit, but could only attain a shallow intersection angle with the surface. This consideration has led us to hypothesize that the total curvature, which does *not* correlate significantly with female rostrum length, is determined by the average upper bound of this insertion angle. Rather than correlating simply with length, total curvature might change as a function of the proportions of **(1)** the legs (i.e., height or clearance), **(2)** maximally possible body and head angles in drilling stance, and **(3)** surface curvature of the host plant.

By contrast, the maximum curvature and curve energy of the rostrum increase with rostrum length, thus becoming concentrated in the apical portion of the rostrum and creating a "hooked" appearance in the female. Although bending energy decreases as a function of length, an apically hooked rostrum is characterized by greater bending strain energy than a comparatively straight rostrum of equal size. We speculate that with increasing length, there is a trade-off between bending energy and ease of surface access that constrains the shape of the curve. There must be sufficient curvature – in the functionally indicated region of the rostrum – to enable vertical surface access, yet without disproportionately (and non-adaptively) increasing the bending energy and risk of fracture. In the female, this could explain why longer rostra are curved *apically*, yet with a similar total curvature across a wide (phylogenetic) range of *Curculio* species, where the latter (i.e., the total curvature) reflects the amount of curvature needed in the focal rostral subregion to initiate bore-hole drilling.

Because male *Curculio* individuals are not subject to the constraint of vertical drilling, it is not surprising that **(1)** total curvature scales simply with arc-length, and

(2) males do not exhibit concentrated apical curvature to the same extent as females at longer length scales. We posit that the exact shape of the female rostrum is determined not only by arc-length, but also by the end-tangent angles (i.e., total curvature) and chord angle of the rostrum, as constrained by the height of the animal and the need for vertical drilling with minimal risk of rostral fracture. An exact representation of the rostrum has not been investigated, but we note that given these parameters, minimization of bending strain energy would lead to a curve that approximates the form of a nonlinear (i.e., "minimum-energy") spline [123, 124].

The various morphotypes of the *Curculio* rostrum (Figs. 5.1–5.2) could be thus considered permutations of a spline family, but constrained by a set of boundary conditions imposed by ecomorphological and biomechanical selective pressures [3]. The repeated convergence in rostral shape among phylogenetically disparate terminals, and within a family of curves, could then be considered a "deep homology" in the evolution of the rostrum, rather than a by-product of allometric scaling with body size [130, 131]. Future research efforts should aim to characterize families of curves that best delineate rostral shape and explain the associations between arc-length and curvature observed in our study.

In summary, we conclude that shape of the acorn weevil rostrum is *not* strictly dependent on allometric scaling with arc-length. Nor is rostral curvature a simple evolutionary by-product of selection for larger body size. Rather, the evolutionary radiation of the *Curculio* rostrum appears to have been driven by a complex and optimization response to biomechanical and ecomorphological constraints.

ACKNOWLEDGMENTS

I am grateful to Robert Anderson (CMNC), Lourdes Chamorro (USNM), and Charles O'Brien (ASUCOB) for their assistance and provision of *Curculio* specimens used in

this study. I also thank Salvatore Anzaldo, Andrew Johnston, Brian Reilly, Sangmi Lee, and other Arizona State University Hasbrouck Insect Collection (ASUHIC) members for their assistance in procuring, treating, and maintaining specimen loans upon entry into the ASUHIC.

REFERENCES

[1] C. Darwin, *On the origin of species by means of natural selection: or the preservation of favored races in the struggle for life*, vol. 2. London: J. Murray, 1859.

[2] S. J. Gould, *The structure of evolutionary theory*. Harvard University Press, 2002.

[3] G. K. Taylor and A. L. R. Thomas, *Evolutionary biomechanics: selection, phylogeny, and constraint*. Oxford University Press (UK), 2014.

[4] R. Oberprieler, R. Anderson, and A. Marvaldi, "Curculionoidea Latreille, 1802: Introduction, Phylogeny.," in *Handbook of Zoology Arthropoda Insecta Coleoptera Vol. 3 Morphology and Systematics* (R. Leschen and R. Beutel, eds.), ch. 3, pp. 503–522, Berlin: De Gruyter, 2014.

[5] L. P. Gibson, "Monograph of the genus *Curculio* in the New World (Coleoptera: Curculionidae). Part I. United States and Canada.," *Miscellaneous Publications of the Entomological Society of America*, vol. 6, no. 5, pp. 239–285, 1969.

[6] R. Bonal, J. M. Espelta, and A. P. Vogler, "Complex selection on life-history traits and the maintenance of variation in exaggerated rostrum length in acorn weevils," *Oecologia*, vol. 167, no. 4, pp. 1053–1061, 2011.

[7] H. Toju and T. Sota, "Imbalance of predator and prey armament: geographic clines in phenotypic interface and natural selection," *The American Naturalist*, vol. 167, no. 1, pp. 105–117, 2006.

[8] M. A. Jansen, S. S. Singh, N. Chawla, and N. M. Franz, "A multilayer micromechanical model of the cuticle of *Curculio longinasus* chittenden, 1927 (coleoptera: Curculionidae)," *Journal of Structural Biology*, vol. 195, no. 2, pp. 139–158, 2016.

[9] S. S. Singh, M. A. Jansen, N. M. Franz, and N. Chawla, "Microstructure and nanoindentation of the rostrum of curculio longinasus chittenden, 1927 (coleoptera: Curculionidae)," *Materials Characterization*, vol. 118, pp. 206–211, 2016.

[10] L. A. Aguirre Uribe, *Biology of the immature stages of the pecan weevil Curculio caryae (Horn) and oviposition habits of the adult weevil*. PhD thesis, Texas A & M University, 1978.

[11] K. Morimoto and H. Kojima, "Morphologic characters of the weevil head and phylogenetic implications (Coleoptera, Curculionoidea)," *Esakia*, vol. 43, pp. 133–169, 2003.

[12] J. Hughes and A. P. Vogler, "Ecomorphological adaptation of acorn weevils to their oviposition site," *Evolution*, vol. 58, no. 9, pp. 1971–1983, 2004.

[13] H. Toju, "Fine-scale local adaptation of weevil mouthpart length and camellia pericarp thickness: altitudinal gradient of a putative arms race.," *Evolution*, vol. 62, no. 5, pp. 1086–1102, 2008.

[14] P. C. Ting, "The mouth parts of the coleopterous group Rhynchophora," *Microentomology*, vol. 1, pp. 93–114, 1936.

[15] P. C. Ting, "Feeding mechanisms of weevils, their function, and relationship to classification," *Monthly Bulletin of the Department of Agriculture of the State of California*, vol. 22, pp. 161–165, 1933.

[16] H. Toju and T. Sota, "Adaptive divergence of scaling relationships mediates the arms race between a weevil and its host plant," *Biology Letters*, vol. 2, no. 4, pp. 539–542, 2006.

[17] M. Moffett, "Life in a Nutshell," *National Geographic Magazine*, vol. 176, pp. 783–784, June 1989.

[18] E. Dumont, I. R. Grosse, and G. J. Slater, "Requirements for comparing the performance of finite element models of biological structures," *Journal of Theoretical Biology*, vol. 256, no. 1, pp. 96–103, 2009.

[19] S. Nikolov, H. Fabritius, M. Petrov, M. Friák, L. Lymperakis, C. Sachs, D. Raabe, and J. Neugebauer, "Robustness and optimal use of design principles of arthropod exoskeletons studied by ab initio-based multiscale simulations," *Journal of the Mechanical Behavior of Biomedical Materials*, vol. 4, no. 2, pp. 129–145, 2011.

[20] S. Nikolov, M. Petrov, L. Lymperakis, M. Friák, C. Sachs, H.-O. Fabritius, D. Raabe, and J. Neugebauer, "Revealing the design principles of high-performance biological composites using ab initio and multiscale simulations: the example of lobster cuticle," *Advanced Materials*, vol. 22, no. 4, pp. 519–526, 2010.

[21] D. Klocke and H. Schmitz, "Water as a major modulator of the mechanical properties of insect cuticle," *Acta Biomaterialia*, vol. 7, no. 7, pp. 2935–2942, 2011.

[22] J. F. V. Vincent, *Structural Biomaterials*. New York: Halsted Press, 1982.

[23] J. F. Vincent and U. G. Wegst, "Design and mechanical properties of insect cuticle," *Arthropod Structure and Development*, vol. 33, no. 3, pp. 187–199, 2004.

[24] J. Blackwell and M. Weih, "Structure of chitin-protein complexes: ovipositor of the ichneumon fly *Megarhyssa*," *Journal of Molecular Biology*, vol. 137, no. 1, pp. 49–60, 1980.

[25] Y. Bouligand, "Twisted fibrous arrangements in biological materials and cholesteric mesophases," *Tissue and Cell*, vol. 4, no. 2, pp. 189–217, 1972.

[26] A. C. Neville, D. A. Parry, and J. Woodhead-Galloway, "The chitin crystallite in arthropod cuticle.," *Journal of Cell Science*, vol. 21, no. 1, pp. 73–82, 1976.

[27] L. Cheng, L. Wang, and A. M. Karlsson, "Mechanics-based analysis of selected features of the exoskeletal microstructure of *Popillia japonica*," *Journal of Materials Research*, vol. 24, no. 11, pp. 3253–3267, 2009.

[28] H. Hepburn and A. Ball, "On the structure and mechanical properties of beetle shells," *Journal of Materials Science*, vol. 8, no. 5, pp. 618–623, 1973.

[29] T. van de Kamp and H. Greven, "On the architecture of beetle elytra," *Entomologie Heute*, vol. 22, pp. 191–204, 2010.

[30] T. van de Kamp, A. Riedel, and H. Greven, "Micromorphology of the elytral cuticle of beetles, with an emphasis on weevils (coleoptera: Curculionoidea)," *Arthropod Structure and Development*, vol. 45, no. 1, pp. 14–22, 2016.

[31] W. C. Flannigan, "Finite element modeling of arthropod exoskeleton," Master's thesis, Case Western Reserve University, 1998.

[32] R. Herbert, P. Young, C. Smith, R. Wootton, and K. Evans, "The hind wing of the desert locust (*Schistocerca gregaria* forskal). iii. a finite element analysis of a deployable structure," *Journal of Experimental Biology*, vol. 203, no. 19, pp. 2945–2955, 2000.

[33] T. Hörnschemeyer, J. Bond, P. G. Young, and A. Deans, "Analysis of the functional morphology of mouthparts of the beetle *Priacma serrata*, and a discussion of possible food sources," *Journal of Insect Science*, vol. 13, no. 1, 2013.

[34] E. L. McCullough, B. W. Tobalske, and D. J. Emlen, "Structural adaptations to diverse fighting styles in sexually selected weapons," *Proceedings of the National Academy of Sciences*, vol. 111, no. 40, pp. 14484–14488, 2014.

[35] D. Raabe, C. Sachs, and P. Romano, "The crustacean exoskeleton as an example of a structurally and mechanically graded biological nanocomposite material," *Acta Materialia*, vol. 53, no. 15, pp. 4281–4292, 2005.

[36] I. Doghri, *Mechanics of deformable solids: linear, nonlinear, analytical, and computational aspects*. New York; Berlin: Springer, 2000.

[37] T. Mura, *Micromechanics of defects in solids*, vol. 3. Dordrecht; Higham, MA; Boston: M. Nijhoff, 1987.

[38] J. N. Reddy, *Mechanics of laminated composite plates and shells: theory and analysis*. CRC press, 2004.

[39] R. Hill, "The Elastic Behaviour of a Crystalline Aggregate," *Proc. Phys. Soc. Sect. A*, vol. 65, no. 5, pp. 349–354, 1952.

[40] T. Mori and K. Tanaka, "Average stress in matrix and average elastic energy of materials with misfitting inclusions," *Acta Metallurgica*, vol. 21, no. 5, pp. 571–574, 1973.

[41] V. a. Buryachenko, V. I. Kushch, V. a. Dudka, and A. Roy, "Effective stiffness of composites reinforced by cylindrical fibers with smooth ends, with potential application to nanocomposites," *Acta Mechanica*, vol. 198, no. 3-4, pp. 129–146, 2008.

[42] Y. Benveniste, "A new approach to the application of Mori-Tanaka's theory in composite materials," *Mechanics of Materials*, vol. 6, no. 2, pp. 147–157, 1987.

[43] M. Kachanov, "Solids with cracks and non-spherical pores : proper parameters of defect density and effective elastic properties," *International Journal of Fracture*, vol. 97, pp. 1–32, 1999.

[44] I. Sevostianov and M. Kachanov, "Explicit cross-property correlations for anisotropic two-phase composite materials," *Journal of the Mechanics and Physics of Solids*, vol. 50, no. 2, pp. 253–282, 2002.

[45] I. Sevostianov, V. Levin, and M. Kachanov, "On the modeling and design of piezocomposites with prescribed properties," *Archive of Applied Mechanics (Ingenieur Archiv)*, vol. 71, no. 11, pp. 733–747, 2001.

[46] I. Sevostianov, N. Yilmaz, V. Kushch, and V. Levin, "Effective elastic properties of matrix composites with transversely-isotropic phases," *International Journal of Solids and Structures*, vol. 42, no. 2, pp. 455–476, 2005.

[47] I. Sevostianov, "On the shape of effective inclusion in the Maxwell homogenization scheme for anisotropic elastic composites," *Mechanics of Materials*, vol. 75, pp. 45–59, 2014.

[48] I. Sevostianov, V. Levin, and E. Radi, "Effective properties of linear viscoelastic microcracked materials: Application of Maxwell homogenization scheme," *Mechanics of Materials*, vol. 84, pp. 28–43, 2015.

[49] F. Saadat, I. Sevostianov, and A. Giraud, "Approximate representation of a compliance contribution tensor for a cylindrical inhomogeneity normal to the axis of symmetry of a transversely isotropic material," *International Journal of Fracture*, vol. 174, no. 2, pp. 237–244, 2012.

[50] I. Sevostianov and M. Kachanov, "On approximate symmetries of the elastic properties and elliptic orthotropy," *International Journal of Engineering Science*, vol. 46, no. 3, pp. 211–223, 2008.

[51] I. Sevostianov and A. Giraud, "Generalization of Maxwell homogenization scheme for elastic material containing inhomogeneities of diverse shape," *International Journal of Engineering Science*, vol. 64, pp. 23–36, 2013.

[52] E. Vilchevskaya and I. Sevostianov, "Effective elastic properties of a particulate composite with transversely-isotropic matrix," *International Journal of Engineering Science*, vol. 94, pp. 139–149, 2015.

[53] M. M. Giraud-Guille, H. Chanzy, and R. Vuong, "Chitin crystals in arthropod cuticles revealed by diffraction contrast transmission electron microscopy," *Journal of Structural Biology*, vol. 103, no. 3, pp. 232–240, 1990.

[54] P. Y. Chen, A. Y. M. Lin, J. McKittrick, and M. A. Meyers, "Structure and mechanical properties of crab exoskeletons," *Acta Biomaterialia*, vol. 4, no. 3, pp. 587–596, 2008.

[55] L. Cheng, L. Wang, and A. M. Karlsson, "Image analyses of two crustacean exoskeletons and implications of the exoskeletal microstructure on the mechanical behavior," *Journal of Materials Research*, vol. 23, no. 11, pp. 2854–2872, 2008.

[56] M. Kaya, E. Lelesius, R. Nagrockaite, I. Sargin, G. Arslan, A. Mol, T. Baran, E. Can, and B. Bitim, "Differentiations of Chitin Content and Surface Morphologies of Chitins Extracted from Male and Female Grasshopper Species," *PLoS One*, vol. 10, no. 1, p. e0115531, 2015.

[57] S. Hyun and S. Torquato, "Effective elastic and transport properties of regular honeycombs for all densities," *Journal of Materials Research*, vol. 15, no. 09, pp. 1985–1993, 2000.

[58] R. F. Ker, *Some structural and mechanical properties of locust and beetle cuticle.* PhD thesis, University of Oxford, 1977.

[59] R. A. Leopold, S. M. Newman, and G. Helgeson, "A comparison of cuticle deposition during the pre- and posteclosion stages of the adult weevil, *Anthonomus grandis* Boheman (Coleoptera : Curculionidae)," 1992.

[60] S. R. Davis, *Morphology, phylogeny, and evolutionary development in the weevils (Insecta: Coleoptera: Curculionoidea).* PhD thesis, University of Kansas, 2014.

[61] M. E. McNamara, D. E. G. Briggs, P. J. Orr, H. Noh, and H. Cao, "The original colours of fossil beetles," *Proceedings of the Royal Society B: Biological Sciences*, vol. 279, no. 1731, pp. 1114–1121, 2012.

[62] M. Kachanov and I. Sevostianov, "On quantitative characterization of microstructures and effective properties," *International Journal of Solids and Structures*, vol. 42, no. 2, pp. 309–336, 2005.

[63] C. Sachs, H. Fabritius, and D. Raabe, "Influence of microstructure on deformation anisotropy of mineralized cuticle from the lobster *Homarus americanus*," *Journal of Structural Biology*, vol. 161, no. 2, pp. 120–132, 2008.

[64] S. Amini, M. Tadayon, S. Idapalapati, and A. Miserez, "The role of quasi-plasticity in the extreme contact damage tolerance of the stomatopod dactyl club," *Nature Materials*, vol. 14, no. 9, p. 943, 2015.

[65] E. L. McCullough, "Mechanical limits to maximum weapon size in a giant rhinoceros beetle," *Proceedings of the Royal Society B: Biological Sciences*, vol. 281, no. 1786, p. 20140696, 2014.

[66] J.-H. Dirks and D. Taylor, "Fracture toughness of locust cuticle," *Journal of Experimental Biology*, vol. 215, no. 9, pp. 1502–1508, 2012.

[67] J.-H. Dirks, E. Parle, and D. Taylor, "Fatigue of insect cuticle," *Journal of Experimental Biology*, vol. 216, no. 10, pp. 1924–1927, 2013.

[68] C. J. Ferraris Jr and W. N. Eschmeyer, "International code of zoological nomenclature," 2000.

[69] R. Dennell, "The structure and function of the mouth-parts, rostrum and foregut of the weevil *Calandra granaria* l," *Philosophical Transactions of the Royal Society of London. Series B, Biological Sciences*, vol. 231, no. 581, pp. 247–291, 1942.

[70] L. Li, C. Guo, X. Li, S. Xu, and C. Han, "Microstructure and mechanical properties of rostrum in *Cyrtotrachelus longimanus* (coleoptera: Curculionidae)," *Animal Cells and Systems*, vol. 21, no. 3, pp. 199–206, 2017.

[71] Y. Matsumura, A. E. Kovalev, and S. N. Gorb, "Penetration mechanics of a beetle intromittent organ with bending stiffness gradient and a soft tip," *Science Advances*, vol. 3, no. 12, p. eaao5469, 2017.

[72] R. H. Arnett Jr., G. A. Samuelson, and G. M. Nishida, *The insect and spider collections of the world*. Gainesville, Florida: Sandhill Crane Press, Inc., 2 ed., 1993.

[73] J. Hughes and A. P. Vogler, "The phylogeny of acorn weevils (genus *Curculio*) from mitochondrial and nuclear DNA sequences: The problem of incomplete data," *Molecular Phylogenetics and Evolution*, vol. 32, no. 2, pp. 601–615, 2004.

[74] R. Bonal, J. M. Espelta, A. Munoz, J. Ortego, J. M. Aparicio, K. Gaddis, and V. L. Sork, "Diversity in insect seed parasite guilds at large geographical scale: the roles of host specificity and spatial distance," *Journal of Biogeography*, vol. 43, no. 8, pp. 1620–1630, 2016.

[75] R. M. Jones, *Mechanics of composite materials*. CRC press, 2014.

[76] MathWorks, "Matlab and statistics toolbox," 2018. Natick, Mass., Release R2018b.

[77] A. Gałecki and T. Burzykowski, *Linear mixed-effects models using R: A step-by-step approach*. Springer Science & Business Media, 2013.

[78] J. Hadfield and S. Nakagawa, "General quantitative genetic methods for comparative biology: phylogenies, taxonomies and multi-trait models for continuous and categorical characters," *Journal of Evolutionary Biology*, vol. 23, no. 3, pp. 494–508, 2010.

[79] E. A. Housworth, E. P. Martins, and M. Lynch, "The phylogenetic mixed model," *The American Naturalist*, vol. 163, no. 1, pp. 84–96, 2004.

[80] G. N. Stone, S. Nee, and J. Felsenstein, "Controlling for non-independence in comparative analysis of patterns across populations within species," *Philosophical Transactions of the Royal Society B: Biological Sciences*, vol. 366, no. 1569, pp. 1410–1424, 2011.

[81] P. C. Team, "Python: A dynamic, open source programming language," 2018. Python Software Foundation, Version 3.5.2.

[82] R Core Team, *R: A Language and Environment for Statistical Computing*. R Foundation for Statistical Computing, Vienna, Austria, 2014.

[83] J. Pinheiro, D. Bates, S. DebRoy, D. Sarkar, and R Core Team, *nlme: Linear and Nonlinear Mixed Effects Models*, 2018. R package version 3.1-137.

[84] E. Paradis and K. Schliep, "ape 5.0: an environment for modern phylogenetics and evolutionary analyses in R," *Bioinformatics*, vol. 35, pp. 526–528, 2018.

[85] T. Münkemüller, S. Lavergne, B. Bzeznik, S. Dray, T. Jombart, K. Schiffers, and W. Thuiller, "How to measure and test phylogenetic signal," *Methods in Ecology and Evolution*, vol. 3, no. 4, pp. 743–756, 2012.

[86] R. Molina-Venegas and M. Á. Rodríguez, "Revisiting phylogenetic signal; strong or negligible impacts of polytomies and branch length information?," *BMC Evolutionary Biology*, vol. 17, no. 1, p. 53, 2017.

[87] E. A. Stone, "Why the phylogenetic regression appears robust to tree misspecification," *Systematic Biology*, vol. 60, no. 3, pp. 245–260, 2011.

[88] S. Nakagawa and H. Schielzeth, "A general and simple method for obtaining r2 from generalized linear mixed-effects models," *Methods in Ecology and Evolution*, vol. 4, no. 2, pp. 133–142, 2013.

[89] B. C. Jaeger, L. J. Edwards, K. Das, and P. K. Sen, "An r 2 statistic for fixed effects in the generalized linear mixed model," *Journal of Applied Statistics*, vol. 44, no. 6, pp. 1086–1105, 2017.

[90] B. Jaeger, *nlme: Linear and Nonlinear Mixed Effects Models*, 2017. R package version 0.1.2.

[91] L. J. Revell, "phytools: An r package for phylogenetic comparative biology (and other things).," *Methods in Ecology and Evolution*, vol. 3, pp. 217–223, 2012.

[92] A. Zeileis and T. Hothorn, "Diagnostic checking in regression relationships," *R News*, vol. 2, no. 3, pp. 7–10, 2002.

[93] L. A. Mihai and A. Goriely, "How to characterize a nonlinear elastic material? a review on nonlinear constitutive parameters in isotropic finite elasticity," *Proceedings of the Royal Society A: Mathematical, Physical and Engineering Sciences*, vol. 473, no. 2207, p. 20170607, 2017.

[94] S. Münster, L. M. Jawerth, B. A. Leslie, J. I. Weitz, B. Fabry, and D. A. Weitz, "Strain history dependence of the nonlinear stress response of fibrin and collagen networks," *Proceedings of the National Academy of Sciences*, vol. 110, no. 30, pp. 12197–12202, 2013.

[95] L. J. Revell, "Phylogenetic signal and linear regression on species data," *Methods in Ecology and Evolution*, vol. 1, no. 4, pp. 319–329, 2010.

[96] J. Felsenstein, "Phylogenies and the comparative method," *The American Naturalist*, vol. 125, no. 1, pp. 1–15, 1985.

[97] J. W. L. Beament, J. E. Treherne, and V. B. Wigglesworth, *Advances in insect physiology*, vol. 1. Academic Press, 2011.

[98] J. Y. Sun, Y. M. Wang, D. H. Chen, J. Tong, and C. X. Pan, "Differential constitutive equation of elytra cuticle by nanoindentation," in *Advanced Materials Research*, vol. 343, pp. 1133–1139, Trans Tech Publ, 2012.

[99] E. Greenhalgh, *Failure analysis and fractography of polymer composites*. Elsevier, 2009.

[100] M. J. Benton, "Studying function and behavior in the fossil record," *PLoS Biology*, vol. 8, no. 3, p. e1000321, 2010.

[101] A. Erdemir, T. M. Guess, J. Halloran, S. C. Tadepalli, and T. M. Morrison, "Considerations for reporting finite element analysis studies in biomechanics," *Journal of Biomechanics*, vol. 45, no. 4, pp. 625–633, 2012.

[102] F. W. Pelsue Jr and R. Zhang, "A review of the genus *Curculio* L. from China with descriptions of new taxa. Part I (Coleoptera: Curculionidae: Curculioninae: Curculionini)," *The Coleopterists' Bulletin*, pp. 125–142, 2000.

[103] F. W. Pelsue Jr, C. W. O'Brien, *et al.*, "A redefinition of the Curculionini of the world, with a key to subtribes and genera, and two new genera: *Pseudoculio* and *Megaoculis* (Coleoptera: Curculionidae: Curculioninae)," *Zootaxa*, vol. 3102, pp. 27–49, 2011.

[104] D. R. Whitehead, M. L. Chamorro, and R. S. Anderson, "An Illustrated Key to the Species of *Curculio* Linnaeus (Coleoptera: Curculionidae) of North America East of the Mississippi River," *Proceedings of the Entomological Society of Washington*, vol. 120, no. 3, pp. 616–642, 2018.

[105] A. C. Neville, *Biology of the arthropod cuticle*, vol. 4. Berlin: Springer Science & Business Media, 2012.

[106] S. R. Davis, "The weevil rostrum (coleoptera: Curculionoidea): internal structure and evolutionary trends," *Bulletin of the American Museum of Natural History*, vol. 2017, no. 416, pp. 1–77, 2017.

[107] A. Blanke, P. J. Watson, R. Holbrey, and M. J. Fagan, "Computational biomechanics changes our view on insect head evolution," *Proceedings of the Royal Society B: Biological Sciences*, vol. 284, no. 1848, p. 20162412, 2017.

[108] S. Kaliyamoorthy, S. N. Zill, R. D. Quinn, R. E. Ritzmann, and J. Choi, "Finite element analysis of strains in a *Blaberus* cockroach leg during climbing," in *Proceedings 2001 IEEE/RSJ International Conference on Intelligent Robots and Systems. Expanding the Societal Role of Robotics in the the Next Millennium (Cat. No. 01CH37180)*, vol. 2, pp. 833–838, IEEE, 2001.

[109] A. van der Meijden, T. Kleinteich, and P. Coelho, "Packing a pinch: functional implications of chela shapes in scorpions using finite element analysis," *Journal of Anatomy*, vol. 220, no. 5, pp. 423–434, 2012.

[110] J.-L. Boevé, V. Ducarme, T. Mertens, P. Bouillard, and S. Angeli, "Surface structure, model and mechanism of an insect integument adapted to be damaged easily," *Journal of Nanobiotechnology*, vol. 2, no. 1, p. 10, 2004.

[111] L. P. Gibson, "A Catalog of the Coleoptera of America North of Mexico Family: Curculionidae Subfamily: Curculioninae)," *Agriculture Handbook*, vol. 529-143b, no. 529, pp. 1–12, 1985.

[112] F. H. F. H. Chittenden, "Classification of the nut curculios (formerly *Balaninus*) of boreal america," *Entomologica Americana*, vol. 7, pp. 129–207, 1927.

[113] J. Michels and S. Gorb, "Detailed three-dimensional visualization of resilin in the exoskeleton of arthropods using confocal laser scanning microscopy," *Journal of Microscopy*, vol. 245, no. 1, pp. 1–16, 2012.

[114] M. Smolla, M. Ruchty, M. Nagel, and C. J. Kleineidam, "Clearing pigmented insect cuticle to investigate small insects' organs *in situ* using confocal laser-scanning microscopy (clsm)," *Arthropod Structure and Development*, vol. 43, no. 2, pp. 175–181, 2014.

[115] P. J. Roache, "Perspective: a method for uniform reporting of grid refinement studies," *Journal of Fluids Engineering*, vol. 116, no. 3, pp. 405–413, 1994.

[116] P. J. Roache, "Quantification of uncertainty in computational fluid dynamics," *Annual Review of Fluid Mechanics*, vol. 29, no. 1, pp. 123–160, 1997.

[117] P. J. Roache, *Verification and validation in computational science and engineering*. Hermosa Publishers, 1998.

[118] H. Hepburn, I. Joffe, N. Green, and K. Nelson, "Mechanical properties of a crab shell," *Comparative Biochemistry and Physiology Part A: Physiology*, vol. 50, no. 3, pp. 551–IN13, 1975.

[119] C. W. O'Brien and G. J. Wibmer, *Annotated checklist of the weevils (Curculionidae sensu lato) of North America, Central America, and the West Indies (Coleoptera: Curculionoidea)*. Ann Arbor, Michigan: American Entomological Institute, 1982.

[120] E. L. McCullough, K. J. Ledger, D. M. O'Brien, and D. J. Emlen, "Variation in the allometry of exaggerated rhinoceros beetle horns," *Animal Behavior*, vol. 109, pp. 133–140, 2015.

[121] A. W. Shingleton and W. A. Frankino, "New perspectives on the evolution of exaggerated traits," *BioEssays*, vol. 35, no. 2, pp. 100–107, 2013.

[122] K. F. Gauss and P. Pesic, *General investigations of curved surfaces*. Courier Corporation, 2005.

[123] J. Glass, "Smooth-curve interpolation: A generalized spline-fit procedure," *BIT Numerical Mathematics*, vol. 6, no. 4, pp. 277–293, 1966.

[124] M. A. Malcolm, "On the computation of nonlinear spline functions," *SIAM Journal on Numerical Analysis*, vol. 14, no. 2, pp. 254–282, 1977.

[125] C. Woodford, "Smooth curve interpolation," *BIT Numerical Mathematics*, vol. 9, no. 1, pp. 69–77, 1969.

[126] E. Jones, T. Oliphant, P. Peterson, *et al.*, "SciPy: Open source scientific tools for Python," 2001.

[127] T. Oliphant, "NumPy: A guide to NumPy." USA: Trelgol Publishing, 2006–.

[128] L. J. Van Vliet and P. W. Verbeek, "Curvature and bending energy in digitized 2d and 3d images," in *Proceedings of the Scandinavian Conference on Image Analysis*, vol. 2, pp. 1403–1403, 1993.

[129] J. M. Sullivan, "Curves of finite total curvature," in *Discrete differential geometry*, pp. 137–161, Springer, 2008.

[130] N. Shubin, C. Tabin, and S. Carroll, "Deep homology and the origins of evolutionary novelty," *Nature*, vol. 457, no. 7231, p. 818, 2009.

[131] R. W. Scotland, "Deep homology: a view from systematics," *Bioessays*, vol. 32, no. 5, pp. 438–449, 2010.

APPENDIX A

COAUTHOR APPROVAL FOR CHAPTER 2

The chapter titled "A Multilayer Micromechanical Model of the Cuticle of *Curculio longinasus* Chittenden, 1927 (Coleoptera: Curculionidae)" was published earlier – 2016 – in the Journal of Structural Biology. The paper had four contributing authors. M. Andrew Jansen was the first and corresponding author. The original publication can be found at: `https://doi.org/10.1016/j.jsb.2016.05.007`

Sudhanshu Singh, Nikhilesh Chawla, and Nico Franz have all consented for the publication to be included in this dissertation by M. Andrew Jansen.

APPENDIX B

SUPPLEMENTARY SCRIPT FILES FOR CHAPTER 3

Raw data, diagnostic plots, scripts, and outputs are available online at:

`https://github.com/entojansen/curculio-tensile`

B.1 Python Script - Tensile Test Data Processing

appendix3/tensile.py

```
# -*- coding: utf-8 -*-
'''
Created on Tue Aug  1 13:59:50 2017

@author: Flashcock
'''

import os
from scipy.stats import linregress as linreg
from itertools import takewhile
from numpy import array, poly1d, sqrt, absolute, arcsin, pi
from scipy.optimize import curve_fit, minimize_scalar
from scipy.integrate import quad
import matplotlib.pyplot as plt
import matplotlib.patches as mpatches
from mpl_toolkits.mplot3d import Axes3D
from numpy import log as ln

class specimen:
    '''
    Args should be formatted as follows:
        asuid (str or int), species (str), length (str), exo (str), endo (str),
        total (str), N (list [float]), mm (list [float]), Sec (list [float]).
    These are converted to their respective types below and used to calculate
        true and engineering stress and strain, young's modulus, and UTS.
    '''
    def __init__(self, asuid, species, length, exo, endo, total, N, mm, Sec):
        self.__asuid__ = asuid
        self.__species__ = species.lower()

        self.__length__ = float(length)
        self.__exo__ = float(exo)
        self.__endo__ = float(endo)
        self.__total__ = float(total)

        self.__N__ = array(N)
        self.__mm__ = array(mm) - min(mm)
        self.__Sec__ = array(Sec) - Sec[0]

        self.__sigmaN__ = self.__N__ / self.__total__ #P/A0
        self.__epsilonN__ = (self.__mm__ / self.__length__) #dL/L0
        self.__sigmaT__ = self.__sigmaN__ * (1 + self.__epsilonN__) #s(1+e)
        self.__epsilonT__ = ln(1 + self.__epsilonN__) #ln(1+e)

        self.__fmax__ = max(N)
        self.__uts__ = max(self.__sigmaN__) #evaluated from engineering stress

        self.__dmax__ = max(self.__mm__)
        self.__ufs__ = max(self.__epsilonN__) #evaluated from engineering strain


        self.__Eindex__ = []
        lower = self.__ufs__ * 0
        upper = self.__ufs__ * 0.33
        self.__Eindex__.append(len([x for x in takewhile(lambda x: x[1] <= lower,
            enumerate(self.__epsilonN__))]))
        self.__Eindex__.append(len([y for y in takewhile(lambda y: y[1] <= upper,
            enumerate(self.__epsilonN__))]))
        xvals = self.__epsilonN__[self.__Eindex__[0]:self.__Eindex__[1]]
        yvals = self.__sigmaN__[self.__Eindex__[0]:self.__Eindex__[1]]
```

```
        self.__E__ = linreg(xvals, yvals) #engineering stress and strain via Hooke's Law

        self.__Etanl__ = self.__E__[0]

        t_upper = 0
        t_lower = 0

        for i in range(len(self.__epsilonN__)-1):
            ub = self.__epsilonN__[i+1]
            lb = self.__epsilonN__[i]
            uh = self.__sigmaN__[i+1]
            lh = self.__sigmaN__[i]
            t_upper += (ub - lb) * uh
            t_lower += (ub - lb) * lh

        self.__U__ = (t_upper + t_lower) / 2

    def asuid(self):
        return self.__asuid__

    def species(self):
        return self.__species__

    def length(self):
        return self.__length__

    def exo(self):
        return self.__exo__

    def endo(self):
        return self.__endo__

    def total(self):
        return self.__total__

    def N(self):
        return self.__N__

    def mm(self):
        return self.__mm__

    def Sec(self):
        return self.__Sec__

    def sigmaN(self):
        return self.__sigmaN__

    def epsilonN(self):
        return self.__epsilonN__

    def sigmaT(self):
        return self.__sigmaT__

    def epsilonT(self):
        return self.__epsilonT__

    def Eindex(self, index):
        return self.__Eindex__[index]

    def recalcE(self, lower=0.00, upper=0.015, graphical=False, normal=False, limits='E_limits.txt'):
        self.__Eindex__ = []
        if normal:
            eps = self.__epsilonT__
            sig = self.__sigmaT__
        else:
            eps = self.__epsilonN__
            sig = self.__sigmaN__
        if graphical:
            file = open(limits, 'r')
```

```
            for line in file:
                asuid, species, lims = line[:-1].split('|', 2)
                if asuid == self.__asuid__:
                    x, y = lims.split(',')
                    lowerg = float(x[1:])
                    upperg = float(y[:-1])
                else:
                    pass
            self.__Eindex__.append(len([x for x in takewhile(lambda x: x[1] <= lowerg
                , enumerate(self.__Sec__))]))
            self.__Eindex__.append(len([y for y in takewhile(lambda y: y[1] <= upperg
                , enumerate(self.__Sec__))]))

        else:
            self.__Eindex__=[0, 1]
            low = False
            high = False
            while (not low) and (not high):
                for i, c in enumerate(self.__epsilonN__):
                    if (c >=lower) and (not low):
                        self.__Eindex__[0] = i
                        low = True
                    elif (c >= upper) and (not high):
                        self.__Eindex__[1] = i
                        high = True
                    else:
                        pass
        xvals = eps[self.__Eindex__[0] : self.__Eindex__[1]]
        yvals = sig[self.__Eindex__[0] : self.__Eindex__[1]]

        self.__E__ = linreg(xvals, yvals) #engineering stress and strain via Hooke's
            Law

    def E(self, index = 0):
        return self.__E__[index]

    def Etanl(self):
        return self.__Etanl__

    def fmax(self):
        return self.__fmax__

    def uts(self):
        return self.__uts__

    def dmax(self):
        return self.__dmax__

    def ufs(self):
        return self.__ufs__

    def U(self):
        return self.__U__

def as_si(x, ndp):
    s = '{x:0.{ndp:d}e}'.format(x=x, ndp=ndp)
    m, e = s.split('e')
    return r'{m:s}\times 10^{{{e:d}}}'.format(m=m, e=int(e))

def get_files(path='.\data'):
    '''
    Retrieves filenames in directory.
    '''
    filelist = os.listdir(path)
    return filelist

def spec_data(files, dims='imagedata.csv'):
    '''
    Returns a set of specimens.
    '''
    spec_set = set()
```

```
196
197     file1 = open(dims, 'r')
198     for line in file1:
199         if line[0] == 'A':
200             pass
201         else:
202             asuid, species, length, exo, endo, total = line[:-1].split(',', 5)
203             N = []
204             mm = []
205             Sec = []
206             normal_order = True
207             for name in files:
208                 if name == '{}-{}-edit.dat'.format(asuid, species):
209                     file2=open('.\data\\' + name,'r')
210                     for line in file2:
211                         if line[0] == 'S':
212                             normal_order = False
213                         elif line[0] in '1234567890':
214                             x, y, z = line[:-1].split('\t', 2)
215                             if normal_order:
216                                 N.append(float(x))
217                                 mm.append(float(y))
218                                 Sec.append(float(z))
219                             else:
220                                 N.append(float(z))
221                                 mm.append(float(y))
222                                 Sec.append(float(x))
223                         else:
224                             pass
225                     file2.close()
226                     identifier, etc= name[:-9].split('-')
227                     spec = specimen(asuid, species, length, exo, endo, total, N, mm,
                            Sec)
228                     spec_set.add(spec)
229                 else:
230                     pass
231     file1.close()
232     return spec_set
233
234 def stress_strain(spec_set, save=True, i=0, j=-1):
235     for spec in spec_set:
236         ssplot, (ax1, ax3) = plt.subplots(2, sharex=False)
237
238         ax1.plot(spec.Sec()[i:j], spec.N()[i:j], color='b')
239         ax1.set_xlabel('Time (s)')
240         ax1.set_ylabel('Axial Force (N)', color='b')
241         ax1.tick_params('y', colors='b')
242         ax1.set_title('Tensile Test Raw Data - ASUHIC_{} - Curculio {}'.format(spec.
                asuid(), spec.species()))
243
244         ax2 = ax1.twinx()
245         ax2.plot(spec.Sec()[i:j], spec.mm()[i:j], color='r')
246         ax2.set_ylabel('Axial Displacement (mm)', color='r')
247         ax2.tick_params('y', colors='r')
248
249         # ax3.plot(spec.epsilonT()[i:j], spec.sigmaT()[i:j], color = 'gray')
250         ax3.plot(spec.epsilonN()[i:j], spec.sigmaN()[i:j], color = 'black')
251         ax3.set_ylabel('Stress (MPa)')
252         ax3.set_xlabel('Strain (dL/L0)')
253
254         print(spec.asuid()+' '+spec.species())
255         new_l = spec.ufs() * 0.00
256         new_u = spec.ufs() * 0.33
257         spec.recalcE(lower = new_l, upper = new_u, graphical=False, normal=False)
258         ax3.plot(spec.epsilonN()[spec.Eindex(0):spec.Eindex(1)],
259                  spec.E()*spec.epsilonN()[spec.Eindex(0):spec.Eindex(1)] + spec.E(1),
260                  color='r')
261
262         ax3.plot([min(spec.epsilonN()), max(spec.epsilonN()[0:-1])],
263                  [min(spec.sigmaN()), max(spec.sigmaN()[0:-1])],
264                  color='gray')
```

```
265
266         # true = mpatches.Patch(color='gray', label='True')
267         eng = mpatches.Patch(color='black', label='Engineering')
268         E1 = mpatches.Patch(color='r', label='E_low = {}MPa'.format(int(round(spec.
                Etanl()))))
269         E2 = mpatches.Patch(color='gray', label='E_sec = {}MPa'.format(int(round(spec
                .uts() / spec.ufs()))))
270         ax3.legend(handles=[eng, E1, E2], loc=2, fontsize = 6)
271         #ax3.set_title('Stress vs. Nominal Strain')
272         #ax3.set_xlim(0, 1)
273         #ax3.set_ylim(0, 300)
274         if save:
275             ssplot.savefig('plots/rawdata/{}-{}.pdf'.format(spec.asuid(), spec.
                    species()))
276             #plt.close()
277         else:
278             plt.show()
279             #plt.close()
280             print('Plot not saved!!')
281
282 def xyplot(spec_set, save = True):
283     spl = []
284     regx = []
285     regy = []
286
287     fig = plt.figure()
288     ax = fig.add_subplot(111)
289
290     #plt.ylim(0,0.04)
291     #plt.xlim(0,8)
292     xlab = 'test (units)'
293     ylab = 'test (units)'
294     ax.set_xlabel(xlab)
295     ax.set_ylabel(ylab)
296     ax.set_title('{}_vs_{}.pdf'.format(xlab, ylab))
297
298     car = mpatches.Patch(color='r', label='caryae')
299     pro = mpatches.Patch(color='lightcoral', label='proboscideus')
300     uni = mpatches.Patch(color='b', label='uniformis')
301     hum = mpatches.Patch(color='skyblue', label='humeralis')
302     sul = mpatches.Patch(color='dodgerblue', label='sulcatulus')
303     vic = mpatches.Patch([], [], color='navy', label='victoriensis')
304     ax.legend(handles=[car, pro, hum, sul, uni, vic], loc=4, fontsize = 7)
305
306     for spec in spec_set:
307         new_l = spec.ufs() * 0.67
308         new_u = spec.ufs() * 1.00
309         spec.recalcE(lower = new_l, upper = new_u, graphical=False, normal=False)
310         x = ln(spec.length())
311         y = ln(spec.Etanl())
312         #spec.uts() / spec.ufs()
313
314         if spec.species() == 'caryae':
315             ax.plot(x, y, color='r', marker ='o')
316         elif spec.species() == 'proboscideus':
317             ax.plot(x, y, color='lightcoral', marker ='o')
318         elif spec.species() == 'uniformis':
319             ax.plot(x, y, color='b', marker ='o')
320         elif spec.species() == 'humeralis':
321             ax.plot(x, y, color='skyblue', marker ='o')
322         elif spec.species() == 'sulcatulus':
323             ax.plot(x, y, color='dodgerblue', marker ='o')
324         elif spec.species() == 'victoriensis':
325             ax.plot(x, y, color='navy', marker ='o')
326         else:
327             pass
328
329         regx.append(x)
330         regy.append(y)
331         spl.append(str(x)+' '+str(y)+' '+spec.asuid()+' '+spec.species())
332
```

```
    x = array(regx)
    y = array(regy)
    regline = linreg(x, y)
    ax.plot(x, regline[0]*x+regline[1], color='black')
    ax.text(0.03,
            3,
            r'$y={:.3f}x+{:.3f}$'.format(regline[0], regline[1])
            +'\n'
            +r'$R={:.3f}$'.format(regline[2])
            +'\n'
            #+r'$p={:.3f}$'.format(regline[3]),
            +r'$p={0:s}$'.format(as_si(regline[3], 2)),
            fontsize=10)

    for  i in sorted(spl):
        print(i)

    plt.show()

    if save:
        fig.savefig('plots/xyplots/{}_vs_{}.pdf'.format(xlab, ylab))
        #plt.close()
    else:
        #plt.close()
        print('Plot not saved!!')

    print('m = {}'.format(regline[0]),
          'b = {}'.format(regline[1]),
          'r = {}'.format(regline[2]),
          'p = {}'.format(regline[3]),
          'std_err = {}'.format(regline[4]),
          sep='\n')

def xyzplot(spec_set):
    spl = []
    regx = []
    regy = []
    regz = []
    xyzfig = plt.figure()
    ax = Axes3D(xyzfig)
    for spec in spec_set:
        spec.recalcE(graphical=False, normal=False)
        x = (spec.length())
        y = (spec.U())
        z = (spec.exo() / spec.endo())
        if spec.species() == 'caryae':
            ax.scatter(x, y, z, c='r')
        elif spec.species() == 'proboscideus':
            ax.scatter(x, y, z, c='lightcoral')
        elif spec.species() == 'uniformis':
            ax.scatter(x, y, z, c='b')
        elif spec.species() == 'humeralis':
            ax.scatter(x, y, z, c='navy')
        elif spec.species() == 'sulcatulus':
            ax.scatter(x, y, z, c='dodgerblue')
        elif spec.species() == 'victoriensis':
            ax.scatter(x, y, z, c='skyblue')
        else:
            pass
        regx.append(x)
        regy.append(y)
        regz.append(z)
        spl.append(str(x)+' '+str(y)+' '+str(z)+' '+spec.asuid()+' '+spec.species())
    x = array(regx)
    y = array(regy)
    z = array(regz)
    ax.set_xlabel('Length')
    ax.set_ylabel('Strain')
    ax.set_zlabel('Stress')
    #regline = linreg(x, y, z)
    #plt.plot(x, regline[0]*x+regline[1], color='black')
```

```
404     #plt.ylim(0,0.04)
405     #plt.xlim(0,8)
406     for  i in sorted(spl):
407         print(i)
408     plt.show()
409     #print('m = {}'.format(regline[0]), 'b = {}'.format(regline[1]), 'r = {}'.format(
            regline[2]), 'p = {}'.format(regline[3]), 'std_err = {}'.format(regline[4]),
            sep='\n')
410
411 def write_data(specimens, filename = 'tensile.csv'):
412     outfile=open(filename,'w')
413     print('asuid,species,specimen,length,exo,endo,total,fmax,uts,dmax,ufs,Etanl,Etanh
            ,Esec,Ut', file=outfile)
414     humeralis = 0
415     caryae = 0
416     proboscideus = 0
417     sulcatulus = 0
418     uniformis = 0
419     victoriensis = 0
420     current_sp = 0
421     for spec in specimens:
422         if spec.species() == 'humeralis':
423             humeralis += 1
424             current_sp = humeralis
425         elif spec.species() == 'caryae':
426             caryae += 1
427             current_sp = caryae
428         elif spec.species() == 'proboscideus':
429             proboscideus += 1
430             current_sp = proboscideus
431         elif spec.species() == 'sulcatulus':
432             sulcatulus += 1
433             current_sp = sulcatulus
434         elif spec.species() == 'uniformis':
435             uniformis += 1
436             current_sp = uniformis
437         elif spec.species() == 'victoriensis':
438             victoriensis += 1
439             current_sp = victoriensis
440         else:
441             print('unrecognized species')
442         print(spec.asuid(),
443               spec.species(),
444               spec.species()+str(current_sp),
445               spec.length(),
446               spec.exo(),
447               spec.endo(),
448               spec.total(),
449               spec.fmax(),
450               spec.uts(),
451               spec.dmax(),
452               spec.ufs(),
453               spec.Etanl(),
454               spec.E(),
455               spec.uts() / spec.ufs(),
456               spec.U(),
457               sep=',',
458               file=outfile)
459     outfile.close()
460
461 def main():
462     specimens = spec_data(get_files())
463     stress_strain(specimens, save=True)
464     xyplot(specimens, save=False)
465     #xyzplot(specimens)
466     write_data(specimens)
467     return specimens
468
469 testlib = main()
```

appendix3/tensile.py

B.2 R Script - Phylogenetic Regression

appendix3/phylo_regress.R

```
# Andrew Jansen
# created x.10.2018

# Miscellaneous Functions ------------------------------------------------------
# Import the data
GetData = function(file.name) {
  test.data = data.frame(read.csv(file.name, sep = ','))
  return(test.data)
}

# Analysis 1 -------------------------------------------------------------------
# Fits models with and without log transformation and phylogenetic covariance
Analysis1 = function(phylogeny, raw.data) {

  # Fit models with variable transformation and phylogenetic covariance
  simple.model = lme(phenotype ~ cofactor,
                     random = ~ 1 | species,
                     data = raw.data,
                     method = 'ML')

  simple.brownian = lme(phenotype ~ cofactor,
                        random = ~ 1 | species,
                        data = raw.data,
                        correlation = phylogeny,
                        method = 'ML')

  y.transformed = lme(log(phenotype) ~ cofactor,
                          random = ~ 1 | species,
                          data = raw.data,
                          method = 'ML')

  y.brownian = lme(log(phenotype) ~ cofactor,
                           random = ~ 1 | species,
                           data = raw.data,
                           correlation = phylogeny,
                           method = 'ML')

  x.transformed = lme(phenotype ~ log(cofactor),
                      random = ~ 1 | species,
                      data = raw.data,
                      method = 'ML')

  x.brownian = lme(phenotype ~ log(cofactor),
                   random = ~ 1 | species,
                   data = raw.data,
                   correlation = phylogeny,
                   method = 'ML')

  xy.transformed = lme(log(phenotype) ~ log(cofactor),
                       random = ~ 1 | species,
                       data = raw.data,
                       method = 'ML')

  xy.brownian = lme(log(phenotype) ~ log(cofactor),
                    random = ~ 1 | species,
                    data = raw.data,
                    correlation = phylogeny,
                    method = 'ML')

  # Summary of model fit and assumption verification, done for each model type
  # No transformation of
  writeLines(strrep('-',80))
  writeLines('\n\nNo transformation of variables\n\n')
  writeLines(strrep('-',80))
  print(summary(simple.model))
  print(anova(simple.model))
  print(leveneTest(residuals(simple.model,
```

```
                            type = 'normalized') ~ raw.data$species,
                  data = raw.data))
print(shapiro.test(residuals(simple.model, type = 'normalized')))
r2sigma = r2beta(simple.model, method = 'sgv')
print(r2sigma)

print(summary(simple.brownian))
print(anova(simple.brownian))
print(leveneTest(residuals(simple.brownian,
                            type = 'normalized') ~ raw.data$species,
                  data = raw.data))
print(shapiro.test(residuals(simple.brownian, type = 'normalized')))
r2sigma.brownian = r2beta(simple.brownian, method = 'sgv')
print(r2sigma.brownian)

# R2 fit test of covariance structure for each transformation
print(r2dt(x = r2sigma, y = r2sigma.brownian))

# Natural log transformation of independent variable
writeLines(strrep('-',80))
writeLines('\n\nNatural log transformation of independent variable\n\n')
writeLines(strrep('-',80))
print(summary(y.transformed))
print(anova(y.transformed))
print(leveneTest(residuals(y.transformed,
                            type = 'normalized') ~ raw.data$species,
                  data = raw.data))
print(shapiro.test(residuals(y.transformed, type = 'normalized')))
r2sigma = r2beta(y.transformed, method = 'sgv')
print(r2sigma)

print(summary(y.brownian))
print(anova(y.brownian))
print(leveneTest(residuals(y.brownian,
                            type = 'normalized') ~ raw.data$species,
                  data = raw.data))
print(shapiro.test(residuals(y.brownian, type = 'normalized')))
r2sigma.brownian = r2beta(y.brownian, method = 'sgv')
print(r2sigma.brownian)

print(r2dt(x = r2sigma, y = r2sigma.brownian))

# Natural log transformation of dependent variable
writeLines(strrep('-',80))
writeLines('\n\nNatural log transformation of dependent variable\n\n')
writeLines(strrep('-',80))
print(summary(x.transformed))
print(anova(x.transformed))
print(leveneTest(residuals(x.transformed,
                            type = 'normalized') ~ raw.data$species,
                  data = raw.data))
print(shapiro.test(residuals(x.transformed, type = 'normalized')))
r2sigma = r2beta(x.transformed, method = 'sgv')
print(r2sigma)

print(summary(x.brownian))
print(anova(x.brownian))
print(leveneTest(residuals(x.brownian,
                            type = 'normalized') ~ raw.data$species,
                  data = raw.data))
print(shapiro.test(residuals(x.brownian, type = 'normalized')))
r2sigma.brownian = r2beta(x.brownian, method = 'sgv')
print(r2sigma.brownian)

print(r2dt(x = r2sigma, y = r2sigma.brownian))

# Natural log transformation of all variables
writeLines(strrep('-',80))
writeLines('\n\nNatural log transformation of both variables\n\n')
writeLines(strrep('-',80))
print(summary(xy.transformed))
```

```
  print(anova(xy.transformed))
  print(leveneTest(residuals(xy.transformed,
                             type = 'normalized') ~ raw.data$species,
                   data = raw.data))
  print(shapiro.test(residuals(xy.transformed, type = 'normalized')))
  r2sigma = r2beta(xy.transformed, method = 'sgv')
  print(r2sigma)

  print(summary(xy.brownian))
  print(anova(xy.brownian))
  print(leveneTest(residuals(xy.brownian,
                             type = 'normalized') ~ raw.data$species,
                   data = raw.data))
  print(shapiro.test(residuals(xy.brownian, type = 'normalized')))
  r2sigma.brownian = r2beta(xy.brownian, method = 'sgv')
  print(r2sigma.brownian)

  print(r2dt(x = r2sigma, y = r2sigma.brownian))

  print(lrtest(simple.brownian, x.brownian, y.brownian, xy.brownian))
  print(AIC(simple.brownian, x.brownian, y.brownian, xy.brownian))
}

# Analysis 2 ------------------------------------------------------------------
# Tests hypothesis that endo is correlated with fmax, and that exo is not
Analysis2 = function(phylogeny, raw.data) {

  # Fit models with and without phylogenetic covariance
  full.model = lme(log(fmax) ~ endo * exo,
                        random = ~ 1 | species,
                        data = raw.data,
                        correlation = phylogeny,
                        method = 'ML')

  full.simple = lme(log(fmax) ~ endo * exo,
                    random = ~ 1 | species,
                    data = raw.data,
                    method = 'ML')

  # Compare with and without phylogenetic covariance
  writeLines(strrep('-',80))
  writeLines('\n\nCompare with and without phylogenetic covariance\n\n')
  writeLines(strrep('-',80))
  print(summary(full.model))
  print(anova(full.model))
  print(leveneTest(residuals(full.model,
                             type = 'normalized') ~ raw.data$species,
                   data = raw.data))
  print(shapiro.test(residuals(full.model, type = 'normalized')))
  r2sigma = r2beta(full.model, method = 'sgv')
  print(r2sigma)

  print(summary(full.simple))
  print(anova(full.simple))
  print(leveneTest(residuals(full.simple,
                             type = 'normalized') ~ raw.data$species,
                   data = raw.data))
  print(shapiro.test(residuals(full.simple, type = 'normalized')))
  r2sigma.simple = r2beta(full.simple, method = 'sgv')
  print(r2sigma.simple)

  print(r2dt(x = r2sigma, y = r2sigma.simple))

  # Fit reduced models for hypothesis testing
  endo.model = lme(log(fmax) ~ endo,
                   random = ~ 1 | species,
                   data = raw.data,
                   correlation = phylogeny,
                   method = 'ML')

  exo.model = lme(log(fmax) ~ exo,
```

```
                  random = ~ 1 | species,
                  data = raw.data,
                  correlation = phylogeny,
                  method = 'ML')

  # R2 calculation for hypothesis testing
  writeLines(strrep('-',80))
  writeLines('\n\nR2 calculation for hypothesis testing\n\n')
  writeLines(strrep('-',80))
  r2m.full = r2beta(full.model, method = 'nsj')
  r2m.endo = r2beta(endo.model, method = 'nsj')
  r2m.exo = r2beta(exo.model, method = 'nsj')

  print(summary(r2m.full))
  print(summary(r2m.endo))
  print(summary(r2m.exo))

  print(r2dt(r2m.full, r2m.endo))
  print(r2dt(r2m.full, r2m.exo))
  print(r2dt(r2m.endo, r2m.exo, cor = FALSE))

  print(plot(r2m.full, r2mthd = 'nsj'))
  print(plot(r2sigma, r2mthd = 'sgv'))

  print(anova(full.model, endo.model))
  print(lrtest(full.model, endo.model))
  print(anova(full.model, exo.model))
  print(lrtest(full.model, exo.model))

  # Residual diagnositcs for full model
  print(plot(full.model,
             resid(., type = 'normalized') ~ fitted(.),
             abline = 0))

  dev.copy(pdf,
           'plots/rplots/exo_endo_fitted.pdf',
           width = 3,
           height = 3)
  dev.off()

  print(plot(full.model,
             resid(., type = 'normalized') ~ fitted(.) | species,
             abline = 0))

  dev.copy(pdf,
           'plots/rplots/exo_endo_resid_species.pdf',
           width = 4.5,
           height = 3)
  dev.off()

  model.residuals = residuals(full.model, type = 'normalized')
  qqnorm(model.residuals, ylab = 'Residual Quantiles', main = NULL)
  abline(0, 1, col = 'blue')

  dev.copy(pdf,
           'plots/rplots/exo_endo_resid_qqplot.pdf',
           width = 3,
           height = 3)
  dev.off()
}

# Analysis 3 ------------------------------------------------------------------
# Final model fitting, hypothesis testing, and phylogenetic signal
Analysis3 = function(phylogeny.vcv, phylogeny.tree, raw.data, axis.labels) {

  # Fit preferred model
  final.model = lme(phenotype ~ cofactor,
                    random = ~ 1 | species,
                    data = raw.data,
                    correlation = phylogeny.vcv,
                    method = 'ML')
```

```
281
282  # REDUNDANT
283  writeLines(strrep('-',80))
284  writeLines('\n\nRedundant readout of chosen model, see above\n\n')
285  writeLines(strrep('-',80))
286  print(summary(final.model))
287
288  # Phylogenetic signal testing in residuals
289  model.residuals = residuals(final.model,
290                              type = 'normalized',
291                              level = 0:1)[, 2]
292  trait = phylo4d(phylogeny.tree, tip.data = model.residuals)
293
294  x = axis.labels[2]
295  y = axis.labels[1]
296
297  # Abouheif's Cmean
298  writeLines(strrep('-',80))
299  writeLines('\n\nAbouheifs Cmean\n\n')
300  writeLines(strrep('-',80))
301  abouheif.test = abouheif.moran(trait, method = 'oriAbouheif')
302  print(abouheif.test)
303  plot(abouheif.test)
304
305  dev.copy(pdf,
306           paste('plots/rplots/', y, x, 'abouheif.pdf', sep = '_'),
307           width = 3,
308           height = 3)
309  dev.off()
310
311  # Moran's I
312  writeLines(strrep('-',80))
313  writeLines('\n\nMorans I\n\n')
314  writeLines(strrep('-',80))
315  moran.test = abouheif.moran(trait, method='Abouheif')
316  print(moran.test)
317  plot(abouheif.test)
318
319  dev.copy(pdf,
320           paste('plots/rplots/', y, x, 'moran.pdf', sep = '_'),
321           width = 3,
322           height = 3)
323  dev.off()
324
325  # If an error pops up for tree with no branch lengths, add a column to the
326  # csv file, specimen, which has the species name and number.
327
328  # Pagel's lambda
329  writeLines(strrep('-',80))
330  writeLines('\n\nPagels lambda\n\n')
331  writeLines(strrep('-',80))
332  pagel.test = phylosig(tree = phylogeny.tree,
333                        x = model.residuals,
334                        method='lambda',
335                        test=TRUE)
336  print(pagel.test)
337
338  # Blomberg's K
339  writeLines(strrep('-',80))
340  writeLines('\n\nBlombergs kappa\n\n')
341  writeLines(strrep('-',80))
342  blomberg.test = phylosig(tree = phylogeny.tree,
343                           x = model.residuals,
344                           method='K',
345                           test=TRUE)
346  print(blomberg.test)
347
348  # R2 hypothesis testing
349  writeLines(strrep('-',80))
350  writeLines('\n\nR2 hypothesis testing\n\n')
351  writeLines(strrep('-',80))
```

```
  r2.marginal = r2beta(final.model, method = 'nsj', partial = FALSE)
  r2.sigma = r2beta(final.model, method = 'sgv', partial = FALSE)

  print(summary(r2.marginal))
  print(summary(r2.sigma))

}

# Analysis 4 ------------------------------------------------------------------
# Data visualization and graphing
Analysis4 = function(phylogeny, raw.data, axis.labels) {

  # Fit preferred model
  final.model = lme(phenotype ~ cofactor,
                    random = ~ 1 | species,
                    data = raw.data,
                    correlation = phylogeny,
                    method = 'ML')

  # create data.frame with new values for predictors
  cofactor = raw.data$cofactor
  new.dat <- data.frame(cofactor)

  # predict normalized
  new.dat$pred <- predict(final.model, newdata = new.dat, level = 0)

  # create design matrix
  Designmat <- model.matrix(eval(eval(final.model$call$fixed)[-2]),
                            new.dat[-ncol(new.dat)])

  # compute standard error for predictions
  predvar = diag(Designmat %*% final.model$varFix %*% t(Designmat))
  new.dat$SE = sqrt(predvar)
  new.dat$SE2 = sqrt(predvar + final.model$sigma ^ 2)

  # plot marginal effects
  gg = ggplot(new.dat, aes(x = cofactor, y = pred)) +
    geom_ribbon(aes(ymin = pred - 2 * SE2, ymax = pred + 2 * SE2),
                alpha = 0.2,
                fill = 'black') +
    geom_ribbon(aes(ymin = pred - 2 * SE, ymax = pred + 2 * SE),
                alpha = 0.2,
                fill = 'black') +
    geom_line(color = 'black', size = 1) +
    geom_point(data = raw.data,
               aes(x = cofactor, y = phenotype, color = species)) +
    scale_y_continuous(axis.labels[1]) +
    scale_x_continuous(axis.labels[2])
  plot(gg)

  x = axis.labels[2]
  y = axis.labels[1]

  dev.copy(pdf,
           paste('plots/rplots/', y, x, 'marginal_effects.pdf', sep = '_'),
           width = 4.5,
           height = 3)
  dev.off()

  # plot transformed conditional residuals vs. fitted values
  print(plot(final.model,
             resid(., type = 'normalized') ~ fitted(.),
             abline = 0))

  dev.copy(pdf,
           paste('plots/rplots/', y, x, 'fitted.pdf', sep = '_'),
           width = 3,
           height = 3)
  dev.off()

  print(plot(final.model,
```

```
            resid(., type = 'normalized') ~ fitted(.) | species,
            abline = 0))

  dev.copy(pdf,
           paste('plots/rplots/', y, x, 'species.pdf', sep = '_'),
           width = 4.5,
           height = 3)
  dev.off()

  print(plot(final.model, species ~ resid(., type = 'normalized')))

  dev.copy(pdf,
           paste('plots/rplots/', y, x, 'boxplot.pdf', sep = '_'),
           width = 4.5,
           height = 3)
  dev.off()

  model.residuals = residuals(final.model, type = 'normalized')
  qqnorm(model.residuals, ylab = 'Residual Quantiles', main = NULL)
  abline(0, 1, col = 'blue')

  dev.copy(pdf,
           paste('plots/rplots/', y, x, 'qqplot.pdf', sep = '_'),
           width = 3,
           height = 3)
  dev.off()
}

# Main Function ------------------------------------------------------------------
main = function() {
  # Clear workspace
  rm(list = ls())
  setwd(paste('C:/Users/Andrew/Documents/GitHub/',
              'curculio-tensile/analysis', sep=''))

  # Load gplots for plotCI
  library(ggplot2)
  library(ggeffects)
  library(ggthemes)
  library(RColorBrewer)
  library(car)
  library(ape)
  library(phylobase)
  library(adephylo)
  library(MCMCglmm)
  library(phytools)
  library(lmtest)
  library(nlme)
  library(r2glmm)
  library(nortest)


  # Create folder for plots
  dir.create('plots/rplots')

  # Minimal margins on graphs
  par(mar = c(4, 4, 1.1, 0.6) + 0.1)

  # Import raw data and phylogeny
  file.name = 'tensile.csv'
  raw.data = GetData(file.name)
  raw.data$ratio = raw.data$exo / raw.data$endo
  row.names(raw.data) = raw.data$specimen

  tree.text = paste('(((uniformis1, uniformis2, uniformis3,',
                    'uniformis4, uniformis5), (caryae1,',
                    'caryae2, caryae3, caryae4)),',
                    '(((proboscideus1, proboscideus2,',
                    'proboscideus3), (sulcatulus1,',
                    'sulcatulus2, sulcatulus3, sulcatulus4)),',
                    '((humeralis1, humeralis2), victoriensis1)));')
```

```
tree.star = ape::read.tree(text = tree.text)
tree.star$edge.length = rep(1,nrow(tree.star$edge))

# Generate phylogenetic variance-covariance matrix, Brownian motion
phylo.vcv = corBrownian(1, tree.star)

plot(tree.star, type = 'phylogram', edge.width = 2)

dev.copy(pdf,
         'plots/rplots/phylogeny.pdf',
         width = 6,
         height = 3)
dev.off()

# All output to file
sink(file = 'phylo_regress_output.txt', append =FALSE)
print('PHYLOGENETIC REGRESSION OUTPUT')
sink()

sink(file = 'phylo_regress_output.txt', append = TRUE)

# Model exploration and initial testing of phylogenetic covariance
# Comparison 1a, model covariance and transformation
readline(prompt = 'fmax vs. endo: press enter to continue.')
writeLines(strrep('=',80))
writeLines(strrep('=',80))
writeLines('Comparison 1a: fmax vs. endo')
writeLines(strrep('=',80))
writeLines(strrep('=',80))
raw.data$phenotype = raw.data$fmax
raw.data$cofactor = raw.data$endo
Analysis1(phylo.vcv, raw.data)

# Comparison 1b, model covariance and transformation
readline(prompt = 'fmax vs. exo: press enter to continue.')
writeLines(strrep('=',80))
writeLines(strrep('=',80))
writeLines('Comparison 1b: fmax vs. exo')
writeLines(strrep('=',80))
writeLines(strrep('=',80))
raw.data$phenotype = raw.data$fmax
raw.data$cofactor = raw.data$exo
Analysis1(phylo.vcv, raw.data)

# Comparison 1c, model covariance and transformation
readline(prompt = 'uts vs. ratio: press enter to continue.')
writeLines(strrep('=',80))
writeLines(strrep('=',80))
writeLines('Comparison 1c: uts vs. ratio')
writeLines(strrep('=',80))
writeLines(strrep('=',80))
raw.data$phenotype = raw.data$uts
raw.data$cofactor = raw.data$ratio
Analysis1(phylo.vcv, raw.data)

# Comparison 2a, model covariance and transformation
readline(prompt = 'ufs vs. Etanl: press enter to continue.')
writeLines(strrep('=',80))
writeLines(strrep('=',80))
writeLines('Comparison 2a: ufs vs. Etanl')
writeLines(strrep('=',80))
writeLines(strrep('=',80))
raw.data$phenotype = raw.data$ufs
raw.data$cofactor = raw.data$Etanl
Analysis1(phylo.vcv, raw.data)

# Comparison 2b, model covariance and transformation
readline(prompt = 'ufs vs. Esec: press enter to continue.')
writeLines(strrep('=',80))
writeLines(strrep('=',80))
writeLines('Comparison 2b: ufs vs. Esec')
```

```
565   writeLines(strrep('=',80))
566   writeLines(strrep('=',80))
567   raw.data$phenotype = raw.data$ufs
568   raw.data$cofactor = raw.data$uts / raw.data$ufs
569   Analysis1(phylo.vcv, raw.data)
570
571   # Comparison 2c, model covariance and transformation
572   readline(prompt = 'U vs. Etanl: press enter to continue.')
573   writeLines(strrep('=',80))
574   writeLines(strrep('=',80))
575   writeLines('Comparison 2c: U vs. Etanl')
576   writeLines(strrep('=',80))
577   writeLines(strrep('=',80))
578   raw.data$phenotype = raw.data$U
579   raw.data$cofactor = raw.data$Etanl
580   Analysis1(phylo.vcv, raw.data)
581
582   # Comparison 2d, model covariance and transformation
583   readline(prompt = 'U vs. Esec: press enter to continue.')
584   writeLines(strrep('=',80))
585   writeLines(strrep('=',80))
586   writeLines('Comparison 2d: U vs. Esec')
587   writeLines(strrep('=',80))
588   writeLines(strrep('=',80))
589   raw.data$phenotype = raw.data$U
590   raw.data$cofactor = raw.data$uts / raw.data$ufs
591   Analysis1(phylo.vcv, raw.data)
592
593   # Comparison 3a, model covariance and transformation
594   readline(prompt = 'Etan low vs. length: press enter to continue.')
595   writeLines(strrep('=',80))
596   writeLines(strrep('=',80))
597   writeLines('Comparison 3a: Etan low vs. length')
598   writeLines(strrep('=',80))
599   writeLines(strrep('=',80))
600   raw.data$phenotype = raw.data$Etanl
601   raw.data$cofactor = raw.data$length
602   Analysis1(phylo.vcv, raw.data)
603
604   # Comparison 3b, model covariance and transformation
605   readline(prompt = 'Esec vs. length: press enter to continue.')
606   writeLines(strrep('=',80))
607   writeLines(strrep('=',80))
608   writeLines('Comparison 3b: Esec vs. length')
609   writeLines(strrep('=',80))
610   writeLines(strrep('=',80))
611   raw.data$phenotype = raw.data$uts / raw.data$ufs
612   raw.data$cofactor = raw.data$length
613   Analysis1(phylo.vcv, raw.data)
614
615   # Comparison 1 Test, compound cross sectional area
616   readline(prompt = 'log(fmax) ~ endo + exo: press enter to continue.')
617   writeLines(strrep('=',80))
618   writeLines(strrep('=',80))
619   writeLines('Comparison 5: log(fmax) ~ endo + exo')
620   writeLines(strrep('=',80))
621   writeLines(strrep('=',80))
622   Analysis2(phylo.vcv, raw.data)
623
624   # Final model fitting, hypothesis testing, and phylogenetic signal
625   # Model 1a: log(fmax) ~ endo
626   readline(prompt = 'fmax vs. endo: press enter to continue.')
627   writeLines(strrep('=',80))
628   writeLines(strrep('=',80))
629   writeLines('Model 1a: log(fmax) ~ log(endo)')
630   writeLines(strrep('=',80))
631   writeLines(strrep('=',80))
632   raw.data$phenotype = log(raw.data$fmax)
633   raw.data$cofactor = log(raw.data$endo)
634   comparison = c('ln(Fmax [N])', 'ln(Endocuticle CSA [mm2])')
635   Analysis3(phylo.vcv, tree.star, raw.data, comparison)
```

```
636   Analysis4(phylo.vcv, raw.data, comparison)
637
638   # Model 1b: log(fmax) ~ exo
639   readline(prompt = 'fmax vs. exo: press enter to continue.')
640   writeLines(strrep('=',80))
641   writeLines(strrep('=',80))
642   writeLines('Model 1b: log(fmax) ~ exo')
643   writeLines(strrep('=',80))
644   writeLines(strrep('=',80))
645   raw.data$phenotype = log(raw.data$fmax)
646   raw.data$cofactor = log(raw.data$exo)
647   comparison = c('ln(Fmax [N])', 'ln(Exocuticle CSA [mm2])')
648   Analysis3(phylo.vcv, tree.star, raw.data, comparison)
649   Analysis4(phylo.vcv, raw.data, comparison)
650
651   # Model 1c:log(uts) ~ log(ratio)
652   readline(prompt = 'uts vs. ratio: press enter to continue.')
653   writeLines(strrep('=',80))
654   writeLines(strrep('=',80))
655   writeLines('Model 1c:log(uts) ~ log(ratio)')
656   writeLines(strrep('=',80))
657   writeLines(strrep('=',80))
658   raw.data$phenotype = log(raw.data$uts)
659   raw.data$cofactor = log(raw.data$ratio)
660   comparison = c('ln(Ultimate Strength [MPa])',
661                  'ln(Exocuticle-Endocuticle Ratio)')
662   Analysis3(phylo.vcv, tree.star, raw.data, comparison)
663   Analysis4(phylo.vcv, raw.data, comparison)
664
665   # Model 2a: log(ufs) ~ log(Etanl)
666   readline(prompt = 'ufs vs. Etanl: press enter to continue.')
667   writeLines(strrep('=',80))
668   writeLines(strrep('=',80))
669   writeLines('Model 2a: log(ufs) ~ log(Etanl)')
670   writeLines(strrep('=',80))
671   writeLines(strrep('=',80))
672   raw.data$phenotype = log(raw.data$ufs)
673   raw.data$cofactor = log(raw.data$Etanl)
674   comparison = c('ln(Ultimate Strain [mm2])', 'ln(Elastic Modulus [MPa])')
675   Analysis3(phylo.vcv, tree.star, raw.data, comparison)
676   Analysis4(phylo.vcv, raw.data, comparison)
677
678   # Model 2b: log(ufs) ~ log(Esec)
679   readline(prompt = 'ufs vs. Esec: press enter to continue.')
680   writeLines(strrep('=',80))
681   writeLines(strrep('=',80))
682   writeLines('Model 2b: log(ufs) ~ log(Esec)')
683   writeLines(strrep('=',80))
684   writeLines(strrep('=',80))
685   raw.data$phenotype = log(raw.data$ufs)
686   raw.data$cofactor = log(raw.data$Esec)
687   comparison = c('ln(Ultimate Strain [mm2])', 'ln(Secant Modulus [MPa])')
688   Analysis3(phylo.vcv, tree.star, raw.data, comparison)
689   Analysis4(phylo.vcv, raw.data, comparison)
690
691   # Model 2c: log(U) ~ log(Etanl)
692   readline(prompt = 'U vs. Etanl: press enter to continue.')
693   writeLines(strrep('=',80))
694   writeLines(strrep('=',80))
695   writeLines('Model 2a: log(U) ~ log(Etanl)')
696   writeLines(strrep('=',80))
697   writeLines(strrep('=',80))
698   raw.data$phenotype = log(raw.data$U)
699   raw.data$cofactor = log(raw.data$Etanl)
700   comparison = c('ln(Fracture Toughness [Jm-3])', 'ln(Elastic Modulus [MPa])')
701   Analysis3(phylo.vcv, tree.star, raw.data, comparison)
702   Analysis4(phylo.vcv, raw.data, comparison)
703
704   # Model 2d: log(U) ~ log(Esec)
705   readline(prompt = 'U vs. Esec: press enter to continue.')
706   writeLines(strrep('=',80))
```

```
  writeLines(strrep('=',80))
  writeLines('Model 2b: log(U) ~ log(Esec)')
  writeLines(strrep('=',80))
  writeLines(strrep('=',80))
  raw.data$phenotype = log(raw.data$U)
  raw.data$cofactor = log(raw.data$Esec)
  comparison = c('ln(Fracture Toughness [Jm-3])', 'ln(Secant Modulus [MPa])')
  Analysis3(phylo.vcv, tree.star, raw.data, comparison)
  Analysis4(phylo.vcv, raw.data, comparison)

  # Model 3a: log(Etanl) ~ log(length)
  readline(prompt = 'Etan low vs. length: press enter to continue.')
  writeLines(strrep('=',80))
  writeLines(strrep('=',80))
  writeLines('Model 3a: log(Etanl) ~ log(length)')
  writeLines(strrep('=',80))
  writeLines(strrep('=',80))
  raw.data$phenotype = log(raw.data$Etanl)
  raw.data$cofactor = log(raw.data$length)
  comparison = c('ln(Elastic Modulus [MPa])', 'ln(Rostrum Length [mm2])')
  Analysis3(phylo.vcv, tree.star, raw.data, comparison)
  Analysis4(phylo.vcv, raw.data, comparison)

  # Model 3b: log(Esec) ~ log(length)
  readline(prompt = 'Esec vs. length: press enter to continue.')
  writeLines(strrep('=',80))
  writeLines(strrep('=',80))
  writeLines('Model 3b: log(Esec) ~ log(length)')
  writeLines(strrep('=',80))
  writeLines(strrep('=',80))
  raw.data$phenotype = log(raw.data$Esec)
  raw.data$cofactor = log(raw.data$length)
  comparison = c('ln(Secant Modulus [MPa])', 'ln(Rostrum Length [mm2])')
  Analysis3(phylo.vcv, tree.star, raw.data, comparison)
  Analysis4(phylo.vcv, raw.data, comparison)

  #Close output file
  sink()
}

# Execute Code ----------------------------------------------------------------
main()
```

appendix3/phylo_regress.R

B.3 Matlab Script - Prediction of Effective Elastic Moduli

appendix3/effective_moduli.m

```
%Author: Andrew Jansen
%Date: January 2019
%Title: Effective moduli of Curculio cuticle

%-------------------------------------------------------------------------
%Definition of elastic constants by cuticle region
%-------------------------------------------------------------------------
%Elastic constants for exocuticle, denoted by 'x'
%E denotes Young's modulus along material axis denoted by number
Ex1 = 6.4;
Ex2 = 6.4;

%nu denotes Poisson ratio along material axes denoted by numbers
nux12 = 0.36;
nux21 = 0.36;

%G denotes shear modulus along material axes denoted by numbers
Gx12 = 2.5;

%Matrix of constants for exocuticle
exo = [Ex1 Ex2 nux12 nux21 Gx12];

%-------------------------------------------------------------------------
%For macrofiber (a.k.a. 'balken') layer in endocuticle, denoted by 'b'
Eb1 = 8.5;
Eb2 = 0.52;
nub12 = 0.49;
nub21 = 0.03;
Gb12 = 0.17;

endo = [Eb1 Eb2 nub12 nub21 Gb12];

cuticle = [exo; endo];
%-------------------------------------------------------------------------
%Cuticle lay-up: layer thicknesses, orientation angles & stacking sequence
%-------------------------------------------------------------------------
%sequence for basal portion of head
base_z = (1 / 480) * [-24 -12:-1 1:12 24]; %48 layers, 50 microns => mm
base_theta = 30 * [ 3:8 -(-5:0); 0:5 -(-8:-3)]; %30 deg angle sequence
%subtract 5 deg  after matrix to maximize flexural stiffness
base_seq = [1, repelem(2, 24) 1]; %1 for exocuticle, 2 for endocuticle
base_layup = [base_z; 0 base_theta(1:24) 0; base_seq];

%-------------------------------------------------------------------------
%sequence for apical portion of head
apex_z = (1 / 800) * [-40 -36:4:-4 -3:-1 1:3 4:4:36 40];
apex_theta = [0 repelem(-45, 6) repelem(45, 6);
    repelem(45, 6) repelem(-45, 6) 0];
apex_seq = [1, repelem(2, 24) 1]; %same sequence as base
apex_layup = [apex_z; apex_theta(1:26); apex_seq];

%-------------------------------------------------------------------------
%permutations: base thickness, apex angle; base angle, apex thickness
mod_theta_layup = [base_layup(1, :); apex_layup(2, :); base_layup(3, :)];

mod_z_layup = [apex_layup(1, :); base_layup(2, :); base_layup(3, :)];

%-------------------------------------------------------------------------
%Run main function
%-------------------------------------------------------------------------
main(base_layup, mod_z_layup, mod_theta_layup, apex_layup, cuticle);

%-------------------------------------------------------------------------
%Function declarations
%-------------------------------------------------------------------------
function Q = reduced(constants)
%function to calculate 2D reduced stiffness matrix
```

```
%Extract elastic constants
E1 = constants(1);
E2 = constants(2);
nu12 = constants(3);
nu21 = constants(4);
G12 = constants(5);

%p denotes the denominator used to find elements of stiffness matrix
p = 1 - nu12 * nu21;

%E*nu is averaged to correct for rounding error in the published values
%because Eb1 * nub21 = Eb2 * nub12 is actually true for exo and endocuticle
Enu_avg = (E1 * nu21 + E2 * nu12) / 2;

Q11 = E1 / p;
Q12 = Enu_avg / p;
Q16 = 0;
Q21 = Enu_avg / p;
Q22 = E2 / p;
Q26 = 0;
Q61 = 0;
Q62 = 0;
Q66 = G12;
Q = [Q11 Q12 Q16; Q21 Q22 Q26; Q61 Q62 Q66];
end

%-------------------------------------------------------------------------
function T = transform(theta)
%function to generate transformation matrix (rotation about angle theta)
%this uses DEGREES, not radians
c = cosd(theta);
s = sind(theta);
T = [(c ^ 2) (s ^ 2) (2 * c * s);
    (s ^ 2) (c ^ 2) (-2 * c * s);
    (-c * s) (c * s) ((c ^ 2) - (s ^ 2))];
end

%-------------------------------------------------------------------------
function [A, D] = stiffness(materials, profile)
%funtion to calculate A, B, D matrices from material and layup
%materials(i,:) for the ith row, all columns (ie vector of elements in row)
A = zeros(3);
%Use this to check that B is actually zero, as needed
%B = zeros(3);
D = zeros(3);

for i = 1:size(profile, 2)
    lamina = profile(:, i);

    if lamina(1) < 0
        z_k1 = lamina(1);
        z_k = profile(1, (i + 1));
    else
        z_k = lamina(1);
        z_k1 = profile(1, (i - 1));
    end

    if (z_k == -z_k1) && (lamina(1) > 0)
        continue
    else
        theta = lamina(2);
        seq = lamina(3);
        Q = reduced(materials(seq, :));
        T = transform(theta);
        Q_k = T \ Q / T';
        A = A + Q_k * (z_k - z_k1);
        %Use this to check that B is actually zero, as needed
        %B = B + (1 / 2) * Q_k * ((z_k ^ 2) - (z_k1 ^ 2));
        D = D + (1 / 3) * Q_k * ((z_k ^ 3) - (z_k1 ^ 3));
    end
end
```

```
139
140 %Use this to check that B is actually zero, as needed
141 %disp(B)
142
143 end
144
145 %-------------------------------------------------------------------------
146 function elasticity = moduli(A, D, profile)
147 %funtion to calculate membrane and flexural elastic moduli along x-axis
148 A_star = inv(A);
149 D_star = inv(D);
150 z = profile(1, end) - profile(1, 1);
151
152 E_mx = 1 / (A_star(1) * z);
153 E_fx = 12 / (D_star(1) * (z ^ 3));
154 elasticity = [E_mx, E_fx];
155 end
156
157 %-------------------------------------------------------------------------
158 function main(base, layers, angles, apex, laminae)
159 %function accepts layups and produces elastic moduli
160 %call stiffness for each permutation
161 [A_base, D_base] = stiffness(laminae, base);
162 [A_layers, D_layers] = stiffness(laminae, layers);
163 [A_angles, D_angles] = stiffness(laminae, angles);
164 [A_apex, D_apex] = stiffness(laminae, apex);
165
166 base_moduli = moduli(A_base, D_base, base);
167 layer_moduli = moduli(A_layers, D_layers, layers);
168 angle_moduli = moduli(A_angles, D_angles, angles);
169 apex_moduli = moduli(A_apex, D_apex, apex);
170
171 fprintf('\nType\tMembrane\tFlexural\n')
172 fprintf('Base\t%6.4f GPa\t%6.4f GPa\n', base_moduli(1), base_moduli(2))
173 fprintf('Layers\t%6.4f GPa\t%6.4f GPa\n', layer_moduli(1), layer_moduli(2))
174 fprintf('Angles\t%6.4f GPa\t%6.4f GPa\n', angle_moduli(1), angle_moduli(2))
175 fprintf('Apex\t%6.4f GPa\t%6.4f GPa\n', apex_moduli(1), apex_moduli(2))
176 end
```

appendix3/effective_moduli.m

APPENDIX C

SUPPLEMENTARY SCRIPT FILES FOR CHAPTER 4

Due to their substantial size (24.5 GB), all raw data, job files, images, scripts, and output databases are not online, but are available upon request.

C.1 R Script - Predicting Margin of Safety

appendix4/phylo_predict.R

```r
# Andrew Jansen
# created x.10.2018

# Miscellaneous Functions ------------------------------------------------------
# Import the data
GetData = function(file.name) {
  test.data = data.frame(read.csv(file.name, sep = ','))
  return(test.data)
}


# Analysis 2 -------------------------------------------------------------------
# Tests hypothesis that endo is correlated with fmax, and that exo is not
Analysis2 = function(phylogeny, raw.data) {
  # Fit reduced models for hypothesis testing
  endo.model = lme(log(fmax) ~ log(endo),
                   random = ~ 1 | species,
                   data = raw.data,
                   correlation = phylogeny,
                   method = 'ML')

  caryae = data.frame('layup' = c('apical', 'basal', 'central', 'dorsal', 'forward'),
                      'exo' = c(0.006, 0.03, 0.022, 0.014, 0.014),
                      'species' = c('caryae', 'caryae', 'caryae', 'caryae', 'caryae')
                        )
  caryae$endo = 11/12*pi*((0.266/2-caryae$exo)^2-(0.266/2-0.06)^2)

  longi = data.frame('layup' = c('apical', 'basal', 'dorsal-basal'),
                     'exo' = c(0.005, 0.025, 0.0068),
                     'species' = c('longinasus', 'longinasus', 'longinasus'))
  longi$endo = 11/12*pi*((0.256/2-longi$exo)^2-(0.256/2-0.05)^2)

  sulc = data.frame('layup' = c('apical', 'basal', 'dorsal'),
                    'exo' = c(0.003, 0.015, 0.006),
                    'species' = c('sulcatulus', 'sulcatulus', 'sulcatulus'))
  sulc$endo = 11/12*pi*((0.202/2-sulc$exo)^2-(0.202/2-0.03)^2)

  caryae$pred = predict(endo.model, newdata = caryae)
  caryae$Fmax = exp(1)^caryae$pred
  caryae$Ut = caryae$Fmax/(((0.266/2)^2-(0.266/2-0.06)^2)*pi)
  caryae$Uc = caryae$Ut * 3

  longi$pred = predict(endo.model, newdata = longi, level = 0)
  longi$Fmax = exp(1)^longi$pred
  longi$Ut = longi$Fmax/(((0.256/2)^2-(0.256/2-0.05)^2)*pi)
  longi$Uc = longi$Ut * 3

  sulc$pred = predict(endo.model, newdata = sulc)
  sulc$Fmax = exp(1)^sulc$pred
  sulc$Ut = sulc$Fmax/(((0.202/2)^2-(0.202/2-0.03)^2)*pi)
  sulc$Uc = sulc$Ut * 3

  print(caryae)
  print(longi)
  print(sulc)
}

# Main Function ----------------------------------------------------------------
main = function() {
  # Clear workspace
  rm(list = ls())
```

```
  setwd(paste('C:/Users/Andrew/Documents/GitHub/',
              'curculio-fea/gitignore/models/factor of safety', sep=''))

  # Load gplots for plotCI
  library(ggplot2)
  library(ggeffects)
  library(ggthemes)
  library(RColorBrewer)
  library(car)
  library(ape)
  library(phylobase)
  library(adephylo)
  library(MCMCglmm)
  library(phytools)
  library(lmtest)
  library(nlme)
  library(r2glmm)
  library(nortest)

  # Import raw data and phylogeny
  file.name = 'tensile.csv'
  raw.data = GetData(file.name)
  raw.data$ratio = raw.data$exo / raw.data$endo
  row.names(raw.data) = raw.data$specimen

  tree.text = paste('(((uniformis1, uniformis2, uniformis3,',
                    'uniformis4, uniformis5), (caryae1,',
                    'caryae2, caryae3, caryae4)),',
                    '(((proboscideus1, proboscideus2,',
                    'proboscideus3), (sulcatulus1,',
                    'sulcatulus2, sulcatulus3, sulcatulus4)),',
                    '((humeralis1, humeralis2), victoriensis1)));')
  tree.star = ape::read.tree(text = tree.text)
  tree.star$edge.length = rep(1,nrow(tree.star$edge))

  # Generate phylogenetic variance-covariance matrix, Brownian motion
  phylo.vcv = corBrownian(1, tree.star)

  Analysis2(phylo.vcv, raw.data)
}

# Execute Code ----------------------------------------------------------------
main()
```

appendix4/phylo_predict.R

APPENDIX D

SUPPLEMENTARY SCRIPT FILES FOR CHAPTER 5

Raw data, images, diagnostic plots, scripts, and outputs are available online at: `https://github.com/entojansen/curculio-curvature`

D.1 Python Script - Curvature Analysis and Data Processing

appendix5/curve_analysis.py

```
# -*- coding: utf-8 -*-
"""
Created on Tue Sep 20 16:07:47 2016

@author: flashcock
"""

import os
from numpy import array, poly1d, sqrt, absolute, arctan
from scipy.optimize import curve_fit, minimize_scalar
from scipy.integrate import quad
import matplotlib.pyplot as plt
from svg.path import parse_path


def get_files(path = "."):
    """
    Retrieves filenames in directory, excluding curve_analysis.py and ".Metadata",
    which is assumed to be in the same folder. Metadata filenames are also extracted.
    """
    filelist = os.listdir(path)
    filelist.remove("curve_analysis.py")
    return filelist

def spec_data(files, normalize = 'off'):
    uids = []
    attributes = []
    for name in files:
        coordlist = []
        coordtemp = []
        if name[-4:] == ".svg":
            file=open(name,"r")
            for line in file:
                if " d=\"m" in line:
                    path = parse_path(line[10:-2])
                    coords = []
                    coords.append(str(path[0].point(0))[1:-2])
                    for obj in path:
                        pnt = obj.point(1)
                        p = str(pnt)
                        q = p[1:-2]
                        coords.append(q)
                elif " d=\"M" in line:
                    path = parse_path(line[10:-2])
                    coords = []
                    coords.append(str(path[0].point(0))[1:-2])
                    for obj in path:
                        pnt = obj.point(1)
                        p = str(pnt)
                        q = p[1:-2]
                        coords.append(q)
                else:
                    pass
            file.close()
            file = open(".Metadata/{}.tif.anx".format(name[:-4]), "r")
            for line in file:
                if "<MetresPerPixel>" in line:
                    scale = float(line.split("<MetresPerPixel>")[1].strip("</
                        MetresPerPixel>\n"))
                else:
                    pass
```

```
61              file.close()
62              for item in coords:
63                  x, y = item.split("+")
64                  #3333 because *1000 to get to mm from meters, and *3.333 to account
                        for the picture resizing in inkscape
65                  coordlist.append(((float(x) * scale * 3333), 10 - (float(y) * scale *
                         3333)))
66              if normalize == "chord":
67                  x1, y1 = coordlist[0]
68                  x2, y2 = coordlist[-1]
69                  chord = sqrt((x2 - x1) ** 2 + (y2 - y1) ** 2)
70                  for x, y in coordlist:
71                      coordtemp.append(((x / chord * 10), (y / chord * 10)))
72                  coordlist = coordtemp
73              elif normalize == "arc":
74                  popt, pcov = curve_fit(poly, array(coordlist)[:,0], array(coordlist)
                        [:,1])
75                  coeffs = popt
76                  [a, b, c, d, e, f, g, h, i] = coeffs.tolist()
77                  x1 = coordlist[0][0]
78                  x2 = coordlist[-1][0]
79                  s = quad(integrand, x1, x2, args=(a, b, c, d, e, f, g, h, i))
80                  arc = s[0]
81                  for x, y in coordlist:
82                      coordtemp.append(((x / arc * 10), (y / arc * 10)))
83                  coordlist = coordtemp
84              else:
85                  pass
86              genus, species, sex, identifier = name[:-4].split("_", 3)
87              uids.append(identifier)
88              attributes.append([genus, species, sex, coordlist])
89          else:
90              pass
91      spec_dict = {i:ii for i,ii in zip(uids, attributes)}
92      return spec_dict
93
94  def poly(x, a, b, c, d, e, f, g, h, i):
95      poly8=poly1d([a, b, c, d, e, f, g, h, i])
96      return poly8([x])[0]
97
98  def neg_curvature(x, a, b, c, d, e, f, g, h, i):
99      y = poly1d([a, b, c, d, e, f, g, h, i])
100     return absolute(y.deriv(2)([x])[0]) / ((1 + (y.deriv()([x])[0]) ** 2) ** 1.5) *
            -1
101
102 def energy(x, a, b, c, d, e, f, g, h, i):
103     y = poly1d([a, b, c, d, e, f, g, h, i])
104     return ((absolute(y.deriv(2)([x])[0]) / ((1 + (y.deriv()([x])[0]) ** 2) ** 1.5))
            ** 2) * ((1 + (y.deriv()([x])[0]) ** 2) ** 0.5)
105
106 def fit_poly(spec_dict, func = poly):
107     for value in spec_dict.values():
108         data = array(value[3])
109         popt, pcov = curve_fit(func, data[:,0], data[:,1])
110         value.append(popt)
111
112 def integrand(x, a, b, c, d, e, f, g, h, i):
113     return sqrt(1 + (poly1d([a, b, c, d, e, f, g, h, i]).deriv()([x])[0]) ** 2)
114
115 def arc_length(spec_dict):
116     for value in spec_dict.values():
117         coeffs = value[4]
118         [a, b, c, d, e, f, g, h, i] = coeffs.tolist()
119         x1 = value[3][0][0]
120         x2 = value[3][-1][0]
121         s = quad(integrand, x1, x2, args=(a, b, c, d, e, f, g, h, i))
122         value.append(s[0])
123         #print(s[0])
124
125 def chord_length(spec_dict, func = poly):
126     for value in spec_dict.values():
```

```
        x1 = value[3][0][0]
        x2 = value[3][-1][0]
        co = value[4]
        y1 = func(x1, co[0], co[1], co[2], co[3], co[4], co[5], co[6], co[7], co[8])
        y2 = func(x2, co[0], co[1], co[2], co[3], co[4], co[5], co[6], co[7], co[8])
        chord = sqrt((x2 - x1) ** 2 + (y2 - y1) ** 2)
        value.append(chord)

def max_curvature(spec_dict, func = neg_curvature, ygen = poly, normalize = "off"):
    for value in spec_dict.values():
        coeffs = value[4]
        [a, b, c, d, e, f, g, h, i] = coeffs.tolist()
        x1 = value[3][0][0]
        x2 = value[3][-1][0]
        if normalize == "chord":
            norv = 2
        elif normalize == "arc":
            norv = 2
        else:
            norv = 0.6
        result1 = minimize_scalar(func, bracket = (x1 + 0.001, norv), bounds = (x1,
            x2), args = (a, b, c, d, e, f, g, h, i), method = 'Golden')
        result2 = minimize_scalar(func, bracket = (x1 + 0.001, norv), bounds = (x1,
            x2), args = (a, b, c, d, e, f, g, h, i), method = 'bounded')
        if result1.x <= x1 or result1.x >= x2:
            result = result2
        else:
            kG = (func(result1.x, a, b, c, d, e, f, g, h, i) * -1)
            kb = (func(result2.x, a, b, c, d, e, f, g, h, i) * -1)
            if kG >= kb:
                result = result1
            else:
                result = result2
        value.append((func(result.x, a, b, c, d, e, f, g, h, i) * -1, result.x, ygen(
            result.x, a, b, c, d, e, f, g, h, i)))

def total_curvature(spec_dict):
    for value in spec_dict.values():
        coeffs = value[4]
        [a, b, c, d, e, f, g, h, i] = coeffs.tolist()
        x1 = value[3][0][0]
        x2 = value[3][-1][0]
        diff = x2-x1
        x2 = x2 - (0.1 * diff)
        p = poly1d([a, b, c, d, e, f, g, h, i])
        d1 = p.deriv()([x1, a, b, c, d, e, f, g, h, i])[0]
        d2 = p.deriv()([x2, a, b, c, d, e, f, g, h, i])[0]
        a1 = arctan(d1)
        a2 = arctan(d2)
        phi = a1 - a2
        value.append(phi)
        #print(value[1], a1*180/pi, a2*180/pi, value[8]*180/pi)

def bend_energy(spec_dict, func = energy):
    for value in spec_dict.values():
        coeffs = value[4]
        [a, b, c, d, e, f, g, h, i] = coeffs.tolist()
        x1 = value[3][0][0]
        x2 = value[3][-1][0]
        diff = x2-x1
        x2 = x2 - (0.1 * diff)
        s = quad(func, x1, x2, args=(a, b, c, d, e, f, g, h, i))
        value.append(s[0])
        #print(value[1], value[2], value[9])

def write_file(out, manual = False, norm = 'raw'):
    if manual:
        outfile = open(input("Enter name for output file: "),"w")
    else:
        fns = 'curves_' + norm + '.txt'
        outfile = open(fns, "w")
```

```
195         print("{}\t{}\t{}\t{}\t{}\t{}\t{}\t{}\t{}\t{}\t{}\t{}".format('asuid', 'genus', '
                species', 'sex', 'L_arc', 'L_chord', 'K_max', 'x_maxk', 'y_maxk', 'K_
                total', 'E'), file = outfile)
196     for key,val in out.items():
197         print("{}\t{}\t{}\t{}\t{}\t{}\t{}\t{}\t{}\t{}\t{}\t{}".format(key, val[0], val
                [1], val[2], val[5], val[6], val[7][0], val[7][1], val[7][2], val[8], val
                [9]), file = outfile)
198     outfile.close()
199
200 def plot(spec_dict, key, func = poly):
201     vals=array(spec_dict[key][3])
202     x = vals[:,0]
203     y = vals[:,1]
204     co = spec_dict[key][4]
205     yaj = func(x, co[0], co[1], co[2], co[3], co[4], co[5], co[6], co[7], co[8])
206     xcurve = spec_dict[key][7][1]
207     ycurve = spec_dict[key][7][2]
208     fig = plt.figure()
209     ax = fig.add_subplot(111)
210     ax.plot(x, y, "x", x, yaj, "r-", xcurve, ycurve, "o")
211     plt.title(spec_dict[key][0] + "_" + spec_dict[key][1] + "_" + spec_dict[key][2] +
            "_" + key)
212     ax.axis('equal')
213     plt.show()
214
215 def plot_curve(spec_dict, key, func = neg_curvature):
216     vals=array(spec_dict[key][3])
217     x = vals[:,0]
218     y = vals[:,1]
219     co = spec_dict[key][4]
220     yaj = func(x, co[0], co[1], co[2], co[3], co[4], co[5], co[6], co[7], co[8])
221     xcurve = spec_dict[key][7][1]
222     ycurve = spec_dict[key][7][2]
223     fig = plt.figure()
224     ax = fig.add_subplot(111)
225     ax.plot(x, y, "x", x, -yaj, "r-", xcurve, ycurve, "o")
226     plt.title(spec_dict[key][0] + "_" + spec_dict[key][1] + "_" + spec_dict[key][2] +
            "_" + key)
227     ax.axis('equal')
228     plt.show()
229
230 def plot_all_nicely(spec_dict, func1 = poly, func2 = neg_curvature, norm = 2):
231     #i = 0
232     for key in spec_dict:
233         print(key)
234         vals=array(spec_dict[key][3])
235         x = vals[:,0]
236         y = vals[:,1]
237         y0 = y[0]
238         diff = y0 - 2
239         y = y - diff
240         co = spec_dict[key][4]
241         ypoly = func1(x, co[0], co[1], co[2], co[3], co[4], co[5], co[6], co[7], co
                [8]) - diff
242         yk = func2(x, co[0], co[1], co[2], co[3], co[4], co[5], co[6], co[7], co[8])
243         xcurve = spec_dict[key][7][1]
244         ycurve = spec_dict[key][7][2] - diff
245 #         if i % 9 == 0:
246 #             fig = plt.figure()
247 #             i = 1
248 #         else:
249 #             i += 1
250         fig = plt.figure()
251         ax = fig.add_subplot(3,3,1)
252         ax.plot(x, y, "x", x, ypoly, "r-", x, -yk*norm, "g-", xcurve, ycurve, "o")
253         plt.title(spec_dict[key][0] + "_" + spec_dict[key][1] + "_" + spec_dict[key
                ][2] + "_" + key, fontsize = 12)
254         ax.axis('equal')
255         ax.set_aspect('equal', 'datalim')
256         plt.show()
257
```

```
258
259 def datagen(normtype = 'raw'):
260     spec_dict = spec_data(get_files(), normalize=normtype)
261     fit_poly(spec_dict, poly)
262     arc_length(spec_dict)
263     chord_length(spec_dict)
264     max_curvature(spec_dict, normalize=normtype)
265     total_curvature(spec_dict)
266     bend_energy(spec_dict)
267     write_file(spec_dict, norm = normtype)
268     #plot_all_nicely(spec_dict, norm = 10)
269
270
271 def main():
272     datagen()
273     print('done')
274     datagen(normtype = 'chord')
275     print('done')
276     datagen(normtype = 'arc')
277     print('done')
278
279 main()
```

appendix5/curve_analysis.py

D.2 R Script - Mixed Effects Modeling

appendix5/mixed_effects_curvature.R

```
# Andrew Jansen
# created iii.22.2018

# Miscellaneous Functions ------------------------------------------------------
# Import the data
GetData = function(file.name) {
  test.data = data.frame(read.csv(file.name, sep = ','))
  return(test.data)
}

# Analysis 1 -------------------------------------------------------------------
# Fits models with and without log transformation and phylogenetic covariance
Analysis1 = function(female, male) {

  # Fit models with variable transformation and phylogenetic covariance
  simple.female = lme(phenotype ~ cofactor,
                      random = ~ 1 | species,
                      data = female,
                      method = 'ML')

  simple.male = lme(phenotype ~ cofactor,
                    random = ~ 1 | species,
                    data = male,
                    method = 'ML')

  y.female = lme(log(phenotype) ~ cofactor,
                     random = ~ 1 | species,
                     data = female,
                     method = 'ML')

  y.male = lme(log(phenotype) ~ cofactor,
               random = ~ 1 | species,
               data = male,
               method = 'ML')

  x.female = lme(phenotype ~ log(cofactor),
                 random = ~ 1 | species,
                 data = female,
                 method = 'ML')

  x.male = lme(phenotype ~ log(cofactor),
               random = ~ 1 | species,
               data = male,
               method = 'ML')

  xy.female = lme(log(phenotype) ~ log(cofactor),
                  random = ~ 1 | species,
                  data = female,
                  method = 'ML')

  xy.male = lme(log(phenotype) ~ log(cofactor),
                random = ~ 1 | species,
                data = male,
                method = 'ML')

  # Summary of model fit and assumption verification, done for each model type
  # No transformation of variables
  writeLines(strrep('-',80))
  writeLines('\n\nNo transformation of variables\n\n')
  writeLines(strrep('-',80))
  print(summary(simple.female))
  print(anova(simple.female))
  print(leveneTest(residuals(simple.female,
                             type = 'normalized') ~ female$species,
                   data = female))
  print(shapiro.test(residuals(simple.female, type = 'normalized')))
  r2sigma.female = r2beta(simple.female, method = 'sgv')
```

```
print(r2sigma.female)

print(summary(simple.male))
print(anova(simple.male))
print(leveneTest(residuals(simple.male,
                           type = 'normalized') ~ male$species,
                 data = male))
print(shapiro.test(residuals(simple.male, type = 'normalized')))
r2sigma.male = r2beta(simple.male, method = 'sgv')
print(r2sigma.male)

# Natural log transformation of independent variable
writeLines(strrep('-',80))
writeLines('\n\nNatural log transformation of independent variable\n\n')
writeLines(strrep('-',80))
print(summary(y.female))
print(anova(y.female))
print(leveneTest(residuals(y.female,
                           type = 'normalized') ~ female$species,
                 data = female))
print(shapiro.test(residuals(y.female, type = 'normalized')))
r2sigma.female = r2beta(y.female, method = 'sgv')
print(r2sigma.female)

print(summary(y.male))
print(anova(y.male))
print(leveneTest(residuals(y.male,
                           type = 'normalized') ~ male$species,
                 data = male))
print(shapiro.test(residuals(y.male, type = 'normalized')))
r2sigma.male = r2beta(y.male, method = 'sgv')
print(r2sigma.male)

# Natural log transformation of dependent variable
writeLines(strrep('-',80))
writeLines('\n\nNatural log transformation of dependent variable\n\n')
writeLines(strrep('-',80))
print(summary(x.female))
print(anova(x.female))
print(leveneTest(residuals(x.female,
                           type = 'normalized') ~ female$species,
                 data = female))
print(shapiro.test(residuals(x.female, type = 'normalized')))
r2sigma.female = r2beta(x.female, method = 'sgv')
print(r2sigma.female)

print(summary(x.male))
print(anova(x.male))
print(leveneTest(residuals(x.male,
                           type = 'normalized') ~ male$species,
                 data = male))
print(shapiro.test(residuals(x.male, type = 'normalized')))
r2sigma.male = r2beta(x.male, method = 'sgv')
print(r2sigma.male)

# Natural log transformation of all variables
writeLines(strrep('-',80))
writeLines('\n\nNatural log transformation of both variables\n\n')
writeLines(strrep('-',80))
print(summary(xy.female))
print(anova(xy.female))
print(leveneTest(residuals(xy.female,
                           type = 'normalized') ~ female$species,
                 data = female))
print(shapiro.test(residuals(xy.female, type = 'normalized')))
r2sigma.female = r2beta(xy.female, method = 'sgv')
print(r2sigma.female)

print(summary(xy.male))
print(anova(xy.male))
print(leveneTest(residuals(xy.male,
```

```
                              type = 'normalized') ~ male$species,
                    data = male))
  print(shapiro.test(residuals(xy.male, type = 'normalized')))
  r2sigma.male = r2beta(xy.male, method = 'sgv')
  print(r2sigma.male)

  print(lrtest(simple.female, x.female, y.female, xy.female))
  print(AIC(simple.female, x.female, y.female, xy.female))

  print(lrtest(simple.male, x.male, y.male, xy.male))
  print(AIC(simple.male, x.male, y.male, xy.male))
}

# Analysis 2 ------------------------------------------------------------------
# Tests hypothesis that endo is correlated with fmax, and that exo is not
Analysis2 = function(females, males) {

  sex = 'female'
  xvar = females$norm_x_k
  yvar = females$norm_y_k
  zvar = females$L_arc
  scatterplot3d(zvar ~ xvar + yvar,
                pch = 16,
                color = 'navy',
                type = 'h',
                main = 'Female rostrm length and (X,Y) Kmax location',
                xlab = 'X coord [mm]',
                ylab = 'Y coord [mm]',
                zlab = 'Length [mm]')

  dev.copy(pdf,
           paste('plots/rplots/', sex, 'xy_len_3d.pdf', sep = '_'),
           width = 6,
           height = 6)
  dev.off()

  sex = 'male'
  xvar = males$norm_x_k
  yvar = males$norm_y_k
  zvar = males$L_arc
  scatterplot3d(zvar ~ xvar + yvar,
                pch = 16,
                color = 'navy',
                type = 'h',
                main = 'Male rostrm length and (X,Y) Kmax location',
                xlab = 'X coord [mm]',
                ylab = 'Y coord [mm]',
                zlab = 'Length [mm]')

  dev.copy(pdf,
           paste('plots/rplots/', sex, 'xy_len_3d.pdf', sep = '_'),
           width = 6,
           height = 6)
  dev.off()

  sex = 'female'
  xvar = log(females$norm_x_k)
  yvar = log(females$norm_y_k)
  zvar = log(females$L_arc)
  scatterplot3d(zvar ~ xvar + yvar,
                pch = 16,
                color = 'navy',
                type = 'h',
                main = 'Female ln(rostrm length and (X,Y) Kmax location)',
                xlab = 'ln(X coord [mm])',
                ylab = 'ln(Y coord [mm])',
                zlab = 'ln(Length [mm])')

  dev.copy(pdf,
           paste('plots/rplots/', sex, 'log(xy_len)_3d.pdf', sep = '_'),
           width = 6,
```

```
          height = 6)
  dev.off()

  sex = 'male'
  xvar = log(males$norm_x_k)
  yvar = log(males$norm_y_k)
  zvar = log(males$L_arc)
  scatterplot3d(zvar ~ xvar + yvar,
                pch = 16,
                color = 'navy',
                type = 'h',
                main = 'Male ln(rostrm length and (X,Y) Kmax location)',
                xlab = 'ln(X coord [mm])',
                ylab = 'ln(Y coord [mm])',
                zlab = 'ln(Length [mm])')

  dev.copy(pdf,
           paste('plots/rplots/', sex, 'log(xy_len)_3d.pdf', sep = '_'),
           width = 6,
           height = 6)
  dev.off()

}

# Analysis 3 ------------------------------------------------------------------
# Final model fitting, R2 hypothesis testing
Analysis3 = function(raw.data, axis.labels) {

  # Fit preferred model
  final.model = lme(phenotype ~ cofactor,
                    random = ~ 1 | species,
                    data = raw.data,
                    method = 'ML')

  # REDUNDANT
  writeLines(strrep('-',80))
  writeLines('\n\nRedundant readout of chosen model, see above\n\n')
  writeLines(strrep('-',80))
  print(summary(final.model))

  # R2 hypothesis testing
  writeLines(strrep('-',80))
  writeLines('\n\nR2 hypothesis testing\n\n')
  writeLines(strrep('-',80))
  r2.marginal = r2beta(final.model, method = 'nsj', partial = FALSE)
  r2.sigma = r2beta(final.model, method = 'sgv', partial = FALSE)

  print(summary(r2.marginal))
  print(summary(r2.sigma))
}

# Analysis 4 ------------------------------------------------------------------
# Data visualization and graphing
Analysis4 = function(raw.data, axis.labels, sex) {

  # Fit preferred model
  final.model = lme(phenotype ~ cofactor,
                    random = ~ 1 | species,
                    data = raw.data,
                    method = 'ML')

  # create data.frame with new values for predictors
  cofactor = raw.data$cofactor
  new.dat <- data.frame(cofactor)

  # predict normalized
  new.dat$pred <- predict(final.model, newdata = new.dat, level = 0)

  # create design matrix
  Designmat <- model.matrix(eval(eval(final.model$call$fixed)[-2]),
                            new.dat[-ncol(new.dat)])
```

```
281
282   # compute standard error for predictions
283   predvar = diag(Designmat %*% final.model$varFix %*% t(Designmat))
284   new.dat$SE = sqrt(predvar)
285   new.dat$SE2 = sqrt(predvar + final.model$sigma ^ 2)
286
287   # plot marginal effects
288   gg = ggplot(new.dat, aes(x = cofactor, y = pred)) +
289     geom_ribbon(aes(ymin = pred - 2 * SE2, ymax = pred + 2 * SE2),
290                 alpha = 0.2,
291                 fill = 'black') +
292     geom_ribbon(aes(ymin = pred - 2 * SE, ymax = pred + 2 * SE),
293                 alpha = 0.2,
294                 fill = 'black') +
295     geom_line(color = 'navy', size = 1) +
296     geom_point(data = raw.data,
297                aes(x = cofactor, y = phenotype)) +#, color = species)) +
298     scale_y_continuous(axis.labels[1]) +
299     scale_x_continuous(axis.labels[2])
300   plot(gg)
301
302   x = axis.labels[2]
303   y = axis.labels[1]
304
305   dev.copy(pdf,
306            paste('plots/rplots/', sex, y, x, 'marginal_effects.pdf', sep = '_'),
307            width = 3,
308            height = 3)
309   dev.off()
310
311   # plot transformed conditional residuals vs. fitted values
312   print(plot(final.model,
313              resid(., type = 'normalized') ~ fitted(.),
314              abline = 0))
315
316   dev.copy(pdf,
317            paste('plots/rplots/', sex, y, x, 'fitted.pdf', sep = '_'),
318            width = 3,
319            height = 3)
320   dev.off()
321
322   print(plot(final.model,
323              resid(., type = 'normalized') ~ fitted(.) | species,
324              abline = 0))
325
326   dev.copy(pdf,
327            paste('plots/rplots/', sex, y, x, 'species.pdf', sep = '_'),
328            width = 4.5,
329            height = 3)
330   dev.off()
331
332   print(plot(final.model, species ~ resid(., type = 'normalized')))
333
334   dev.copy(pdf,
335            paste('plots/rplots/', sex, y, x, 'boxplot.pdf', sep = '_'),
336            width = 4.5,
337            height = 3)
338   dev.off()
339
340   model.residuals = residuals(final.model, type = 'normalized')
341   qqnorm(model.residuals, ylab = 'Residual Quantiles', main = NULL)
342   abline(0, 1, col = 'blue')
343
344   dev.copy(pdf,
345            paste('plots/rplots/', sex, y, x, 'qqplot.pdf', sep = '_'),
346            width = 3,
347            height = 3)
348   dev.off()
349 }
350
351 # Main Function ------------------------------------------------------------
```

```
main = function() {
  # Clear workspace
  rm(list = ls())
  setwd(paste('C:/Users/Andrew/Documents/Current Projects',
              '/Curculio Curvature', sep=''))

  # Load gplots for plotCI
  library(ggplot2)
  library(ggeffects)
  library(ggthemes)
  library(RColorBrewer)
  library(car)
  library(ape)
  library(phylobase)
  library(adephylo)
  library(MCMCglmm)
  library(phytools)
  library(lmtest)
  library(nlme)
  library(r2glmm)
  library(nortest)
  library(scatterplot3d)


  # Create folder for plots
  dir.create('plots/rplots')

  # Minimal margins on graphs
  par(mar = c(4, 4, 1.1, 0.6) + 0.1)

  # Import raw data for females
  file.name = 'curvature_f.csv'
  raw.f = GetData(file.name)
  row.names(raw.f) = raw.f$asuid
  raw.f$norm_y_k = raw.f$norm_y_k + 10

  # Import raw data for males
  file.name = 'curvature_m.csv'
  raw.m = GetData(file.name)
  row.names(raw.m) = raw.m$asuid
  raw.m$norm_y_k = raw.m$norm_y_k + 10

  # All output to file
  sink(file = 'nlme_output.txt', append =FALSE)
  print('MIXED_EFFECT MODEL OUTPUT')
  sink()

  sink(file = 'nlme_output.txt', append = TRUE)

#-------------------------------------------------------------------------------

  # Model exploration and initial testing of phylogenetic covariance
  # Comparison 1, model covariance and transformation
  readline(prompt = 'kmax vs. length: press enter to continue.')
  writeLines(strrep('=',80))
  writeLines(strrep('=',80))
  writeLines('Comparison 1: kmax vs. length')
  writeLines(strrep('=',80))
  writeLines(strrep('=',80))
  raw.f$phenotype = raw.f$K_max
  raw.f$cofactor = raw.f$L_arc
  raw.m$phenotype = raw.m$K_max
  raw.m$cofactor = raw.m$L_arc
  Analysis1(raw.f, raw.m)

  # Comparison 2, model covariance and transformation
  readline(prompt = 'norm_kmax vs. length: press enter to continue.')
  writeLines(strrep('=',80))
  writeLines(strrep('=',80))
  writeLines('Comparison 2: norm_kmax vs. length')
  writeLines(strrep('=',80))
```

```
  writeLines(strrep('=',80))
  raw.f$phenotype = raw.f$norm_K_max
  raw.f$cofactor = raw.f$L_arc
  raw.m$phenotype = raw.m$norm_K_max
  raw.m$cofactor = raw.m$L_arc
  Analysis1(raw.f, raw.m)

  # Comparison 3, model covariance and transformation
  readline(prompt = 'x_kmax vs. length: press enter to continue.')
  writeLines(strrep('=',80))
  writeLines(strrep('=',80))
  writeLines('Comparison 3: x_kmax vs. length')
  writeLines(strrep('=',80))
  writeLines(strrep('=',80))
  raw.f$phenotype = raw.f$norm_x_k
  raw.f$cofactor = raw.f$L_arc
  raw.m$phenotype = raw.m$norm_x_k
  raw.m$cofactor = raw.m$L_arc
  Analysis1(raw.f, raw.m)

  # Comparison 4, model covariance and transformation
  readline(prompt = 'y_kmax vs. length: press enter to continue.')
  writeLines(strrep('=',80))
  writeLines(strrep('=',80))
  writeLines('Comparison 4: y_kmax vs. length')
  writeLines(strrep('=',80))
  writeLines(strrep('=',80))
  raw.f$phenotype = raw.f$norm_y_k
  raw.f$cofactor = raw.f$L_arc
  raw.m$phenotype = raw.m$norm_y_k
  raw.m$cofactor = raw.m$L_arc
  Analysis1(raw.f, raw.m)

  # Comparison 5, model covariance and transformation
  readline(prompt = 'ktotal vs. length: press enter to continue.')
  writeLines(strrep('=',80))
  writeLines(strrep('=',80))
  writeLines('Comparison 5: ktotal vs. length')
  writeLines(strrep('=',80))
  writeLines(strrep('=',80))
  raw.f$phenotype = raw.f$K_total
  raw.f$cofactor = raw.f$L_arc
  raw.m$phenotype = raw.m$K_total
  raw.m$cofactor = raw.m$L_arc
  Analysis1(raw.f, raw.m)

  # Comparison 6, model covariance and transformation
  readline(prompt = 'E vs. length: press enter to continue.')
  writeLines(strrep('=',80))
  writeLines(strrep('=',80))
  writeLines('Comparison 6: E vs. length')
  writeLines(strrep('=',80))
  writeLines(strrep('=',80))
  raw.f$phenotype = raw.f$E
  raw.f$cofactor = raw.f$L_arc
  raw.m$phenotype = raw.m$E
  raw.m$cofactor = raw.m$L_arc
  Analysis1(raw.f, raw.m)

  # Comparison 7, model covariance and transformation
  readline(prompt = 'norm_E vs. length: press enter to continue.')
  writeLines(strrep('=',80))
  writeLines(strrep('=',80))
  writeLines('Comparison 7: norm_E vs. length')
  writeLines(strrep('=',80))
  writeLines(strrep('=',80))
  raw.f$phenotype = raw.f$norm_E
  raw.f$cofactor = raw.f$L_arc
  raw.m$phenotype = raw.m$norm_E
  raw.m$cofactor = raw.m$L_arc
  Analysis1(raw.f, raw.m)
```

```
494
495 #------------------------------------------------------------------------------
496
497   # X, Y, Length 3d plot
498   readline(prompt = '3D Plot: press enter to continue.')
499   Analysis2(raw.f, raw.m)
500
501   # Model 3a: x_kmax ~ y_kmax
502   readline(prompt = 'ln(x_kmax vs. y_kmax): press enter to continue.')
503   writeLines(strrep('=',80))
504   writeLines(strrep('=',80))
505   writeLines('Comparison 3: ln(x_kmax vs. y_kmax)')
506   writeLines(strrep('=',80))
507   writeLines(strrep('=',80))
508   raw.f$phenotype = log(raw.f$norm_x_k)
509   raw.f$cofactor = log(raw.f$norm_y_k)
510   raw.m$phenotype = log(raw.m$norm_x_k)
511   raw.m$cofactor = log(raw.m$norm_y_k)
512   comparison = c('ln(Xmax [mm])', 'ln(Ymax [mm])')
513   sex.label = 'female'
514   Analysis3(raw.f, comparison)
515   Analysis4(raw.f, comparison, sex.label)
516   sex.label = 'male'
517   Analysis3(raw.m, comparison)
518   Analysis4(raw.m, comparison, sex.label)
519
520   # Model 3a: x_kmax ~ y_kmax
521   readline(prompt = 'x_kmax vs. y_kmax: press enter to continue.')
522   writeLines(strrep('=',80))
523   writeLines(strrep('=',80))
524   writeLines('Comparison 3: x_kmax vs. y_kmax')
525   writeLines(strrep('=',80))
526   writeLines(strrep('=',80))
527   raw.f$phenotype = raw.f$norm_x_k
528   raw.f$cofactor = raw.f$norm_y_k
529   raw.m$phenotype = raw.m$norm_x_k
530   raw.m$cofactor = raw.m$norm_y_k
531   comparison = c('Xmax [mm]', 'Ymax [mm]')
532   sex.label = 'female'
533   Analysis3(raw.f, comparison)
534   Analysis4(raw.f, comparison, sex.label)
535   sex.label = 'male'
536   Analysis3(raw.m, comparison)
537   Analysis4(raw.m, comparison, sex.label)
538
539 #------------------------------------------------------------------------------
540
541   # Final model fitting, hypothesis testing, and phylogenetic signal
542   # Model 1: kmax ~ length
543   readline(prompt = 'kmax vs. length: press enter to continue.')
544   writeLines(strrep('=',80))
545   writeLines(strrep('=',80))
546   writeLines('Comparison 1: kmax vs. length')
547   writeLines(strrep('=',80))
548   writeLines(strrep('=',80))
549   raw.f$phenotype = log(raw.f$K_max)
550   raw.f$cofactor = log(raw.f$L_arc)
551   raw.m$phenotype = log(raw.m$K_max)
552   raw.m$cofactor = log(raw.m$L_arc)
553   comparison = c('ln(Kmax [mm-1])', 'ln(arc length [mm])')
554   sex.label = 'female'
555   Analysis3(raw.f, comparison)
556   Analysis4(raw.f, comparison, sex.label)
557   sex.label = 'male'
558   Analysis3(raw.m, comparison)
559   Analysis4(raw.m, comparison, sex.label)
560
561   # Model 2: norm_kmax ~ length
562   readline(prompt = 'norm_kmax vs. length: press enter to continue.')
563   writeLines(strrep('=',80))
564   writeLines(strrep('=',80))
```

```
writeLines('Comparison 2: norm_kmax vs. length')
writeLines(strrep('=',80))
writeLines(strrep('=',80))
raw.f$phenotype = log(raw.f$norm_K_max)
raw.f$cofactor = log(raw.f$L_arc)
raw.m$phenotype = log(raw.m$norm_K_max)
raw.m$cofactor = log(raw.m$L_arc)
comparison = c('ln(adjusted Kmax [mm-1])', 'ln(arc length [mm])')
sex.label = 'female'
Analysis3(raw.f, comparison)
Analysis4(raw.f, comparison, sex.label)
sex.label = 'male'
Analysis3(raw.m, comparison)
Analysis4(raw.m, comparison, sex.label)

# Model 3: x_kmax ~ length
readline(prompt = 'x_kmax vs. length: press enter to continue.')
writeLines(strrep('=',80))
writeLines(strrep('=',80))
writeLines('Comparison 3: x_kmax vs. length')
writeLines(strrep('=',80))
writeLines(strrep('=',80))
raw.f$phenotype = log(raw.f$norm_x_k)
raw.f$cofactor = log(raw.f$L_arc)
raw.m$phenotype = log(raw.m$norm_x_k)
raw.m$cofactor = log(raw.m$L_arc)
comparison = c('ln(Xmax [mm])', 'ln(arc length [mm])')
sex.label = 'female'
Analysis3(raw.f, comparison)
Analysis4(raw.f, comparison, sex.label)
sex.label = 'male'
Analysis3(raw.m, comparison)
Analysis4(raw.m, comparison, sex.label)

# Model 4: y_kmax ~ length
readline(prompt = 'y_kmax vs. length: press enter to continue.')
writeLines(strrep('=',80))
writeLines(strrep('=',80))
writeLines('Comparison 4: y_kmax vs. length')
writeLines(strrep('=',80))
writeLines(strrep('=',80))
raw.f$phenotype = log(raw.f$norm_y_k)
raw.f$cofactor = log(raw.f$L_arc)
raw.m$phenotype = log(raw.m$norm_y_k)
raw.m$cofactor = log(raw.m$L_arc)
comparison = c('ln(Ymax [mm])', 'ln(arc length [mm])')
sex.label = 'female'
Analysis3(raw.f, comparison)
Analysis4(raw.f, comparison, sex.label)
sex.label = 'male'
Analysis3(raw.m, comparison)
Analysis4(raw.m, comparison, sex.label)

# Model 5: ktotal ~ length
readline(prompt = 'ktotal vs. length: press enter to continue.')
writeLines(strrep('=',80))
writeLines(strrep('=',80))
writeLines('Comparison 5: ktotal vs. length')
writeLines(strrep('=',80))
writeLines(strrep('=',80))
raw.f$phenotype = log(raw.f$K_total)
raw.f$cofactor = log(raw.f$L_arc)
raw.m$phenotype = log(raw.m$K_total)
raw.m$cofactor = log(raw.m$L_arc)
comparison = c('ln(Ktotal [rad])', 'ln(arc length [mm])')
sex.label = 'female'
Analysis3(raw.f, comparison)
Analysis4(raw.f, comparison, sex.label)
sex.label = 'male'
Analysis3(raw.m, comparison)
Analysis4(raw.m, comparison, sex.label)
```

```
636
637   # Model 6: E ~ length
638   readline(prompt = 'E vs. length: press enter to continue.')
639   writeLines(strrep('=',80))
640   writeLines(strrep('=',80))
641   writeLines('Comparison 6: E vs. length')
642   writeLines(strrep('=',80))
643   writeLines(strrep('=',80))
644   raw.f$phenotype = log(raw.f$E)
645   raw.f$cofactor = log(raw.f$L_arc)
646   raw.m$phenotype = log(raw.m$E)
647   raw.m$cofactor = log(raw.m$L_arc)
648   comparison = c('ln(E_bend [mm-1])', 'ln(arc length [mm])')
649   sex.label = 'female'
650   Analysis3(raw.f, comparison)
651   Analysis4(raw.f, comparison, sex.label)
652   sex.label = 'male'
653   Analysis3(raw.m, comparison)
654   Analysis4(raw.m, comparison, sex.label)
655
656   # Model 7: norm_E ~ length
657   readline(prompt = 'norm_E vs. length: press enter to continue.')
658   writeLines(strrep('=',80))
659   writeLines(strrep('=',80))
660   writeLines('Comparison 7: norm_E vs. length')
661   writeLines(strrep('=',80))
662   writeLines(strrep('=',80))
663   raw.f$phenotype = log(raw.f$norm_E)
664   raw.f$cofactor = log(raw.f$L_arc)
665   raw.m$phenotype = log(raw.m$norm_E)
666   raw.m$cofactor = log(raw.m$L_arc)
667   comparison = c('ln(adjusted E_bend [mm-1])', 'ln(arc length [mm])')
668   sex.label = 'female'
669   Analysis3(raw.f, comparison)
670   Analysis4(raw.f, comparison, sex.label)
671   sex.label = 'male'
672   Analysis3(raw.m, comparison)
673   Analysis4(raw.m, comparison, sex.label)
674
675   #Close output file
676   sink()
677 }
678
679 # Execute Code ---------------------------------------------------------------
680 main()
```

appendix5/mixed_effects_curvature.R